



The
University
Of
Sheffield.

Peptide Scaffolds for Nerve Tissue Engineering

By:

Weizhen Sun

A dissertation submitted to the University of Sheffield
for the degree of Doctor of Philosophy

The University of Sheffield
Faculty of Engineering
The Department of Chemical and Biological
Engineering

Submission date:
September 2021

Abstract

Scaffolds are one of the most important components in tissue engineering (TE), which should satisfy the following properties: biocompatibility, biodegradability, good mechanical properties and reliable batch production. Therefore, the material chosen for the fabrication of scaffolds is of critical importance. Silk fibroin (SF) is an attractive scaffold material that has been extensively used in TE. However, SF shows poor performance in nerve TE due to lack of active peptide sequences. Peptide amphiphiles are another type of recognized scaffold materials for TE. They can be further divided into a few sub-classes, of which ionic self-complementary peptides and lipidated peptide amphiphiles have been reported to be applied in nerve TE, while surfactant-like peptides have not as of yet. Therefore, in this study surfactant-like peptides will be a focus and their suitability will be investigated for nerve TE applications.

In this thesis, a variety of surfactant-like peptides, including typical examples (I₃K and I₃QGK) as well as custom designed short peptides sequences, based on active sequences found in the extracellular matrix (I₃RGDS, I₃KVAV, I₃YIGSR, I₃PDSGR and I₃PHSRN), were fabricated aiming at improving cellular attachment, cellular density and morphology of neuron cells. SF was used to act as a cell-repellent surface that allowed the coating or printing of short peptides onto flat surfaces. Atomic force microscopy (AFM) was used to characterise the dynamic process of self-assembly of surfactant-like peptides. The results indicated that the peptides I₃PDSGR and I₃PHSRN were unable to self-assemble into secondary structures, such as nanofibers, whilst the rest were able to. AFM was further used to characterise the topography of the peptide nanofibers adhered on SF surfaces, indicating nanofibers could strongly adhere on SF surfaces via charge-charge interactions or hydrogen bonding. Subsequently, these scaffolds were used to culture neuron cells *in vitro*. Live/dead and Immunofluorescence staining assays demonstrated that these short peptides had low cytotoxicity against neuron cells and also improved cellular attachment, cellular density and morphology of neuron cells. Amongst the investigated peptide sequences I₃RGDS was unable to regulate a morphology change of neuron cells. AFM was used to characterise the topography of neuron cells adhered on the scaffolds. Results also indicated all

short peptides could promote neurite outgrowth with the exception of I₃RGDS. However, I₃RGDS provided a synergistic effect with the peptides I₃YIGSR or I₃KVAV or a combination of both, resulting in a significantly improved morphology change of neuron cells. Moreover, the peptides I₃K and I₃QGK were patterned onto SF surfaces via inkjet printing, enabling the direct control of neuronal cell growth. This might provide a way to further analyse and understand neurite development and cell-cell interactions *in vitro*.

Dedication

The thesis is dedicated to my parents and younger sister.

For their endless love, meticulous care and attention.

Acknowledgements

First of all, I am grateful to my supervisor, Dr Xiubo (Jon) Zhao, who progressed me straight from a bachelor to a doctoral student. I also thank him for supporting me throughout my entire PHD, including experimental design, paper publications, conference attendance and so forth. More importantly, he invested lots of time to help me develop, which has positively influenced my life.

I also thank all the people in Jon's group who offered me support and guidance within last four years, in particular Dr David A. Gregory for supporting me with my research and improving my English skills and Dr Yi Zhang for helping me print the patterns I needed.

Furthermore, I would like to thank Professor John W. Haycock and his postdoctoral researcher Dr Caroline S. Taylor as well as my second supervisor Dr Patrick J. Smith for their helpful suggestions, contributions and allowing me to use their facilities.

I am also grateful to my friends, Zhaoyu Li and Lufei Yu for their encouragement and company when I hit rock bottom.

Last but not least, I would like to thank the entire CBE department for their support throughout my entire PhD as well as undergraduate career.

Publications

1. Sun, W.; Zhang, Y.; Gregory, D. A.; Jimenez-Franco, A.; Tomeh, M. A.; Lv, S.; Wang, J.; Haycock, J. W.; Lu, J. R.; Zhao, X., Patterning the neuronal cells via inkjet printing of self-assembled peptides on silk scaffolds. *Progress in Natural Science: Materials International* 2020, 30 (5), 686-696.
2. W. Sun, D.A. Gregory, M.A. Tomeh, X. Zhao, Silk Fibroin as a Functional Biomaterial for Tissue Engineering, *International Journal of Molecular Sciences* 22(3) (2021) 1499.
3. Sun, W.; Taylor, C. S.; Zhang, Y.; Gregory, D. A.; Tomeh, M. A.; Haycock, J. W.; Smith, P. J.; Wang, F.; Xia, Q.; Zhao, X., Cell guidance on peptide micropatterned silk fibroin scaffolds. *Journal of Colloid and Interface Science* 2021, 603, 380-390.
4. Tomeh, M. A.; Hadianamrei, R.; Sun, W.; Xu, D.; Brown, S.; Zhao, X., Stiffness-tuneable nanocarriers for controlled delivery of ASC-J9 into colorectal cancer cells. *Journal of Colloid and Interface Science* 2021, 594, 513-521.

Poster

"Patterning the neuronal cells via inkjet printing of self-assembled peptides on silk scaffolds" in 3D BioNet conference on 6th June 2019, Sheffield.

Table of contents

Abstract.....	i
Acknowledgements.....	iv
Publications.....	v
Poster.....	v
Table of contents	vi
List of figures.....	ix
List of tables.....	xi
1. Introduction.....	1
1. 1. Silk Fibroin as a Functional Biomaterial for Tissue Engineering.....	1
1.1.1. Introduction	1
1.1.2. Sources of silk and silk fibroin.....	3
1.1.3. Properties of silk fibroin.....	5
1.1.4. Silk fibroin dissolution techniques	10
1.1.5. Morphological diversity of silk fibroin scaffolds	11
1.1.6. Application of silk fibroin in tissue engineering.....	22
1. 2. Designer peptide amphiphiles as scaffolds for tissue engineering applications .	31
1.2.1. Introduction	31
1.2.2. The Natural building blocks: amino acids	33
1.2.3. Peptide amphiphiles: classification and design rule.....	37
1.2.4. The fabrication of 3D peptide amphiphilic scaffolds	47
1.2.5. Application of peptide amphiphile scaffolds in tissue engineering.....	51
1. 3. Identification of Problem	64
1. 4. Aims and Objectives.....	65
2. Experimental section.....	67
2. 1. Materials	67
2. 2. Methods.....	67
2.2.1. Preparation of regenerated silk fibroin	67
2.2.2. Preparation of RSF/peptide samples	68
2.2.3. Atomic force microscopy	68

2.2.4. Surface patterning of self-assembled peptide using inkjet printing.....	69
2.2.5. Culture of PC12 or NG108-15 neuronal cells on scaffolds.....	69
2.2.6. Cell adhesion assay	69
2.2.7. Live and dead assay.....	70
2.2.8. Statistical analysis	70
2.3. Theories of the technologies.....	71
2.3.1. Atomic force microscopy (AFM)	71
2.3.2. Optical microscopy.....	76
2.3.3. Scaffold preparation techniques.....	81
2.3.4. Fluorescent labels techniques.....	84
3. Patterning the neuronal cells via inkjet printing of self-assembled peptides on silk scaffolds	88
3.1. Introduction	89
3.2. Methods	92
3.2.1. Time effect of peptide self-assembly.....	92
3.3. Result and discussion	93
3.3.1. Time effect of peptide self-assembly.....	93
3.3.2. Characterization of RSF/I3QGK scaffolds	94
3.3.3. Cellular adhesion and viability	95
3.3.4. Cell morphology	97
3.3.5. PC12 neuronal cell alignment to micro-patterns produced by inkjet printing.....	103
3.3.6. NG108-15 neuronal cells growth on RSF/I3QGK scaffolds	106
3.4. Conclusions	111
4. Cell Guidance on Peptide Micropatterned Silk Fibroin Scaffolds.....	112
4.1. Introduction	113
4.2. Methods	115
4.2.1. Resazurin assay	115
4.2.2. Immunostaining of the neurites assay.....	115
4.3. Result and discussion	116
4.3.1. Attachment of PC12 neuronal cells on SF films	116
4.3.2. Characterization of RSF/I ₃ K scaffolds.....	117

4.3.3. Neuronal cell attachment and morphology on RSF/I3K scaffolds	121
4.3.4. Differences between RSF/I ₃ K scaffolds and collagen scaffolds on the function of PC12 cells	128
4.3.5. Micropatterning PC12 cells on RSF scaffolds via inkjet printing of peptide nanofibers	132
4.3.6. Investigation of topographical and thickness of RSF/I ₃ K scaffolds with different layers	133
4. 4. Conclusions	138
5. Short peptides induce neurite outgrowth of neuronal cells	140
5. 1. Introduction	140
5. 2. Methods	143
5.2.1. Peptide solution preparation	143
5.2.2. Investigation of time dependent peptide self-assembly	143
5.2.3. Preparation of RSF/peptide bilayer scaffolds	143
5. 3. Results and discussion.....	144
5.3.1. Investigation of the properties of designed short peptides	144
5.3.2. Time effect of peptides self-assembly	147
5.3.3. Further characterize designed short peptides	149
5.3.4. Characterization of RSF/peptide bilayer scaffolds	151
5.3.5. Cellular adhesion and viability.....	152
5.3.6. Cell morphology	154
5. 4. Conclusions	160
6. Conclusions and future work.....	161
6. 1. Conclusions	161
6. 2. Future work.....	163
6.2.1. Based on this thesis.....	163
6.2.2. Silk fibroin	167
6.2.3. Peptide amphiphiles	167
7. References.....	169

List of figures

Figure 1-1 Schematic diagram of the silk structure.....	6
Figure 1-2 A) Schematic illustrating the SF degradation process mechanism.....	9
Figure 1-3 A schematical representation of the LiBr dissolution process to obtain RSF solution.	11
Figure 1-4 SF-based scaffolds with different representative structures:.....	12
Figure 1-5 Micro-patterning of silk-based biomaterials.....	19
Figure 1-6 A) Regenerated silk fibroin (RSF) was chemically modified with glycidyl methacrylate (GMA) to form (Sil-MA) as a pre-hydrogel.	21
Figure 1-7 A) Schematic diagram illustrating the fabrication of a 3D of scaffold made via Bioprinting up to the final in vivo implantation.	26
Figure 1-8 A) Schematic diagram of silk fibroin films via Temperature Controlled Water Vapour annealing (TCWVA).	29
Figure 1-9 Chemical structures, standard accepted abbreviations and hydrophobicity (π value) of the 20 natural amino acids.....	36
Figure 1-10 A , Schematic process of ionic self-complementary peptides in aqueous solution,	39
Figure 1-11 A , Chemical structure of a representative single tail lipopeptide, highlighting four designed chemical entities.....	44
Figure 1-12 Schematic representation of A , chemical structure of β -cyclodextrin which can self-assemble into cyclodextrin vesicles,	46
Figure 1-13 A . Schematic representation of the electrospinning process.	51
Figure 1-14 Schematic design of peptide amphiphile scaffolds for cartilage tissue engineering.	56
Figure 1-15 Schematic diagram illustrating the injection of β -cyclodextrins poly(organophosphazene) (β -CD PPZ; host),	58
Figure 1-16 A , Schematic representation of the injury model and repair strategy.	62
Figure 2-1 Schematic representation of the basic principles of atomic force microscopy (AFM).....	72
Figure 2-2 Schematic representation of the force regimes under the three typical AFM imaging modes happens, including contact, noncontact and tapping mode.....	73
Figure 2-3 The schematic diagrams illustrate A , how the probe tip is subject to attractive and repulsive forces during an individual approach-retract cycle.	75
Figure 2-4 The image displays how to get the diameter of nanofiber through AFM software (NanoScope Analysis).	76
Figure 2-5 Schematic diagrams indicate main components of optical microscopy and the difference in illumination between brightfield microscopy and darkfield microscopy.....	77
Figure 2-6 Schematic drawing of the principle of fluorescence microscopy.....	78
Figure 2-7 Schematic drawing of how confocal laser-scanning microscopy works.....	79
Figure 2-8 Schematic representation of the basic set up of confocal laser-scanning microscopy.....	80
Figure 2-9 Schematic representation of spin coating process.....	81
Figure 2-10 Schematic representation of two sub-classes of drop-on-demand inkjet printing, which are piezoelectric inkjet printing and thermal inkjet printing.	83
Figure 2-11 Schematic representation of how piezoelectric drop-on-demand inkjet printing works.	84
Figure 2-12 Schematic representation of the principle of A , direct immunofluorescence and B , indirect immunofluorescence.	85
Figure 2-13 Schematic representation of the principle of resazurin assay, in which resazurin is directly reduced by reductase enzymes to form resorufin.	87
Figure 3-1 A schematic diagram illustrating the fabrication of micro-patterns on RSF substrates via spin coating and inkjet printing,	92
Figure 3-2 AFM topographical images of I ₃ QGK dynamic self-assembly (1 mg/mL in 20 mM HEPES buffer at pH 6.0) at different time scales.	93
Figure 3-3 AFM topographical images (25 μm^2) of RSF/I ₃ QGK scaffolds (1-layer).....	95
Figure 3-4 A , Live / dead assay of PC12 neuronal cells on different RSF/I ₃ QGK coated substrates (green: live cells (Syto-9TM staining) and red: dead cells (propidium iodide staining).	97

Figure 3-5 Fluorescence images of PC12 neuronal cells attached to various RSF/I ₃ QGK coated surfaces .	98
Figure 3-6 A, AFM peakforce images of PC12 neuronal cells attached to different concentrations of RSF/I ₃ QGK coated substrates.	101
Figure 3-7 A, AFM height images of PC12 neuronal cells attached on different concentrations of RSF/I ₃ QGK coated surfaces.	102
Figure 3-8 AFM topography images indicate peptide I ₃ QGK droplets (3 mg/ml) were printed at (a) 1 layer, (b) 3 layers and (c) 5 layers on silk substrates (40 mg/ml).	103
Figure 3-9 Inkjet printing of I ₃ QGK peptide lines (5 layers) on RSF (40 mg/mL) coated surfaces.	105
Figure 3-10 Fluorescence microscopy images of PC12 neuronal cells growing along the I ₃ QGK (3 mg/mL) printed lines on silk substrates (40 mg/ml).	105
Figure 3-11 (a) Inkjet-printed University of Sheffield logo (on RSF a coated glass surface) using I ₃ QGK peptide ink, with PC12 neuronal cells growing along the printed pattern.	106
Figure 3-12 AFM topographical images (25 μm ²) of RSF/I ₃ QGK scaffolds (2-layers).	107
Figure 3-13 The light microscope images of NG108-15 cells adhesion on RSF/I ₃ QGK scaffolds (2-layers).	109
Figure 3-14 A and B show fluorescent microscope images of NG108-15 cells adhesion on RSF/I ₃ QGK scaffolds (2-layers).	110
Figure 4-1 A, AFM topographical images of RSF coated scaffolds on Si-wafers at (a) 5 mg/mL;	117
Figure 4-2 AFM topographical images of self-assembled I ₃ K nanofibers in HEPES buffer (20 mM; pH 6.0) at (a) 1 mg/mL for 2 weeks	118
Figure 4-3 AFM topographical images (25 μm ²) showing 1-layer RSF/I ₃ K scaffolds coated at different concentration ratios:	119
Figure 4-4 AFM topographical images (25 μm ²) showing 1-layer RSF/I ₃ K scaffolds coated at different concentration ratios:	120
Figure 4-5 AFM topographical images (25 μm ²) showing 1-layer RSF/I ₃ K scaffolds after immersion in deionized water and incubation under a 5% CO ₂ atmosphere at 37 °C for 6 days.	121
Figure 4-6 A, Live / dead assay of PC12 neuronal cells adhered on RSF/I ₃ K scaffold surfaces.	123
Figure 4-7 A, AFM Peak Force Error images of PC12 neuronal cells attached on a series of RSF and I ₃ K coated surfaces.	125
Figure 4-8 AFM topographical images of PC12 neuronal cells attached on various coated surfaces.	126
Figure 4-9 F-actin staining of PC12 neuronal cells attached on different ratios of RSF/I ₃ K coated surfaces:	127
Figure 4-10 Metabolic activity of PC12 cells adhered on different surfaces assessed using resazurin assay	129
Figure 4-11 A, Representative confocal images of live / dead analysis from PC12 neuronal cell culture on different surfaces,	130
Figure 4-12 A, confocal images of PC12 neuronal cells adhered onto different surfaces,	132
Figure 4-13 A, Inkjet-printing of 1 layer of "SHEF" letters onto RSF coated glass surfaces (40 mg/mL) using I ₃ K peptide (3 mg/mL) as the ink,	133
Figure 4-14 AFM topographical images (25 μm ²) showing 2-layers RSF/I ₃ K scaffolds coated at different concentration ratios:	134
Figure 4-15 AFM topographical images (25 μm ²) showing 3-layers RSF/I ₃ K scaffolds coated at different concentration ratios:	135
Figure 4-16 AFM topographical images (25 μm ²) showing RSF/I ₃ K scaffolds coated at the ratio 5:3 in different layers	136
Figure 4-17 Layer thickness of RSF/I ₃ K coated surface (5:0, 5:1, 5:2, 5:3, 5:4, 5:5).....	138
Figure 5-1 A, Chemical structures of the designed short peptides. (a) I ₃ RGDS; (b) I ₃ PDSGR; (c) I ₃ KVAV; (d) I ₃ PHSRN and (e) I ₃ YIGSR.	147
Figure 5-2 AFM topographical images of peptide I ₃ RGDS dynamic self-assembly.....	148
Figure 5-3 AFM topographical images of peptide I ₃ KVAV dynamic self-assembly.....	149
Figure 5-4 AFM topographical images of peptide I ₃ YIGSR self-assembly.....	149
Figure 5-5 A, AFM topographical images (25 μm ²) of self-assembled short peptides in HEPES buffer (20 mM; 1 mg/mL) for 3 days,.....	150

<i>Figure 5-6 AFM topographical images of RSF/peptides scaffolds after immersion in deionized water and incubation under a 5% CO₂ atmosphere at 37 °C for 6 days.</i>	152
<i>Figure 5-7 A, Live/dead assay of PC12 neuronal cells adhered on various RSF/peptides scaffolds surfaces.</i>	154
<i>Figure 5-8 F-actin staining of PC12 neuronal cells attached to various RSF/peptides scaffolds.</i>	155
<i>Figure 5-9 A, AFM peak force images (left) and topographical images (right) of PC 12 neuronal cells attached to different RSF/peptides scaffolds,</i>	159
<i>Figure 5-10 AFM topographical images (left) and peak force images (right) of PC 12 neuronal cells attached to different RSF/peptides scaffolds,</i>	160
<i>Figure 6-1 A, the addition of glutaraldehyde and TEMED at various volume ratios into RSF solutions (120 mg/mL),</i>	164
<i>Figure 6-2 AFM topographical images of the mixed short peptides at equimolar concentrations self-assembled at A, 1 day and B, 7 days.</i>	166

List of tables

<i>Table 1-1 Key silk fibroin hydrogel fabrication techniques.</i>	15
<i>Table 1-2 Advantages and disadvantages of key PAs scaffolds fabrication techniques.</i>	48

1. Introduction

1. 1. Silk Fibroin as a Functional Biomaterial for Tissue Engineering

Abstract

Tissue engineering (TE) is the approach to combine cells with scaffold materials and appropriate growth factors to regenerate or replace damaged or degenerated tissue or organs. The scaffold material as a template for tissue formation plays the most important role in TE. Among scaffold materials, silk fibroin (SF), a natural protein with outstanding mechanical properties, biodegradability, biocompatibility and bioresorbability has attracted significant attention for TE applications. SF is commonly dissolved into an aqueous solution and can be easily reconstructed into different material formats, including films, mats, hydrogels and sponges via various fabrication techniques. These include spin coating, electrospinning, freeze drying, physical and chemical crosslinking. Furthermore, techniques include micro-patterning and bio-printing have been recently explored in order to fabricate more complex SF-based scaffolds with high precision. This review introduces the physicochemical and mechanical properties of SF and looks into a range of SF-based scaffolds that have been recently developed. The typical TE applications of SF-based scaffolds including bone, cartilage, ligament, tendon, skin, wound healing and tympanic membrane, will be highlighted and discussed, followed by future prospects and challenges needing to be addressed.

Keywords: Silk fibroin, Biomaterial, Scaffold, Tissue engineering

1.1.1. Introduction

Damaged and degenerated tissues and failed organs are some of the most serious issues in human healthcare, generating many challenges in modern medicine. For example, musculoskeletal tissue (bone, tendons, and cartilage) as well as the peripheral nervous system are easily impaired by trauma and degenerative diseases such as osteoarthritis. This affects millions of people

worldwide, severely affecting quality of life and resulting in extreme pressure on the healthcare systems worldwide.¹ Typically, autografts and allografts are the common clinical techniques to replace damaged tissues, but restricted by various factors, such as lack of tissue that can be removed from the patient in healthy areas as well as a shortage of suitable donors.² Success rates of allografts can be low as tissue from others may have an immune response. In the case of extensive damage large surface areas of defects, it is hard to source suitable material in time leading to low success rates.²⁻⁴ It is for these reasons that tissue engineering (TE) has attracted increasing attention as the alternative method to produce patient specific tissues for repair and replacement applications.

TE combines several principles and methods to regenerate damaged tissues or organs by restoring, maintaining or improving tissue functions. Furthermore, TE relies extensively on the use of biocompatible scaffolds which are typically seeded with cells and contains supportive moieties such as growth factors.^{5, 6} Regardless of the tissue types, there are several key factors that should be considered when designing a scaffold. These include biocompatibility, biodegradability, mechanical properties, structure and fabrication methods.^{6, 7} The extracellular matrix (ECM) secreted from tissues or organs is an excellent natural option as a scaffold material for TE, and exists in a state of “dynamic reciprocity” with resident cells.⁸ Therefore, ECM components such as collagen⁹, fibronectin¹⁰, laminin¹¹, elastin¹² and glycosaminoglycan¹³ have been widely used as natural scaffold materials to support tissue regeneration applications. In addition, other natural polymers such as alginate,¹⁴ cellulose¹⁵ and chitosan¹⁶ have also been used in TE. Although the natural polymers discussed above have demonstrated promising results, these materials also have many drawbacks including high cost, poor mechanical properties, and large batch to batch variation, making them difficult to be applied to clinical applications.¹⁷ On the other hand, synthesized polymers such as polylactic acid (PLA), polyurethane (PU), poly(lactide-co-glycolide) (PLGA), and polycaprolactones (PCL) have been widely used in TE due to their good mechanical properties and degradation rates.¹⁸ However, many degradation products of these polymers comprise of acidic compounds that are harmful to body and can cause undesired immune responses.¹ As most of the natural and synthesized

polymeric scaffolds possess their inherent limitations, finding a biomaterial that combines the goodness of both natural and synthesized polymeric materials have become the aspirations of researchers in the last decades.¹⁹ Recent studies have explored the possibilities of silkworm silk as an excellent biomaterial for TE scaffolds.

Silkworm silk has been commercialized in the traditional textile industry for more than 4000 years, due to its outstanding physical properties, such as lustre, lightweight, flexibility and strong mechanical strength.²⁰ Moreover, silk has been approved by the Food and Drug Administration (FDA) for use in sutures and has been applied to biomedical applications for the last 2 decades.^{21, 22} Silk fibroin (SF), extracted from silkworm silk, is a unique natural protein that has been used as a potential biopolymer for TE, due to many desired physiochemical properties such as excellent biocompatibility, biodegradability, bioresorbability, low immunogenicity and tuneable mechanical properties.²³⁻²⁶ SF also can be combined synergistically with other polymers to form SF-based composite scaffolds, that can further promote cellular behaviour (e.g. differentiation, proliferation and attachment).²⁷⁻²⁹ Further to this it is possible to fabricate SF-based biomaterials into various material formats, such as films³⁰, hydrogels³¹, sponges³², 3D structures³³, and nanoparticles²⁴. In this review, we introduce the sources, material properties, fabrication techniques and applications of silk scaffolds with an emphasis on bone, cartilage, ligament, tendon, skin and wound tissue regeneration.

1.1.2. Sources of silk and silk fibroin

Silks are proteins which are produced within glands after biosynthesis in epithelial cells. There are over 200,000 different silk producing arthropods that exist in nature.³⁴ Out of these there are many different taxonomic silk producing families such as silkworms, spiders, lacewing, glowworm and mites, some of which can spin silk into fibres during their metamorphosis (cocoon generation).^{35, 36} Recently, Yoshioka et al.³⁷ discovered that the Psychidae family, also known as bagworm moths, are thought to produce the toughest form of moth silk currently known. Silks originating from silkworms and spiders are the most commonly used for biological applications.³⁸⁻⁴⁰ However, in the case of spider silk once it is spun and contacts air it hardens, which restricts

mass production of spider silks. Compared to spiders, the yield of fibres obtained from one silkworm cocoon is around 10 fold that of the ampullate gland of a spider.^{35, 41} Although researchers have used a biomimetic spinning process to replicate spider silks, producing spider silk-like fibres with mechanical properties similar to natural spider silk fibres is challenging.⁴² Andersson et al.⁴³ designed a chimeric recombinant spider silk protein that can produce large quantities artificial spider silks via a bacterial shake-flask culture. The mechanical properties of these artificial spider silks are highly reproducible. However, the reported ultimate tensile strength and toughness are still lower than those of native spider silk fibres.

Bombycidae and Saturniidae are known to play the most important roles in silkworm silk research, which feed on either the mulberry tree (Bombycidae) or other food sources, the latter being regarded as non-mulberry (Saturniidae) silks. The most common silk originates from *Bombyx mori* (*B. mori*), a mulberry feeding silkworm that produces higher quality fibres than most Saturniidae.^{44, 45} Additionally, unlike other silk moths, over the last 5000 years, *B. mori* was domesticated from an ancestral species in China and has since then been extensively reared worldwide to obtain its silk.⁴⁶ *B. mori* silkworm cocoons consist of 75-83.3% SF and 16.7-25% of sericin.⁴⁷ SF is a semi-crystalline structured protein functioning mainly for its load-bearing capacity. Sericin on the other hand is an amorphous protein polymer functioning as a gumming agent.⁴⁸ It has been found that sericin-free fibroin fibres show better mechanical properties than sericin encased fibroin, where a 50% increase in tensile strength, a modulus of up to 15-17 GPa and strain at breakage reaching 19% has been observed.⁴⁹ Furthermore, sericin-free fibroin fibres also show better biocompatibility *in-vitro* and *in-vivo* according to previous reports.⁵⁰ In addition, sericin has been shown to cause inflammation.⁵¹ Therefore, sericin proteins are often removed from SF to ensure biocompatibility in TE applications.

Sericin is removed from the SF fibres by a degumming process, which is normally carried out under boiling alkaline conditions.⁵² Researchers continuously work on improving the degumming process which typically requires reagents and organic solvents to obtain higher quality of pure SF. The sodium carbonate (Na_2CO_3) degumming method has, at present replaced the

standard Marseilles soap method, and is now the most used method due to being rapid (~30 min) and low cost.^{53, 54} It is worth noting that, after degumming, the average diameter of silks fibres is reduced from 15-35 μm to 10-25 μm .⁵⁵

1.1.3. Properties of silk fibroin

1.1.3.1. Structure of SF

SF consists of two main chains, a heavy (H-) chain (390 kDa) and a light (L-) chain (26 kDa), which are linked via disulphide bonds to form a H-L complex (Figure 1-1 A).^{38, 39, 56, 57} P25 (25 kDa) is a glycoprotein including Asn-linked oligosaccharide chains, which is hydrophobically linked to H-L complex.⁵⁸ The H-chain, L-chain and P25 are the three polypeptides that form the cocoon of *B. mori* and are at a molar ratio of 6:6:1, respectively.⁵⁹ The amino acid sequence of the H-chain consists of Glycine (45.9%), Alanine (30.3%), Serine (5.3%), Valine (1.8%) as well as 4.5% of 15 other amino acid types. The Gly-X (GX) dipeptide motif repeats account for 60-75% of the H-chain. The hydrophobic residues of the dipeptide repeats can form stable antiparallel β -sheet crystallites. Two hexapeptides occupy 70% of the GX dipeptide motif region, for which the peptide sequences are known to be Gly-Ala-Gly-Ala-Gly-Ser and Gly-Ala-Gly-Ala-Gly-Tyr.⁶⁰⁻⁶³ Silk I and silk II are the dominant crystalline structures of SF (Figure 1-1 B), where silk I is a metastable crystalline structure that includes bound water molecules and silk II is the most stable state due to strong hydrogen bonding between adjacent peptide blocks, resulting in increased mechanical properties including rigidity and tensile strength.^{38, 64, 65}

The secondary structure obtained from regenerated silk fibroin (RSF) solutions contains crystalline and amorphous structures, which will be discussed below. In a crystalline structure silk includes β -turns (silk I) and insoluble structures formed by folded β -sheets (silk II), while in an amorphous state silk consists of α -helices, turns and random coil structures.⁶⁶ Methanol or potassium chloride can easily convert silk I to silk II, a process which is widely used for biomaterial engineering applications.³³ Silk III is the unstable crystal structure of SF, which exists at the air/water interface of RSF solutions.⁶⁷

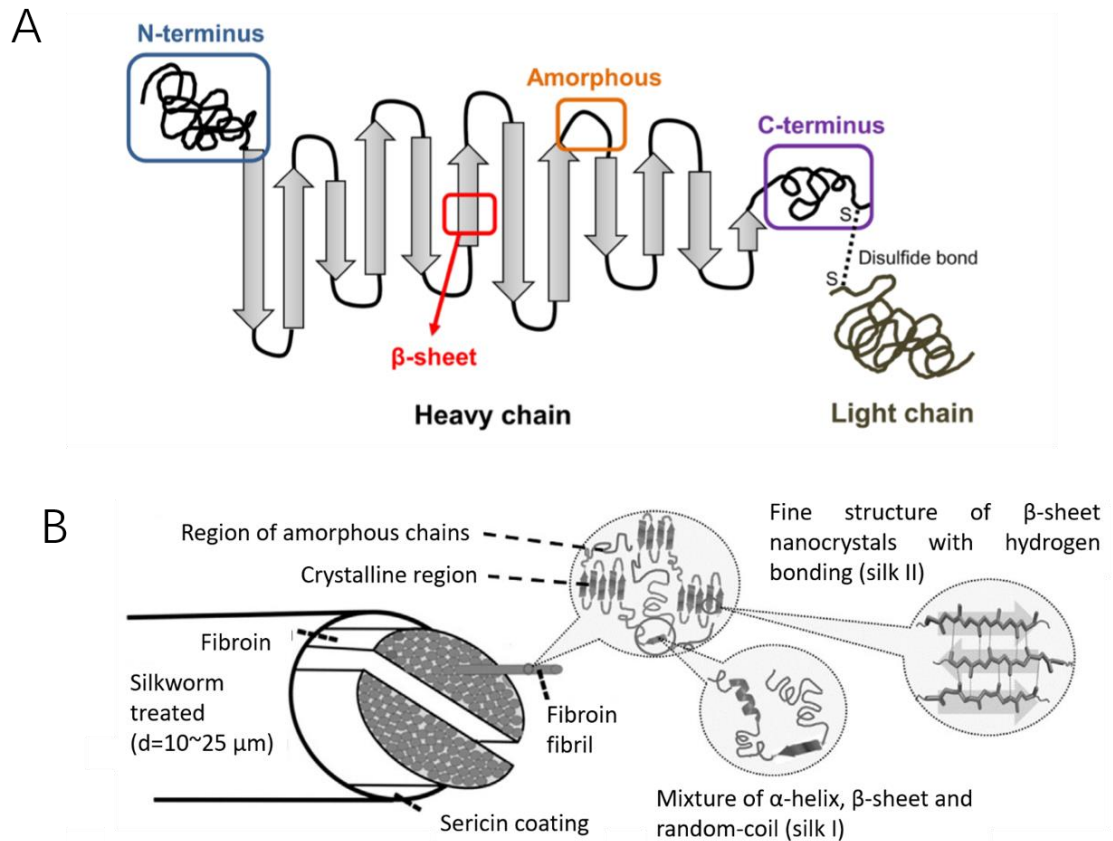


Figure 1-1 Schematic diagram of the silk structure. **A**) heavy chain (i.e., N-terminus, β -sheets, Amorphous and C-terminus) and light chain which linked via disulphide bonds, reproduced with permission from³⁹ **B**) silkworm thread, fibril overall structure and silk fibroin polypeptide chains, reproduced with permission from³⁸.

1.1.3.2. Mechanical properties

SF fibres have demonstrated outstanding mechanical properties.^{55, 68, 69} These include a large break strain (4-26%), ultimate strength (300-740 MPa) and toughness (70-78 MJ m⁻³).⁶⁹ In addition, the reported toughness of SF fibres is higher than many synthetic fibres such as Kevlar (50 MJ m⁻³), carbon fibre (25 MJ m⁻³) and some collagens such as tendon collagen (7.5 MJ m⁻³).^{42, 70} In addition, SF fibres exhibit the highest strength among common natural materials such as wool, resilin, elastin, byssus and cotton as well as some synthetic fibres such as synthetic rubber and viscose rayon.⁴² Considering these strong mechanical properties of SF, many researchers have used SF as a scaffold material for load bearing TE applications, especially in musculoskeletal TE.¹ It is however important to note that SF scaffolds in biomaterial engineering are

normally made from RSF solutions and the produced scaffolds are brittle and weak. This is due to the fact that RSF lacks hierarchical and secondary structures compared to unprocessed raw SF fibres.⁷¹ In order to ensure RSF has good mechanical properties, many different strategies have been trialled. For example, the breaking stress of RSF fibres made via a dry-spinning technique was 252 MPa, 28.6% less than raw SF fibres (353 MPa), whereas, the breaking stress of RSF and graphene oxide composite silk fibres (dry-spun from a mixed dope of RSF and graphene oxide at mass ratio 1000/1) was 435 MPa.²³ Amongst others crosslinking,³¹ porogens⁷² and 3D bioprinting³³ technologies can be used to improve mechanical properties of RSF produced silk scaffolds. The resulting SF-based scaffolds are therefore sufficiently strong to allow handling during surgical procedures needed for implantation and have mechanical properties closely resembling the native tissue being repaired thus allowing for optimal repair conditions of the area in question.

1.1.3.3. Biocompatibility

Biocompatibility is a key factor for the implementation of successful scaffolds, which enables cells to adhere onto scaffold surfaces and migrate into the scaffold undergoing proliferation and differentiation within the scaffold. In addition, it is important for the scaffold to cause no or a negligible immune reaction after implantation.⁵ SF is known to be a biologically inert and therefore biocompatible natural polymer.²⁵ Since 1989, SF has been shown to have blood compatibility in *in-vivo* experiments.⁷³ In 1993, SF was approved by the FDA as a biomaterial for use as a suture material.²⁵ In 1995, Minoura *et al.*⁷⁴ conducted pioneering research and successfully grew fibroblast cells on SF coated films. SF has more recently been used as an alternative to collagen in cell culture to guide bone regeneration in rat calvarial defects, for example, demonstrating that SF membranes can replace the collagen membranes.⁷⁵ *In vitro* studies showed that, there is no significant macrophage response to SF films⁷⁶ or fibres²². In addition, the *in vivo* inflammatory reaction to SF films is similar to that of collagen.⁷⁷

1.1.3.4. Biodegradability and bioresorbability

Biodegradability and bioresorbability are important features to successful scaffold materials as the scaffolds should gradually be replaced with the patients' own cells and ECM over the course of recovery.⁷⁸ Therefore, it is important that by-products of biodegradation are non-toxic and do not interfere with other tissue, organs and functions when being metabolised in the body. SF is an enzymatically degradable polymer and has been shown not to cause an immunogenic response.⁷⁹ The degradation process starts when enzymes are adsorbed onto the surface of the SF scaffold via surface-bonding domains. The enzymes then digest SF via hydrolysis of ester bonds.^{18, 79, 80} The mechanism of SF degradation is shown in [Figure 1-2 A](#).⁸¹ Non-crystalline SF structures (hydrophilic blocks) were degraded in an enzyme solution resulting in hydrophobic crystal structures and then further dissolved in enzyme solutions. SF can be proteolytically degraded through enzymes, such as α -chymotrypsin, protease XIV and collagenase IA.^{79, 82, 83} Protease XIV, obtained from *Streptomyces griseus*, has shown a higher SF degradation activity in comparison to α -chymotrypsin and collagenase IA. This therefore meant that protease XIV degraded SF achieved the lowest average molecular weight of SF residues.⁸² It is for this reason that protease XIV is the mostly commonly used enzyme for silk degradation. The preparation methods of SF also affect the degradation process, which result in different morphology of SF particles that dissolved in enzymes ([Figure 1-2 B](#)).⁸¹ As the degradation products of SF are amino acids and peptides, they are easily absorbed *in-vivo*.⁷⁹ *In vivo* studies undertaken on SF porous scaffolds implanted in Lewis rats showed that the scaffolds decomposed within 8 weeks. After 1 year, the implanted scaffolds were fully degraded, due to macrophage degradation.⁸⁴ This proves that SF scaffold are not only biodegradable, but also is bioresorbable.

The degradation of native silk fibres is much slower compared to that of RSF silk scaffolds. This is due to the fact that native silk fibres have higher content of β -sheet secondary structure than RSF structures have.⁸⁵ The degradation rate of SF is therefore highly dependent on the amount of β -sheet secondary structures present. For example, RSF films obtained by methanol treatment, converting water soluble silk I to water insoluble silk II structures, resulted in a

higher amount of β -sheet structures⁸⁶ in contrast, RSF films obtained via a slow air drying process possess a lower content of β -sheet structures.⁸⁷ The latter therefore resulted in faster degradation rates. γ -radiation also has been shown to promote SF fibre degradation, due to the conversion of silk II to silk I.⁸⁸

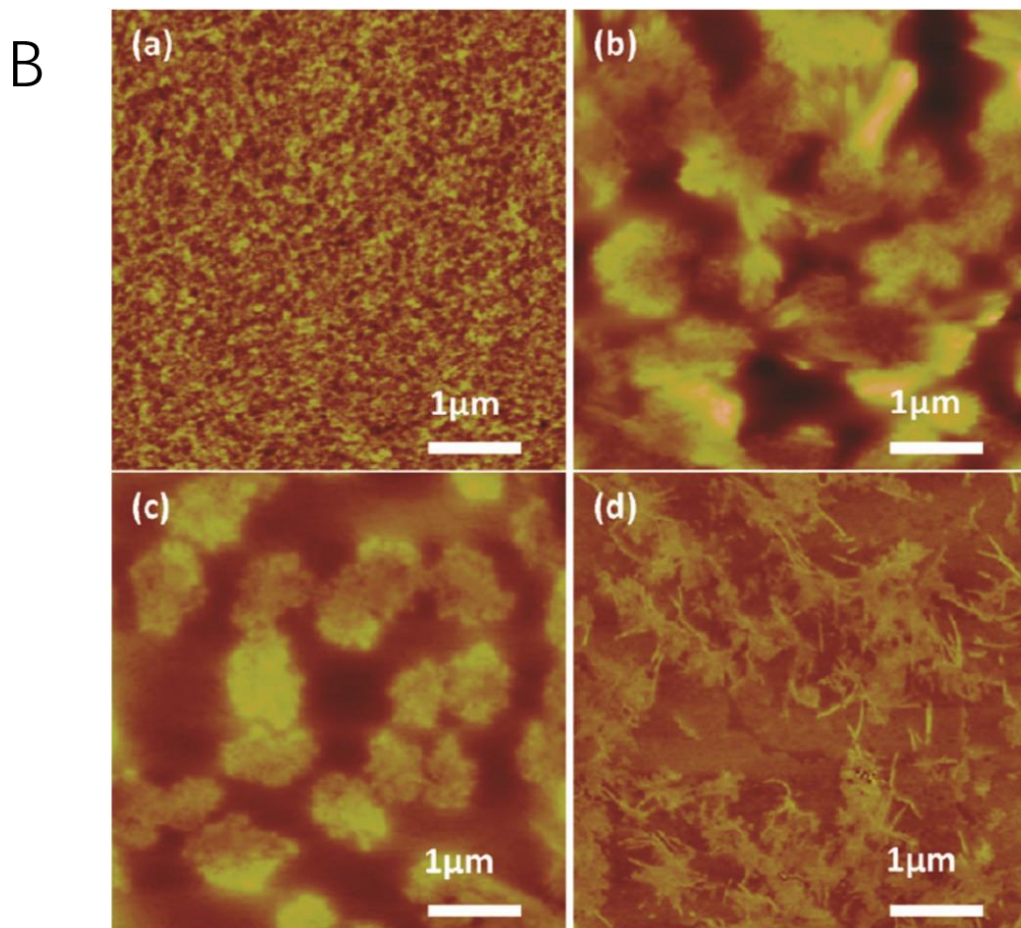
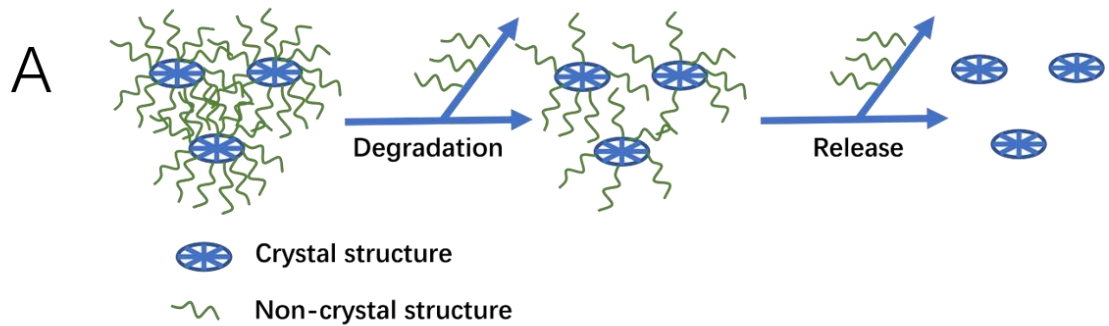


Figure 1-2 **A**) Schematic illustrating the SF degradation process mechanism. **B**) Representative AFM images of (a) pure protease XIV solution and differently fabricated SF films: (b) slow drying process, (c) water annealing treatment and (d) stretching treatment, after 12 hours of exposure to protease XIV solution. The degraded SF particles that dissolved in protease XIV can be seen in (b), (c) and (d). **B**) reproduced with permission from⁸¹.

1.1.4. Silk fibroin dissolution techniques

Proper dissolution of SF is an essential step before processing SF into different structures for various TE applications.⁸⁹ Therefore, a robust protocol for the complete and correct dissolution of silk cocoons to produce RSF is required. SF is insoluble in organic solvents and water, because of its tightly packed structure which has a high content of β -sheet structures.^{86, 90} To obtain an aqueous SF solution, it must undergo a water-based dissolution process.⁹¹ As RSF solutions are used for biological applications, strong and toxic solvents / solutions should be avoided during the dissolution process. Typically, concentrated salt solutions with various concentrations of salt ions (Ca^{2+} ;⁹² Sr^{2+} ; Li^{2+} ; Zn^{2+}) in combination with anions (Cl^- ; Br^- ; SCN^-)⁹³ were employed to dissolve SF fibres. These include the very well-known 9.3 M lithium bromide (LiBr) solution method (Figure 1-3),^{20, 91} as well as 9 M lithium thiocyanates (LiSCN) methods.⁹⁴ Another common method uses Ajisawa reagent⁹² which consists of a ternary ($\text{CaCl}_2/\text{EtOH}/\text{water}$) solvent (1:2:8 molar ratio) solution to dissolve SF. However, all these aqueous methods require a final dialysis step against pure DI-water or appropriate buffers to remove salt ions from the RSF solutions.

Recently, Ajisawa's reagent has increasingly been applied in SF dissolution, due to its cost efficacy. However, compared to the LiBr method, Ajisawa's reagent appears to lead to a complete unfolding of the silk polymers, which are therefore more prone to form β -sheet structures and aggregate during dialysis.⁹⁵ Zheng et al.⁹⁵ adapted this method dissolving degummed silk fibres in Ajisawa's reagent at 80 °C for 2 hours and then dialysing against urea solution with stepwise decrease in concentration. When the SF solution was dialysed against water and urea (4 M constant concentration) solutions for 30 hours (referred to as Silk-TS-0), the hydrodynamic radius of RSF ranged from 100 to 1000 nm. However, when the SF solution was dialysed against 4 M urea for 3 hours, then in 2 M urea for 3 hours, followed by 1 M urea for 3 hours and then water for 30 hours (referred to as Silk-TS-4210), the hydrodynamic radius range of RSF solution reduced to 5 -11 nm. In addition, Silk-TS-4210 had small aggregates (< 10 nm), and a low content of β -sheets ($\approx 15\%$) compared to Silk-TS-0, an outcome similar to RSF via the LiBr method.⁹⁵

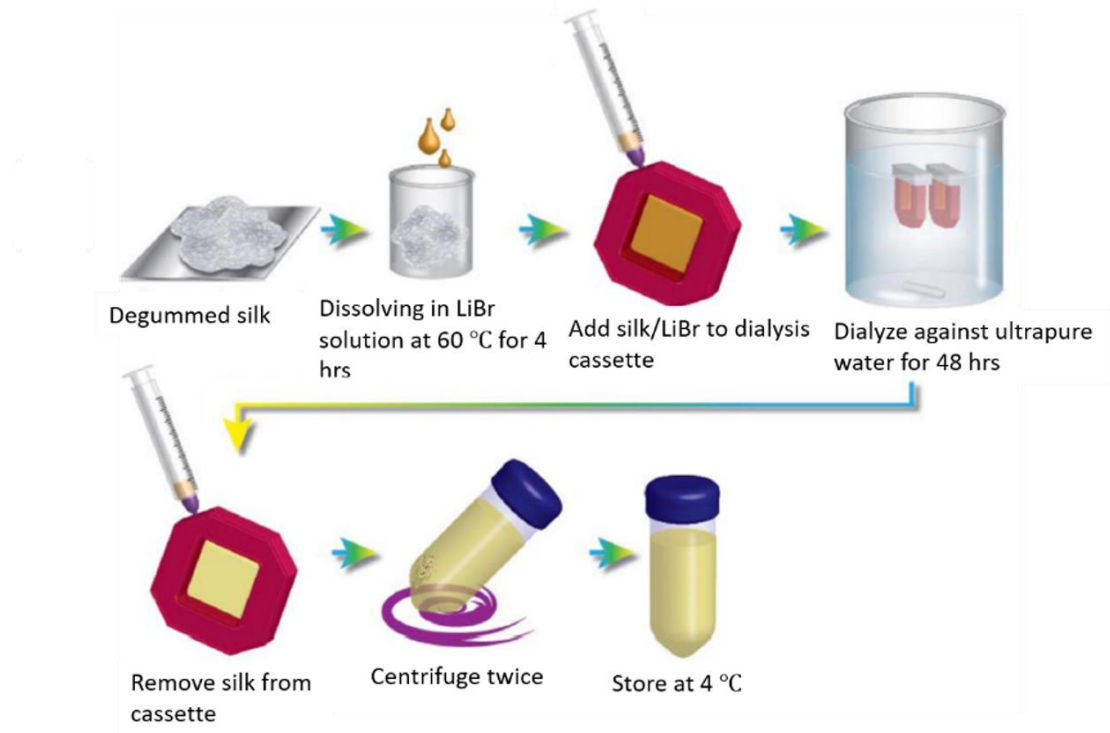


Figure 1-3 A schematical representation of the LiBr dissolution process to obtain RSF solution. The degummed silk is dissolved in 9.3 M LiBr solution at 60 °C for 4 hours. The obtained solutions are dialyzed against ultrapure water to remove salt. Until a conductivity of < 5 μ S is reached, RSF solutions are centrifuged twice and stored at 4 °C, reprinted with permission from²⁰.

1.1.5. Morphological diversity of silk fibroin scaffolds

RSF solutions have been used to fabricate SF-based scaffolds with different structures (Figure 1-4), including films⁹⁶, mats⁹⁷, artificial fibres⁹⁸, hydrogels⁹⁹, sponges³². Different techniques used for micro-patterning¹⁰⁰ and 3D structures fabrication¹⁰¹ are described in the following sections.

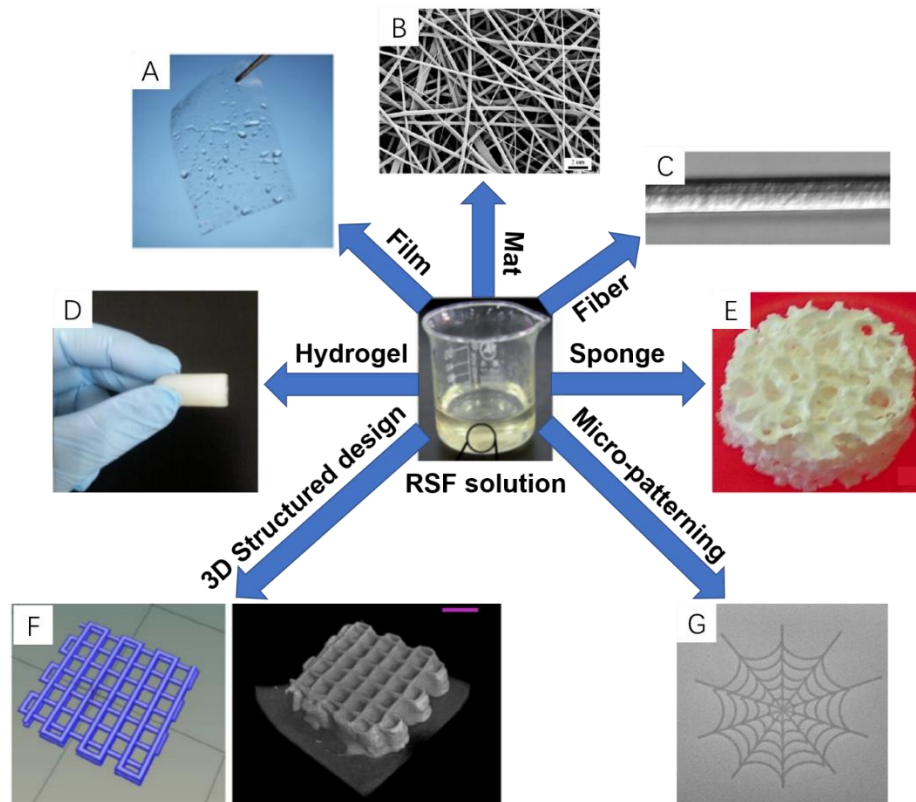


Figure 1-4 SF-based scaffolds with different representative structures: **A)** Film⁹⁶; **B)** Mat⁹⁷; **C)** artificial fibre⁹⁸; **D)** Hydrogel⁹⁹; **E)** Sponge³²; **F)** 3D structure design and printed scaffold¹⁰¹; **G)** Inkjet-printed silk pattern¹⁰⁰.

1.1.5.1. Films

Spin coating and vertical deposition are the main techniques used to fabricate RSF films. In the case of spin coating, RSF solution and ethanol are alternately coated onto substrates. As previously described ethanol is able to convert the structure of RSF from high content α helices (Silk I) into beta sheet conformation (Silk II). The ethanol concentration used can affect the surface properties of RSF film. If the concentration of ethanol is less than 80%, the outermost surface of the treated film will have a hydrogel structure.¹⁰² However, when 90% w/V ethanol is used the silk film surface becomes rigid, and cells show better adhesion.¹⁰² Vertical deposition is another method to prepare RSF films that is typically achieved by dipping a clean glass surface into a RSF solution, and then drying it in an oven at 50 °C. This method however generates non-homogeneous structures, which show the presence of “valleys and ridges”. Recent studies have indicated that a poor cell attachment was achieved when using this deposition method of RSF films.¹⁰³ Temperature Controlled Water

Vapour Annealing (TCWVA) is a physical method that can change the structure of RSF films to the insoluble Silk II state.⁹⁶ In this method RSF films are casted into flat moulds and placed in a constant temperature and humidity chamber at 65 °C with a relative humidity of 90% for 100 min (Figure 1-8 A). RSF films obtained via this method ((Figure 1-4 A) were successfully applied in skin TE applications,⁹⁶ which are described in more details below.

1.1.5.2. Mats and artificial fibres

Fibre spinning techniques including electro-spinning, wet-spinning and dry-spinning are the most commonly used techniques to make RSF mats or artificial silk fibres. The electro-spinning technique can be employed to make polymeric nanofibrous scaffolds, which can mimic properties of fibrous ECM components. RSF can be fabricated on a large scale with porous structure using electrospinning, which is of great benefit for cell seeding in TE.^{104, 105} RSF mats produced by electro-spinning usually involve spinning solvents (e.g. polyethylene oxide (PEO)), which can adversely affect biocompatibility.³⁸ Jin *et al.*¹⁰⁶ reported RSF/PEO electro-spun mats were immersed in water for two days to remove the PEO solvent, and in return the number of human marrow stromal (BMSC) cells attached on their surface increased. Additionally, electro-spinning allows for modified RSF mats to be produced by adding different moieties for extra functions. For example, the addition of cellulose 'nanowhiskers' (CNWs)¹⁰⁷ and polycaprolactone (PCL)¹⁰⁸ can strengthen the young's modulus and tensile strength of RSF mats, whereas the addition of silver (Ag)¹⁰⁹ or titanium oxide (TiO₂)¹¹⁰ nanoparticles confer enhanced antimicrobial properties to RSF mats. Recently, Yin *et al.*⁹⁷ developed a finite element model that expressed the mechanical response of RSF/PCL mats under biaxial tension. This model could be used to guide the design of RSF/PCL mats for TE applications. Wet-spinning also can be used to fabricate RSF fibres, but on the micrometre scale (fibre diameter) in contrast to nanofibres from electrospinning. Wet-spinning allows the tuning of fibre morphologies and properties, and allows the combination with other biomolecules whilst fabricating.^{35, 111} For example, Jacobsen *et al.*⁹⁸ reported RSF/fibronectin (Fn) silk fibres obtained from RSF solutions and fibronectin proteins via wet-spinning, which demonstrated better cell attachment to those

made of pure silk fibres via wet-spinning. In contrast to the former methods, dry-spinning does not require the use of organic solvents or coagulation baths, which is environmentally friendly.²³ In this context Zhang *et al.*²³ reported the fabrication of RSF/graphene oxide (GO) hybrid silk fibres obtained from aqueous RSF blends with graphene oxide via the dry-spinning technique. Compared with silk fibres, RSF/GO composite silk fibres showed good biocompatibility and enhanced mechanical properties that have great potential for TE applications. In addition, a newly developed approach uses centrifugal electrospinning (CES) that was shown to spin RSF nanofibers with better structural stabilities and thermostabilities than those obtained from electrospinning.¹¹² Moreover, compared to electrospinning, this method allowed for a higher production rate at lower cost and was able to quickly produce highly interconnected nanofiber nonwoven meshes.^{113, 114}

1.1.5.3. Hydrogels

Hydrogels are water-swollen 3D polymer networks, which can be cross-linked via physical or chemical methods, and are excellent for the implementation of cell seeding and encapsulation in the development of tissue engineering applications.¹¹⁵ To date RSF hydrogels have been used with increasing popularity alongside other RSF morphologies, which is mirrored by the ever-increasing silk-based publication records.³¹ Table 1-1 illustrates to date the developed fabrication techniques of RSF hydrogels.

Research shows that RSF hydrogel gelation kinetics can be modified from minutes to hours by adjusting pH, temperature, protein concentration as well as the addition of precipitating agents. In general, during sol-gel transition of RSF solutions, the SF structural conformation changes from a random coil structure (Silk I) to a β -sheet conformation (Silk II).¹¹⁶ However it is worthy to note that electro-gelation hold an exception to this, where the random coil conformation changes to α -helices rather than β -sheet and the transition process is reversible by reversing the polarity of applied potential.^{117, 118} Cells can be encapsulated into RSF hydrogels that can be consequently used as a delivery system.¹¹⁹ For example Wang *et al.*¹²⁰ encapsulated mesenchymal stem cells (hMSCs) into sonication-induced RSF hydrogels, and reported proliferation and viability in static cultures after a week of *in vitro* cultivation.

Table 1-1 Key silk fibroin hydrogel fabrication techniques.

Methods	Fabrication techniques	Comments
Chemically induced gelation	Salts	Salts can promote protein-protein association for example the addition of Ca ²⁺ ions reduce the gelation time of RSF solution. ^{121, 122}
	Polymer agents	Polymer agents, such as polyethylene glycols and PEO, have been shown to promote protein-protein associations, and protein aggregation through volume exclusion and movement of water by osmosis. ^{121, 122}
	Organic solvents	Alcohols are the most common used among organic solvents, which can induce structural conformation changes of RSF from α -helix to β -sheet structures. ¹²³
	Surface active agents	Surface active agents readily bind with proteins leading to protein unfolding and aggregation. ¹²⁴ For example, adding the anionic surfactant sodium dodecyl sulfate (SDS) into RSF solutions and incubating at 60 °C can induce stable hydrogels with good mechanical properties. ⁹⁹
	Small neutral additives	Small neutral additives through their ionic strength and/or specific interactions with proteins can influence protein aggregation. ¹²⁴ For example, the addition of glycerol (30%; v/v) can reduce the gelation time of RSF solution and has been applied in biomedical applications. ^{125, 126}
	pH	As the pH of RSF solution is adjusted near the isoelectric point (PI =3.8-3.9), stable hydrogels can be formed as well as reduced gelation time of RSF scaffolds. ¹²⁷ This is because the pH of protein solution near its isoelectric point can induce protein precipitation. ³¹
	High pressure CO ₂	High-pressure CO ₂ as a volatile acid can be used as a fine tuning adjustment of the solutions pH, therefore, RSF solutions subjected to high-pressure CO ₂ at 60 bar, has been shown to form stable hydrogels within 2 hours. ¹²⁸

	Chemical crosslinking	Chemical crosslinking agents (e.g. hydrogen peroxide and horseradish peroxidase) can be used to covalently crosslink phenol groups of tyrosine residues on silk fibroin proteins to form highly elastic RSF hydrogels. ¹²⁹
	Chemical coupling	Diazonium coupling chemistry can functionalize tyrosine residues of SF protein, resulting in an adjustment of the hydrophobic and hydrophilic properties, giving rise to the ability to rapidly produce controlled RSF hydrogels from as little as 5 minutes to two hours. ¹³⁰
Physically induced gelation	Temperature	The gelation time of RSF solutions decreases with increasing temperature, this is because molecular collisions increase with respect to temperature. ^{116, 122}
	Shear force	A strong enough shear force applied to an RSF solution can promote molecule-molecule interactions and improve concentration fluctuation, resulting in gelation and aggregation phenomena. ^{131, 132} Vortex mixing is the way to initiate RSF gelation due to the high shear forces applied to the solution. ¹³³
	Ultrasound	Sonication can lead to local areas of extreme pressure and temperature, resulting in gelation and aggregation. ¹³⁴
	Electric fields	Applying electric fields across RSF solutions leads to local pH decreases and thus silk protein aggregates. ¹³³

1.1.5.4. Sponges

Sponges are made up of interconnected porous structures that have been shown to closely mimic physiological environments *in vivo*.¹ RSF sponge scaffolds with different pores size can be formed by use of porogens, freeze-drying and gas foaming fabrication techniques.^{72, 135} Sodium chloride (NaCl) particles are a classic example of a porogen and are added into SF solutions cast into Teflon (PTFE) moulds. After scaffold formation the salt is left to leach out of the construct (in di-water).⁷² This method leads to RSF sponge scaffolds with highly homogeneous uniform pore size distribution, providing the NaCl particles added have a homogenous size distribution.¹³⁵ Another method of regulating the pore size of sponges is via freeze drying, here the freeze drying temperature, fibroin concentration, and pH of the RSF solution affect the pore size.¹³⁶ For example, Mandal *et al.*¹³⁷ reported that at fixed fibroin concentrations, the pore size decreased with decreasing temperature. In contrast, with a constant freeze-drying temperature but increasing fibroin concentration the pore size decreased. In addition, the pore size increased further with repeated freeze and thawing cycles.¹³⁸ Gas foaming techniques also can form RSF sponges. Ammonium bicarbonate added into fibroin solutions will sublime in hot water aiding the formation of porous sponge structures.⁷² Yan *et al.*³² also combined the aforementioned and mixed NaCl particles in highly concentrated RSF solutions, followed by freeze drying, which showed a favourable stability in the formation of macro/microporous structures. RSF sponges have been widely used in tissue engineering, especially in bone and cartilage,^{1, 25} because of excellent porosity and pore size control.¹³⁹

1.1.5.5. Micro-patterning structures

The extracellular matrix (ECM) is made up of complex micro/nano-scale topographies, which can affect cell behaviour. It is therefore important to try and mimic these topographies as much as possible to ensure cell behaviour to be similar *in-vitro* to *in-vivo* scenarios. Micro-patterning structures of RSF have been shown to affect cell migration, proliferation and adhesion.^{140, 141} At present lithographic techniques are the most commonly used method in micropatterning RSF biomaterials. These methods include, ultraviolet lithography (UVL)¹⁴², soft

lithography (SL)¹⁴³, electron-beam lithography (EBL)¹⁴⁴ and scanning probe lithography (SPL)¹⁴⁵.

UVL as schematically shown in [Figure 1-5 A](#) is done by spin coating RSF onto silica substrates as positive-tone photoresist which was illuminated by argon fluoride excimer laser through a patterned chrome mask. After washing the exposed area with Di-water, the patterned RSF film showed diffracted colours with minimum line widths of 1 μm . Note that, this is water-based process and does not require photoinitiators.¹⁴² In comparison to UVL, SL is cheaper and requires less steps.¹⁴⁶ For example, Gupta *et al.*¹⁴³ spin coated RSF onto polydimethylsiloxane (PDMS) stamps, and submerged into a methanol solution. The crystallized RSF films were then peeled from the stamp, as shown in [Figure 1-5 B](#). In the case of EBL shown in [Figure 1-5 C](#), RSF functioned as a resist material whose solubility could be regulated by different dosages of electron radiation. Therefore, amorphous RSF can be crosslinked while crystalline RSF can be de-crosslinked through electron bombardment. The RSF that has not been crosslinked can then be simply washed away with water. In detail, RSF was spin coated on the substrate to form RSF films. Then, for positive resist fabrication, inelastic collision of electrons with RSF in water-insoluble state were protein degraded (de-crosslinked) into a water-soluble state, followed by washing away during 'water development' process. In contrast, for negative resist fabrication, high electron beam doses combined with RSF water-soluble solution can be crosslinked into the water-insoluble state. After that, 'water development' process can wash away the area have not been crosslinked and left the area exposed to the electron beam.¹⁴⁴ The reported critical feature sizes of UVL, SL, and EBL techniques are around 1.5 μm , 40 nm and 20 nm respectively.¹⁴⁷ Another technique, SPL as shown in [Figure 1-5 D](#) also offers high precision and resolution by means of for example an AFM tip. One type of SPL uses atomic force microscopy (AFM) as a tool to pattern RSF solutions under aqueous solutions via AFM tip in tapping mode or contact mode.¹⁴⁵ Piezoelectric-based Inkjet printing can be used in large-scale fabrication and no cast or spin coating is needed for inducing structural transformation of SF.¹⁴⁷ Inkjet printing can print functional inks in CAD designed patterns, such as RSF inks mixed with enzymes,¹⁴⁸ growth factors, gold nanoparticles, antibiotics or other moieties on different surfaces suitable for tissue engineering applications.

Tao et al.¹⁰⁰ reported inkjet printing of a spider web (Figure 1-5 E) pattern using RSF as the ink and the thickness of the pattern could be regulated by controlling the amounts of printed drops.

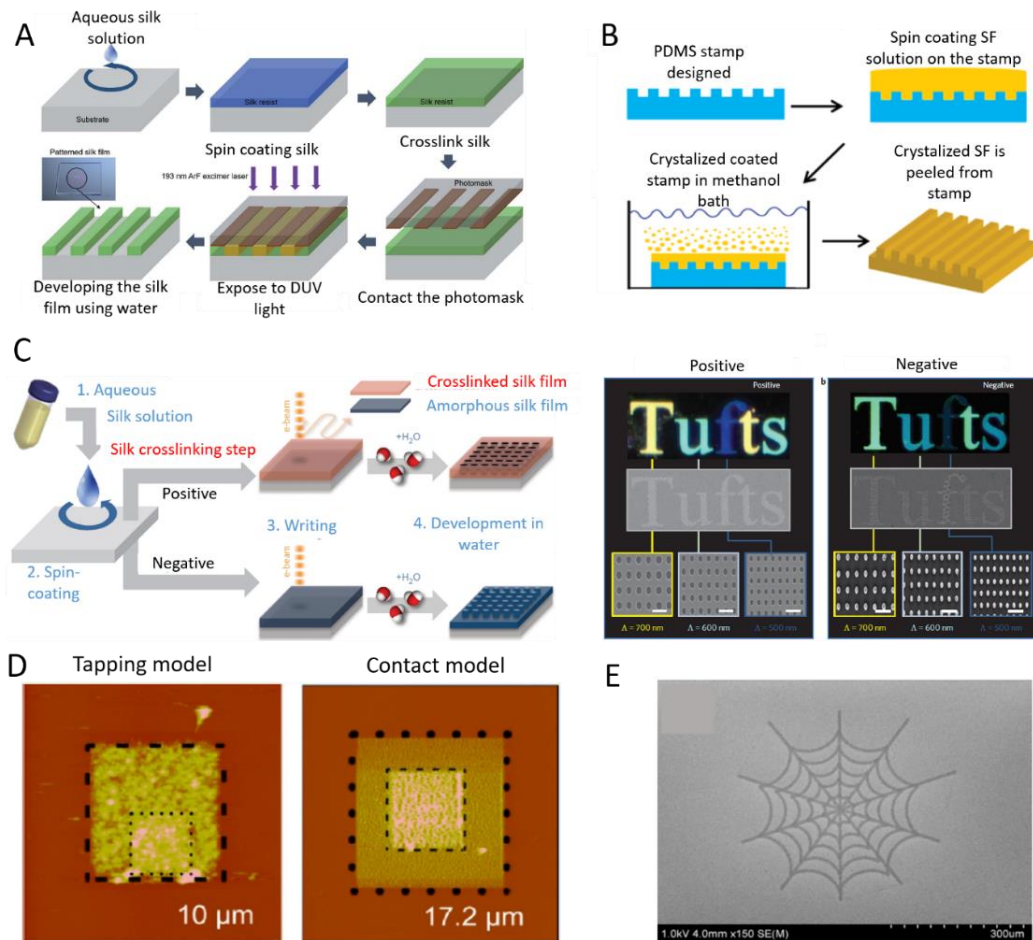


Figure 1-5 Micro-patterning of silk-based biomaterials. **A)** Schematic diagram of ultraviolet lithography process which can form high-resolution silk fibroin micro-patterns by ArF excimer laser. **B)** Schematic diagram of soft lithography of fabricating patterned silk films. **C)** Schematic diagram of water-based electron-beam patterning on a silk film. Dark-field and electron microscopy images of silk nanostructures generated on positive and negative resist. **D)** Atomic force microscopy (AFM) images of patterned silk films fabricated by AFM patterning in tapping mode and contact mode. **E)** SEM images of micro-spider web fabricated by inkjet printing. (A reprinted with permission from ¹⁴²; B from ¹⁴³; C from ¹⁴⁴; D from ¹⁴⁵; E from ¹⁰⁰).

1.1.5.6. 3D bioprinting structures

Sponges prepared with typical methods have no defined internal pore architecture which can obstruct cellular response. Bioprinting is a bottom-up additive manufacturing technology that can be used to manufacture complex

structures via CAD design at high definition. For example, biocompatible hydrogels can be printed via 3D extrusion bioprinting. It is possible to encapsulate cells in the hydrogels which give them mechanical support in a 3D environment similar to their native tissue.¹⁴⁹ Although 3D bioprinting has been applied in tissue engineering, there are still many challenges to overcome, including a limited range of materials and choice of cell types.¹⁵⁰ RSF is a unique material for 3D printing owing to its biocompatibility and polymorphic nature.²⁰ RSF can be printed via inkjet printing to fabricate “nest” shapes. RSF printed “nests” of 70-100 μm diameters, were stabilized by ionic pairing followed by a drying process to form silk II crystalline secondary structures, and could act as anchored nests for cell incubation and proliferation.¹⁵¹ Das *et al.*¹⁵² reported 3D bioprinting RSF-gelatin scaffolds which could be used in culturing human nasal inferior turbinate tissue-derived mesenchymal progenitor cells. The sonication treated RSF-gelatin hydrogels possessed higher β -sheet content compared to that of tyrosinase enzyme treated hydrogels, further to this only the sonication produced RSF-gelatin hydrogels demonstrated enhanced osteogenic differentiation. In addition, a recent study by Rodriguez *et al.*¹⁰¹ reported the successful printing of RSF / synthetic nanoclay (Laponite) / polyethylene glycol (PEG) scaffolds via extrusion based 3D Printing. Here, a key advantage is that gelation of the scaffolds occurs during the printing process and therefore there is no need of additional post processing such as chemical or photochemical crosslinking. This allowed for simple and rapid fabrication of complex geometries of the biomaterials down to the microscale. Generally, 3D printed RSF scaffolds are macroscopic in structure, but can be regulated into mesostructures and nanostructures by using mechanical stresses and dopants. For example, Sommer *et al.*¹⁵³ reported the pore size of a RSF structure could be regulated by adding sacrificial monodisperse organic microparticles with varying sizes into RSF-based inks to create well-defined porous RSF scaffold structures. Recently, Kim *et al.*¹⁵⁴ reported RSF can be chemically modified with glycidyl methacrylate (GMA) to form a printable bioink (Sil-MA) (Figure 1-6 A) which could be printed to form complex structures, e.g. brain and ear, via a digital light processing (DLP) 3D printer ((Figure 1-6 B). The produced 3D scaffolds possessed strong mechanical properties, which can be used in cartilage TE applications.¹⁵⁵ Following this work, Ajiteru *et al.*¹⁵⁶ further

improved the properties of the Sil-MA bioink by conjugating it with reduced graphene oxide (rGO) to form a composite bioink, which was shown to exhibit better thermal stability as well as higher solubility.

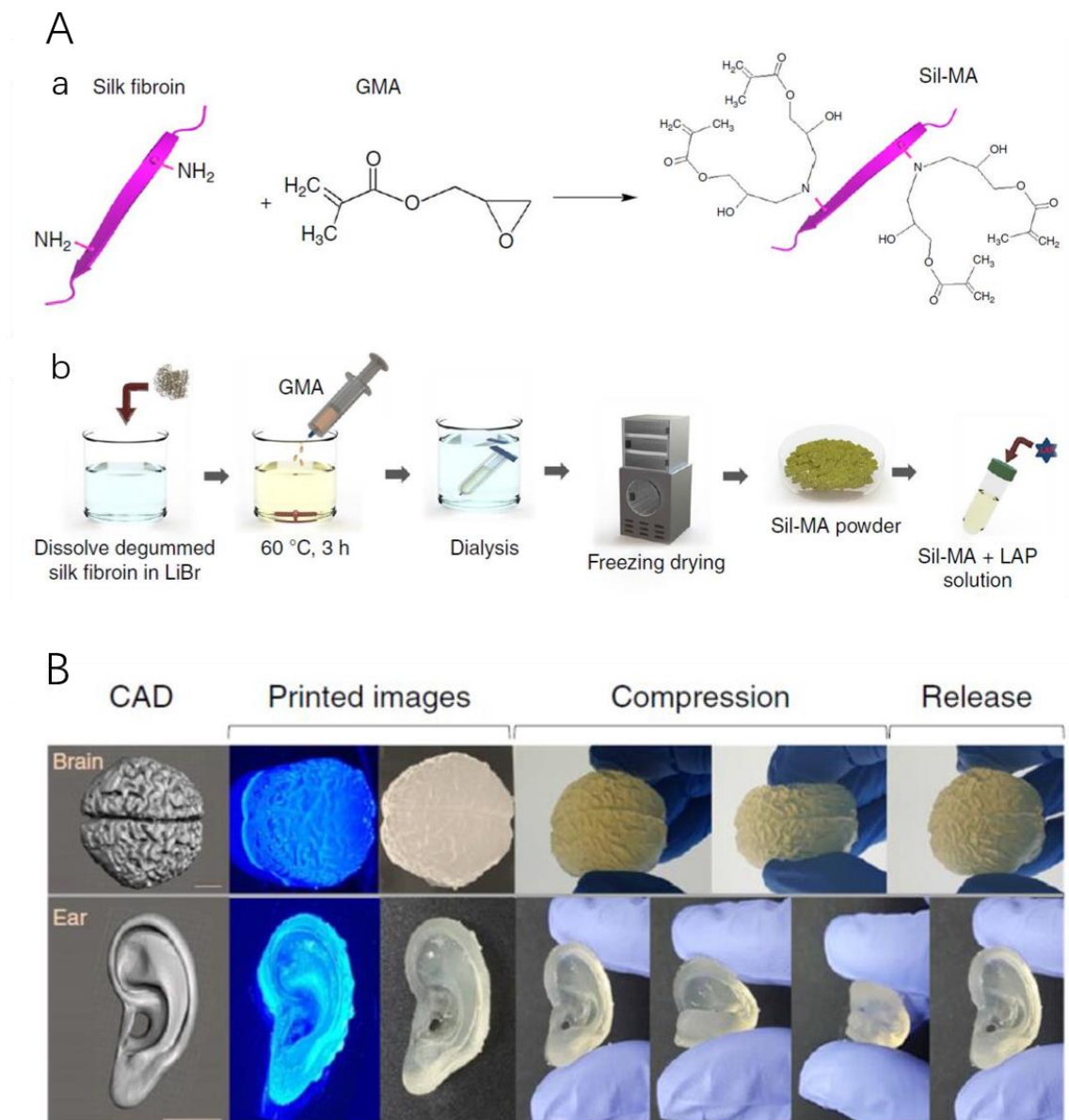


Figure 1-6 **A**) Regenerated silk fibroin (RSF) was chemically modified with glycidyl methacrylate (GMA) to form (Sil-MA) as a pre-hydrogel. **(a)** RSF covalently immobilized with GMA, generating a vinyl double bond as a UV-crosslinking site. **(b)** Schematic diagram of the methacrylation process of SF; LAP represents Lithium phenyl(2,4,6-trimethylbenzoyl) phosphinate which is a photoinitiator. **B**) Representative 3D printed models (brain and ear) via a digital light processing (DLP) printer using Sil-MA as a bioink, showing complex structure reflecting their CAD images. Reprinted with permission from¹⁵⁴.

1.1.6. Application of silk fibroin in tissue engineering

1.1.6.1. Bone tissue regeneration

Bone is a specialized connective tissue, and is composed of 35% organic parts and 60% inorganic matrix.¹⁵⁷ More than 90% of the organic extracellular matrix of bone is made up of collagen and the rest contains hyaluronan, proteoglycans, bone sialoprotein, osteopontin, osteonectin and osteocalcin.¹⁵⁸ Hydroxyapatite (HA) is the major component of the inorganic mineral phase of bone, while the remaining is composed of inorganic salts and carbonate.¹⁵⁹ This means that collagen and HA are the major components of bone tissue, which enhances the strength and hierarchical architecture of bone.¹⁶⁰ Designed scaffold materials for the use in bone tissue engineering should guarantee matrix toughness and allow for ECM deposition. SF has high toughness, mechanical strength and proven biocompatibility which has already been widely studied in bone TE.¹⁶¹ For example, RSF scaffolds have been shown to promote osteogenic differentiation of human mesenchymal stem cells (HMSCs) *in vitro*. These constructs have been shown to heal femoral defects *in vivo* in nude rat models.¹⁶² Meinel *et al.*¹³⁹ demonstrated that after initial incubation in bioreactors for 5 weeks, porous SF-based scaffolds could be implanted into cranial defects in mice and showed advanced bone formation within 5 weeks, *in vivo*.

RSF scaffolds are used in combination with other biomaterials such as collagen, or calcium phosphate based inorganic components to enhance osteogenic properties.^{27, 163} For example, HA/RSF porous scaffolds were fabricated through an alternate soaking process in CaCl_2 and Na_2HPO_4 or alternatively by mixing NaCl particles with HA and then mixing these with RSF solutions.^{164, 165} These composite scaffolds were shown to have better osteoconductivity and exhibited an enhanced formation of tissue engineered bone, compared to unmodified RSF scaffolds.

Bone morphogenetic protein (BMP)-2 and BMP-7 are FDA recognised growth factors that can support bone formation and regeneration.¹⁶⁶ It has been shown that RSF combined with these growth factors together with HMSCs exhibited enhanced osteoblast adhesion and differentiation, stimulated alkaline

phosphatase activity and promoted bone formation *in vivo*.^{167, 168} In addition, Li *et al.*¹⁶⁹ reported the modification of electrospun RSF mats with BMP-2 and HA nanoparticles, which support HSMCs differentiation and growth and resulted in more calcium deposition in comparison to RSF mats only. Moreover, demineralized bone matrix (DBM) powder or particles are mainly composed of collagen and BMP which also possess osteoinductive and osteoconductive properties. Ding *et al.*¹⁷⁰ reported RSF as a carrier for loading DBM. This carrier can form stable porous structures and has been shown to promote osteogenesis in mice together with bone marrow stem cells (BMSCs).

Rapid and thorough vascularization is required in order to increase the success of bone regeneration. For example, RSF matrices pre-incubated with osteoblasts *in vitro* and then implanted into mice showed enhanced vascularization *in vivo*.¹⁷¹ In addition, co-cultures of endothelial cells and osteoblasts in RSF scaffolds *in vitro* showed the formation of microcapillary-like structures¹⁷² and pre-vascular structures¹⁷³. Subsequently, pre-formed microcapillary-like structures implanted into immune-deficient mice, not only survived, but successfully interfaced with the host vasculature, and further stimulated the host capillaries for vascularization.¹⁷⁴ Further to this the vascular endothelial growth factor (VEGF) could not only promote osteoblast differentiation but also caused neovascularization.¹⁷⁵ In this context Farokhi *et al.*¹⁷⁶ embedded VEGF into RSF/calcium phosphate/poly(lactic-co-glycolic acid) scaffolds. The results indicated that the scaffolds maintained about 83% bioactivity after VEGF release up to 28 days *in vitro*. For *in vivo* study, the neo-bone formation in defects site of rabbits after implanted for 10 weeks. Another study conducted by Zhang *et al.*¹¹⁹ reported that a sonicated silk hydrogel carrier loaded with BMP-2 and VEGF could promote both osteogenesis and angiogenesis in rabbit's maxillary sinus floor after implanted for 12 weeks.

1.1.6.2. Cartilage tissue regeneration

Cartilage is avascular and aneural connective tissue surrounded by a dense ECM and lacks the innate ability to self-repair after injury degeneration. Collagen and proteoglycans make up the main parts of the cartilage ECM, which can provide adequate mechanical properties for tissues *in vivo*.^{177, 178} Therefore, maintaining and preserving this tissue is an important aspect in

tissue engineering. SF scaffolds can be used to enhance the production of cartilaginous ECM¹⁷⁹ and owing to its tuneable properties the resulting scaffolds can be fabricated into different morphologies¹⁸⁰. For example, porous RSF scaffolds combined with HMSCs can provide zonal structures similar to that of native cartilage tissue, which was shown by Wang *et al.*¹⁸¹ after 3 weeks of incubation, HMSCs grew along the chondrogenic route within the scaffold.¹⁸¹ In addition, the Insulin-like growth factor I (IGF-I) can promote different progenitor cell growths, which can be loaded into porous RSF scaffolds promoting chondrogenic differentiation of HMSCs.¹⁸²

Other natural biopolymers can be blended with RSF to produce biocompatible cartilage constructs. One example is chitosan, which can provide sufficient support to chondrocytes due to the existing glycosaminoglycan residues.¹⁸³ Both Bhardwaj *et al.*¹⁸⁴ and Silva *et al.*¹⁸⁵ investigated this showing that chitosan could increase cell attachment, proliferation and chondrogenic phenotype of chondrocytes or chondrocyte-like cells. Another biopolymer combination that has been studied is Gelatin/RSF. Gelatin is a partial derivative of collagen and both collagen and gelatin possess the ability to promote chondrogenic differentiation.¹⁸⁶ RSF/collagen dense mats fabricated by electrospinning and seeded with MSCs showed better chondrogenic differentiation of MSCs and promoted expression of cartilaginous matrix compared to collagen-only dense mats.¹⁸⁷ It is assumed the reason for this might be caused by the increase in scaffold strength. In addition, Wang *et al.*²⁹ fabricated porous RSF/collagen scaffolds combined with poly-lactic-co-glycolic acid (PLGA) microspheres which exhibited good cell affinity and promoted articular cartilage in rabbits. Recently, Shi *et al.*¹⁸⁸ reported that a mixture of SF solution (6.9% w/v) and gelatin solution (6.9% w/v) at a mass ratio 1:2 could be used to fabricate SF/Gelatin (SFG) scaffolds with good degradation and mechanical properties via 3D printing for the use in cartilage repair (Figure 1-7 A and B). SFG scaffolds have chondrogenic differentiation abilities of bone marrow stem cells (BMSCs), the native round shape of chondrogenic cells could be observed after 21 days of *in vitro* incubation (Figure 1-7 C). In addition, it has been shown that SFG scaffolds implanted into defective rabbit cartilage positions repaired the cartilage defect after 24 weeks (Figure 1-7 D). Except from the above mentioned, RSF also can be blended with other biopolymers such as

cellulose¹⁸⁹, hyaluronic acid¹⁹⁰, agarose¹⁹¹ and poly(D,L- lactic acid)¹⁹² to provide sufficient support to chondrogenesis.

It has been shown that the mechanical and structural characteristics of RSF-based scaffolds can be improved by argon plasma treatment.¹⁹³⁻¹⁹⁵ For example, Baek et al.¹⁹³ reported that porous RSF scaffolds treated with microwave-induced argon plasma exhibited a significantly increased hydrophilicity and therefore increased chondrocyte adherence, and proliferation. It has been shown that cells seeded on the RSF scaffolds and then incubated in physically stimulated bioreactors under physiological conditions could further improve cartilaginous constructs.^{196, 197} For example, the amounts of glycosaminoglycan, total collagen, collagen II and DNA along with cartilage-related gene produced by cells increased significantly by seeding porous SF scaffold with HMSCs and incubated in perfusion bioreactors for 4 weeks. Additionally, the same study found that the mechanical stiffness of the stimulated scaffold also increased in comparison to a static culture.¹⁹⁶ These results indicate that hydrodynamic factors as well as cell types¹⁹⁸, scaffold architectures e.g. pore size and distribution are key components to successful constructs for cartilage TE.³⁵

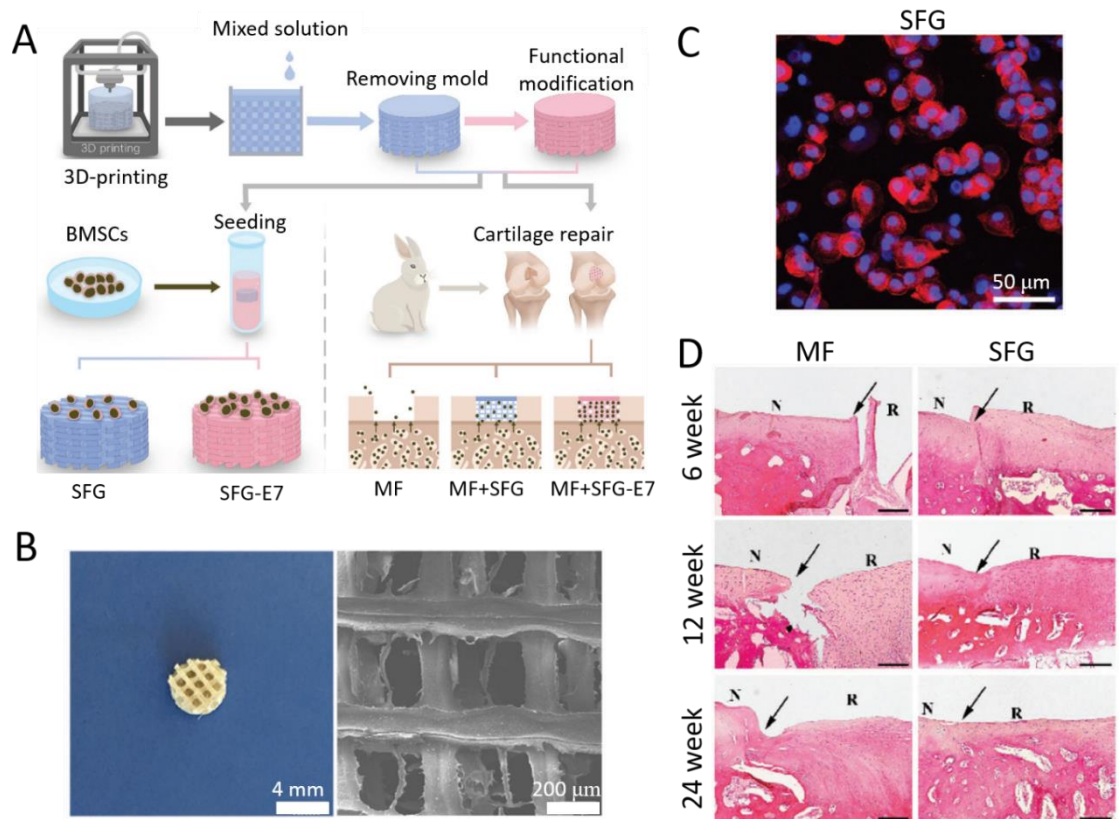


Figure 1-7 **A)** Schematic diagram illustrating the fabrication of a 3D scaffold made via Bioprinting up to the final in vivo implantation. **B)** Microscopy and SEM images of the SFG scaffold (mixture of SF solution and gelatin solution at a mass ratio 1:2). **C)** Phalloidin/Hoechst assay of chondrogenic morphology on the SFG scaffold after 21 days incubation. **D)** Hematoxylin-eosin staining of repaired cartilage at 6, 12 and 24 weeks. (MF represents the microfracture control group; N represents normal cartilage; R represents repaired cartilage; the margins between repaired and normal cartilage are indicated by black arrows; scale bar: 200 μ m). Reprinted with permission from¹⁸⁸.

1.1.6.3. Ligament and tendon tissue regeneration

Ligament and tendon tissues are composed of collagen and fibrocytes which are made up of a dense fibrous connective tissue, which can be easily impaired and severely lacks the ability of natural regeneration.^{199, 200} Due to its unique mechanical properties (such as high toughness values and good elasticity) and structural integrity, RSF scaffolds have become a preferred biopolymer for the use in ligament and tendon TE.³⁵ In 2002 the first RSF matrix was successfully implemented in engineering an anterior cruciate ligament (ACL) that matched the mechanical properties of the human ACL.⁷¹ Based on these promising results, researchers started fabricating knitted SF-based scaffolds for the regeneration of ligaments and tendons. For example, Liu *et al.* fabricated web-like SF sponges on knitted scaffolds on which HMSCs were seeded, these scaffolds are more cellular actively compared to RSF hydrogel knitted scaffolds. The results demonstrated SF-based knitted scaffolds proved structural strength, while the web-like microporous RSF sponges can enhance cellular activity.²⁰¹ Subsequently, Fan *et al.* implanted RSF porous knitted scaffolds with MSCs into rabbit²⁰² and pig²⁰³ models to regenerate ACL. After 24 weeks of implantation, the direct ligament–bone insertion with four zones (bone, fibrocartilage, mineralized fibrocartilage, ligament) in rabbit and three zones (bone, Sharpey’s fibres and ligament) in pig was reconstructed, which was similar to native structures of ACL–bone insertion. The tensile strength of regenerated ligaments also compared to the mechanical properties of the native ligaments. In addition, Chen *et al.*²⁰⁴ combined RSF knitted scaffolds with collagen and then implanted these into rabbit medial collateral ligament (MCL) defected regions, which was

shown to promote scaffold–ligament interface healing, compared with untreated MCL or only SF knitted scaffold.

An arginine-glycine-aspartic acid (RGD) peptide sequence can also be immobilised onto RSF scaffolds and has been shown to promote the attachment of BMSC cells leading to higher human bone marrow cells and ligament fibroblast formation.²⁰⁵ Additionally, sequential administration of growth factors, including epidermal growth factors, transforming growth factor- β and basic fibroblast growth factor, induced BMSCs cells to proliferate and differentiate on RGD-coupled RSF scaffolds, which can boost the development of ligament tissue.²⁰⁶ Growth factors stimulate biochemical and mechanical properties, thereby inducing cell differentiation toward a fibroblast lineage and enhanced matrix in-growth, as well as collagen production.^{207, 208}

In conclusion, blending RSF with natural biomaterials such as collagen type I²⁰⁹, hyaluronic acid²¹⁰ and gelatin²¹¹ and synthetic materials e.g. polyelectrolyte²¹² and PLGA²¹³ leads to the enhancement of scaffolds for use in the reconstruction of ligament and tendon connective tissues.

1.1.6.4. Skin and wound tissue regeneration

The skin holds a critical role as the first line of defence to infectious organisms. Epidermis and dermis are the main layers of skin, which mainly consist of keratinocytes and ECM (mainly collagen and elastin). In cases with extreme loss of skin integrity, e.g. severe burns, this can lead to disability and even death.^{214, 215} RSF biomaterials have been shown to influence the attachment of keratinocytes and fibroblasts¹⁰⁵ and are widely applied to skin regeneration in TE. Recently, Zhang et al.⁹⁶ reported RSF films could be implanted into full-thickness skin defects in rabbit models (Figure 1-8 B) and porcine models (Figure 1-8 C), which significantly reduced the healing time and showed better skin regeneration compared to current commercial wound dressings. In clinical trials, RSF films have also been shown to significantly reduce the healing time and lower the probability of adverse events, compared to commercial wound dressings. Additionally, RSF mats coated with antibacterial silver nanoparticles (AgNPs) could be used as antimicrobial wound dressings to inhibit the growth of *Staphylococcus aureus* and *Pseudomonas aeruginosa*.¹⁰⁹ The hydrophilicity of

RSF nanofibers has been shown to increase after O₂ plasma treatment, which has been shown to promote human keratinocytes and fibroblasts activities.²¹⁶

Appendages on the skin (e.g. hormonal glands and hair) make skin tissue complex.³⁵ Chitosan has been widely used in skin TE, due to its biocompatibility, biodegradability and antimicrobial ability as well as being known to promote collagen formation from fibroblast cells, which increases the tensile strength of the regenerated tissue in the defected area.²¹⁵ Cai et al.²⁸ fabricated RSF/chitosan scaffolds via electrospinning and found the mechanical strength increased with increasing RSF concentration as well as an increase of antimicrobial activity with increasing chitosan concentration. Moreover, SF/chitosan scaffolds were shown to promote cellular proliferation and antimicrobial property against *Escherichia coli*.^{28, 217} Furthermore, alginate dialdehyde (ADA) enhances cell proliferation and attachment and has a lower toxicity when used as corsslinker.²¹⁸ Therefore, ADA can be used to crosslink RSF/chitosan scaffolds in defected skin areas and shows good water absorption, high water transmission and increased cell activity.²¹⁹ Guang et al.²²⁰ reported chitosan coatings on porous RSF scaffolds via a hydrogen-bonding technique to form 3D RSF/chitosan scaffolds, and then implanted these into a rat wound. Their data showed the wound was fully repaired after 21 days and without any teratogenic effects and infections. In comparison non-mulberry RSF from *Antheraea assama* (*A. assama*) was also shown to be a promising material for skin TE. This is because it naturally contains the RGD peptide sequence that promotes cell attachment.²²¹ Chouhan et al.²²² fabricated RSF hydrogels by blending SF solutions isolated from *A. assama* and *B. mori*, which promoted the differentiation of primary human dermal fibroblast and keratinocytes cells *in vitro*. In addition, the blended SF solutions were injected into third-degree burn wounds *in-vivo* and formed gels that firmly adhered to the wounds. The blended RSF hydrogel not only acted as a supportive matrix for skin repair, but also showed transition stages from inflammation to proliferation.

The above mentioned illustrate the vast capabilities the RSF scaffold materials and how they can be blended with natural and synthetic materials, such as dextrose²²³, TEMPO-oxidized cellulose nanofiber²²⁴, Manuka honey²²⁵, Ag particles²²⁶, collagen²²⁷, chitin²²⁸ to increase mechanical properties, decrease

wound infections and improve wound healing. Therefore, the use of composite RSF scaffolds were able to provide overall better results to pure RSF scaffolds in skin TE applications.

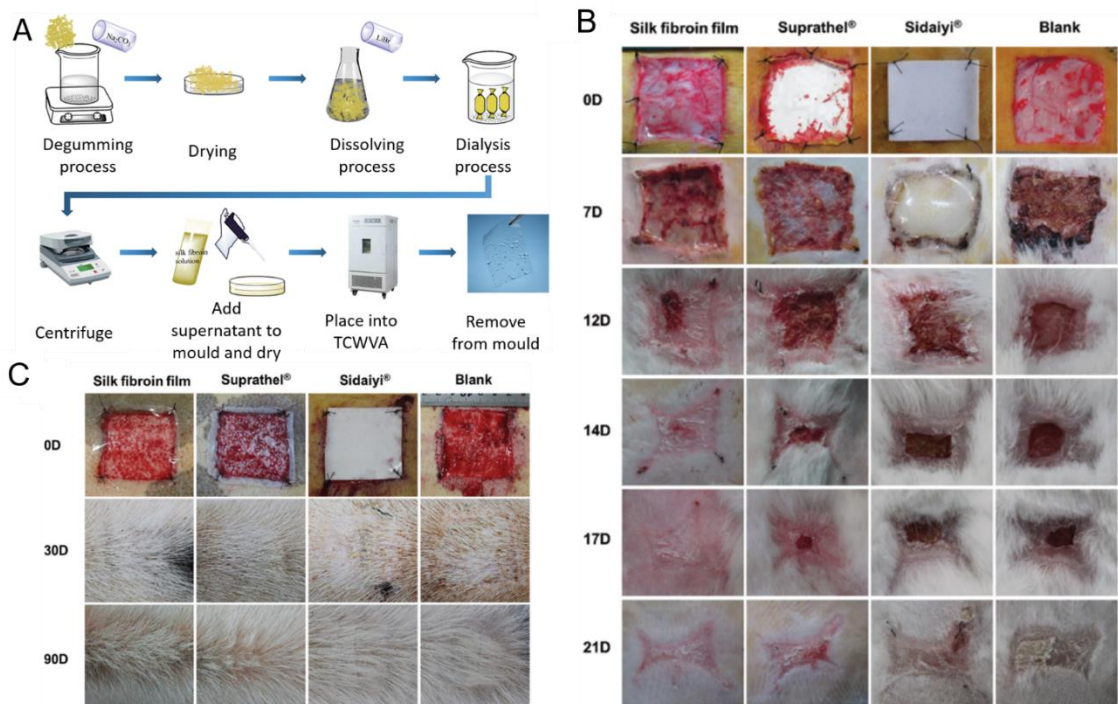


Figure 1-8 **A)** Schematic diagram of silk fibroin films via Temperature Controlled Water Vapour annealing (TCWVA). **B)** RSF films implanted into full-thickness skin defects in rabbit models compared to Suprathel, Sidaiyi and untreated tissue at 0, 7, 12, 14, 17 and 21 days. **C)** RSF films implanted into full-thickness skin defects in a porcine model and compared to Suprathel, Sidaiyi or untreated at 0, 30 and 90 days. Reprinted with permission from⁹⁶.

1.1.6.5. Tympanic membrane tissue regeneration

Tympanic membrane (TM) is a transparent structure located between outer and middle ear, whose functions is receiving sound vibrations and protecting medium ear. TM is composed of the epidermal outer layer, fibrous middle layer and mucosal inner layer, which mainly consist of keratinocytes, fibroblasts and collagen (type II and type III).^{229, 230} TM perforations are normally caused by middle ear infections or traumatic ruptures caused by mechanical trauma and pressure blasts. If the rupture has not self-repaired within 3 months, it will become a chronic perforation, which can lead to hearing loss and recurrent infections.²²⁹⁻²³¹ The excellent properties of RSF as mentioned above make it an idea material for tympanic membrane TE, supporting the growth and spread

of keratinocytes derived from human TM cells.²³²⁻²³⁴ Shen *et al.* implanted RSF films into rat²³⁵ and guinea pig²³⁶ models to regenerate acute TM perforations using onlay myringoplasty. After implantation, a perforation closure for both rat and guinea pig models were observed after 7 days, where no recovery was observed in the control groups. In addition, RSF films were shown to not only repair TM perforation but also accelerate the regeneration of TM, leading to a significantly faster hearing recovery. Furthermore, Shen *et al.*²³⁷ demonstrated RSF films showed no significant macrophage response in host tissue, less inflammation, and was degradable *in vivo*. In addition, Allardyce *et al.*²³⁸ reported that RSF membranes possess good acoustic energy transfer capability and excellent tensile strengths to cartilage, indicating the great potential of these membranes to regenerate chronic TM perforations *in vivo*.

1. 2. Designer peptide amphiphiles as scaffolds for tissue engineering applications

Abstract

Peptide amphiphiles (PAs) are composed of a hydrophobic tail and hydrophilic head, which can self-assemble into well-ordered nanostructures eventually leading to the formation of hydrogels. In addition, the diversity of natural amino acids endows PAs the possibility to produce range of sequences with different biological functions. These properties along with their biocompatibility, biodegradability and a high resemblance to native extracellular matrix have resulted in PAs being considered ideal scaffold materials for use in tissue engineering (TE) applications. This review introduces the 20 natural canonical amino acids followed by highlighting the three categories of PAs, including amphiphilic peptides, lipidated peptide amphiphiles and supramolecular peptide amphiphile conjugates, as well as their design rules that dictate the peptide self-assembly process. Furthermore, 3D bio-fabrication strategies of PAs hydrogels are discussed and recent advances of PA-based scaffolds in TE with an emphasis on bone, cartilage and neural tissue regeneration *in vitro* and *in vivo* are considered. Finally, future prospects and challenges are discussed.

Keywords: Peptide amphiphiles, Biomaterial, Scaffold, Tissue engineering

1.2.1. Introduction

Tissue engineering (TE) is a highly multidisciplinary field the aim of which is to regenerate damaged tissues or organs through developing biological substitutes that maintain, restore or improve the function of the target tissues or organs, rather than replace them. TE relies extensively on scaffolds which are typically seeded with cells. This can be either cultured *in vitro* to synthesize tissue that is then implanted into the injured site or implanted directly into injured site exploiting the body's own systems for the regeneration of tissue.⁵ These scaffolds can be divided into natural²³⁹ or synthetic categories²⁴⁰. Part of the natural category comprises silk fibroin, collagen, hyaluronic acids and Matrigel, while the synthetic category includes polylactic acid (PLA), polycaprolactone (PCL), polyglycolic acid (PGA) and poly (lactic-co-glycolic acid)

(PLGA) amongst others.^{239, 240} However, with the aforementioned scaffolds several disadvantages and limitations exist. For example, Matrigel and collagen I hydrogel have high variations in batch to batch production, and the synthetic scaffolds normally lack cell adhesion sites, whose degradation products contain acidic compounds that are harmful to human body.²⁴¹⁻²⁴³ On the other hand the precise control of protein-based scaffolds give rise to many benefits for TE which include structural tunability, excellent biocompatibility and an abundance of sites for easy functionalisation and modification.¹⁹

Proteins, made from amino acids as building blocks, are ubiquitous in nature and can perform specific biological functions, these include DNA replication, catalysis, transporting desired molecules and supporting cells in the extracellular matrix (ECM).²⁴⁴ In the early 1990s, the first self-assembling peptide EAK16 (AC-(AEAEAKAK)₂-CONH₂ where the N terminal charge is blocked by an acetyl group and the C terminal carboxylic group is blocked by an amine group) was designed according to a repeating segment in the yeast protein Zuotin. This discovery led to the concept of self-assembling peptides as TE materials for scaffolds fuelling increased interest by many researchers to date. Subsequently, numerous de novo or biomimetically derived synthesised peptides mimicking the peptide EAK16 have been designed.^{241, 245, 246} The “Bottom-up” approach is known as the strategy for the fabrication of self-assembled peptides, which exploits amino acids as building blocks to form various nanoarchitectures, which include: nanotubes, nanovesicles, nanobelts, nanofibers, nanorods, nanoparticles. These ordered aggregates are formed spontaneously by non-covalent bonds, such as electrostatic and Van der Waals forces, hydrogen bonding, hydrophobic and π - π stacking. Based on the inherent biocompatibility and biodegradability of self-assembling peptides, they can be applied to a ranging array of medically related applications, these include: drug and gene delivery, skincare and cosmetics as well as the stabilisation of membrane proteins.²⁴⁷⁻²⁴⁹

Peptide amphiphiles (PAs) are one important class of self-assembling peptides that have been extensively researched over the past two decades.²⁵⁰⁻²⁵³ These can self-assemble into high-aspect-ratio nanostructures under certain solution conditions, such as pH, ionic strength and temperature.²⁵⁴ Recent research

suggests that the group of PAs can be classified into amphiphilic peptides, lipidated peptide amphiphiles and supramolecular peptide amphiphile conjugates.²⁵² In general, PAs contain a hydrophobic tail that can be designed via conjugating hydrophobic segments (e.g., lipid tail) at the ends of the peptide sequence or on specific residues. The hydrophobic tail of PAs is responsible for driving self-assembly and exposes the functional peptide group on the surface of the self-assembled nanostructures.²⁵⁵ One example of a PA molecule was designed in 2001, it could be self-assembled into long nanofibers and produce a nanostructured fibrous scaffold with biological signals giving it great potential to mimic the ECM.²⁵⁶ Since then, the use of PAs as functional biomaterials has been extensively researched and has been recognised as remarkable materials for scaffolds,²⁵⁷⁻²⁵⁹ resulting in several advantages including: 1) Most PAs are composed of natural L-amino acids, giving them good biocompatibility.²⁶⁰ 2) Owing to the natural diversity of amino acids, there are 5²⁰ possible sequences for the fabrication of pentapeptides. 3) A high density of surface signals that can interact with cells.²⁶¹ 4) Hydrogen bonding assisting the self-assembly process of PAs forming highly stabilized β -sheet conformation.²⁶² 5) PAs can be designed based on bioactive sequences, such as Fmoc-RGD²⁶³, and the functional core of fragments of protein, for example the C₁₂-GAGAGAGY peptide sequence is designed based on the structure of silk fibroin, and can be self-assembled into robust and plastic hydrogels induced by pH change.²⁶⁴

This review focuses on the design of PA molecules for use as cell culture scaffolds for use in 2-dimensional (2D) and 3-dimensional (3D) TE applications. We outline recent advances in the design of PAs, in light of their composition and types as well as introducing the fabrication technologies of PA-based scaffolds. We then discuss the applications of these scaffolds in TE, with an emphasis on bone, cartilage and neural tissue regeneration.

1.2.2. The Natural building blocks: amino acids

There are 20 different natural amino acids which can serve as building blocks for peptide biosynthesis (Figure 1-9). Out of these proline, glycine and cysteine are rather special due to their unique structures and play special roles in driving peptide folding. Apart from proline, where the side chain (R group) is covalently

linked with the amino terminus, all other amino acids possess the same α -HN-CH-COOH motif, but bearing different R groups attached to the centre carbon (α) atom. This enables the molecules to possess different properties and resulting in different biological functions. This difference in R group of proline results in a locked conformation, giving a conformational rigidity over other amino acids that therefore introduces intramolecular folding during peptide self-assembly. For example, hairpin peptide MAX1: (VK)₄-V^DPPPT-(KV)₄-NH₂ contains a turn-forming -V^DPPPT- segment that can promote the folding into β -hairpin-like structure.²⁶⁵ Glycine is the only achiral molecule of all amino acids, its R-group contains only a single hydrogen atom and therefore it does not have an L-configuration or D-configuration. In addition, the hydrophobicity (π value) of glycine is defined as 0.0 meaning glycine is neither hydrophilic nor hydrophobic. Moreover, glycine possesses a higher degree of flexibility than other amino acids, this is because there are no steric hindrances imposed by its R group in the structure of glycine. The amino acid cysteine possesses a sulphur-containing thiol side chain that enables the formation of disulphide bonds between two peptide chains or alternatively a loop formation with a single peptide chain. For example, the cyclisation of the peptide sequence AC-C(FKFE)₂CG-NH₂ is driven by intramolecular disulphide bonds of cysteine residues, which prevents β -sheet conformation and consequently stops the self-assembly. When the reduction of disulphide bond, the peptide starts to self-assemble and can form fibrillar superstructures and can even form hydrogels under certain concentrations.²⁶⁶

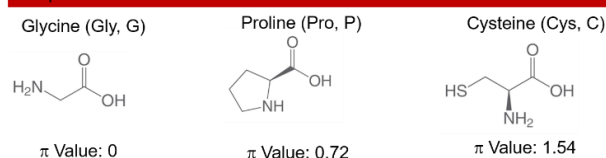
According to the properties of the R groups, amino acids can be classified into electrically charged, polar uncharged and hydrophobic species, excluding the special cases previously discussed (proline, glycine and cysteine). Electrically charged residues can be divided into positively charged (histidine, arginine and lysine) and negatively charged (aspartic acid and glutamic acid), these can form charge-charge interactions that have the potential to promote or prevent self-assembly. For example, the peptide MAX1 has many positively charged amino acids that leads to repulsions, which in turn affect the nanostructures formed.²⁶⁷ The electrically charged residues are projected on the bottom and top sides of peptide assemblies, which dominate the peptide stability and hydration degree of the peptide in an aqueous condition. To reduce intermolecular electrostatic

repulsion between the same charged amino acids, control of pH has been widely used.^{267, 268} Therefore, when designing ionic self-complementary peptides, oppositely charged amino acids should be considered, such as in the peptides EAK16²⁶⁹ and AC-KFEFKFEF-NH₂ (EFK8)²⁷⁰. For the case of the polar uncharged residues, these bear different types of side groups being hydroxyl (serine and threonine) and amide (asparagine and glutamine), which can cause hydrogen bonding interactions either via OH or CONH groups and thus drive the formation of secondary structures (e.g., α -helix, β -turn and β -sheet). For example, Wang et al.²⁷¹ reported the peptide AC-I₃XGK-NH₂ (where X represents polar uncharged residues such as glutamine, asparagine and serine) could form polar zippers between neighbouring β -sheets of X via their R group, which in turn intermesh β -sheets into wide and flat ribbons. It is noted that the hydrogen bonding formed via side chain - side chain interactions can stabilise the formation of secondary structures whereas when formed via side chain and main chain interactions the formation of secondary structure may be destabilise.^{272, 273}

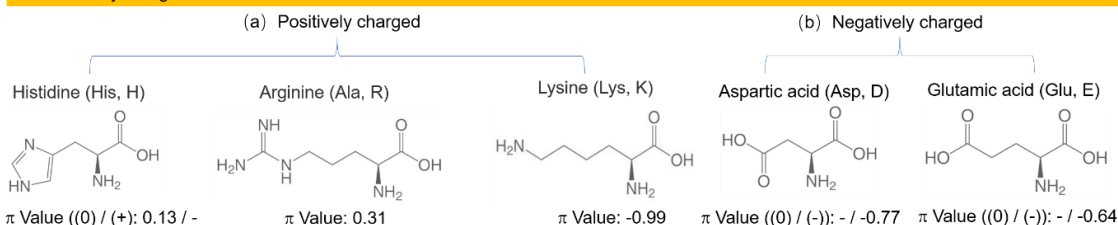
Hydrophobic residues can be divided into two groups being, aromatic residues (phenylalanine, tryptophan and tyrosine), which can form π - π stacking to facilitate peptide self-assembly and aliphatic residues (alanine, isoleucine, leucine, methionine and valine), which hold hydrophobic interactions. π - π stacking refers to p-orbitals in π -conjugated systems, which plays a key role in peptide self-assembly. For example, the ultrashort peptide FF and Fmoc-FF can self-assemble into long and flat nanoribbons based on π - π interlocked β -sheets between phenyl rings.^{274, 275} The hydrophobic interaction in contrast arises from aliphatic residues but can sometimes also arise from residues with a high hydrophobicity, such as is the case for threonine.²⁷⁶ Hydrophobic interactions are the opposite to hydrogen bonding and unlike π - π stacking, they cannot provide directionality during the peptide self-assembly process.²⁴⁶ However, they still play a significant role during self-assembly in aqueous solutions, which can promote the aggregation of peptide monomers and further accelerate secondary structural self-assembly. The self-assembly can be readily tuned by using solvents with different polarities. For example, Zhao et al.²⁷⁷ reported the addition of acetonitrile to water could tune the structure of the peptide KI₄K from

nanotubes to helical/twisted ribbons and further to thin fibrils. This is because acetonitrile can reduce the hydrophobic interactions, which in turn weaken the lateral stacking of β -sheets in K14K. In summary, amino acids possess a diversity, where each type of amino acid has its own unique physical, chemical and biological properties, which in turn gives a great potential to fabricate advanced functional peptides through the combination of various amino acids sequences and lengths. In addition, the process of peptide self-assembly is mostly caused by non-covalent bonds as mentioned above working in a cooperative way.

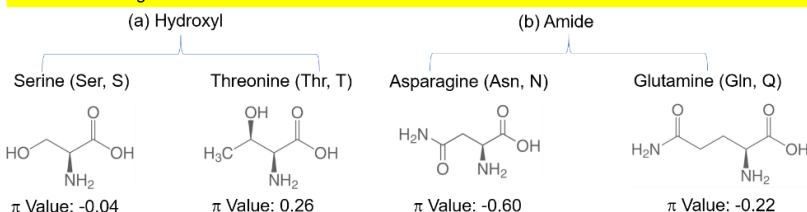
A. Special residues



B. Electrically charged residues

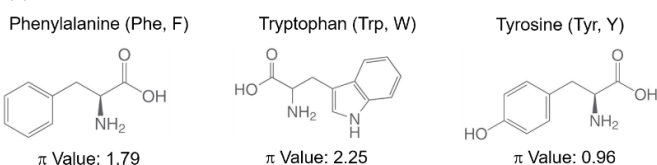


C. Polar uncharged residues



D. Hydrophobic residues

(a) Aromatic residues:



(b) Aliphatic residues:

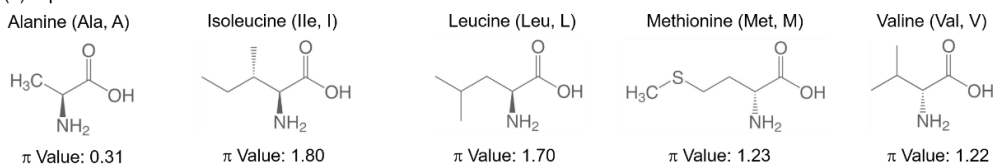


Figure 1-9 Chemical structures, standard accepted abbreviations and hydrophobicity (π value) of the 20 natural amino acids can be used as building blocks for constructing peptides. Please note that (0), (+) and (-) represent the neutral, positively charged, and negatively charged form of ionizable side chains. The data of π value reproduced with the permission from²⁴⁶.

1.2.3. Peptide amphiphiles: classification and design rule

As previously introduced PAs are an essential category of amphiphiles that can self-assemble into different aggregated structures dependant on building optimal peptide sequences controlled via their hydrophilic–lipophilic balance (HLB) within their functional groups. The self-assembly process is similar to that of lipids with a critical micelle concentration (CMC). Here, when a critical aggregation concentration (CAC) is at low concentrations, only monomers appear in aqueous solutions, while for concentrations above their CAC, the process of aggregation starts and results in the formation of different kinds of nanostructures, such as nanotubes²⁷⁸, nanobelts²⁷⁹, nanorods²⁸⁰, nanovesicles²⁸¹ and so forth.²⁸² In essence, PAs are oligopeptides that possess a hydrophilic head and a hydrophobic tail, which is comparable to lipids. In the following sections we look at the three categories of peptides and their design rules which are: amphiphilic peptides, lipidated peptide amphiphiles and supramolecular peptide amphiphile conjugates.

1.2.3.1. Amphiphilic peptides

Amphiphilic peptides belong in the category of PAs which are solely composed of amino acids.²⁸³ For the normal N-C type of sequences the N terminal connected hydrophobic tails are blocked by an acyl group increasing a tendency of aggregation, whilst C terminal connected hydrophilic heads are blocked by an amine group or left open. There are two main subclasses of amphiphilic peptides, these are ionic self-complementary peptides²⁸⁴ and surfactant-like peptides²⁴⁶.

The first subclass of amphiphilic peptides is composed of 12 to 16 alternating hydrophobic and hydrophilic residues, which drive the formation of stable β -sheets or β -strand structures in aqueous solutions.²⁸⁵ The hydrophobic residues (hydrophobic faces) of ionic self-complementary peptides are composed of alanine and leucine, and self-assemble in aqueous media in order to protect the hydrophobic faces from the hydrophilic media. In addition, hydrophilic residues contain arginine and lysine as positive residues as well as aspartic acid and glutamic acid as negative residue which corresponds to a hydrophilic face in aqueous media. The complementary ionic sides on the hydrophilic surface can

be classified into four moduli, including modulus I, modulus II, modulus III and modulus IV, for which the charge arrangements are as follow: - + - + - + - +; - - + + - - + +; - - - + + + and - - - - + + + +, respectively.^{286, 287} In order to reduce the electrostatic repulsion between the peptide monomers of ionic self-complementary peptides electrolytes need to be added. As shown in [Figure 1-10 A](#), hydrophobic faces are sequestered in the core of a bilayer by the hydrophilic faces to form a “hydrophobic sandwich”. The R group of hydrophobic faces in this sandwich are able to minimize contact with the surrounding aqueous solution. Furthermore, hydrophobic interactions, such as intermolecular hydrogen bonds between adjacent peptide backbones and electrostatic interactions occur between hydrophobic faces of neighbouring peptides to form β -sheet structures which in general conclude the final steps of self-assembly.^{244, 288-290} The first published example of this subclass is EAK16, categorised as modulus II (also named as EAK16-II), with an ability to self-assemble into stable membranes²⁴⁵ and well-ordered nanofibers²⁶⁹. Subsequently, AC-(RARADADA)₂-CONH₂ (RADA16-II) was designed, and both RADA16-II and EAK16-II scaffolds exhibited excellent adherence to mammalian cell types.²⁹¹ This pioneering work resulted in the design of many ionic self-complementary peptides which have been successfully applied in tissue engineering. These include AC-(RADA)₄-CONH₂ (RADA16-I), AC-(AEAK)₄-CONH₂ (EAK16-I), EFK8.²⁹²⁻²⁹⁴

Mostly, surfactant-like peptides are composed of one or two repetitive hydrophilic amino acid residues as heads and several same hydrophobic amino acid residues as tails. Structurally, the hydrophilic head of PAs is generally composed of charged residues, for example, cationic peptide residues include AC-I₃K-NH₂ and AC-A₆K-NH₂, and anionic residues AC-V₆D, AC-V₆D₂ and AC-A₆D.²⁹⁵⁻²⁹⁷ The hydrophobic tails of PAs are normally made up of 3-9 hydrophobic residues or 12-16 carbons in an acyl chain. AC-I₃K-NH₂ is a typical example of surfactant-like peptides that can self-assemble and are made up of hydrophobic isoleucine residues and hydrophilic lysine residues.²⁹⁸ The self-assembly process of AC-I₃K-NH₂ can be divided into 4 steps ([Figure 1-10 B](#)). Stage 1: Isoleucine tail residues (keep in interior) and lysine head residues (projected on the top and bottom sides) form interdigitated bilayers, which aggregate into small peptide segments. Stage 2: hydrophobic interactions,

including electrostatic repulsion, hydrogen bonding, surface curving and molecular chirality, among the isoleucine side chains leads to small peptide segments assembling into ribbons. With the growth of the ribbons, they start to twist due to electrostatic repulsion and molecular chirality (Stage 3). Finally, when the twisted ribbons continued growth, which can lead the edge of twisted ribbons to fuse, resulting in nanotube structure formation (Stage 4).^{299, 300}

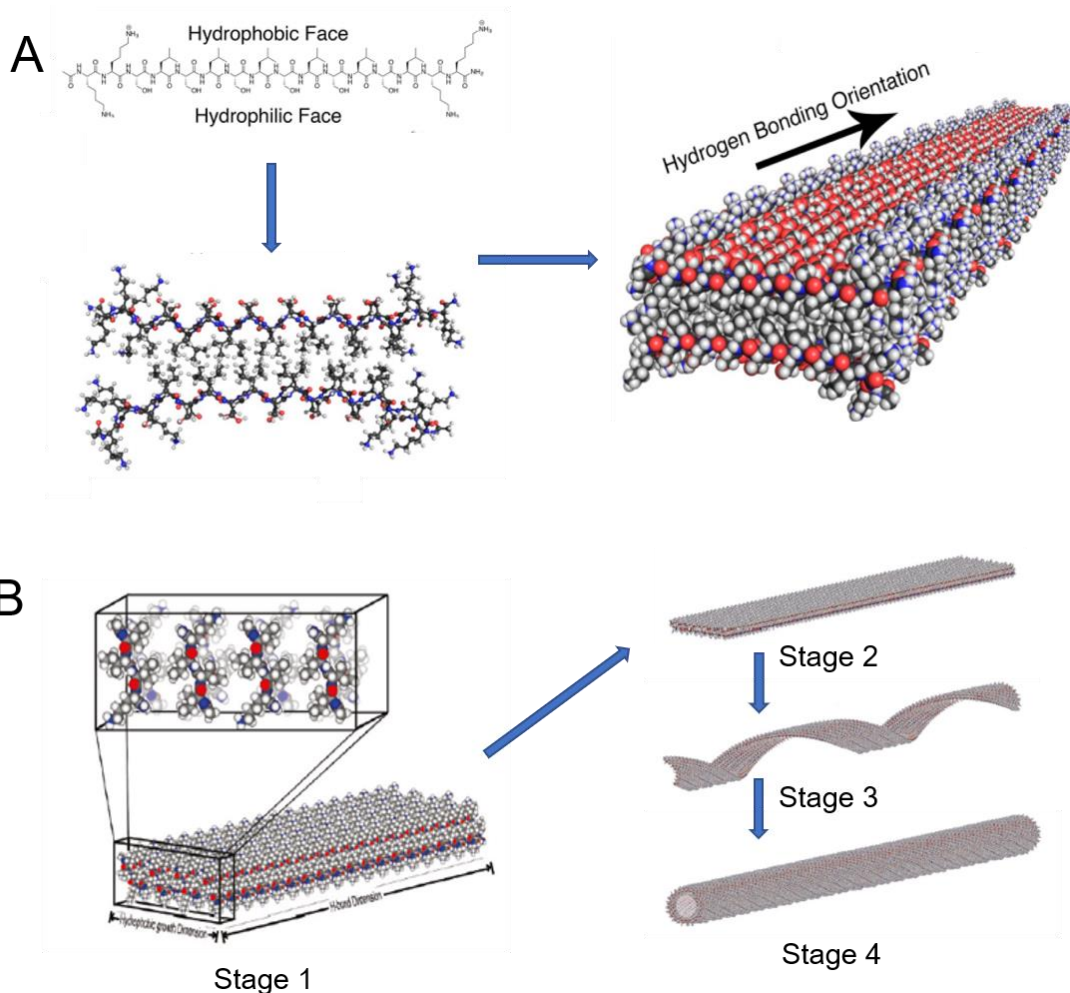


Figure 1-10 **A**, Schematic process of ionic self-complementary peptides in aqueous solution, from primary structure to nanofiber formation, reproduced with the permission from.²⁸⁹; **B**, surfactant-like peptides to form nanotubes in aqueous buffer, Reproduced with the permission from.²⁹⁹

There are a few effective and convenient rules for design of surfactant-like peptides will be outlined, including amino acids substitution and incorporation, length variation, sequence variation as well as chirality.²⁴⁶ Amino acids substitution and / or incorporation means that one or more residues are substituted or inserted into well-designed self-assembled peptide. In an

example, as mentioned before, AC-I₃K-NH₂ possesses strong self-assembly ability and stability. This characteristic makes this a desirable base peptide for modifications, for example isoleucine residues can be replaced by leucine residues to form AC-L₃K-NH₂ or AC-LI₂K-NH₂.³⁰¹ In addition, according to Han et al.³⁰¹, the hydrophobicity of AC-L₃K-NH₂ is similar with AC-I₃K-NH₂, but the CAC of AC-L₃K-NH₂ is much higher than AC-I₃K-NH₂, this is due to a lack of β -sheet structures in the previous one. For the case of amino acid incorporation, cysteine and glycine residues have been incorporated into the AC-I₃K-NH₂ sequence at the hydrophobic/hydrophilic interfaces to form AC-I₃CGK-NH₂ which has been shown to form hydrogels at much lower concentrations than AC-I₃K-NH₂.³⁰² It is worth to note that, cysteine residues can couple to form disulphide bonds, while glycine residues are able to provide more space for the disulphide bond formation. Another characteristic that can affect the properties of surfactant-like peptides is the length of the hydrophobic tails. For example, self-assembled peptides with long tail possess poor solubility in aqueous solutions, however with decreasing tail lengths solubility is increased, however aggregation ability is decreased. Xu et al.³⁰³ designed a series of cationic peptides AC-A_mK-NH₂, where m is the length of alanine tail (m=3, 6, 9). Here, their self-assembled architectures show a reduction in size and diameter, spanning from stacked bilayers for AC-A₃K-NH₂, long nanofibers for AC-A₆K-NH₂ to short nanorods for AC-A₉K-NH₂. This illustrates that increasing the hydrophobic tails the CAC value decreases, which in turn increases the aggregation at low concentrations. In addition to hydrophobicity, the CAC of PAs can be influenced by β -sheet hydrogen bonding. For sequence variation, Zhao et al.³⁰⁴ designed two hexapeptides that possess the same amino acid composition, but bear different amino acid sequences, namely AC-I₄K₂-NH₂ and AC-KI₄K-NH₂. The latter case contains a symmetric distribution of two lysine residues in the backbone, this causes an electrostatic repulsion between the sides of lysine residues. This interaction has a limited effect to hydrophobic attraction among isoleucine side chains, resulting in a helical ribbon with larger width formation giving rise to wide nanotubes. Similar to AC-I₃K-NH₂, in the previously discussed case, two lysine residues are at C terminus, destabilising the isoleucine side chains of neighbouring β -sheets, resulting in twisting and the formation into nanofibers. In another example, Wang et al.³⁰⁵ designed three

pairs of enantiomeric peptides, which include AC-^DI₃^DK-NH₂ / AC-^LI₃^LK-NH₂, AC-^LI₃^DK-NH₂ / AC-^DI₃^LK-NH₂ and the pair AC-^{Da}I₃^DK-NH₂ / AC-^{La}I₃^LK-NH₂, to investigate the chirality of self-assembled nanofibrils. Their results indicate the chirality of lysine residues can be used to determine morphological handedness, while the chirality of isoleucine residues can be used to determine the resulting main characteristic of secondary structures. They found that change of constituent amino acid chirality in short peptides might regulate the handedness of peptide-based aggregates, this feature may provide a simple tool to design supramolecular materials.³⁰⁶

1.2.3.2. Lipidated peptide amphiphiles

Lipidated PAs also named as lipopeptides are one class of biosurfactants, which are obtained from microorganisms, such as bacteria, yeast and fungi.³⁰⁷ These biosurfactants possess the ability to reduce the surface and interfacial tension, they have evolved in this way to disrupt biological activity as part of the organism's host defence mechanism.³⁰⁸ *Bacillus* and *Pseudomonas* produced lipopeptides have been extensively researched and applied, because they have diverse biological activities, such as antibacterial, antifungal and antiviral.³⁰⁹⁻³¹² Structurally, they are constructed of a cyclic peptide head linked to a single lipid chain.³¹³ For example, surfactin, a cyclic heptapeptide produced by the *Bacillus subtilis* family, is comprised of seven amino acids residues and one β-hydroxy fatty acid residues of variable length.³¹⁴ When the concentration of surfactin reaches its critical micelle concentration (CMC), lipid bilayers can be disrupted and dissolved with the formation of mixed micelles.³¹⁵ Because surfactin possesses specific bioactive functions (e.g. antiviral, anti-inflammatory, antimicrobial and anticancer), it has been widely used for biopharmaceutical and TE applications.^{316, 317}

Inspired by these bacterially-expressed lipopeptides, many synthesized lipopeptides have been designed and applied to many fields, such as drug and gene delivery, membrane protein stabilization and TE.^{318, 319} Part of the reason for this is because this type of designed lipopeptides are easy to be synthesised and readily form well-defined nanostructures that can tolerate a large chemical diversity.³²⁰ The structure of simple lipopeptides is composed of a hydrophobic aliphatic tail of variable length attached to a hydrophilic peptide sequence via an

amide bond, such as is the case for C_mK_n , where m is the length of aliphatic tail and n is the number of lysine residues.²⁵⁰ Apart from this, lipopeptides can also be designed with a coating of bioactive epitopes with a chemical structure composed of four key features (Figure 1-11 A).^{261, 321} These features include: the most important region, a **hydrophobic tail**, typically consisting of a long acyl chain, making the molecule amphiphilic when attached to peptide sequence. This amphiphilicity allows the periphery of self-assembled nanostructure specially presents peptide signals, such as different types of bioactive epitopes. The second region is a **β -sheet forming segment**, which typically is comprised of hydrophobic amino acids. This enables the formation of one-dimension (1D) self-assembled nanostructures that can be further entangled into networks. Additionally, biological signals can be present on the nanostructure surface at a high density due to molecular packing within a cylindrical geometry. It is worth to note that, the mechanical properties of lipopeptide gels and the shapes of formed 1D nanostructures can be tuned through modifying this region.^{279, 322} The third region is made up of **short charged amino acids sequences** that promote solubility in water. These charged amino acids are relatively weak acids and weak bases and therefore control of the pH increases in the concentration of electrolytes in the bulk solution can trigger nanostructure growth. pH and salt sensitive designed lipopeptides play an essential role in injectable therapies,³²³ allowing unassembled lipopeptides to combine with bioactive entities, such as growth factors, or with live cells to form low viscosity liquids.²⁶¹ Electrolytes can thus induce the self-assemble of lipopeptides into gels spontaneously within the physiological environment for encapsulating the desired payload.²⁶¹ The last region considered is made of **bioactive epitopes**, these can be designed for different purposes without changing the final formation of self-assembled nanostructures. Active sequences, such as RGDS, YIGSR and IKVAV, can be incorporated into designed lipopeptides, thus mimicking the structure and function of native ECM.^{256, 324, 325}

In the case of region 1, lipopeptides can also contain more than one lipid group as designing hydrophobic tail. For example, Dasgupta et al.³²⁶ designed two-chain and single-chain lipopeptides that have same head groups but bear a different number of lipid chains and investigate their self-assembly properties.

Their results indicated two-chain lipopeptides could self-assemble into nanostructures, ranging from twisted ribbons to dense helical fibrillar networks, and further to form hydrogels, while single-chained lipopeptides failed to self-assemble. The assumed self-assembly mechanisms of for the structures of two-chain lipopeptides are shown in [Figure 1-11 B](#). Initially, the hydrogen bonding of head groups and the stacking of hydrophobic lipid chains leads to the formation of ribbons. With the growth of the ribbons, the authors expect them to form networks of twisted fibres via hydrogen bonding among the head groups in antiparallel strands.³²⁶ In addition, increasing the length of hydrophobic aliphatic tails of two-chain lipopeptides increased their tendency for aggregation, ranging from spheroidal micelles to strand-like structures.³²⁷

To enhance the self-assembly of lipopeptides aromatic groups such as Fmoc, naphthalene and arylenediimides, can be incorporated into region 2 of the peptide.^{253, 328-330} This does not only increase the hydrophobicity, but also provides a number of possible aromatic stacking conformations, including parallel, antiparallel, and interlocked antiparallel confirmation between the molecules.²⁵³ The commonly used arylenediimides aromatic groups used for this are e.g. naphthalenediimide (NDI) and perylenddiimide (PDI) and have been widely used for organic electronics, as antimicrobial agents and for the development of chemo-sensors.^{331, 332} For example, Singha et al.³³³ designed a lipopeptide with NDI where both sides are linked to a hexyl chain and the cell targeting sequence RGDS. The self-assembly process of this NDI-based lipopeptide can be divided into three steps as shown in [Figure 1-11 C](#). In detail: at the minimum aggregation concentration 1 (MAC1; around 0.05 mM), smaller aggregates are formed by NDI groups via π - π stacking. With increasing concentration to another critical concentration MAC2 (around 0.45 mM), smaller aggregates further assemble into spherical aggregates (mostly micellar assemblies). By further increasing the concentration to above 16.9 mM (MAC3), the spherical aggregates assemble into nanofibers that eventually turn into hydrogels.³³³ Additionally, PDI also can be introduced into the place of NDI to construct PDI-based lipopeptide.³³⁴ For the case of Fmoc incorporated lipopeptides, including the derivatives of Fmoc-protected glycine and Fmoc-protected lysine.^{335, 336} In the previous case, one side of glycine residue is coupled with C₁₈ chain and the other side is linked with Fmoc, which can self-

assemble into twisted nanofibers and the formation of organogels. In the latter case, one side of lysine residue is coupled with C₁₆ chain and the other side is linked with Fmoc which can self-assemble into helical fibres.

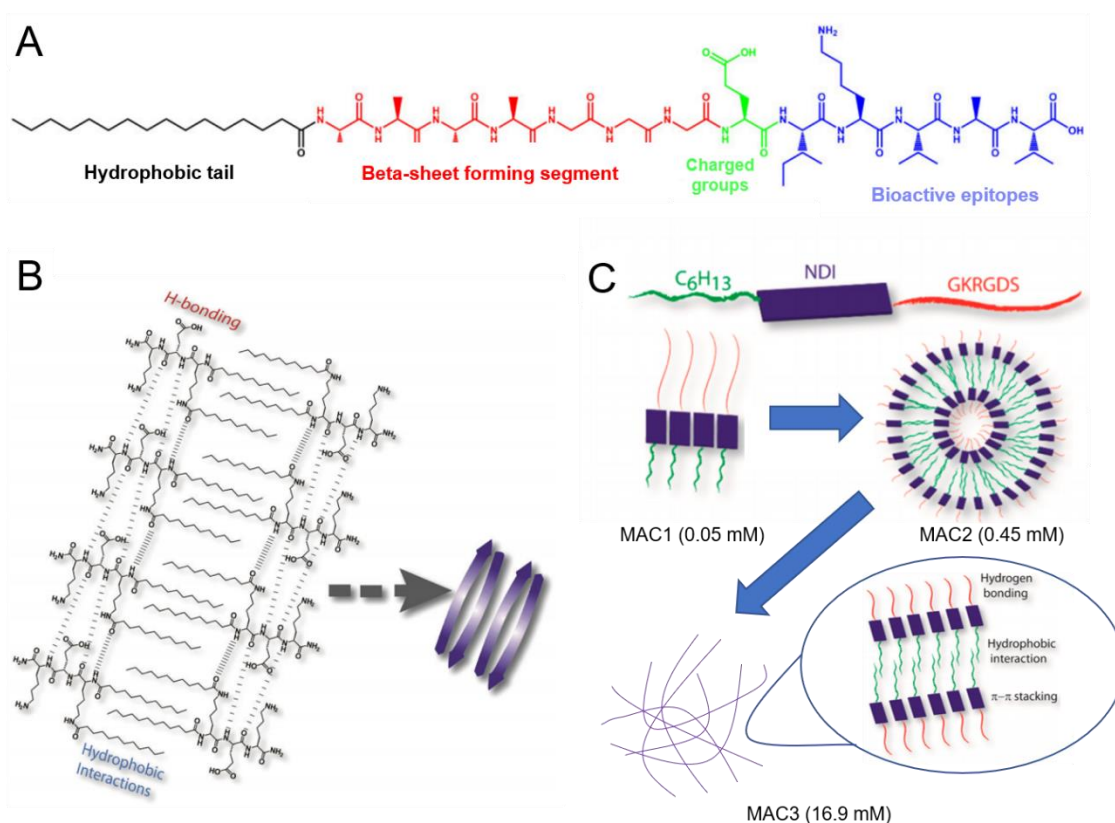


Figure 1-11 **A**, Chemical structure of a representative single tail lipopeptide, highlighting four designed chemical entities. Schematic diagram shows **B**, A probable mechanisms of a representative two-chain lipopeptides self-assembly process. **C**, Stepwise hierarchical aggregation of NDI-based lipopeptide. NDI represents naphthalenediimide, MAC1, 2 and 3 represent at or above minimum aggregation concentration 1, 2 and 3, NDI-based lipopeptide can assemble into small aggregates, spherical aggregates (presumably micellar assemblies) and nanofibers, respectively. **A** with the permission from²⁶¹; **B** with the permission from³²⁶; **C** with the permission from³³³.

1.2.3.3. Supramolecular peptide amphiphile conjugates

The traditional amphiphile structure is composed of a hydrophilic head and a hydrophobic tail via covalent bonds.³³⁷ In contrast the supramolecular amphiphile structure is constructed via non-covalent driving forces, including host-guest recognition, π - π stacking, hydrogen bonding, electrostatic forces and metal coordination interactions.^{252, 338} It is worth to note that soft materials are

often fabricated by supramolecular amphiphile approaches, thus giving them a high degree of structural complexity and giving them the ability to be stimuli-responsive.³³⁹ The fabrication of supramolecular amphiphile PAs is commonly based on host-guest recognition interactions. Structurally this system is composed of a receptor molecule (host) and a ligand molecule (guest). Macrocyclic hosts, such as cyclodextrins (CD), cucurbiturils (CB) and pillararenes, as molecular receptors can be introduced into supramolecular systems enabling them to construct distinctive properties of such supramolecular conjugates.³⁴⁰ For example, supramolecular hydrogels fabricated by CD and CB have been successfully used for cell delivery.^{341, 342}

In an early study Versluis *et al.*³⁴³ designed a pH-sensitive supramolecular PAs loaded with β -CD (host) and an adamantane-modified octapeptide (VE)₄ (guest), as shown in [Figure 1-12 A](#). Three orthogonal interactions were reported to take place in this two-component system, including: (i) hydrophobic interactions with the lipid-functionalized β -CD, (ii) host–guest inclusion complexation between β -CD and adamantane, and (iii) hydrogen bonding in the octapeptide (VE)₄. On this basis, Hong *et al.*³⁴⁴ designed thermosensitive poly(organophosphazene) (PPZ) loaded with β -CD and adamantane-modified RGD. In addition, biocompatible poly(ethylene glycol) (PEG) was inserted between adamantane and RGD to avoid steric hindrance between mesenchymal stem cells (MSCs) and β -CD PZZ. Supramolecular hydrogels can be constructed by means of mixing this peptide-decorated vesicle and β -CD PPZ at physiological temperature (37 °C), this application will be discussed in the cartilage TE section.

Although the cavity size of CB is the same as that of CD, CB possesses two identical cavity entrances with carbonyl edges, which allow two different guests inside its cavity.³⁴⁵ In another words, CB acts like a “supramolecular handcuff” combining the two molecules together. Cucurbit[8]uril (CB[8]) is one type of the CB family which provides a platform for designing supramolecular amphiphile PAs.³⁴⁶ Asymmetric viologen surfactants (first guest molecule) can provide hydrophobic interactions to promote the assembly process, which can form unilamellar vesicles upon addition of CB[8] and an appropriate second guest molecule.^{347, 348} For example, Jiao *et al.*³⁴⁹ designed supramolecular PAs via

host-guest complexation between the pyrene-functionalized peptide (GGGKKK), a viologen lipid and CB[8]. The charge-transfer interactions between the two guests inside the CB[8] cavity are the dominant factors promoting the construction of supramolecular PAs into vesicles. According to this concept, Mondal et al.³⁵⁰ constructed light-responsive supramolecular PAs. In this work, azobenzene, a photoisomerizable group, was connected at the N-terminus of the peptide (WGGKK) as the second guest for CB[8]. The azobenzene containing peptide was supramolecularly conjugated with a viologen surfactant using CB[8] allowing for photolabile vesicle formation. Therefore, the formation and deformation of these vesicles could be controlled by exposing the solution to different wavelengths. In another similar example, Loh et al.³⁵¹ constructed a thermosensitive supramolecular amphiphile Pas, as shown in [Figure 1-12 B](#). It could self-assemble into double layered vesicles, allowing efficient encapsulation of the basic fibroblast growth factor (bFGF) to regulate cellular activity.

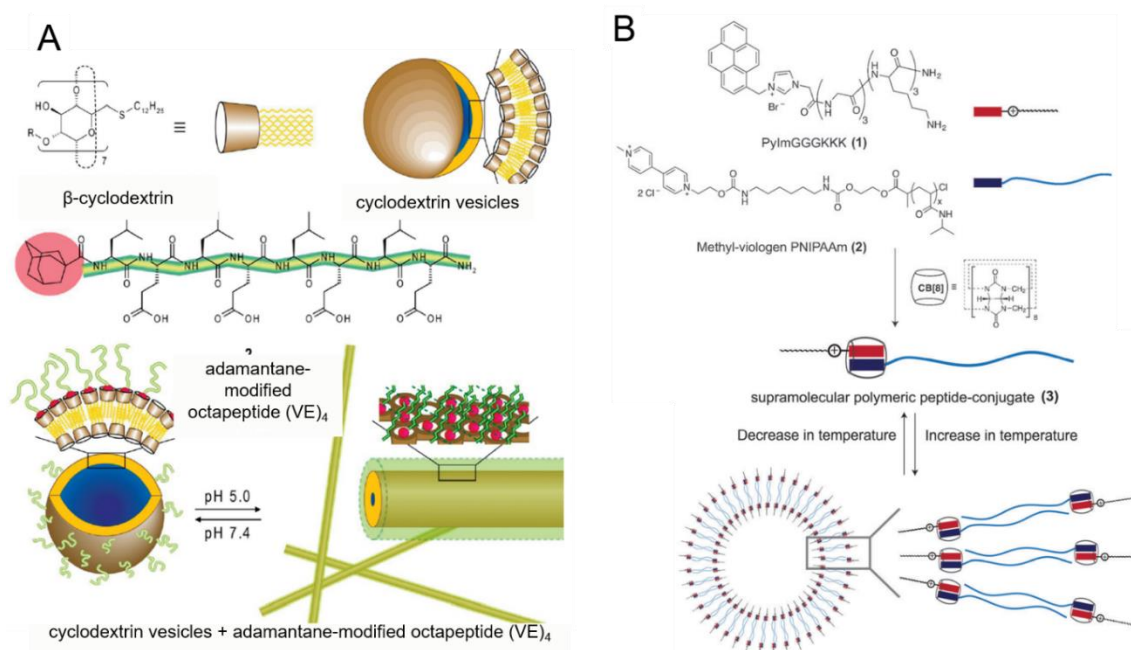


Figure 1-12 Schematic representation of **A**, chemical structure of β -cyclodextrin which can self-assemble into cyclodextrin vesicles, and the chemical structure of adamantane-modified octapeptide (VE)₄ which binds to cyclodextrin vesicles. The addition of adamantane-modified octapeptide (VE)₄ at pH 7.0 did not alter the shape of cyclodextrin vesicles. While a reduction of pH to 5, resulted in random coil structures to transition to β -sheet conformation (this change is reversible and repeatable), and these vesicles are transformed into fibres. **B**, (1)

chemical structure of pyrene-functionalized peptide (GGGKKK), and (2) viologen-functionalized poly(N-isopropylacrylamide) (PNIPAAm), and (3) supramolecular polymeric peptide conjugate. As the temperature increased to 37 °C, PNIPAAm moiety becomes hydrophobic and makes the supramolecular conjugate (3) amphiphilic. Subsequently, double layer vesicles were formed. A with the permission from³⁴³; B with the permission from³⁵¹.

1.2.4. The fabrication of 3D peptide amphiphilic scaffolds

1.2.4.1. Self-assembly

Nowadays, the gelation of PAs is no longer a random event but can be achieved by altering design a PAs sequences. In addition to this researchers are able to exploit external factors, such as temperature, pH, solvent, ionic strength, light and enzymes, to stimulate solubility or help with the self-aggregation of PAs.^{249, 253, 352-354} This is because the driving forces in self-assembly systems are weak non-covalent interactions, which are sensitive to the external environmental conditions.³⁵³. For example, 1) adding organic solvents to PAs solutions can adjust solution polarity, thereby affecting hydrophobic interactions in peptide self-assembly systems.^{277, 355} 2) PAs mostly contain charged residues, therefore, pH change affects charge-charge interactions during peptide self-assembly.³⁵⁶ 3) In addition, tuning the ionic strength of PA solutions can mask the effect of charged residues which in turn can remove pH trigger function.²⁴⁹ 4) Unlike some external factors, including solvents, pH and ionic strength, light does not perturb the solution, but directly interacts with PAs, which in turn can induce self-assembly.^{357, 358} 5) Enzyme-instructed self-assembly (EISA) is the integration of enzymatic reaction and molecular self-assembly. In the last two decades a number of PAs have been developed by means of EISA to form various nanostructures through diverse enzymatic reactions.³⁵⁹⁻³⁶² Ulijn's group has intensively developed EISA and first mentioned the surface-localized EISA method that can produce localised self-assembling hydrogels.³⁶³⁻³⁶⁵ As a rule of thumb, the final outcome of these self-assembling PAs is the formation of hydrogels.³²⁸

The general hydrogelation process resulting from the self-assembly of PAs involves three hierarchies. These are: Firstly, the formation of peptide second structures from primary peptide sequences under certain external factors,

secondly the formation of long and entangled nanofibers, and finally the further assembly of these into a fibrillar network. These self-supporting hydrogels have been extensively researched and largely covered in some recent reviews.^{252, 328, 366, 367} Therefore we only briefly discuss these here. Advantages and disadvantages of the developed fabrication techniques of PAs scaffolds are shown in [Table 1-2](#). Apart from this, there are a few methods to promote PAs scaffolds reach mechanical microenvironment favouring cell cultures. These include, increasing the concentration of the PA solution; mixing PAs with multibranched PAs sharing the same self-assembling sequences³⁶⁸; crosslinking PAs with synthetic³⁶⁹ or natural³⁷⁰ crosslinkers; and increasing the overall hydrophobicity of the peptide sequence of PAs by tuning amino acid residues^{371, 372}.

Table 1-2 Advantages and disadvantages of key PAs scaffolds fabrication techniques.³⁷³⁻³⁷⁵

Fabrication Techniques	Advantages	Disadvantages
Self-assembly	Highly porosity (80-90%); Cell viability (60-95%); Diameter of fibres (5-300 nm).	Non-scalable; Poor control of fibres dimension.
Electrospinning	Highly porosity (80-95%); Cell viability (<80%); Diameter of fibres (100-1100 nm); Uniform; large surface area; Good mechanical properties; Simple fabrication; Low cost.	A high voltage source needed; Toxic solvents may be needed.
3D bioprinting	Manufacture of complex structures at high definition.	Needs sophisticated and expensive apparatus; Low mechanical strength; Toxic organic solvents typically used.

1.2.4.2. Electrospinning

Electrospinning is a 'top-down' manufacturing technology that can be used to produce fibres from nano to micro scale resulting in fibre matts with a large accessible surface area.³⁷⁶ In the electrospinning process ([Figure 1-13 A](#)), polymer solutions are ejected from needle spinnerets under a high voltage

electrostatic force. The nanofibers are formed during solvent evaporation.³⁷⁷ Although electrospinning is the one of the most frequently used technologies in TE, the application of PAs for electrospinning scaffolds is rarely utilised owing to the limited molecular weight and viscoelastic properties of PAs.^{370, 378} With further development of electrospinning, there have however been some reported PAs scaffolds via electrospinning.^{379, 380} For example, Tayi *et al.*³⁸⁰ demonstrated low molecular weight (<1 kDa) self-assembled PAs at very low concentrations (<4 wt %) in water could be electrospun after critical parameters (e.g. viscosity, surface tension and solution conductivity) for the electrospinning technique were optimized. In contrast, Maleki *et al.*³⁷⁸ have successfully spun biomimetic nanofibrous mats with a number of PAs at high concentrations by optimising solvents. (Figure 1-13 B). They found that PAs with β -sheet structures appeared to be unfavourable to the spinnability compared to PAs with random coil or α -helical conformations. Bruggeman *et al.*³⁸¹ designed two-component composite materials that combine tissue-specific peptide hydrogels (Fmoc-DIKVAV) and electrospun nanofibers were made of PLA. In addition, they demonstrated varying the size of nanofibers can enhance structural biomimicry of the ECM. Hamedani *et al.*³⁸² reported tyrosine-based oligopeptides nanofibers prepared by electrospinning and then crosslinked with 1,6-diisohexanecyanate to improve physiological stability, registering no cytotoxicity against human and rat neuronal cells. In another example, Pugliese *et al.*³⁷⁰ demonstrated the crosslinked peptide FAQ(LDLK)₃ via genipin could be also electrospun into nanofibrous mats. These electrospun crosslinked nanofibrous scaffolds demonstrated good biodegradability and mechanical properties, which also could support human neural stem cells (hNSCs) resulting in progenies proliferating and differentiating into branching neural morphology. In recent years, researchers have shown considerable interest in the electrospinning of PAs, but further studies will be required, especially in the preparation of 3D PAs scaffolds via electrospinning.

1.2.4.3. 3D Bioprinting

3D bioprinting is a 'bottom-up' additive manufacturing technology, which can be used to construct reproducible and complex scaffolds via computer aided design software (CAD) with high precision.¹⁴⁹ Especially, this technology can

encapsulate cells at specific position of hydrogels, enabling a higher cell viability than with traditional culture methods.³⁸³ Within the field of bioprinting, droplet-on-demand-based inkjet printing, including thermal and piezoelectric categories (Figure 1-13 C), has gained much interest due to high precision for the deposition of multiple types of cells, allowing the generation of elaborate spatial architectures.³⁸⁴ Ink formulation is the greatest challenges in 3D bioprinting, and various parameters need to be considered including biocompatibility, low viscosity, fast gelation time and gel stiffness.^{384, 385} PAs are attractive candidates for bioprinting owing to their versatile physicochemical properties.³⁸⁶ Loo et al.³⁸⁶ reported one of the first peptide-based inks namely, AC-ILVAGK-NH₂ which was able to flow through fine-gauged needles with ease into a concentrated salt solution. The resulting hydrogel structure was measured to have a stiffness of up to 40 kPa. The scaffolds were shown to support the 3D culture of human mesenchymal stem cells. In another example Dubbin *et al.*³⁸⁷ designed gel-phase inks, containing proline-rich peptide domains, which were shown to increase mechanical support in the 3D environment via a dual-stage crosslinking and prevented dehydration during printing. Yan et al.³⁸⁸ reported IKVAV-based PAs integrated within a thiolated-gelatin bioink which was successfully 3D printed at 4 °C and demonstrated excellent long term stability in cell culture for up to over 4 weeks. The cell-laden scaffolds could stimulate cholangiocytes to form functional tubular structures. Raphael et al.³⁸⁹ demonstrated self-assembling peptide-based hydrogels that could be printed to form 3D matrices constructed with well-defined architectures and high structural integrity through optimisation of printing parameters (e.g. valve opening time and extrusion pressure). In addition, inkjet printing also can be used for modular tissue assembly that allow complex 3D constructs to be fabricated with direct control over deposition of bioink.³⁹⁰ For example, Hedegaard et al.³⁸⁵ exploited inkjet printing to guide shear force-mediated co-assembly of PAs with keratin in order to fabricate toroidal microgels (Figure 1-13 D (D1)). These microgels with channel-like micro topographies on the inner surface of ring-shape (Figure 1-13 D (D2)) and spiral layering shape within the bulk of the material (Figure 1-13 D (D3)). Additionally, the 3D scaffolds could support viable cell populations. Overall, 3D bioprinting technology is a breakthrough technology in the development of 3D PAs scaffolds that have the

ability to control position of cells at specific positions in the 3D scaffolds. These described methods however still need more research in terms of standardization for future work to increase success rates and accuracy.

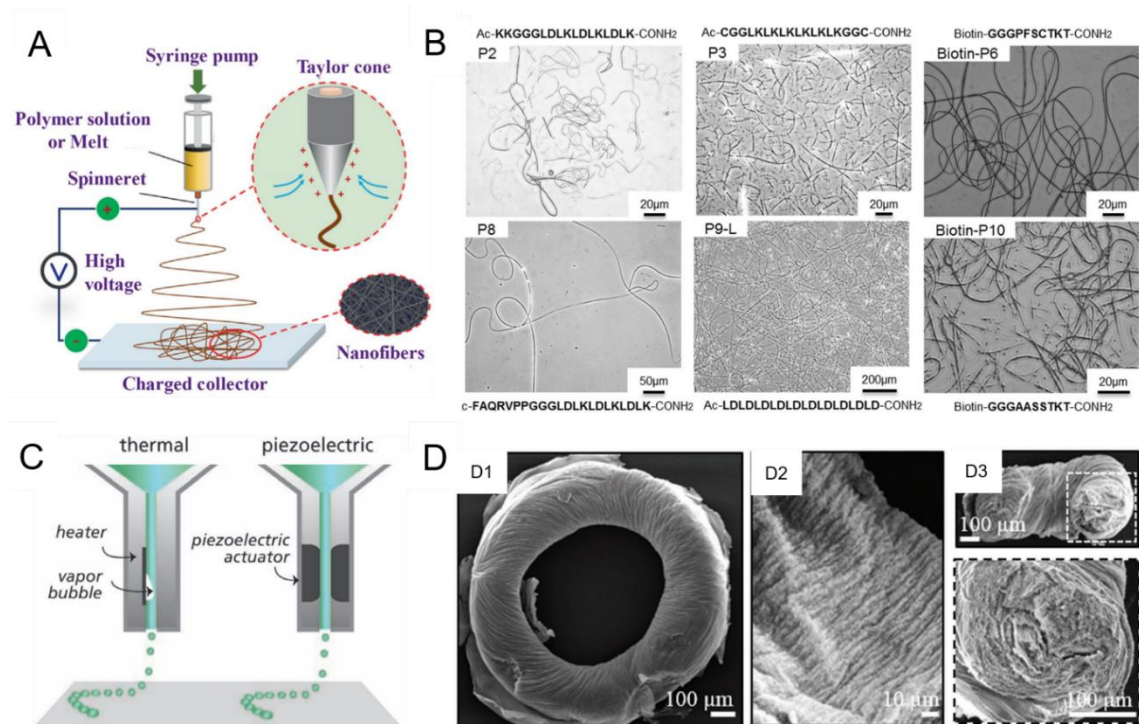


Figure 1-13 **A.** Schematic representation of the electrospinning process. **B.** Optical microscope images of different nanofiber morphologies of electrospun peptide amphiphilic hydrogels. **C.** Schematic representation of thermal and piezoelectric inkjet printing. **D.** SEM images indicate the toroidal microgels (D1) with channel-like surface topography (D2) and spiral layering cross-section (D3). A with the permission from³⁷⁷; B with the permission from³⁷⁸; C with the permission from³⁸⁴; D with the permission from³⁸⁵.

1.2.5. Application of peptide amphiphile scaffolds in tissue engineering

1.2.5.1. Bone tissue regeneration

Bone TE, is an approach in which stem cells, such as chondrocytes or osteoblasts are loaded into an appropriate scaffold, either to regenerate or replace damaged bone tissue. Here the scaffold function is meant to temporarily replace the role of ECM during bone formation, including promote cell proliferation and differentiation, stimulate mineral deposition and secretion of bone ECM compositions.³⁹¹⁻³⁹³ In addition to biological performance,

mechanical strength of scaffold should match that of native hard tissue with an aim to replicate native microenvironment for optimal bone healing.³⁹⁴

1.2.5.1.1. Amphiphilic peptides

In this context, it has been demonstrated that PAs can provide an adequate nanoscale microenvironment for bone cell penetration and settlement. PuraMatrix™, a synthetic peptide comprising of RADA16-I, was injected into defective rat calvaria and demonstrated the ability to promote mature bone formation.³⁹⁵ After this initial work, many researchers have continued to study RADA16-I peptide hydrogels for bone TE applications. In another example He et al.³⁹⁶ reported the use of both L-RADA16-I and D-RADA16-I scaffolds could promote bone healing of defective rat condyles. Furthermore, the authors demonstrated that D-RADA16-I is capable of the controlled release of bFGF, further increasing the stimulation of bone regeneration. The release of bFGF from the RADA16-I hydrogel possesses biological activities that promotes NIH-3T3 cells proliferation.³⁹⁷ In addition, bFGF is known to be an angiogenic factor and at lower concentrations and can stimulate neovascularization which in turn results in a better supply of oxygen and nutrients to the regeneration site.³⁹⁸ He et al.³⁹⁹ further developed the functional motif of RGD-modified D-RADA16-I scaffolds, which significantly enhanced bone repair regardless if bFGF was present or not. Apart from the bFGF growth factor, Ikeno et al.⁴⁰⁰ further demonstrated that RADA16-I hydrogels doped with the bone morphogenetic protein (BMP)-2 growth factor could extensively promote bone healing in a bone augmentation rabbit model. Moreover, dexamethasone also can load into RADA16-I hydrogel, used in a perfusion bioreactor for bone TE. Although dexamethasone-loaded RADA16-I hydrogels were shown to promote osteoblast differentiation, it was not suitable for long-term use due to the potential toxicity of dexamethasone.⁴⁰¹ RADA16-I scaffolds have also been used in combination with hyaluronic acid and demonstrated that they could be used to control the release of recombinant adeno-associated virus (rAAV) vectors, allowing to genetically modify human mesenchymal stem cells (hMSCs). The results also indicated these composite scaffolds can foster effectively transduction of hMSCs (up to 80%) and chondrogenic differentiation (up to 21 days).⁴⁰² Similar to PuraMatrix™, SPG-178-Gel, a neutral peptide consisting of

RLDLRLALRLDLR, was implanted into a rat calvarial defect model and showed new bone formation after three weeks.⁴⁰³ Additionally, FEFEFKFK peptide scaffolds, without additional modifications were able to host hMSCs in a 3D microenvironment and promote osteoblast differentiation. After 12 days of culture hMSCs differentiated into osteoblasts, which was characterized with the production of collagen, alkaline phosphatase, osteocalcin and the deposition of hydroxyapatite (HA), the latter of which is the major inorganic mineral needed for bone formation.⁴⁰⁴ According to a recently published article by Ghosh et al.⁴⁰⁵, the short peptide Fmoc-FF was used which could self-assemble together with alginate to form composite hydrogels and were able to direct osteogenic differentiation and promote calcium mineralization.

1.2.5.1.2. Lipidated peptide amphiphiles

The first described lipopeptides were functionalized with phosphoserine and RGDS residues, and demonstrated the capability of direct mineralization of HA to form a composite material.²⁵⁶ Subsequently, several reports have been published where lipopeptides were formed by modification with functional motifs and consequently successfully used in bone TE.⁴⁰⁶ In this context, Mata et al.⁴⁰⁷ reported the lipopeptide C₁₆-GAEELLAAA, individually functionalized with phosphoserine and RGDS which was implanted into a femoral defect (5 mm) rat model resulting in significantly increased ossified tissue. In another study the Lipopeptide C₁₆-GTAGLIGQ was modified with DGEA, a collagen type I adhesive motif, or RGDS residues and both of them can promote the osteogenic differentiation of hMSCs culture.⁴⁰⁸ Furthermore C₁₆-GTAGLIGQ-RGDS hydrogels embedded with HA nanoparticles, formed a biphasic gel, which has been demonstrated to foster femoral defect regeneration *in vivo* in rat models.⁴⁰⁹ Moreover, Tansik et al.⁴¹⁰ demonstrated that lipopeptides functionalized with both glycosaminoglycan and lysine not only stimulated osteogenic differentiation of rat MSCs, but also aided the regeneration of bone tissue, *in vivo*. In addition to above mentioned, Gulseren *et al.*⁴¹¹ designed functional mimicry lipopeptides that could replicate the function of alkaline phosphatases, enabling the promotion and rapid maturation of both osteoblast-like and mesenchymal cell lines into osteoblasts. Trisulfated monosaccharide conjugated with lipopeptides were able to mimic heparin sulphate. The resulting

nanofibers amplified signalling of (BMP)-2 significantly, more than natural sulphated heparin and promoted bone repair in the spine at growth factor doses of 100-fold lower than those normally required in the rat model.⁴¹² Although these functionalized lipopeptides have been widely studied in bone TE, some lack mechanical properties closely resembling bone tissue.²⁹³ To combat this issue lipopeptides were attached to the surfaces of nickel-titanium implants significantly facilitating the adhesion and proliferation of preosteoblastic cells.⁴¹³ Furthermore, they could also be used as pore fillers for titanium foams carrying preosteoblastic cells to achieve mineralization, vascularization, and bone regeneration in rat femur defect models.⁴¹⁴

1.2.5.2. Cartilage tissue regeneration

Cartilage is an avascular and aneural connective tissue that is mainly composed of collagen and proteoglycans. The absence of vascularization within this tissue however gives it limited self-repairing capability.^{415, 416} PAs-based hydrogels have made considerable strides in the development of scaffold materials to tackle the problem of poor cartilage repair, owing to their biomimetic, tuneable mechanical properties and similarity with native ECM.²⁹³

1.2.5.2.1. Amphiphilic peptides

In 2002, the first peptide hydrogel (KLDL)₃ was developed to support encapsulated chondrocytes that produced a cartilage ECM rich in proteoglycan and collagen type II after 4 weeks incubation *in vitro*.⁴¹⁷ This scaffold was shown to also promote the cartilage-like ECM production via inducing chondrogenic differentiation of adult bone marrow stromal cells (BMSCs).⁴¹⁸ In addition to this, the transforming growth factor β 1 (TGF- β 1), insulin-like growth factor-1 (IGF-1) and dexamethasone were used to promote chondrogenesis of BMSCs, which can be loaded into (KLDL)₃ hydrogels. These hydrogels were demonstrated to be injectable and could promote cartilage repair in a rabbit model.⁴¹⁹ Liebesny *et al.*⁴²⁰ recently reported the development of (KLDL)₃ hydrogels imbued with heparin-binding IGF-1 and associated with chondrocytes, in combination with trypsin pre-treatment for cartilage regeneration, *in vitro*. The trypsin pre-treatment not only can remove sulphated glycosaminoglycan (sGAG) from the edge of the defect position, but also can migrate chondrocytes that

seeded in the hydrogel to surrounding cartilage annuli. The addition of heparin-binding IGF-1 was shown to enhance the proteoglycan synthesis rate and deposition as well as integration of (KLDL)₃ hydrogels into native ECM over 4 weeks. In another study the same (KLDL)₃ hydrogel implanted into osteochondral defective tissue in a rabbit model show a slight improvement for cartilage repair and regeneration.⁴²¹ Moreover, the self-assembling peptide (KLDL)₃ can be conjugated with the functional binding motif HAVDI, which is an N-cadherin mimetic peptide. This functional hydrogel leads to chondrogenic differentiation of hMSCs by the inhibition of canonical Wnt/ β -catenin signalling at early the early stage.⁴²² The peptide sequence RADA16 is another example that can be applied in cartilage TE. For example, Florine *et al.*⁴²³ reported RADA16 hydrogels loaded with the heparin-binding IGF-1 factor could stimulate in chondrocyte encapsulated within hydrogels or chondrocytes within adjacent native cartilage explants, resulting in the increased production of sGAG and hydroxyproline. The authors also functionalized RADA16 with the bioactive bone marrow homing peptide PFS (PFSSTKT), which in combination with acellular cartilage matrix (ACM) to form novel composite hydrogel scaffold for cartilage regeneration (Figure 1-14 A). This composite scaffold quickly recruited more endogenous stem cells and facilitated their chondrogenic differentiation that confirmed by gene expression analysis. In addition, after 6 months implantation, the defective rabbit joint completely filled with cartilage-like tissue and continuous surface as smooth as the surrounding native tissue (Figure 1-14 B).⁴²⁴

1.2.5.2.2. Lipidated peptide amphiphiles

Lipopeptides can be functionalized with a binding site for TGF- β 1 to promote chondrogenic differentiation of hMSCs and the regeneration of articular cartilage in rabbits.³¹⁹ Lipopeptides have also been extended with sulfonate groups to mimic sGAG molecules. This functionalized lipopeptides seeded with prechondrogenic cells allowed the formation of cartilage-like nodules and deposited sGAG.⁴²⁵ Yaylaci *et al.*⁴²⁶ designed GAG-like glycopeptides that co-assemble via Ser-linked β -D-glucose and carboxylic acids, mimicking the active site of hyaluronic acid (Figure 1-14 C). GAG-like glycopeptides can self-assemble, allowing the organization of multiple glucose residues in enabling the

chondrogenic differentiation of MSCs *in vitro*. In another study, GAG-like glycopeptide nanofibers were also tested in osteochondral defects *in vivo*. After 12 weeks of incubation the scaffolds presented hyaline-like cartilage repair, with a morphology and composition similar to the adjacent healthy native cartilage in the rabbit model (Figure 1-14 D).⁴²⁶

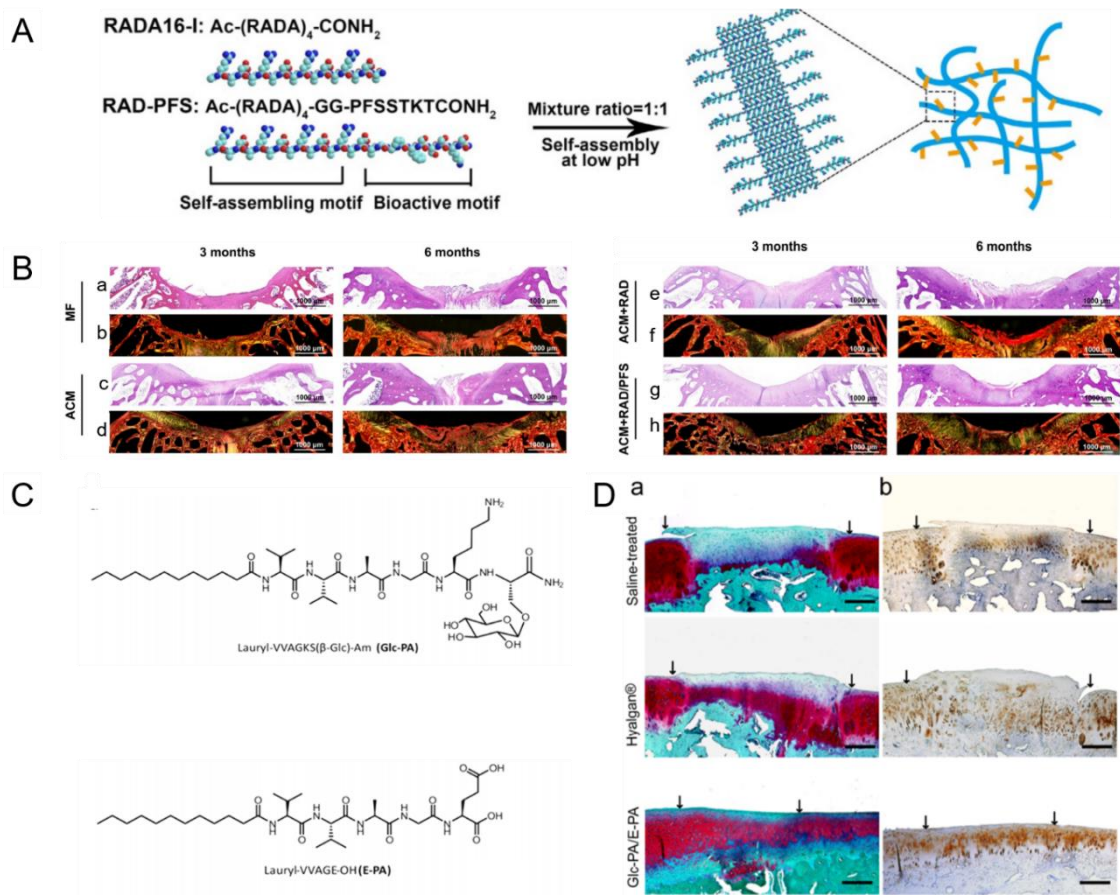


Figure 1-14 Schematic design of peptide amphiphile scaffolds for cartilage tissue engineering. **A**, Schematic diagram illustrating the design and fabrication of RADA/PFS hydrogels. **B**, Histological images of Hematoxylin-eosin staining (a, c, e, g) and sirius red staining (b, d, f, h) of repaired cartilage at 3 months and 6 months post different treatment. (MF represents the microfracture control; ACM represents acellular cartilage matrix). **C**, Chemical structure of lipopeptides that modified with Ser-linked β -D-glucose and carboxylic acids, respectively. **D**, Histological images of osteochondral defect site after 12 weeks treatment, with (a) Safranin-O staining for glycosaminoglycans (b) and collagen type II staining. A and B with the reproduced with permission from⁴²⁴; C and D with the permission from⁴²⁶.

1.2.5.2.3. Supramolecular peptide amphiphile conjugates

As mentioned earlier, supramolecular hydrogels can be fabricated through mixing β -CD PPZ (host) and adamantane-modified RGD (guest), in which the behavior of MSCs can be regulated by the control amount of adamantane-modified RGD.³⁴⁴ Their results indicated an increased content of adamantane-modified RGD levels within hydrogels improved MSCs survival rate and enhanced chondrogenic differentiation, in both *in vitro* and *in vivo* studies. In a similar study, thermosensitive supramolecular hydrogels were fabricated composed of β -CD PPZ (host) and two different kinds of adamantane-modified peptides (guests; functional peptides derived from TGF- β 1 and N-cadherin). These hydrogels were then seeded with MSCs and the composite was injected into subcutaneous pockets in a rat model (Figure 7). The results showed different chondrogenic differentiation levels in 21 days post injection via strict stoichiometric control of adamantane-modified peptides based on host-guest interaction system (Figure 7). When two adamantane-modified peptides at stoichiometrically balance, the highest level of MSC chondrogenesis was observed. That is might due to the stimulation of mitogen-activated protein kinase (MAPK) for MSC chondrogenesis in balanced adamantane-modified peptides is stronger than that in slanted adamantane-modified peptides.⁴²⁷ This is therefore, another example of a system that can be used for cartilage repair that provides another tool to construct peptide hydrogels via the control of guest molecules, such as changing the different categories of peptides bearing adamantane or altering their adamantane ratios.

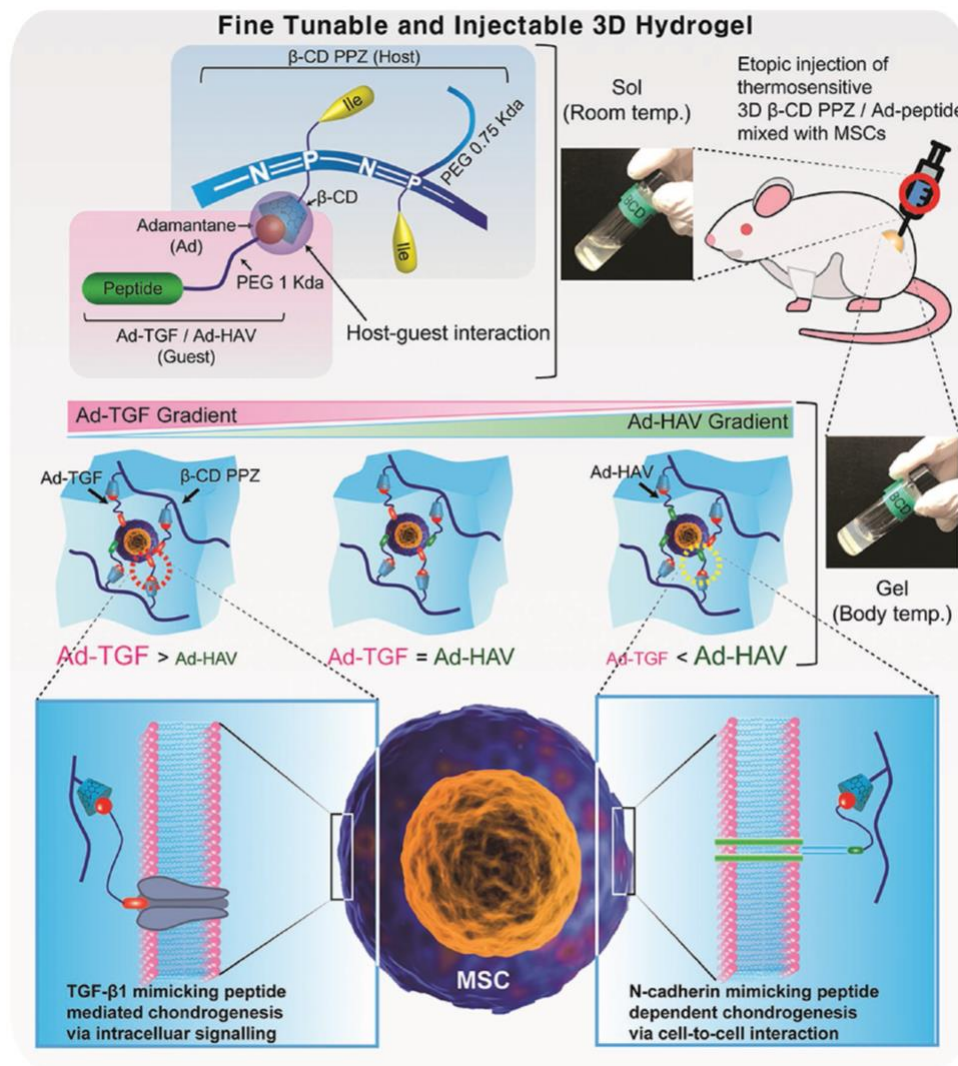


Figure 1-15 Schematic diagram illustrating the injection of β -cyclodextrins poly(organophosphazene) (β -CD PPZ; host), adamantane-TGF and HAV (guests) mixed with mesenchymal stem cells (MSCs) into subcutaneous pockets in rat. After injecting, the liquid mixture was converted into a solidified gel at body temperature. The fate of MSCs is achieved by controlling the stoichiometric ratio of adamantane that was incorporated to TGF- β 1 peptide and N-cadherin peptide. Reprinted with permission from⁴²⁷.

1.2.5.3. Neural tissue regeneration

The nervous tissue system is made up of the central nervous system (CNS) and peripheral nervous system (PNS). This system is fragile and can be easily impaired by injuries and diseases and has limited capacity for self-repair. Currently applied treatments consist of autografts and allografts, but these have several limitations, including shortage of donor, immunological tissue, lack of functional recovery and size/site mismatch of tissue.^{428, 429} The application of

PAs-based scaffolds have been exploited in neural TE for many years, especially for RADA-based hydrogels. This is because PAs can be easily biofunctionalized with various motifs to provide bioactivity of the surrounding microenvironment for neural cells.

1.2.5.3.1. Amphiphilic peptides

According to very early studies, the peptide RADA16 has already been successfully functionalized with laminin derived motifs (IKVAV, RGDS and PDSGR), bone marrow homing motifs (SKPPGTSS and PFSSTKT) and the cell adhesion motif RGD.⁴³⁰⁻⁴³² All of these functionalized RADA16 peptides can not only promote neuronal cell proliferation and adhesion, but also can induce neurite outgrowth and synapse formation. Additionally, in a recent study, dual functionalized hydrogels were fabricated with a combination of two functionalized RADA16 peptides carrying IKVAV and RGD epitopes. The results indicated dual functionalized hydrogels can improve viability and differentiation of neural stem cells (NSCs) into neurons and astrocytes, compared to single functionalized hydrogels.⁴³³ Subsequently, Wu et al.⁴³⁴ loaded dual functionalized hydrogels into poly-L-lactic acid (PLLA) electrospun nanofibrous conduits and then sutured these to stump gaps on rat sciatic nerves (Figure 1-16 A). After 12 weeks, the nerves grew into the dual functionalized hydrogels and grew toward distal ends in the PLLA microchannels (Figure 1-16 B (a) and (c)). In contrast the non-functionalized RADA16 hydrogel grafts had parallel axons at proximal ends, but axons were randomly distributed in the radial direction of electrospun conduit (Figure 1-16 B (b) and (d)). This is most likely due to large cavities existing in non-functionalized RADA16 hydrogels (Figure 1-16 C (d) to (f)), leading to nerves growing along the wall of cavities. In addition, the authors discovered axons and Schwann cells uniformly distributed within the dual functionalized hydrogels, while axons and Schwann cells seldomly grew within the non-functionalized RADA16 hydrogels (Figure 1-16 C). Dual functionalized hydrogels were found to induce more axon regeneration and Schwann cells migration. In another recent study, Lu et al.⁴³⁵ showed how double functionalization of RADA16 with binding sites for the brain derived neurotrophic factor BDNF and nerve growth factors could enhance neurite outgrowth of PC12 cells *in vitro*. They could foster axonal regeneration as well

as functional recovery in sciatic nerve defects in rat models. In addition to this, RADA16-based hydrogels also have been shown to significantly foster the regeneration of brain injury.⁴³⁶⁻⁴³⁸ For example, Shi et al.⁴³⁹ prepared BDNF functionalized RADA16 hydrogels with encapsulated human umbilical cord mesenchymal stem cells (HUC-MSCs) and activated astrocytes, which were successfully used to repair injured brain tissue within the cortical gap in rat models. This composite hydrogel was shown to foster more BDNF secretion which in turn promoted neural differentiation of HUC-MSCs cells. In addition, the composite hydrogels were found to stimulate axon, dendrite outgrowth and synapse formation to repair moderate-size cavities. Another study reported RADA16 hydrogels could be used as a cell carrier for co-transplantation of epileptic brain-derived hNSCs and human adipose-derived stem cells. The composite hydrogels can enhance functional recovery, reduce neuroinflammation, lesion volume, and reactive gliosis at the injured site in rats with traumatic brain injuries.⁴⁴⁰

Other well-known ionic self-complementary peptides (LDLK)₃ and K₂(QL)₆K₂ have been tested for the treatment of spinal cord injuries. The self-assembling peptide (LDLK)₃ can be conjugated to the phage-derived peptide FAQRVPP, which was shown to be able to support the differentiation of NSCs into neurons, and foster the regeneration of acute spinal cord injuries in rats.⁴⁴¹ It was found that mixing the functional peptide FAQRVPP with natural guar gum polysaccharide at a weight ratio 1:1 the shear modulus of the gel significantly increased from 0.2 kPa to over 68 kPa. This therefore makes the composite a possible candidate for use in 3D bioprinting to fabricate well-define scaffolds with complex structures, which have a great potential for future CAD designed neural tissue regeneration applications.⁴⁴² Liu et al.⁴⁴³ first reported that K₂(QL)₆K₂ could suppress astrocytic differentiation and promote neuronal differentiation *in vitro*. In addition, according to their results, K₂(QL)₆K₂ not only promoted axonal regeneration but could also reduce astrogliosis and inflammation in chronic spinal cord injuries. Moreover, K₂(QL)₆K₂ could also be used as a cell carrier for transplantation of neural progenitor cells (NPCs) enhancing forelimb neurobehavioral recovery in cervical spinal cord injuries.⁴⁴⁴ However, a conjoint injection of K₂(QL)₆K₂ and NPCs was shown to have poor cell survival rates. Therefore, K₂(QL)₆K₂ was firstly injected in cervical spinal

cords 1 day post-injury to optimize the post-traumatic environment for a subsequent NPCs transplantation 14 days later. This strategy enhanced survival rates and differentiation of NPCs, reduced lesion volume and improved functional recovery.⁴⁴⁵

More recently, Nam et al.⁴⁴⁶ demonstrated the self-assembling peptide KVKEVFFVKEVFFVKEVY (betaVhex) can associate with carbon nanotubes (CNTs) to form neural interface gels, leading to the acceleration for signal transmission from neurons (Figure 1-16 D). In addition, the viscoelastic properties of this betaVhex/CNTs hydrogel are similar to that of natural native neural tissue, enabling seamless integration in neural tissue. The neural signal intensities of the β and γ bands improved by 3-fold when CNTs were incorporated in betaVhex hydrogels (Figure 1-16 E). Moreover, the authors injected betaVhex/CNTs hydrogels into layers II/III of the somatosensory cortex of chronic epileptic rats for real-time local field potential (LFP) measurements. The results indicated betaVhex hydrogels showed a higher degree of signal augmentation (around 2.4-fold) than those of a bare electrode (Figure 1-16 F).

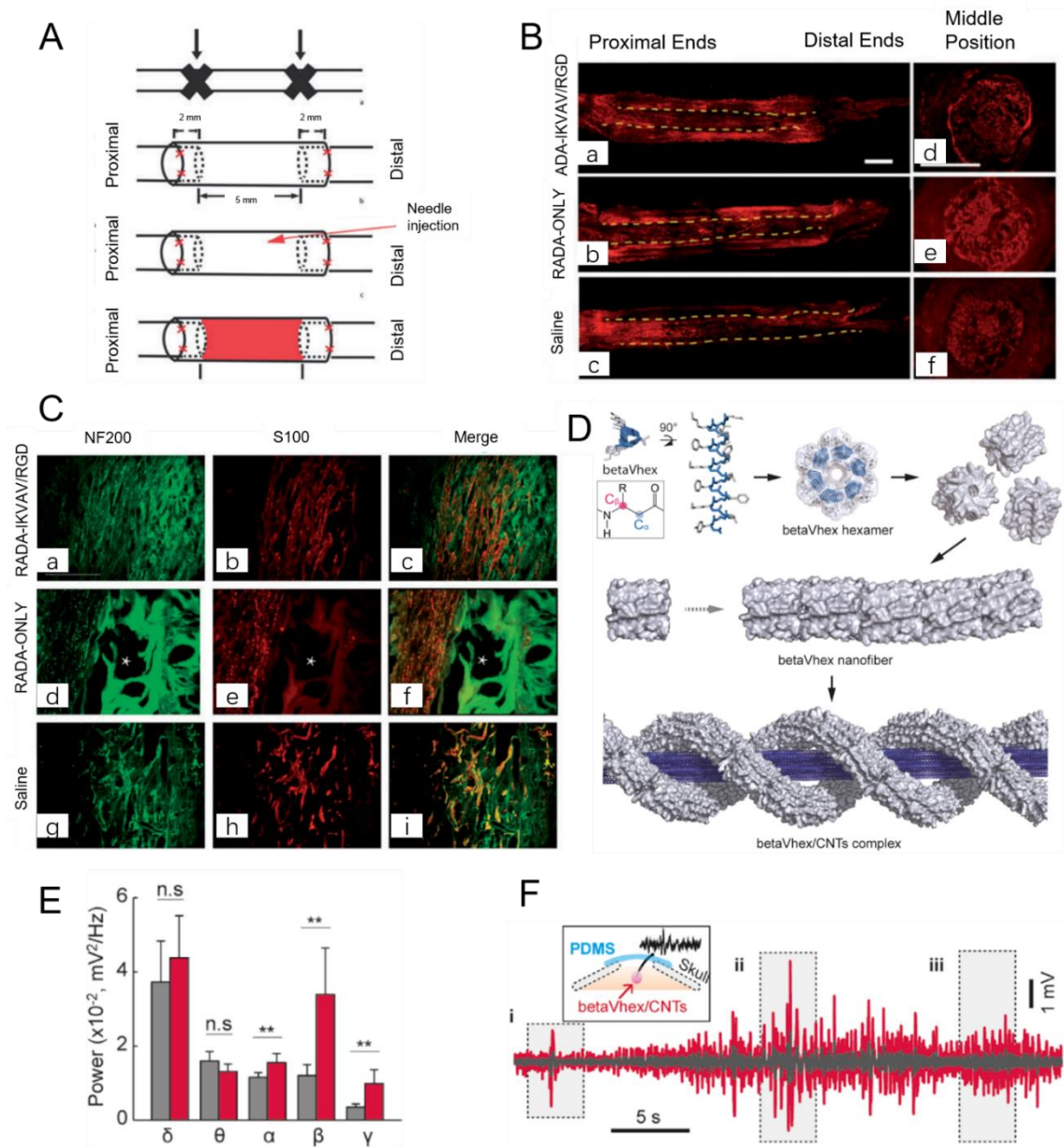


Figure 1-16 **A**, Schematic representation of the injury model and repair strategy. **B**, Longitudinal (a-c) transverse (d-f) full observation of axon regeneration on various grafts after transplanted for 12 weeks. The yellow dash lines represent the inside wall of electrospun conduits. RADA-IKVAV/RGD represents the mixture of RADA-IKVAV and RADA-RGD. Axons were stained by rabbit anti-NF200 (red). **C**, Stained longitudinal sections of middle position on various grafts, after transplanted for 12 weeks. The * indicates the large cavities formed inside the RADA-only hydrogel. NF200 staining for axons (green); S100 staining for Schwann cells (red). **D**, Schematic representation of self-assembly betaVhex/CNTs hydrogel via incorporating acetyl group to betaVhex. **E**, Bar graph of neural oscillations on betaVhex/CNTs hydrogel (red bar) and betaVhex hydrogel during seizures (gray bar). **F**, Measurement of real-time local field potential (LFP) signals on betaVhex/CNTs hydrogel (red) and 1-mm inserted bare electrodes

(gray). Polydimethylsiloxane (PDSM) was covered to brain surface for repeatable measurements. A, B and C with the permission from⁴³⁴; D, E and F with the permission from⁴⁴⁶.

1.2.5.3.2. Lipidated peptide amphiphiles

The first reported application of lipopeptides for neural TE was from a study by Mattiace et al.⁴⁴⁷. They demonstrated that the functionalized lipopeptide IKVAV was able to suppress glial differentiation of NSCs and enhance cell viability as well as the number of oligodendrocytes formed at the site of injury. In addition, IKVAV functionalized lipopeptide were reported to not only foster regeneration of ascending sensory fibres and descending motor fibres, but also could promote regeneration of serotonergic fibres through the lesion site. In summary this means IKVAV was able to facilitate functional recovery after spinal cord injury in both rat and mice models.^{447, 448} IKVAV functionalized lipopeptides have also been used to successfully culture rat dorsal root ganglion neurons *in vitro*. This indicates that IKVAV possesses good biocompatibility with sensory neurons.⁴⁴⁹ The co-assembly of IKVAV functionalized lipopeptides and nonfunctionalized lipopeptides can provide an aligned substrate to control the direction and migration of neural cells.⁴⁵⁰ In addition to this, Li et al.⁴⁵¹ reported lipopeptides can also be functionalized with RGDS epitopes to form nanofiber gels. They loaded this type of functional gel into PLGA conduits and then implanted them into sciatic nerve defects. The resulting composite hydrogel facilitated motor/sensory function recovery and encouraged a high-density axon regeneration, similar to those of nerve autografts. Moreover, lipopeptides can be functionalized with binding sites for Tenascin-C to regulate migration and differentiation of neural precursor cells. Functional gels were injected into the rostral migratory stream in adult rat brains, leading to the redirection of migrating resident neural progenitor cells to the cortex instead of olfactory bulb. Therefore, this approach can be used to redirect neuroblasts to the specific injured sites in adult brains.⁴⁵²

1. 3. Identification of Problem

The future of modern TE is to regenerate and replace damaged tissue and organs. This means that implanted scaffolds should be fully integrated into the surrounding tissue without any immune response or adverse effects. As previously mentioned, SF and PAs are recognized scaffolds and have all been successfully deployed in a large variety of TE applications, due to its unique biomedical properties. However, both of them still have several disadvantages and limitations. For example, pure SF has poor biological interactivity due to inert properties, including overall weak negatively charged and a lack of cell adhesive components, such as arginine-glycine-aspartic acid (RGD) sequence and isoleucine-lysine-valine-alanine-valine (IKVAV) sequence. Therefore, SF scaffolds normally have low cell binding efficiency, which is particularly significant for neuronal cells. On the other hand, PAs can be designed based on bioactive sequences, enable to a high density of surface signals that can interact with cells. In addition, hydrogen bonding assisting the self-assembly process of PAs forming highly stabilized β -sheet conformation. This means PAs have strong stability that cannot easily biodegrade in the human body. However, pure PAs have poor mechanical properties and expensive. Fortunately, SF has good mechanical performance and tunability, which has been fabricated into various morphologies including films, mats, artificial fibres, sponges and hydrogels. In addition, SF is a cost-effective biomaterial. Therefore, the combination of SF and PAs has great potential to be used in the future for the fabrication of scaffolds for neuron TE.

1. 4. Aims and Objectives

Over the past three decades, numerous PAs have been designed and synthesized by using the 20 natural amino acids available. Despite the successful use of many PAs in nerve TE, most of them are ionic self-complementary peptides and lipidated peptide amphiphiles. It is anticipated that surfactant-like peptides also have a great potential as a cell adhesive matrix for the regeneration of neural tissue. In addition, surfactant-like peptides are more cost-effectively than other categories of PAs due to their short sequence. Therefore, the purpose of this PhD project is to explore surfactant-like peptides and their suitability for nerve TE applications. In this thesis, a variety of surfactant-like peptides, including typical examples (I₃K and I₃QGK) and custom designed short peptides sequences, based on active sequences found in the extracellular matrix (I₃RGDS, I₃KVAV, I₃YIGSR, I₃PDSGR and I₃PHSRN), were fabricated aiming at improving cellular attachment, cellular density and morphology of neuron cells.

As previously mentioned, SF scaffolds have low cell binding efficiency, which is particularly significant for neuronal cells. Therefore, SF can be used as cell-repellent surface, allowing surfactant-like peptides coat or pattern on its surface via spin coating or inkjet printing. In addition, the combination of two different surfactant-like peptides may provide synergistic effect, enabling them to promote cellular attachment, cellular proliferation and morphology change of neuronal cells. In this thesis, atomic of microscopy will be used to investigate the dynamic process of surfactant-like peptides, characterize the topography of the combined surfactant-like peptides and RSF scaffolds and investigate the specific interaction between neuronal cells and surfactant-like peptides. Fluorescent labels techniques, including Immunofluorescence staining, live / dead and resazurin assay, will be used to study cell behavior on the combined surfactant-like peptides and RSF scaffolds, such as proliferation, attachment, cellular density, morphology and neurite outgrowth of cells. Moreover, inkjet printing will be used to print surfactant-like peptides as the complex patterns (e.g., University logo and letters "SHEF") onto RSF coated substrates.

With the results obtained, we hope to unravel the relations between surfactant-like peptides and cellular behaviour of neuronal cells and provide a way for further analysing and understanding fundamental cellular functions such as axonal development and cell-cell interaction *in vitro*.

2. Experimental section

2. 1. Materials

The synthetic peptides AC-I₃K-NH₂ (purity > 98%, w/w) and AC-I₃QGK-NH₂ (> 98%, w/w); AC-I₃RGDS-COOH (purity > 98%, w/w); AC-I₃YIGSR-COOH (purity > 98%, w/w); AC-I₃KVAV-COOH (purity > 98%, w/w); AC-I₃PDSGR-COOH (purity > 98%, w/w) and Ac-I₃PHSRN-COOH (purity > 98%, w/w); were purchased from GL Biochem Ltd. (Shanghai, China). *B. mori* silkworm cocoons were supplied by Biological Science Research Centre, Southwest University, China. PC12 Adh (CRL-1721.1) cell line was obtained from the American Type Culture Collection (ATCC). Silicon wafers were purchased from Compact Technology Ltd, UK. Prior to each experiment the glass slides were immersed in 1 M HCl and 1 M NaOH for 1 h separately and then rinsed with deionized (DI) water before being dried using a compressed air line. Silicon wafers (Compact Technology Ltd, UK) were cut into 1 cm² squares and immersed in DI water for 1 day, then cleaned with 5% Decon 90 solution (Decon Laboratories Ltd, UK), before rinsing with copious amounts of DI water.⁴⁵³ Unless otherwise specified, chemicals and reagents (analytical grades) were purchased from Sigma Aldrich, UK.

2. 2. Methods

2.2.1. Preparation of regenerated silk fibroin

B. mori silkworm cocoons were cut into small pieces (~1 cm²) and degummed in 0.02 M Na₂CO₃ solution at 100 °C for 1.5 hours under stirring. Degummed silk was rinsed three times with deionized water (DI water) to ensure the removal of sericin. After which the degummed silk fibres were dried for 2 days in a drying oven at 60 °C and dissolved under stirring in Ajisawa's reagent (CaCl₂/ethanol/deionized water = 1:2:8 molar ratio) at 80 °C for 1.5 hours. The resulting viscous solution was dialyzed against DI water until a conductivity below 10 µS of the dialysis fluid was reached. The resulting RSF solution was then centrifuged for 10 minutes at 10,000 rpm to remove any particulates. The RSF concentration was determined by weighing dried RSF peptide residues on

microscope slides. Stock RSF solutions of 5 mg/mL and 40 mg/mL were made by diluting with DI water and stored at 4 °C prior to use.

2.2.2. Preparation of RSF/peptide samples

I₃K and I₃QGK peptides were dissolved in 20 mM HEPES buffer (pH 6.0) at a concentration of 5 mg/mL 5 mg/mL and incubated for 7 days under ambient conditions for self-assembly. The samples were then diluted with 20 mM HEPES buffer (pH 6.0) to 4, 3, 2, 1 mg/mL prior to use. RSF/peptide bilayer scaffolds were made by spin coating (Laurell Technologies Corporation, USA) onto 1 cm² microscope cover glasses or silicon wafers. The first layer of RSF (30 μL, 8,000 rpm, 25 seconds) was coated followed by fixing using 95% wt/vol ethanol (20 μL, 4,000 rpm, 25 seconds), to convert the RSF layer from the soluble random coil structure (silk I) to the insoluble β-sheet structure (silk II).³³ The second layer, i.e. the positively charged peptide (30 μL, 8,000 rpm, 25 seconds) was coated and adhered onto the negatively charged RSF substrate via charge interaction. The solution concentration ratios of RSF/peptide were 5:0; 5:1; 5:2; 5:3; 5:4; 5:5; 20:1; 20:5; 40:0; 40:1; 40:2; 40:3; 40:4; 40:5 and 0:5, respectively.

2.2.3. Atomic force microscopy

AFM measurements (Bruker Dimension Icon, Bruker Corporation, USA) were performed in tapping model with SCANASYST-AIR probes at room temperature. To image peptide nanostructures, the peptide solution was dripped onto freshly cleaved mica and dried under gentle air flow. AFM was also used to characterise the topography of RSF/I₃K scaffolds and attached cells. PC12 neuronal cells were fixed with 3.7% paraformaldehyde (PFA) in phosphate buffered saline (PBS) for 45 minutes at room temperature. The PBS solution was then removed carefully with a pipette and the samples were washed with DI water gently to avoid crystallisation of PBS buffer salts. The samples were then left to dry at room temperature for 1 min prior to AFM characterisation. Images were analysed by means of NanoScope Analysis software (Version 1.5).

2.2.4. Surface patterning of self-assembled peptide using inkjet printing

All glass slide surfaces were cleaned with 5% Decon90 solution and rinsed with plenty of DI water before printing: 1 layer of RSF solution (40 mg/mL) was coated via spin coating on the glass slides (30 μ L per cm^2 , 8000 rpm, 25 seconds) followed by 95% wt/vol ethanol solution (20 μ L, 4000 rpm, 25 seconds) via spin coating. A Jetlab 4xL (MicroFab Inc., Texas, US) equipped with a piezoelectric drop-on-demand (DoD) printhead (60 μ m nozzle diameter) was used for the printing of the I₃QGK and I₃K peptide nanofibers (3 mg/mL aged for 1 week prior to use). The actuation voltage and frequency used were 90 V and 300 Hz respectively. The distance between the print head tip and the substrate was approximately 1-10 mm. To investigate the effect different patterns of peptides had on cell growth, straight lines, the university logo and the letters "SHEF" were printed. Lines were printed with varying number of layers of peptide (i.e. 1, 3, 5, layers).

2.2.5. Culture of PC12 or NG108-15 neuronal cells on scaffolds

PC12 and NG108-15 neuronal cells were cultured in Dulbecco's Modified Eagle Medium (DMEM) with high glucose supplemented with 10% foetal calf serum (FCS), 1% penicillin/streptomycin, 1% glutamine and 0.5% fungizone in an incubator at 37 °C under 5% (v/v) CO₂. The medium was replaced every 3 days. Scaffolds were sterilized under ultraviolet light for 30 minutes before being washed in PBS three times, and then placed in 12 well plates under metal rings (to secure the samples). Confluent cells were detached with 0.25% (w/v) trypsin-EDTA (ethylenediaminetetraacetic acid) and then seeded onto scaffolds' surface at 10,000 cells/ cm^2 through the holes of metal rings. These samples were cultured in DMEM medium containing 10% FCS for 6 days.

2.2.6. Cell adhesion assay

Following incubation, neuronal cells were fixed in 3.7% formaldehyde for 45 minutes at room temperature followed by washing twice with PBS and incubated for a further 45 minutes with 0.1% Triton X-100. Finally, the cells were washed twice with PBS and stained with FITC-phalloidin (6.7 μ M) to

visualize actin filaments and 4,6-diamidino-2-phenylindole dihydrochloride (DAPI, 300 nM) to visualize the nuclei. The staining process is last for 60 minutes. The samples were then imaged using a fluorescence microscope (Nikon Eclipse LV100).

2.2.7. Live and dead assay

A live / dead assay was carried out by exchanging the medium with serum-free medium containing 0.001% (v/v) Syto-9™ (Invitrogen) and 0.0015% (v/v) propidium iodide (PI) and then incubated for 30 minutes in an incubator at 37 °C under 5% (v/v) CO₂. The samples were then imaged using an upright Zeiss LSM 510 confocal microscope. An argon ion laser was used to visualise live cells stained with Syto-9™ ($\lambda_{\text{ex}} = 494 \text{ nm} / \lambda_{\text{em}} = 515 \text{ nm}$) and a helium-neon laser for dead cells stained with PI ($\lambda_{\text{ex}} = 536 \text{ nm} / \lambda_{\text{em}} = 617 \text{ nm}$). ImageJ software (National Institutes of Health, USA) was used to count the number of live and dead cells for several images of 2500 μm^2 sample areas randomly and averaged. Microscope images were converted to grayscale 8-bit images and then converted to a binary image via selecting the best threshold to generate a high contrast image, cell number was then counted via the 'analyse particles' algorithm in ImageJ.

2.2.8. Statistical analysis

GraphPad Prism V.6 software was used to analyse data quantitatively. One-way or two-way analysis of variance (ANOVA) with multiple comparisons was used for all multiple group experiments, and equality of variances was confirmed by Tukey's multiple comparisons test. P values < 0.05 were deemed significant. Values in graphs are presented as mean \pm one standard deviation.

2. 3. Theories of the technologies

2.3.1. Atomic force microscopy (AFM)

In this thesis, atomic force microscopy (AFM) was used to investigate the morphology and size of self-assembled peptides and PC12 neuronal cells. The principle of AFM and its image modes, with a focus for tapping mode, are introduced in following sections.

2.3.1.1. The basic principle of AFM

AFM is one of categories of scanning probe microscopy (SPM), whose aim is to measure the local properties, such as surface topography, through a probe.⁴⁵⁴ A diagram showing the basic principles of AFM is shown in [Figure 2-1](#), a sharp tip (probe) is mounted on the end of microcantilever which not only can scan across the sample, but also can measure interaction between the probe tip and the sample surface for imaging or qualification of tip-sample forces. The geometries of these tips are normally in the form of a cone or pyramid, which are typically made of silicon or silicon nitride, dependant on application use.⁴⁵⁵ As the tip approaches the sample surface, the interaction between the probe tip and the sample surface results in a deflection of the cantilever. In general, this deflection is detected through a reflected laser beam that is collected by a split photodiode.^{247, 248} Therefore, the deflections from the cantilever can be measured through the laser deflection signal, thus recording the motion orbits of the tip, enabling the acquisition of numerous data, such as 3D topography of the sample surface.²⁴⁹ When the probe tip encounters topographical features of the sample surface it will lead to bending, for which the interaction forces are according to the principle of Hooke's law:

$$F = -k \cdot x \quad 2.1$$

Where F is the interaction forces between probe tip and sample surface; k is the spring constant of the cantilever and x is the distance of the cantilever deflection.

The spring constant of the cantilever depends on its shape.⁴⁵⁶ Here, in this thesis, rectangular-shape cantilever was used, with a spring constant (k) which can be calculated by the following equation⁴⁵⁷:

$$k = \frac{Ewt^3}{l^3} \quad 2.2$$

Where E is the Young's modulus of the cantilever, w , t and l are the cantilever width, thickness and length, respectively.

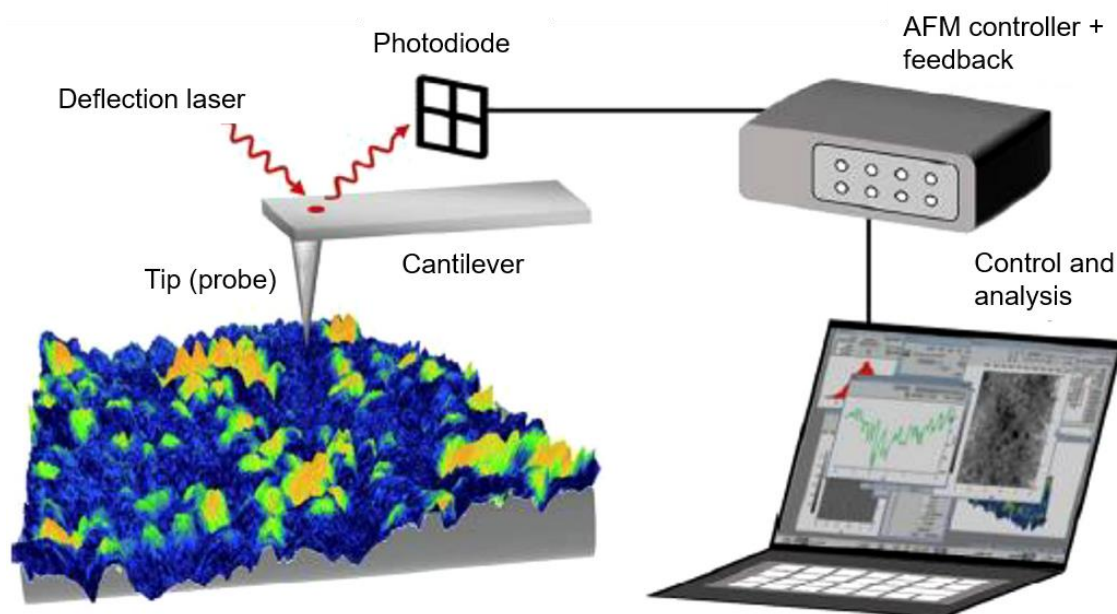


Figure 2-1 Schematic representation of the basic principles of atomic force microscopy (AFM) which was reprinted from⁴⁵⁴.

2.3.1.2. The imaging modes of AFM

Due to development of the AFM, there are several imaging modes now available, which are generally divided into contact mode, tapping mode (also named as intermittent contact mode) and noncontact mode. These modes not only can supply detailed 3D topographies, but also can give information in regard to the sample surface.⁴⁵⁸ The force regimes corresponding to these three AFM measurements are shown in [Figure 2-2](#). The repulsive regime in contact mode is due to the hard contact retained between the probe tip and the sample surface. In tapping mode, the cantilever is able to vibrate at a fixed frequency, allowing it to repeatedly make contact and disengage with the sample surface at lower interaction forces. Compared to tapping mode, the amplitude of the cantilever oscillation is smaller in noncontact mode. The

amplitude shift occurring in long range interactions, such as van der Waals forces, is used to gain the set point. Then, the amplitude set point is used to manipulate the height of tip relative to sample surface using feedback loop systems.⁴⁵⁹ There is no hard contact between probe tip and sample surface, thus, noncontact mode occurs in the attractive force regime.

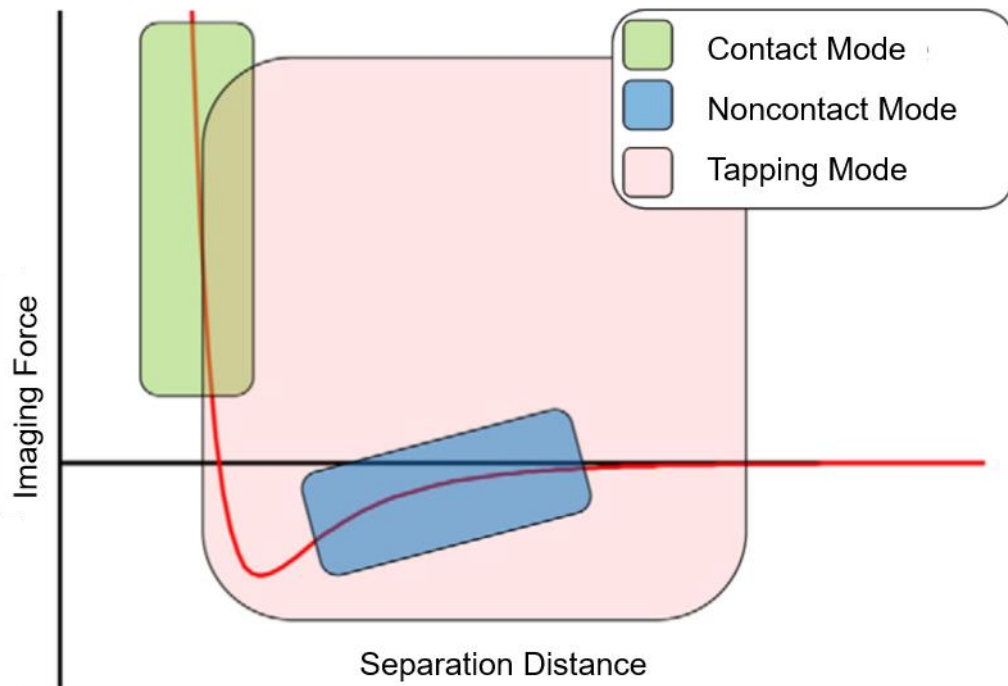


Figure 2-2 Schematic representation of the force regimes under the three typical AFM imaging modes happens, including contact, noncontact and tapping mode. This was reprinted from⁴⁵⁸.

2.3.1.3. Tapping mode of AFM

The AFM mode used through this thesis is belongs to tapping mode and therefore focus will be for this technique.

Tapping mode is a dynamic imaging technique, allowing the cantilever to oscillate near its resonant frequency, enabling close enough to the sample surface to become detectable. The resonant frequency of a cantilever with rectangular geometry (f_0) is given by the following equation⁴⁶⁰:

$$f_0 = \frac{1}{2\pi} \left(\frac{k}{m_0} \right)^{\frac{1}{2}} \quad 2.3$$

Where k is the spring constant with rectangular geometry and m_0 is the mass of the cantilever.

In contrast to contact mode, tapping mode can overcome many of the contamination issues of the tip from the sample surface.⁴⁶¹ In addition, lateral forces are avoided by intermittently approaching sample surface and thus tips damage will be minimized.⁴⁵⁵ In this mode, the amplitude and frequency of the cantilevers oscillation are kept constant via feedback loop systems, in order to ensure the interaction force of tip with the sample surface is constant during scanning. This mode can operate in both air and liquid for imaging soft samples and biological specimens.⁴⁶² After scanning over the sample surface, it can provide the surface features in regard to height topography.

Peak force tapping mode is a newly evolved tapping mode, where the probe tip oscillates at low frequency ranging from 0.25 to 2.0Khz a frequency well below the cantilever's resonance frequency. This enables the probe tip to periodically contact the sample surface for short times (less than 100 μ s), allowing oscillating force periodically applied on sample surface.⁴⁶³ Therefore, peak force tapping mode can not only control the damping of oscillation to the cantilever like normal tapping mode, but also can directly control the force like in contact mode. Once the tip has successfully engaged with sample surface, the interaction forces can be reflected by the cantilever deflection. Through control "peak force" (maximum interaction force) that is applied on the sample at each pixel, then surface topography can be obtained. This maximum interaction force is remained constant during scanning through feedback system, where the feedback is based on the peak force of force-distance curves.⁴⁶⁴ The individual force-distance curve at each pixel of image is shown in [Figure 2-3 A](#). This recorded curve can reflect various nanomechanical properties ([Figure 2-3 B](#)), including tip-sample deformation, adhesion force, dissipation and Young's modulus.

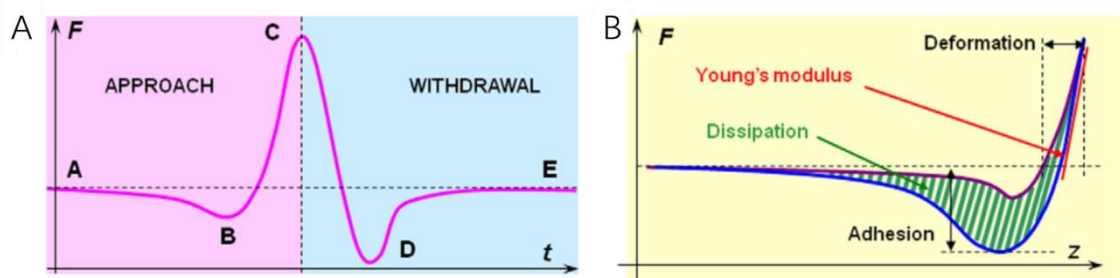


Figure 2-3 The schematic diagrams illustrate A, how the probe tip is subject to attractive and repulsive forces during an individual approach-retract cycle. B, how nanomechanical properties can be collected from each force curve. A and B were reprinted from⁴⁶⁴.

In peak force tapping mode, the Derjaguin–Muller–Toporov (DMT) model can be used to estimate the Young’s modulus of the sample.⁴⁶³ The equations are described below:

$$F_{interaction} = \frac{4}{3}E^* \sqrt{R(d - d_0)^3} + F_{adh} \quad 2.4$$

$$E^* = \left[\frac{1 - \nu_s^2}{E_s} - \frac{1 - \nu_{tip}^2}{E_{tip}} \right]^{-1} \quad 2.5$$

Where $F_{interaction}$ is the interaction forces between probe tip and sample surface; E^* is the reduced elastic modulus of the probe tip and sample; R is the radius of tip; $d - d_0$ is the sample deformation; F_{adh} is the adhesion force during contact; ν_s and ν_{tip} are the Poisson’s ratio of sample and probe tip, respectively; E_s and E_{tip} are the Young’s modulus of sample and probe tip, respectively.

ScanAsyst mode is a developed operational mode from Bruker Corporation, whose mechanism principle is same with peak force tapping mode. Unlike peak force tapping mode, this mode is able to automatically adjust all critical imaging parameters, resulting in high-resolution images. Therefore, ScanAsyst mode with SCANASYST-AIR tips has been used in this thesis. Moreover, NanoScope Analysis software (version 1.5) was used to analysis images, which is shown in Figure 2-4.

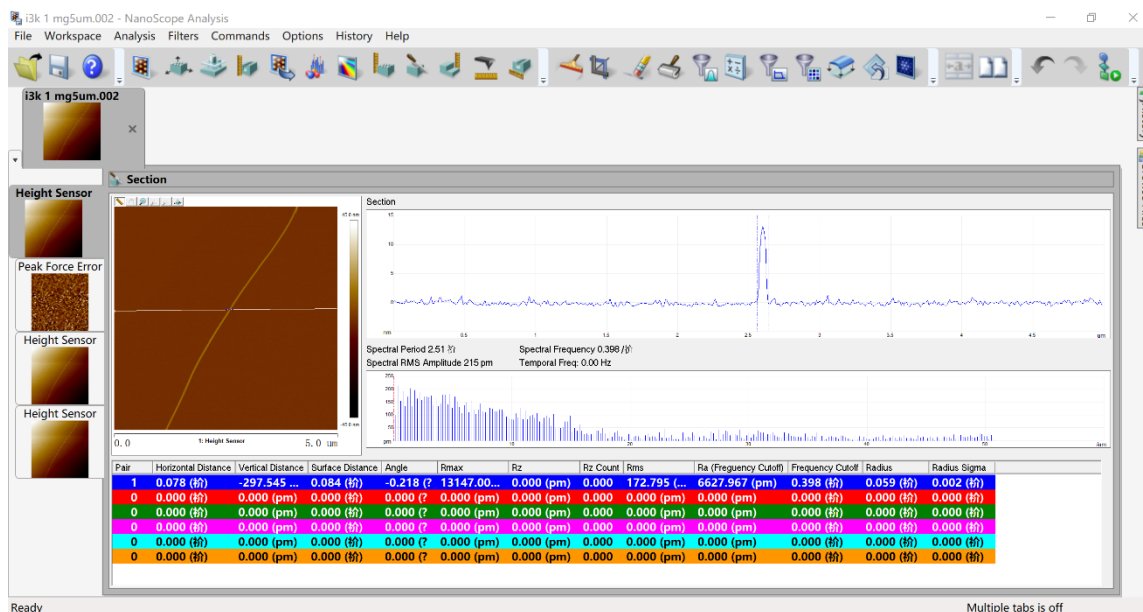


Figure 2-4 The image displays how to get the diameter of nanofiber through AFM software (NanoScope Analysis).

2.3.2. Optical microscopy

2.3.2.1. Brightfield microscopy and darkfield microscopy

Optical microscopy is an essential tool for studies in cell biology, which is mainly composed of an objective lens with various magnification powers, ocular lens, focus knobs, eyepiece, light source and condenser.⁴⁶⁵ The aim of optical microscopy is creating magnified images of a specimen by means of an objective lens and eyepiece.⁴⁶⁶ In addition a charge-coupled device (CCD) camera can be attached to the microscope to capture digital images. Brightfield microscopy and darkfield microscopy are the two main types in optical microscopy. For brightfield microscopy (Figure 2-5), the specimen is placed between a light source and objective, allowing transmitted light to pass through the specimen.

Brightfield microscopy can be easily converted to darkfield microscopy by placing an opaque disc (around 1 cm in diameter) underneath the condenser lens (Figure 2-5). Therefore, most lights from the light source is blocked, only some light passes through the outer edge of the condenser. This leads to only the light being scattered by the sample to reach the objective lens. The resulting images illustrate bright objects on a dark background, which is directly opposite to what is observed in brightfield microscopy (Figure 2-5). Note that, darkfield microscopy is very sensitive to dust, which can light up on the dark background. It is well known that cells are transparent and thin. In addition, they cannot absorb light.⁴⁶⁷ So that, darkfield microscopy was used to observe unstained cells in this thesis.

Brightfield vs. Darkfield Microscopy

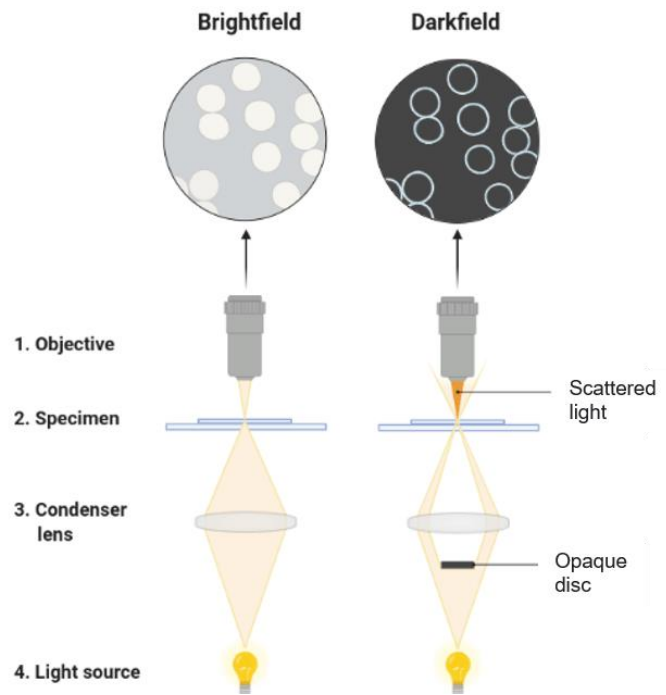
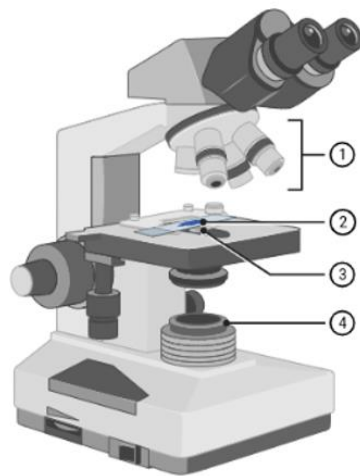


Figure 2-5 Schematic diagrams indicate main components of optical microscopy and the difference in illumination between brightfield microscopy and darkfield microscopy.

2.3.2.2. Fluorescence microscopy

Fluorescence microscopy is a conventional tool for molecular biologists and especially for neurobiologists. Proper choice of fluorescence filter cubes is the key to successful fluorescence microscopy. These filter cubes normally consist of an excitation filter, an emission filter and a dichroic mirror at 45° . In fluorescence microscopy (Figure 2-6), multiple wavelengths of excitation light is supplied by a mercury or xenon high pressure bulb, which is directed through the excitation filter to obtain the required wavelength.⁴⁶⁸ The function of the dichroic mirror is to separate the excitation and emission light. In detail, the selected excitation (shorter wavelength) light is reflected to the sample, exciting the fluorescent dye molecules (also named as fluorophores) in the sample of interest. The resulting emission (longer wavelengths) light is transmitted to the emission filter, and can be observed by means of a CCD camera. The emission filter needs to filter out any spurious excitation light from the sample to ensure there is only emission light imaged.⁴⁶⁷⁻⁴⁶⁹

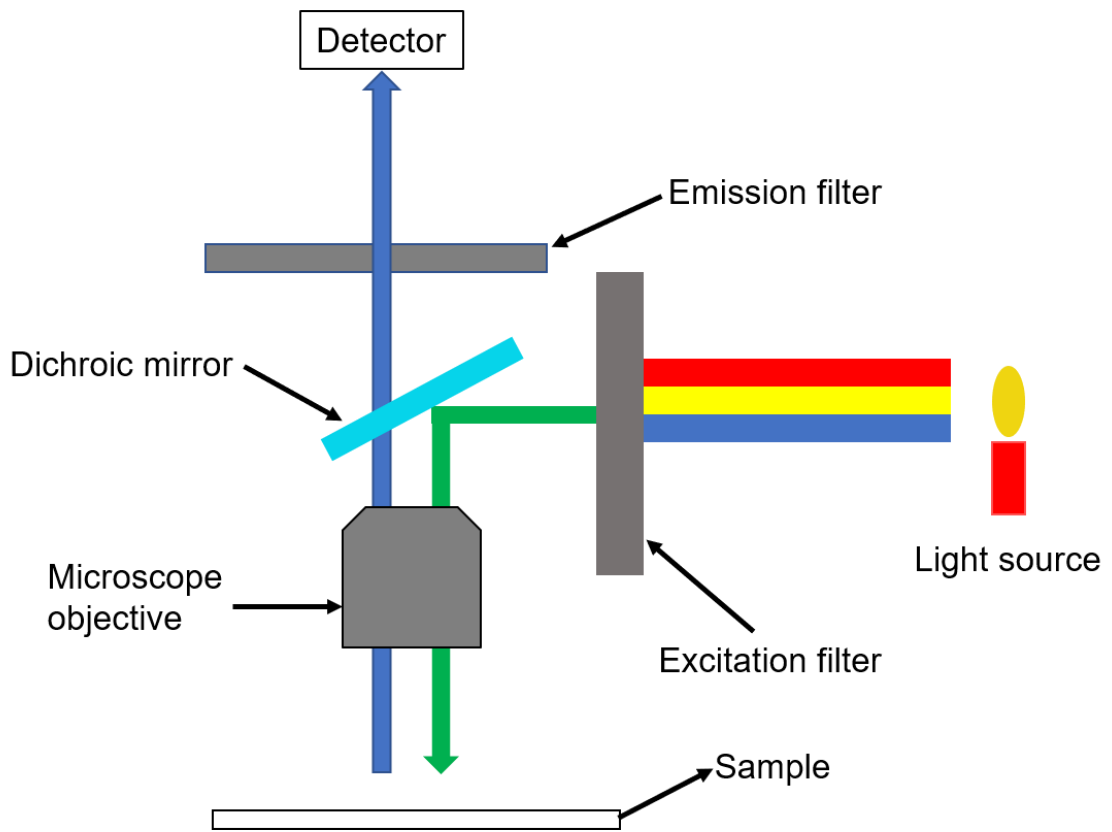


Figure 2-6 Schematic drawing of the principle of fluorescence microscopy.

In addition, it is important to understand the process of fluorescence. Upon the selected excitation light reaching the sample, the fluorescent molecules absorb the light energy (a photon). After a few nanoseconds, another photon (some of this light energy) is emitted by the fluorescent molecules. During this process, part of absorbed energy is lost, thus, the photon emitted has less energy. Light with higher energy possesses a shorter wavelength while light with lower energy has a longer wavelength. This is why emitted light from fluorescent molecules usually has a longer wavelength than that of the excitation light.⁴⁶⁸ For example, fluorescein Isothiocyanate (FITC) is one of the most popular organic fluorophores, with an excitation wavelength of 495 nm and emission wavelength of 520 nm.

2.3.2.3. Confocal microscopy

Confocal microscopy was developed from traditional fluorescence microscopy, which providing a modest advantage in resolution. In addition, with increased thicknesses of specimens, more out-of-focus emission light is collected by a detection camera in traditional fluorescence microscopy. This can be severely

hindering during imaging. Confocal microscopy is able to block out-of-focus light, which in turn allows the user to obtain high-contrast images by optical sectioning.⁴⁷⁰ As described in the previous section the fluorescence microscopy process is the same for confocal imaging.

The main components and principle of confocal imaging are shown in [Figure 2-7](#). In detail, a laser beam (blue line) is reflected by beam splitter to an objective lens, where it is focused onto a specimen. The laser light then excites fluorescent molecules throughout the focal volume and fluorescence emission light (green line) is collected by objective lens and focused by pinhole lens. Finally, fluorescence emission light is detected after its passage through a pinhole. Note that, the pinhole aperture is an essential component in confocal microscopy, its aim is to reject light from out-of-focus planes. This means the detector will only record emission light comes from the equivalent (confocal) point in the specimen where the laser beam was focused.^{471, 472}

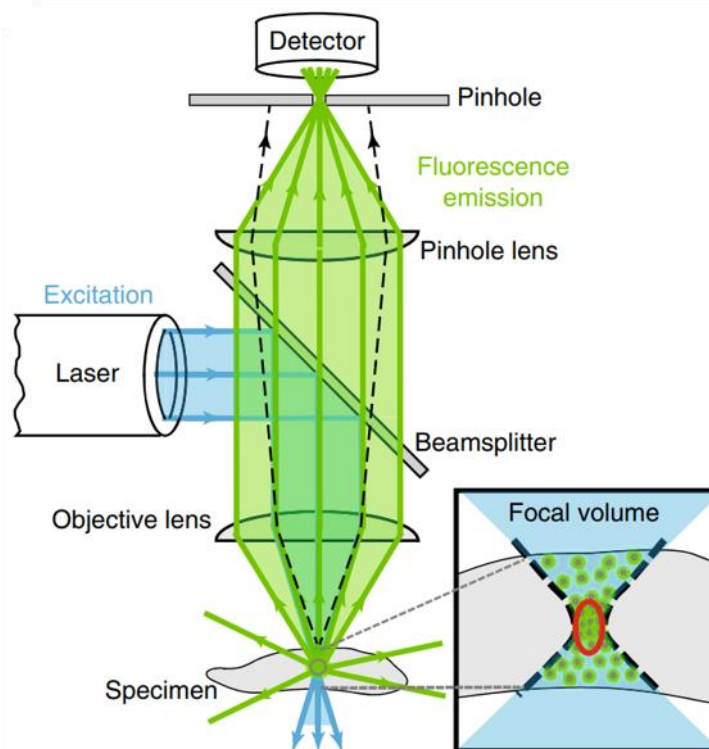


Figure 2-7 Schematic drawing of how confocal laser-scanning microscopy works. This was reprinted from⁴⁷⁰.

Confocal laser-scanning microscopy is continuous scanning technique of the point source of illumination, which only can record fluorescence intensity from one focal point at one time. Therefore, an orthogonal pair of rotating mirrors are

set up which can be used to sweep the laser beam across the fluorescent sample (Figure 2-8), enabling the generation of an image point by point. In addition, a photomultiplier tube (PMT) is a conventional point detector to detect emitted fluorescence through the pinhole. Normally, the PMT collects enough fluorescence data and takes around 1 μ s dwell time on each pixel, so that building a modest image of 1024 \times 1024 pixel takes around 1 s.

Confocal laser-scanning microscopy is also able to build up crisp 3D image of fluorescent samples by combining a series of confocal images (or “slices”) at different depths. Note that for confocal laser-scanning microscopy there is no need to physically slice the sample. It can generate optical sectioning with less than 1 μ m thickness, through a high-resolution objective lens.

In this thesis, both conventional fluorescence microscopy and confocal laser-scanning microscopy were used to image stained cells.

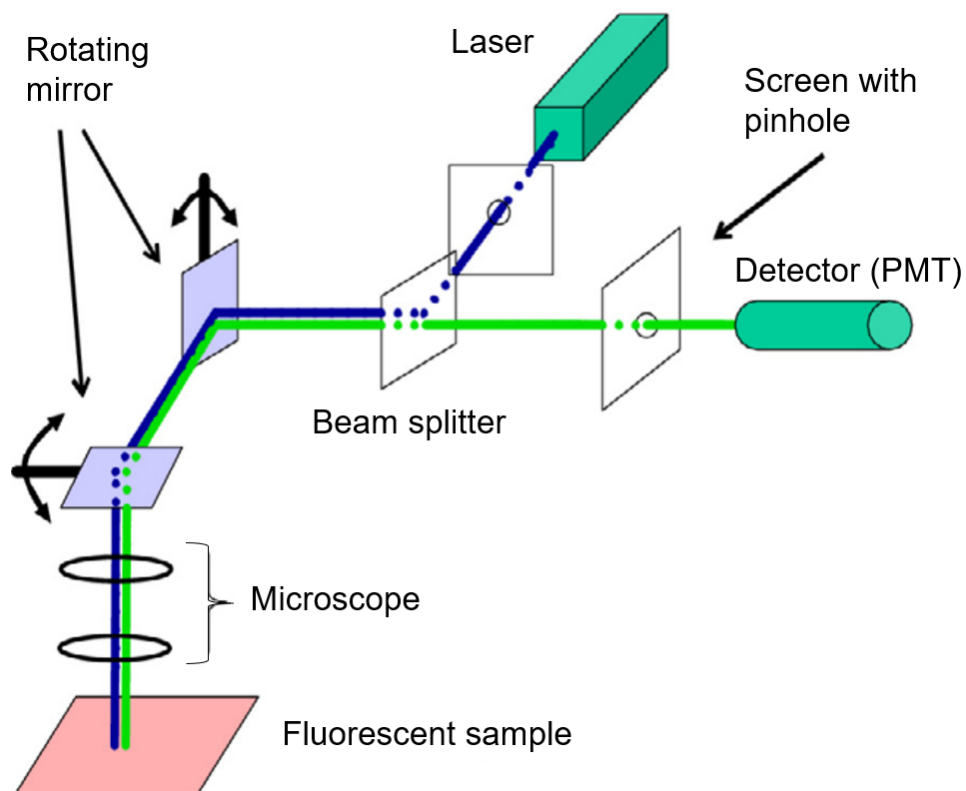


Figure 2-8 Schematic representation of the basic set up of confocal laser-scanning microscopy. This was reprinted from⁴⁷¹.

2.3.3. Scaffold preparation techniques

2.3.3.1. Spin coating

Spin coating (Figure 2-9) is an inexpensive technique to fabricate uniform thin films on flat surfaces. Normally, the process of spin coating can be divided into four main stages, including sample deposition, spin up, spin off and evaporation.⁴⁷³ Firstly, the solution of material is deposited onto the centre of the substrate (generally glass slides) by pipette. At this stage, it does not matter if the substrate has already started to spin, the solution will be spread out across the substrate by centrifugal motion. When the substrate rotates at the programmed speed, the fluid will become level and some of fluid is will also be flung off. Generally, the rotation speed is in the range of 1000-8000 rpm.⁴⁷⁴ Higher speeds will lead to thinner layers. Upon the fluid become thinner by outflow, the films often change colour due to interference effects. Based on rapid rotation, high volatile components are evaporated while low volatile components remain on the substrate surface. Finally, superhydrophobic thin film are obtained.

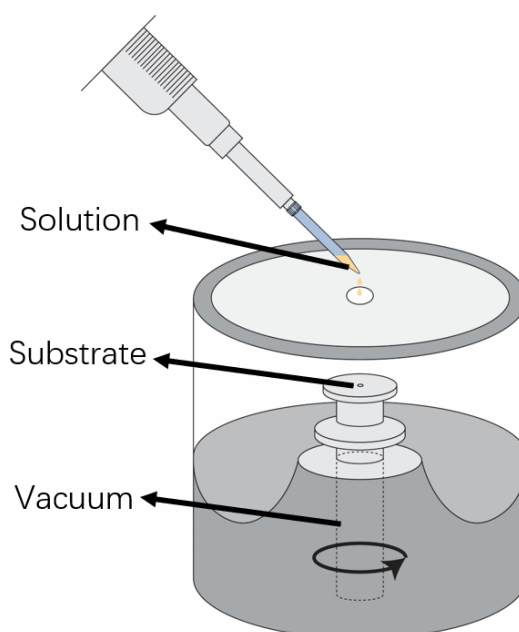


Figure 2-9 Schematic representation of spin coating process. The solution is directly dropped onto substrate and rotating at the programmed speed. The substrate is fixed by ultrahigh vacuum.

There are several parameters that can affect film thickness, the relationships are described by the following equation.^{473, 475}

$$h = \left(1 - \frac{\rho_A}{\rho_{A0}}\right) \times \left(\frac{3\varphi m}{2\rho_{A0}\omega^2}\right)^{\frac{1}{3}} \quad 2.6$$

where h is the thickness of the film; ρ_A is the density of the volatile liquid; ρ_{A0} is the density of the coating solution; φ is the viscosity of the coating solution; ω is the angular speed and m is the rate of evaporation.

In this thesis the spin coating technique was used to coat silk fibroin solution, ethanol and self-assembled peptides onto glass slides or silicon wafers, layer by layer, to obtain scaffolds that could be used for tissue engineering.

2.3.3.2. Inkjet printing

Inkjet printing was originally developed for printing graphics and text at the office and home. In a principle, inkjet printing is a “bottom-up” approach, by which ink is jetted through a nozzle of a print head device in the form of small droplets, enabling the printing of text or images on papers.⁴⁷⁶ With the development, many researchers have been focusing their attention on inkjet printing for the biological field, such as exploiting biomaterials as ink to print scaffolds with specific morphologies. There are two main modes of inkjet printing, which are continuous and drop-on-demand inkjet printing.⁴⁷⁷ Continuous inkjet printing, can produce high-speed droplet flow (almost in the form of a continuous stream) with controllable drop size. For drop-on-demand inkjet printing, ink droplets are only ejected as voltage signals are received. Therefore, this mode is able to be used to obtain intricate patterns at high resolution.⁴⁷⁶ In addition to this, unlike continuous inkjet printing, drop-on-demand inkjet printing does not need a recycling system. This means ink in the fluid chamber is always fresh and no contamination, which is very important for the biological field, can occur.⁴⁷⁸ Therefore, drop-on-demand inkjet printing was chosen in this thesis.

In drop-on-demand inkjet printing, a transducer is used to receive electrical signals, which in turn control the ink droplets to desired places. According to the type of transducers, it can be further divided into two sub-classes (Figure 2-10), namely piezoelectric inkjet printing and thermal inkjet printing. In piezoelectric inkjet printing, a piezoelectric ceramic surrounds the ink chamber undergo mechanical deformations, which leads to a sudden volume change, thereby

generating droplets from nozzle.⁴⁷⁸ In thermal inkjet printing, the actuator can be locally heated by impulse voltage causing partial vaporization of the fluid. This leads the formation of small vapor bubbles, which squeeze the ink and thus droplets are formed at the nozzle.⁴⁷⁸ Piezoelectric inkjet printing was used in this thesis, so that this mode will be mainly discussed.

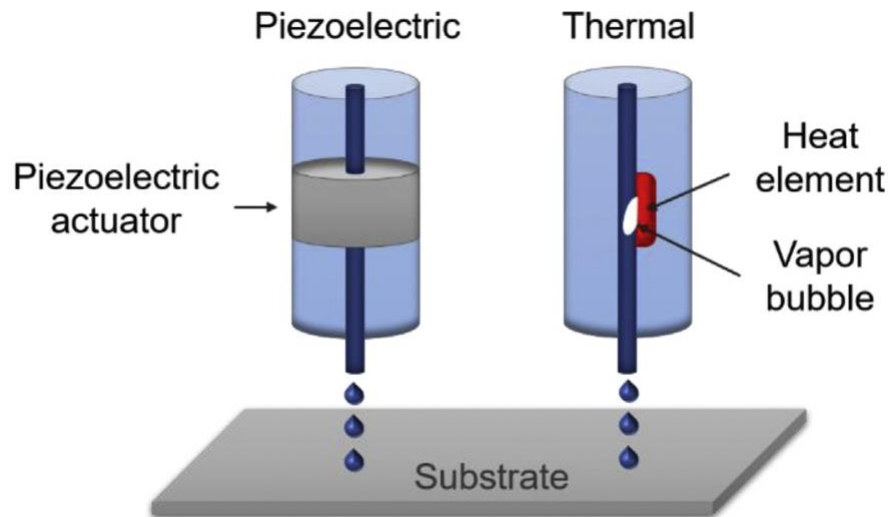


Figure 2-10 Schematic representation of two sub-classes of drop-on-demand inkjet printing, which are piezoelectric inkjet printing and thermal inkjet printing. This was reprinted from⁴⁷⁸.

The principle of piezoelectric drop-on-demand inkjet printing is shown in [Figure 2-11](#). When piezoelectric actuator receives voltage signals, the ink chamber wall will lead to deformation. According to the deformation modes of ink chamber, piezoelectric inkjet printing can be classification into four different types, including push, bend, squeeze and shear.⁴⁷⁶ By controlling the voltage pulses characteristics and the driving mode of piezoelectric elements, the major parameters of droplets, such as velocity, volume, shape and consistency, can be adjusted.⁴⁷⁶ In addition to these, piezoelectric inkjet heads give a more convenient way to control droplet parameters. There are a wide range of different diameter nozzles that can be chosen from and are easy to replace. Therefore, cross contamination from different inks can be avoided by replacing nozzles for every type of experiment.⁴⁷⁶ Generally, the diameter of piezoelectric inkjet nozzles are in the range of 18-120 μm , which can produce the diameters of droplets between 50 μm and 100 μm .⁴⁷⁶

In this thesis, piezoelectric drop-on-demand inkjet printing was used to print self-assembled peptides onto silk fibroin substrate, in the form of complex patterns.

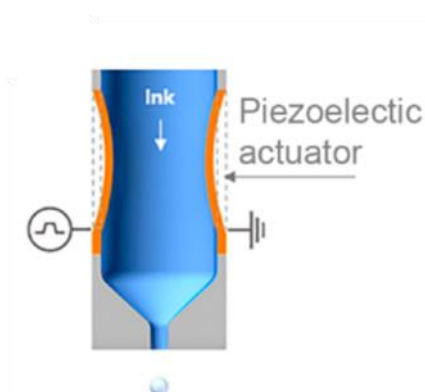


Figure 2-11 Schematic representation of how piezoelectric drop-on-demand inkjet printing works. This was reprinted from⁴⁷⁶.

2.3.4. Fluorescent labels techniques

All the cells used here were not fluorescent in this thesis. Therefore, it was necessary to introduce fluorophores to the cells of interest, enabling the observation via fluorescence microscopy or fluorescence plate reader. The principle of immunofluorescence staining, viability staining and resazurin assay are reviewed in the following sections.

2.3.4.1. Immunofluorescence staining

Immunofluorescence staining is a type of immunochemical technique, by which fluorescently labelled antibodies are used to detect and localize a wide variety of components within cells.⁴⁷⁹ Fixation is the first step in immunofluorescence staining, with the purpose to immobilize target antigens while maintaining cell morphology, enabling antibodies maximum access to the cellular component of interest.⁴⁷⁹ In this thesis, formaldehyde was used to fix the cells through binding to cellular components. In another words, formaldehyde was used as a cross-linking agent that can react with some atoms of proteins, leading to the formation of methylene bridge.⁴⁸⁰ In addition, Triton X-100 is a detergent, which can be used to permeabilize intact membranes within a cell. This can enhance the penetration of antibodies, enabling antibodies a maximum access to the cellular milieu.⁴⁶⁷

There are two immunofluorescence techniques that use fluorophores to visualize different cellular antigens (e.g., proteins), these are direct immunofluorescence and indirect immunofluorescence.⁴⁷⁹ In the direct approach (Figure 2-12 A), primary antibodies are directly coupled to fluorophores and then react with target antigens. In the indirect immunofluorescence approach (Figure 2-12 B), a secondary fluorophore-conjugated antibody that specifically binds to the primary antibody is used to visualize the structure of interest.⁴⁷⁹ In this thesis, 4,6-diamidino-2-phenylindole dihydrochloride (DAPI) and FITC-phalloidin were used to visualize nuclei and actin filaments of cells, respectively. This type of staining belongs to the direct immunofluorescence section. In addition, the indirect immunofluorescence technique was also employed to visualize neurites of cells. In detail, cells were incubated with a mouse anti- β III-tubulin (a neurite marker) antibodies, washed, and incubated with a Texas Red-conjugated anti-mouse IgG antibodies.

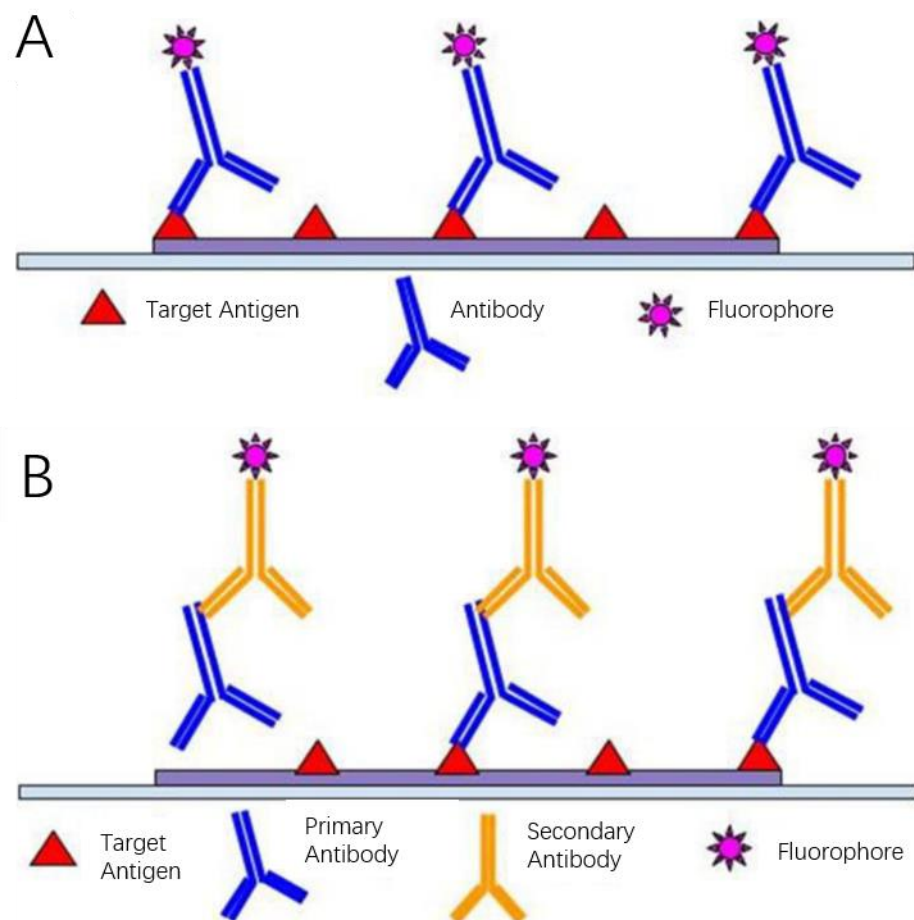


Figure 2-12 Schematic representation of the principle of A, direct immunofluorescence and B, indirect immunofluorescence. A and B were reprinted from⁴⁷⁹.

2.3.4.2. Cell viability staining

Fluorophores can also be used as indicators to evaluate cell viability. This technique uses indirect measurements of the cellular state rather than direct to prove that cells are capable to proliferate and grow.⁴⁸¹ Researchers have different views relating to the criteria to define a cell as alive or dead. Cellular membrane integrity is one of the standards to determine cell viability. Upon on this standard, live cells are considered to possess intact and tight membranes, in which some fluorophores are unable to penetrate. In contrast, dead cells are assumed to have broken or disrupted membranes.^{481, 482} In this thesis, dual staining kits, consisting of Syto-9™ (green) and propidium iodide (red), were used to detect membrane integrity to distinguish between live and dead cells in a population. In detail, Syto-9™ can enter all cell membranes while propidium iodide only penetrates cells with broken or disrupted membranes.⁴⁸² Both Syto-9™ and propidium iodide can intercalate with nucleic acids, allowing an increase in the fluorescent signal. However, the affinity of Syto-9™ is stronger than that of propidium iodide. Therefore, when both fluorophores exist, propidium iodide can replace Syto-9™.⁴⁸¹ Finally, fluorescence microscopy was used to distinguish live and dead cells based on the relative green and red fluorescence.

2.3.4.3. Resazurin assay

The resazurin assay, also known as Alamar Blue, provides another method to evaluate the viability of mammalian cells. Briefly, this method is based on the detection of mitochondrial activity within cells, which is linearly related to the viability of target cells.⁴⁸³ Resazurin (7-hydroxy-3H-phenoxazin-3-one 10-oxide) is a cell permeable redox indicator, which gives poor fluorescence.⁴⁸⁴ It can be easily dissolved in physiological buffer, leading to deep blue coloured solutions.⁴⁸⁵ Viable cells which are metabolically active are capable to reduce the dye via reductase enzymes from mitochondria. Therefore, resazurin is reduced by viable cells to form the strong-fluorophore resorufin (7-hydroxy-3H-phenoxazin-3-one), with a pink colour ([Figure 2-13](#)).⁴⁸⁴ The fluorescence output is proportional to the population of viable cells, which can be quantified by a fluorescence plate reader.

In this thesis, PC12 cells were incubated for 4 hours to check for cell metabolism via this assay.

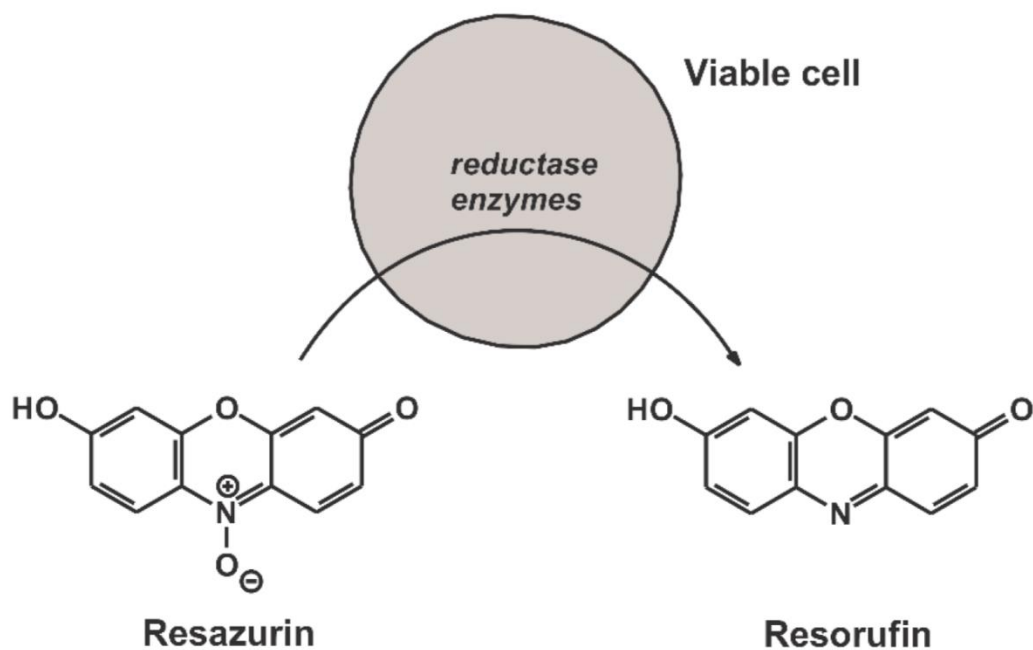
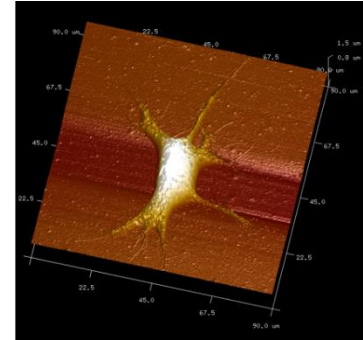


Figure 2-13 Schematic representation of the principle of resazurin assay, in which resazurin is directly reduced by reductase enzymes to form resorufin. This was reprinted from⁴⁸⁴.

3. Patterning the neuronal cells via inkjet printing of self-assembled peptides on silk scaffolds

Abstract



The patterning of neuronal cells and guiding neurite growth are important for neuron tissue engineering and cell-based biosensors. In this paper, inkjet printing has been employed to pattern self-assembled I₃Q GK peptide nanofibers on silk substrates for guiding the growth of neuron-like PC12 cells. Atomic force microscopy (AFM) confirmed the dynamic self-assembly of I₃Q GK into nanofiber structures. The printed self-assembled peptide strongly adheres to regenerated silk fibroin (RSF) substrates through charge-charge interactions. It was observed that in the absence of I₃Q GK, PC12 cells exhibited poor attachment to RSF films, while for RSF surfaces coated or printed with peptide nanofibers, cellular attachment was significantly improved in terms of both cell density and morphology. AFM results revealed that peptide nanofibers can promote the generation of axons and terminal buttons of PC12 cells, indicating that I₃Q GK nanofibers not only promote cellular attachment but also facilitate differentiation into neuronal phenotypes. Inkjet printing allows complex patterning of peptide nanofibers onto RSF substrates, which enabled us to engineer cell alignment and provide an opportunity to direct axonal development *in vitro*. The live/dead assay showed that printed I₃Q GK patterns exhibit no cytotoxicity to PC12 cells demonstrating potential for future nerve tissue engineering applications.

Keywords: Neurobiology, Micro-patterning, Inkjet printing, Self-assembling peptides, PC12 cells

3. 1. Introduction

Peripheral nerve injuries account for 2.8% of all trauma injuries worldwide, which are typically the results of crush, penetration, traction, electric shock and vibration injuries.¹ These injuries affect millions of people worldwide resulting in a reduction of people's life expectancy as well as increasing social and economic burdens. Although injured nerves have the ability to regenerate external therapeutic interventions are needed to ensure proper healing. Therefore, the development of engineered nerve scaffolds to guide neural cell attachment, alignment and proliferation has attracted significant attention.⁴⁸⁶⁻⁴⁸⁹

Fabricating scaffolds to direct neuron cell growth is however challenging. Cell patterning is an important technology that enables researchers to accurately position populations of cells to designated areas on a substrate and promote the design of complex biological systems to study cell behaviour such as cell alignment, interaction, cell-environment interaction, drug screening and cell based sensors.^{142, 183, 490} In these applications the chemical and topographical patterning of the systems become important factors that affect cell behaviour such as attachment and migration.⁴⁹¹ A technology that provides fast fabrication of patterned scaffolds/substrates allowing researchers to better understand cell behaviour and program the cell functions is therefore essential. Such studies will provide valuable information for future tissue engineering, drug screening and biosensor applications. Common techniques currently employed for surface patterning include lift off patterning, micro-contact printing and a variety of direct writing techniques, which are complex and expensive.⁴⁹²⁻⁴⁹⁶

Polydimethylsiloxane (PDMS) and polyvinyl alcohol (PVA) , are often used to provide patterns via lift-off patterning techniques.²²² Although such systems have the ability to modify mechanical, optical and chemical properties of substrates, it requires complex steps (such as master moulds) and also high standard clean rooms.^{143, 497} In addition to this the fabrication of master moulds for different patterns is also very costly. Deposition of cell attractive substances⁴⁹⁸ such as fibronectin⁴⁹⁹, collagen⁵⁰⁰ or gelatin⁵⁰¹ or cell repelling

agents such as wax⁵⁰² and polyethylene glycol (PEG)⁵⁰³ onto a substrate is another approach for cell patterning. Such methods are normally combined with photolithography or chemical vapour deposition. For example, Ren et al.⁴⁹⁵ deposited biotin-BSA onto glass with the help of photolithography and successfully patterned the cells into dot arrays. Wang et al.⁴⁹⁶ have patterned a notch signalling ligand (Jagged1) and cell adhesion molecule (N-cadherin) using micro-contact printing to study cell-microenvironment and cell-cell interactions. However, such methods are costly, and the materials used are expensive. It is desirable to use cost-effective methods for patterning, with biocompatible and degradable materials for both attractive and repelling agents. Here, we use a self-assembled peptide as a cell attractive agent and regenerated silk fibroin (RSF) as a repelling agent to pattern neuronal PC12 cells by inkjet printing. Inkjet printing is a non-contact, cost effective, highly controllable and time saving technique that can print complex patterns (via CAD/BITMAP design) onto substrates. The particular strength of inkjet printing is its ability to precisely place pico-litres of ink at predetermined locations either side by side, or one on top of the other, resulting in 2D and 3D patterns/structures.⁵⁰⁴ Multiple print heads also allow the rapid changeover of inks making it ideal for fabrication through reaction/crosslinking between different inks and also the incorporation of multiple components (e.g. different peptides and growth factors) during fabrication. It also enables fast and personalized fabrication at large scale. Silk fibroin (SF), a protein produced by silkworms during their pupation, is a well-known biomaterial, and many silk-based medical devices have been approved by FDA (Food and Drug Administration).^{24, 505} In recent years, SF has been extensively used as a tissue engineered scaffold for bone⁵⁰⁶, vascular⁵⁰⁷ and skin¹⁸⁸ repair due to its beneficial properties including excellent biocompatibility, biodegradability, low immunogenicity, high mechanical performance and commercial availability.^{508, 509} RSF solution has used to produced many different types of scaffolds including gels¹²², sponges⁵¹⁰, films⁵¹¹ and fibres.^{30, 512} However, pure SF materials are known to have poor biological interactivity due to their inert properties (e.g. overall weak negatively charged and a lack of cell recognized peptide segments such as RGD), which normally manifests itself by a low cell binding efficiency, particularly to neuronal cells.^{22, 513} Therefore, addition of cell recognized moieties (e.g. poly-L-lysine⁵¹⁴, extracellular matrix

(ECM) proteins⁵¹⁵) is required to improve neuronal cell attachment and proliferation ensuring its successful implementation as a scaffold biomaterial in neural tissue engineering.

ECM secreted by tissue or organs has been widely used in scaffold fabrication to provide a niche for tissue growth and regeneration.^{516, 517} Over the last two decades, it has been shown that active peptide sequences such as IKVAV, YIGSR and RGD in ECM can promote cell proliferation and attachment as well as promote neurite outgrowth.⁵¹⁸⁻⁵²⁰ For example, Motta et al.⁵²¹ recently reported on grafting a series of laminin-derived peptides to substrate surfaces with different concentration gradients and used them for the study of Schwann cell adhesion, proliferation and alignment with the concentration direction. It was found that Schwann cells displayed faster migration in the direction of the concentration profile. Self-assembly nanoscale fibrous scaffolds mimicking ECM have also been successfully employed in tissue regeneration.⁵²² The 'bottom-up' approach allows the fabrication of scaffold materials with well-ordered nanostructures.^{523, 524} For example, RAD16-I^{525, 526}, RAD16-II⁵²⁷, EAK16-I⁵²⁸, EAK16-II⁵²⁹, have been successfully used as hydrogel scaffolds for tissue engineering. Shorter self-assembling peptides have also been used for biomedical applications. For example, I₃QGK has been used for haemostasis in animal models with no immunogenic responses.⁵³⁰ The peptide contains a hydrophobic tail made of three isoleucine residues (Ile or I) and a hydrophilic head group (QGK), and can form long and uniform nanofibers in aqueous solutions. The peptide self-organized itself with the tails inside the nanofibers to form a hydrophobic core with the hydrophilic head group on the outside of the nanofibers. The positively charged peptide exhibited excellent biocompatibility and can be potentially used for enhancing cell attachment and proliferation.⁵³⁰ In addition, compared to neutral biomaterial, cationic biomaterial has been reported to causes less significant lysosome and DNA damage, as well as having a higher success rate in the self-repair of neural cells.⁵³¹

In this study, self-assembled I₃QGK peptide nanofibers were patterned onto negatively charged RSF films⁵³² via spin coating and inkjet printing to guide cell attachment (Figure 3-1). Rat pheochromocytoma neuronal (PC12) cells were then studied as an *in vitro* model for neuronal differentiation and neurite

formation.⁵³³⁻⁵³⁵ The cell attachment, viability and phenotype of PC12 cells on the patterned surfaces were investigated.

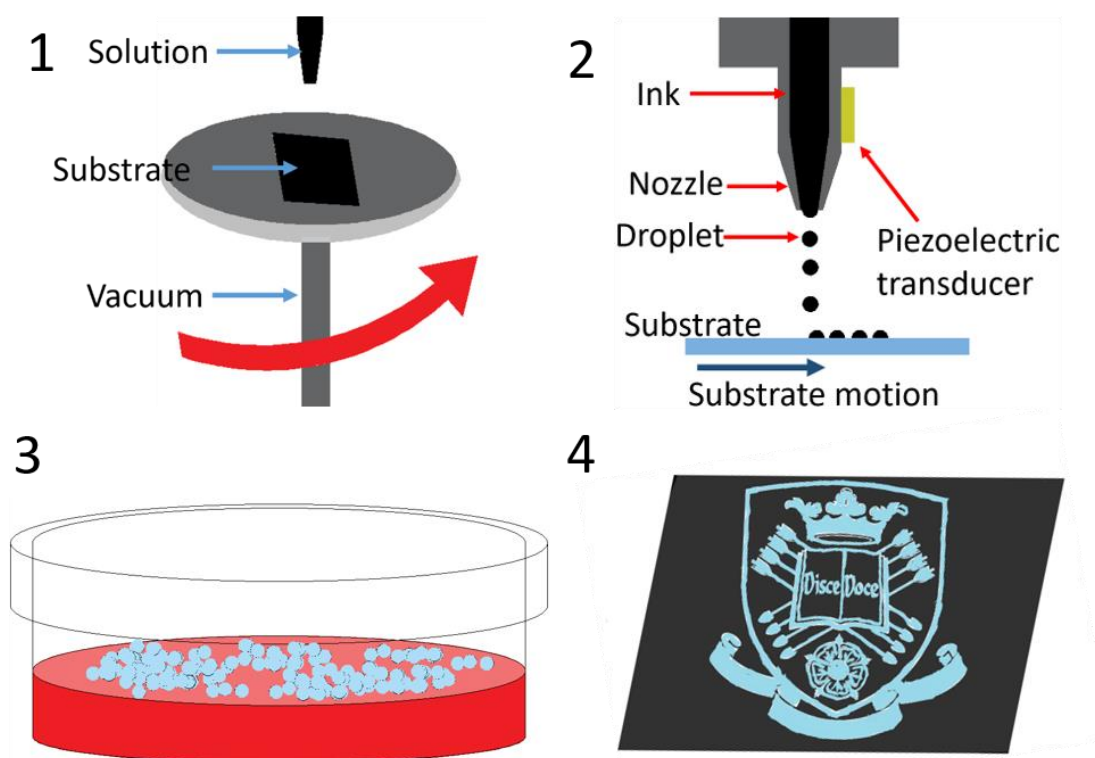


Figure 3-1 A schematic diagram illustrating the fabrication of micro-patterns on RSF substrates via spin coating and inkjet printing, as well as up to the cell attachment on the surface of printed patterns. Briefly, 1, RSF solution (40 mg/mL) was coated onto glass via spin coating. 2, Inkjet-printing of “University of Sheffield” logo onto RSF substrate using peptide I₃QGK (3 mg/mL) as ink. 3, Culture of PC12 cells on printed scaffold for 6 days. 4, PC12 cells only grew along the printed pattern.

3. 2. Methods

3.2.1. Time effect of peptide self-assembly

The synthetic peptide I₃QGK was dissolved in 20 mM HEPES buffer (pH 6.0) at 1 mg/mL. 20 μ L samples were taken at different time intervals over the course of two weeks (0 h, 3 h, 6 h, 9 h, 1 week and 2 weeks), and were dripped onto fresh mica and dried under ambient conditions prior to atomic force microscopy (AFM) characterisation.

3. 3. Result and discussion

3.3.1. Time effect of peptide self-assembly

The dynamic self-assembly process of I₃QGK was similar to that of I₃K.^{299, 300} Small I₃QGK molecules aggregated through hydrophobic interactions between the I₃ tails within the first several hours (Figure 3-2 a and b) and formed bilayer stacks. Continued growth of the bilayer stacks was observed resulting in the formation of twist nanoribbons (Figure 3-2 c to e) due to molecular chirality and electrostatic repulsion. Long uniform nanoribbons with widths of 30 nm and heights of 5-10 nm were observed after 2 weeks incubation (Figure 3-2 f). The size of the nanofibers is consistent with the result reported by Chen et al.⁵³⁰

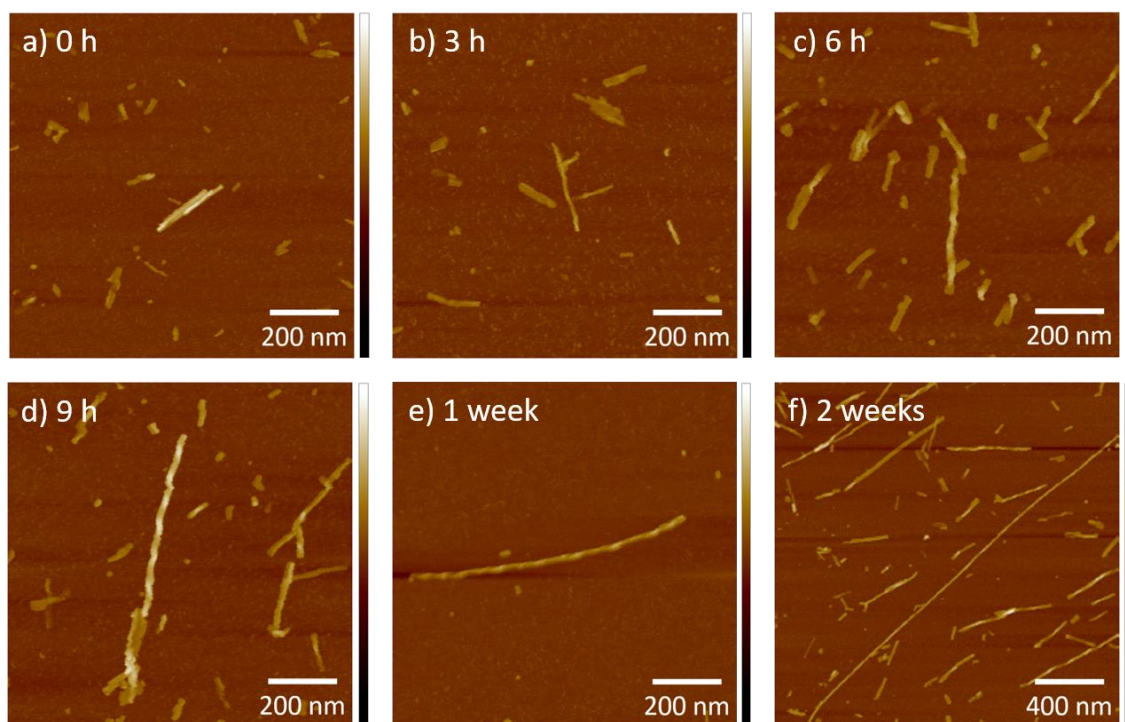


Figure 3-2 AFM topographical images of I₃QGK dynamic self-assembly (1 mg/mL in 20 mM HEPES buffer at pH 6.0) at different time scales. (a) 0 h; (b) 3 h; (c) 6 h; (d) 9 h; (e) 1 week and (f) 2 weeks. The Z scales for all images = 30 nm as indicated. The self-assembly process of the peptide was a dynamic process. In the early stages (< 6 h), the peptides formed short stacks through hydrophobic interactions between the I₃ tails. Further growth of the stacks leads to formation of twisted fibres (> 6 h).

3.3.2. Characterization of RSF/I₃QGK scaffolds

The surface topography of the scaffolds has significant effect to the cell attachment. To establish the relation between the scaffold surfaces and the cell attachment, AFM was used to characterize the topography of the RSF/I₃QGK scaffolds as shown in [Figure 3-3](#). Coating of the I₃QGK peptide onto cover glass formed a uniform layer of peptide nanofibers ([Figure 3-3 a](#)), however, the peptide layer can be easily washed away by water ([Figure 3-3 i](#)), making it unsuitable for direct coating on glass surfaces for cell culture applications. Coating of RSF resulted in a smooth layer of silk on glass surface ([Figure 3-3 b](#)), compared to the atomically flat silica surface ([Figure 3-3 h](#)). Ethanol treatment converted Silk I to Silk II structure³³ (rich in β -sheet), making it water insoluble. While the RSF is overall negatively charged¹²⁰, coating of the positively charged I₃QGK peptide nanofibers on top of a silk layer resulted in a strong charge-charge interaction between the silk coating and the peptide material. With increasing concentration of I₃QGK, the amounts of nanofibers adhered to the RSF scaffold surface increased and a near full coverage was observed at a concentration of 3 mg/mL ([Figure 3-3 c to f](#)). Further increasing the concentration of I₃QGK resulted in stacking of nanotubes [Figure 3-3 f and g](#)), which could potentially lead to cell detachment during cell culture.

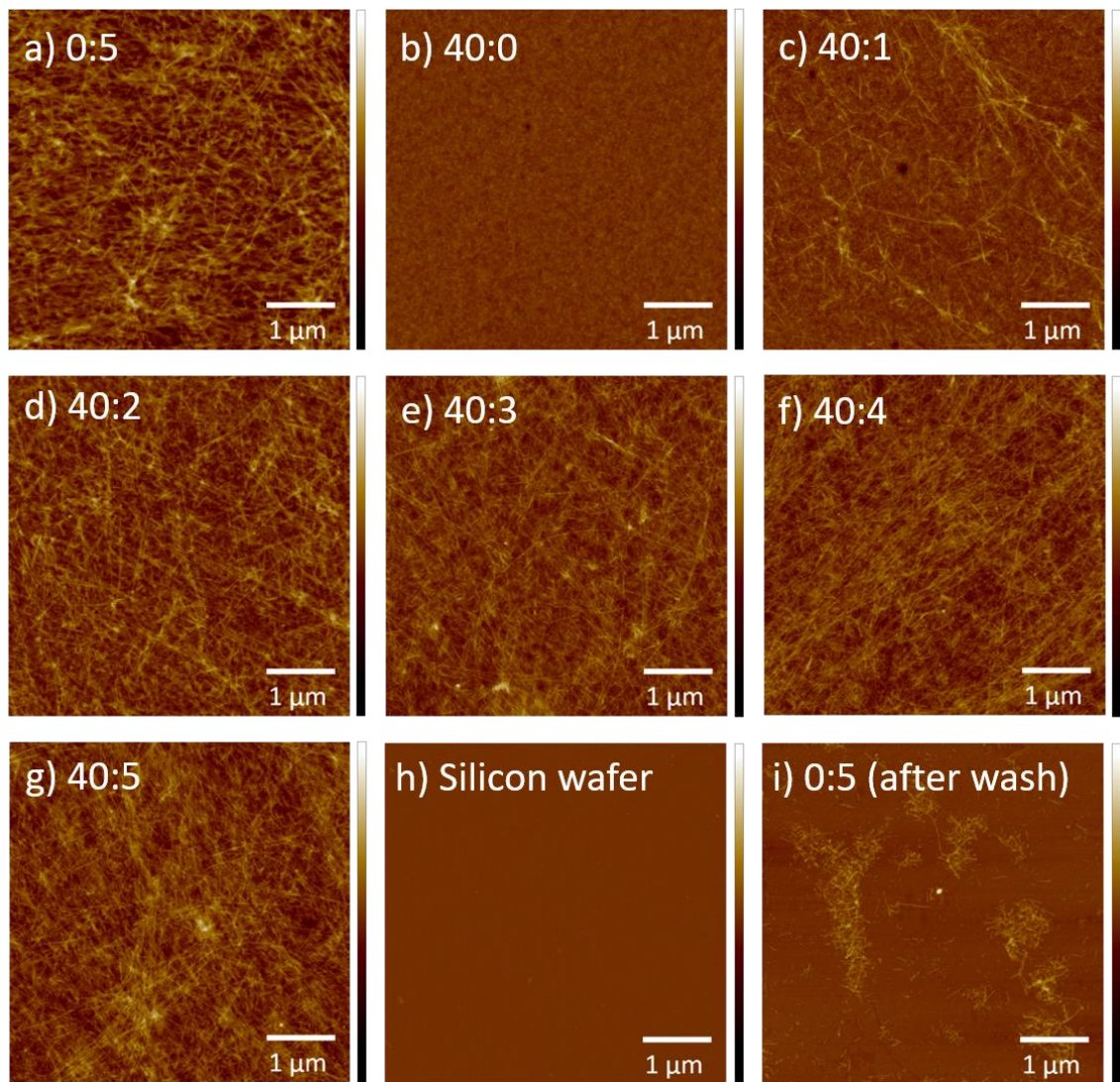


Figure 3-3 AFM topographical images ($25 \mu\text{m}^2$) of RSF/I₃QGK scaffolds (1-layer). The solution concentration ratios of RSF/peptide were (a) 0:5 (only peptide), (b) 40:0 (only RSF), (c) 40:1, (d) 40:2, (e) 40:3, (f) 40:4 and (g) 40:5. For example, 40:1 means I₃QGK (1 mg/mL) coated on RSF (40 mg/mL) surface. (h) is an uncoated silicon wafer. (i) Shows the I₃QGK (5 mg/mL) coated glass surface after being washed with DI water. The Z scales (height) of all images are 60 nm.

3.3.3. Cellular adhesion and viability

The cell adhesion and viability experiments were carried out by live / dead assay on different RSF/I₃QGK coated scaffolds as shown in [Figure 3-4](#). Poor PC12 cell attachment was observed on I₃QGK coated glass surfaces compared to RSF/I₃QGK coated surfaces ([Figure 3-4 A](#)). This is assumed to be due to the washing off of I₃QGK nanofibers during cell culture, which resulted in exposure of the underlying bare glass surface. This result was consistent with the AFM analysis shown in [Figure 3-3 i](#). Pure RSF coated surfaces also exhibited poor

cell attachment due to the lack of cell recognized functional groups and a weak negatively charged surface property (Figure 3-4 A (b)). However, samples coated with I₃QGK peptide nanofibers on RSF substrates provided enhanced cell adhesion due to the electrostatic charge-charge interactions between the RSF layer and I₃QGK nanofibers, providing enough positively charged lysine residues on the surface to facilitate cell binding.⁵¹⁴ A significant difference in cell density was observed between I₃QGK (3-5 mg/mL)/RSF and pure RSF (40 mg/mL) coated scaffolds (Figure 3-4 B, ****p < 0.0001), indicating that PC12 neuronal cells have a low bonding affinity on pure RSF (40 mg/mL) substrates. The scaffold surface topography has a significant effect to the cell spreading. In general, with increasing I₃QGK concentration (onto RSF substrates) the number of cells attached onto the surface increased (Figure 3-4 B), indicating higher surface roughness resulted in better cell spreading. However, when the concentration of I₃QGK increased to 5 mg/mL, the number of cells decreased slightly with some areas having no cell attachment (Figure 3-4 A (g) and Figure 3-4 B, ***p < 0.001). This may result from the detachment of the stacked nanofibers (Figure 2(g)) when using a high concentration of peptide solution for surface coating. This means the biomechanical factors also play an important role. When more peptide fibres are on the surface, the binding between some peptide fibres become loose and detachment happened upon the buffer wash after live/dead staining. PC12 cells on bare glass slides showed poor attachment with aggregation (Figure 3-4 A (h)). The Live / dead assay demonstrated that cells attached on the different concentration ratio (RSF/I₃QGK) coated substrates were ~100% live (green) with no detectable dead cells, indicating that RSF/I₃QGK scaffolds have excellent biocompatibility (Figure 3-4 C). In contrast, some dead cells (red) were observed on bare glass surfaces. From this it can be inferred that the combination of RSF and I₃QGK provide a good solution for neuronal cell attachment and proliferation. The best I₃QGK concentrations for coating RSF surfaces were seen to be 3-4 mg/mL. The results demonstrate that the I₃QGK peptide nanofibrous scaffolds exhibited a similar efficacy to other previously reported peptide scaffolds for tissue engineering.^{526, 536, 537}

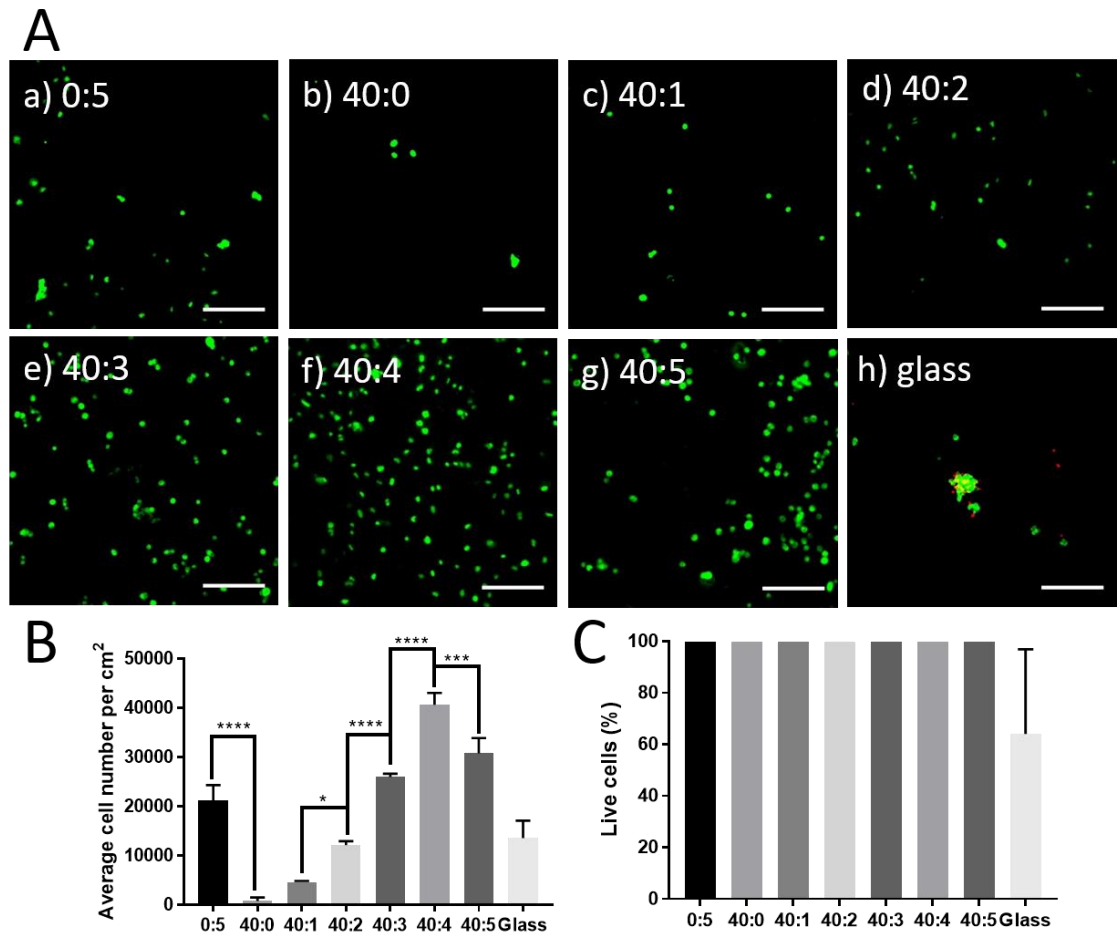


Figure 3-4 **A**, Live / dead assay of PC12 neuronal cells on different RSF/I₃QGK coated substrates (green: live cells (Syto-9™ staining) and red: dead cells (propidium iodide staining). The amounts of total cells seeded onto each RSF/I₃QGK coated substrate were 10,000 cells/cm². The concentration ratios for coating between RSF and I₃QGK were: (a) 0:5, (b) 40:0, (c) 40:1, (d) 40:2, (e) 40:3, (f) 40:4, (g) 40:5 and (h) glass control. Scale bars = 100 μm for all images. **B**, Average cell number (per cm²) attached on various coated surfaces. **C**, Percentage of live cells on various coated surfaces. The percentage of live cells on the different concentration ratio (RSF/I₃QGK) coated substrates were 100% and on the glass was 61 ± 39%. (n ≥ 3; **** p < 0.0001; *** p < 0.001; * p < 0.05).

3.3.4. Cell morphology

To investigate cell morphology, cell nuclei and F-actin were stained for neuronal cells attached on the different RSF/I₃QGK coated substrates (Figure 3-5). Cell morphology on RSF (40 mg/mL) and RSF/I₃QGK (at a concentration ratio of 40:1) coated substrates showed poor spreading. All cells were round shaped and the number of cells attached on the substrates was very low. Cell

morphology on 5 mg/mL I₃QGK coated glass surface (0:5) showed better cell spreading. However, the number of cells attached was also low due to the wash off of peptide from the surface. Cell morphology on the RSF/I₃QGK coated scaffolds at the concentration ratios of 40:2, 40:3 and 40:4 showed improved spreading and the number of cells also increased. In contrast the cell attachment on 40:5 ratios and cover glass were in patches, although the spreading was also excellent.

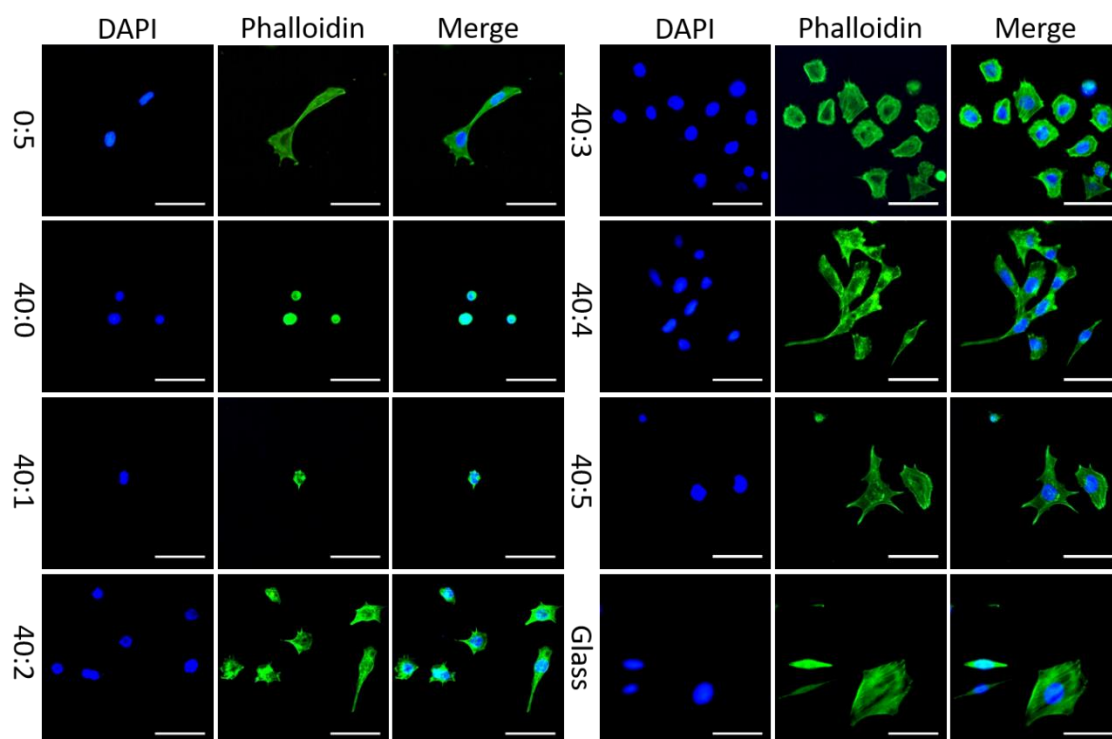


Figure 3-5 Fluorescence images of PC12 neuronal cells attached to various RSF/I₃QGK coated surfaces (blue: DAPI staining for nucleus, and green: phalloidin staining for F-actin). Scale bars for all images = 50 μ m.

AFM was used to further characterize the morphology of the PC12 neuronal cells adhered to the different RSF/I₃QGK coated substrates (Figure 3-6 A and E; Figure 3-7 A and B). On 5 mg/mL I₃QGK coated glass, cell spread out on the glass surface (Figure 3-6 A (a)). However, as shown in Figure 3-6 A (b), cells attached to the pure RSF (40 mg/mL) substrate did not spread out, while cells on I₃QGK coated on RSF samples (Figure 3-6 A (c)-(g)) started to spread and become elongated onto RSF/I₃QGK coated scaffolds. The process of cell adhesion on a polymer surface can be divided into three phases.^{494, 538} Cell attachment on pure RSF coated substrate corresponds to phase I, passive cell

adhesion. In phase I, cells adhere on coated substrate by physicochemical interactions, including van der Waals, hydrophobic and coulombic forces, and can easily detach.⁵³⁹ While on the I₃Q GK coated RSF substrates, cells have interactions with the positively charged lysine residues as active adhesion. At different concentration ratios (40:1; 40:2; 40:3 and 40:4) of RSF/I₃Q GK coated substrates, cells started to spread and become flattened due to integrin binding, which is considered as phase II. At a concentration ratio of 40:5 (RSF/I₃Q GK) cells were fully spread and the cytoskeleton was organized to form focal adhesion, which is known as phase III. Therefore, RSF/I₃Q GK coated scaffolds possess highly cell-adhesive properties. With the increasing concentration of I₃Q GK used for coating, cells attachment to the substrate surfaces was enhanced.

The average cell height and size on the different RSF/I₃Q GK coated substrates were analysed to further investigate the cell adhesion and spreading (Figure 3-6 B and C). A steady decrease of the cell height was observed while increasing the peptide concentration for coating. The average height of the cells on RSF coated surface was found around 1800 ± 80 nm while on the 4-5 mg/mL I₃Q GK coated substrates the average height was found only 450 ± 40 nm (Figure 3-6 B, ****p < 0.0001), which is very similar to (but slight lower than) that on silicon wafer surfaces. In contrast, the average cell size (footprint) increased gradually with increasing peptide concentration and up to an 8 folds increase was observed at 5 mg/mL (Figure 3-6 C, ****p < 0.0001). The variance of average cell size was high on the 5 mg/mL I₃Q GK coated glass and silicon wafer surfaces, indicating the poor uniformity on these surfaces. These results illustrate I₃Q GK coated substrates show a better cellular adhesion and spreading than the RSF (40 mg/mL) coated substrates, indicating I₃Q GK is an excellent biomaterial for PC12 cell growth.

The morphology of a typical neuron cell (Figure 3-6 D) includes a nucleus, dendrites, axon and axon terminal buttons.⁵⁴⁰ To further investigate the structure of neurites, the areas within the red boxes on Figure 3-6 A were scanned by AFM and shown in Figure 3-6 E. It can be seen from the enlarged AFM morphology images that dendrites were not well spread on silicon wafer, 0:5 and 40:0 surfaces. In contrast, when increasing the peptide concentration

from 1-5 mg/mL for the coating, enhanced neurite growth was observed. Terminal buttons can be clearly seen in [Figure 3-6 E \(e\) – \(g\)](#). Increasing the I₃QGK concentration for coating resulted in increased length of axons as well as the increased size of the terminal buttons. These results comparable to those that use ECM proteins such as collagen for neuron patterning, in which neurite outgrowth was observed due to the interaction of collagen with the cell surface integrins.⁴⁹³ The close proximity of the axon terminal buttons gives great potential to conduct electrical signals to another axon by a nerve synapse response. Although cells adhered on glass and silicon wafer surfaces ([Figure 3-6 E \(a\) and \(h\)](#)) had long axons, terminal buttons were not observed. And neurites adhered onto silicon wafers appeared very unhealthy ([Figure 3-6 E \(h\)](#)). These results strongly indicate that I₃QGK can promote neurite formation. These results are consistent with previously work⁵³⁰ that I₃QGK nanofibers showed excellent biocompatibility (similar to collagen) and can facilitate rapid and effective hemostasis by gelling the blood and promoting platelet adhesion. It is likely that I₃QGK nanofibers provide a suitable niche for cell attachment and spreading. The amino groups in the peptides serve as ligands for cell surface interactions, similar to that in RGD and poly(L)-lysine.⁵⁴¹ It has been shown that the slope, density and affinity of ligand all had significant effect to the cell attachment and migration.⁵⁴¹ The surfaces coated with different concentrations of I₃QGK therefore had different effects to PC12 cell attachment and spreading and subsequently affected the development of neuronal phenotype.

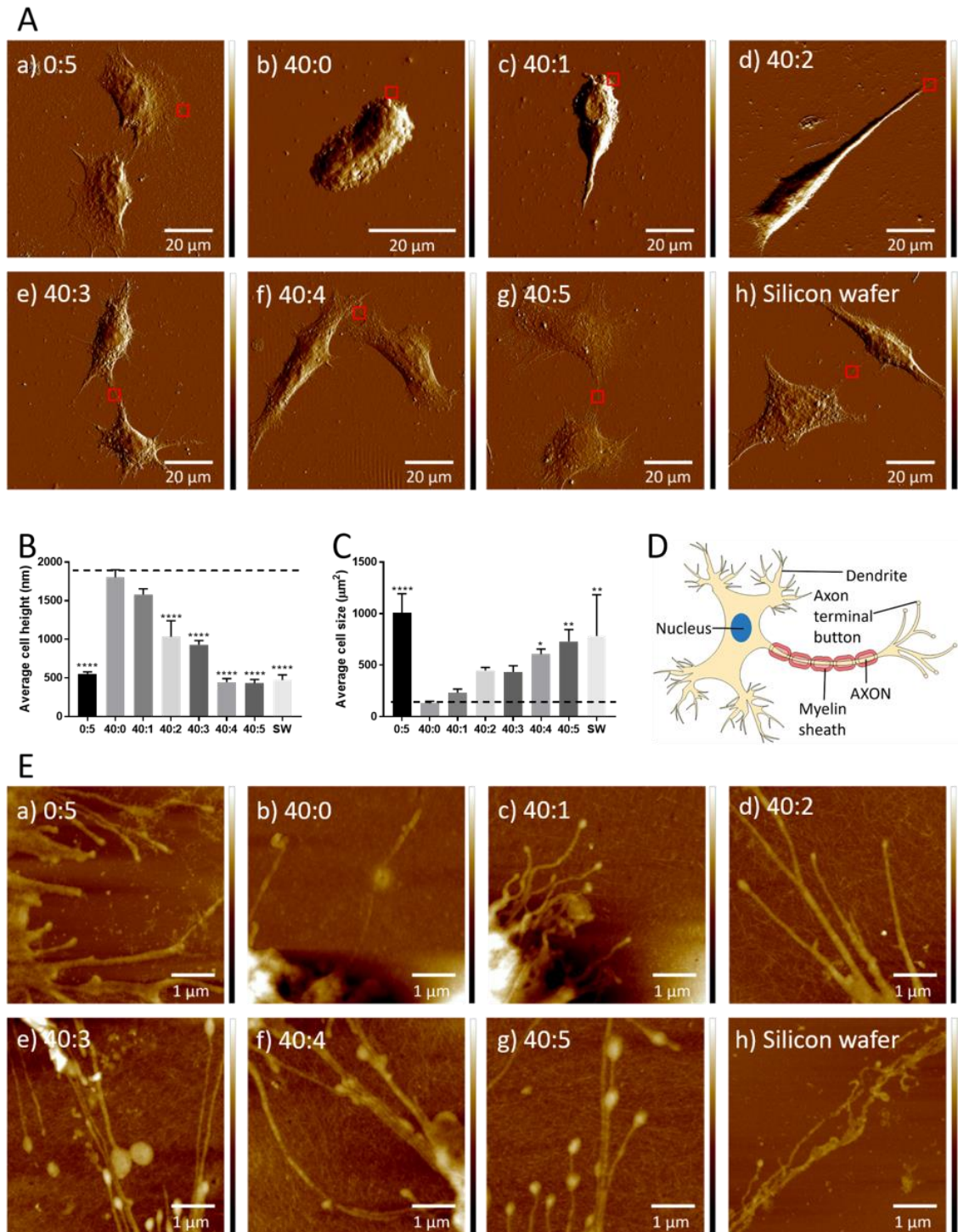


Figure 3-6 **A**, AFM peakforce images of PC12 neuronal cells attached to different concentrations of RSF/I₃QGK coated substrates. The concentration ratios of RSF and I₃QGK were: (a) 0:5, (b) 40:0, (c) 40:1, (d) 40:2, (e) 40:3, (f) 40:4, (g) 40:5 and (h) bare silicon wafer. The force setpoint constant was 30 nN in all images. The areas indicated by the red boxes were scanned and are shown in **E**. Average cell height and size of PC12 cells on various coated samples are shown in **B** and **C**, where 'SW' denotes the bare silicon wafer surface. All values were compared to RSF (40 mg/mL) coated surfaces. ($n \geq 3$; **** $p < 0.0001$; ** $p < 0.01$; * $p < 0.05$).

D, a schematic shows representative morphology of a typical neuron cell. E, AFM topographical images ($25 \mu\text{m}^2$) of the red box areas shown in Figure 3-6 A. The Z scale (height) bars are 150 nm for all images.

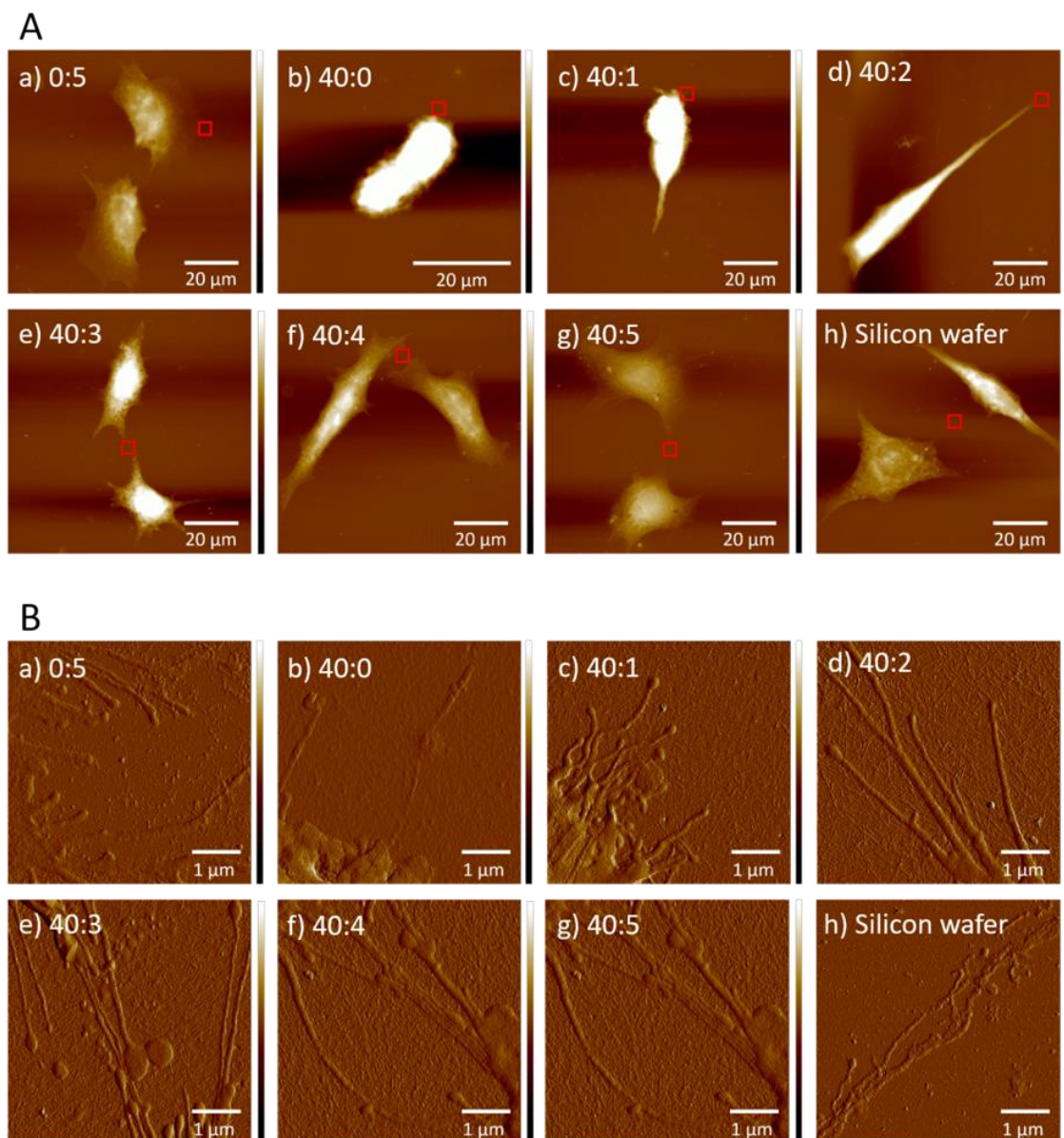


Figure 3-7 A, AFM height images of PC12 neuronal cells attached on different concentrations of RSF/I₃QGK coated surfaces. The concentration ratios of RSF and I₃QGK were: (a) 0:5, (b) 40:0, (c) 40:1, (d) 40:2, (e) 40:3, (f) 40:4, (g) 40:5 and (h) bare silicon wafer. The Z scale (height) bars = 1.5 μm for all images. The peak force images of the areas in the red boxes were enlarged and shown in B. The force setpoint constant was 5 nN for all images.

3.3.5. PC12 neuronal cell alignment to micro-patterns produced by inkjet printing

Neuronal cell alignment plays an essential role in axonal regeneration and is a key aspect of nerve tissue engineering.^{542, 543} Inkjet printing is an emerging technology that can be used to micro-pattern biological materials in a non-contact fashion therefore, has been employed here to pattern the peptide nanofibers onto RSF coated substrates.^{100, 150, 544, 545} The printed peptides in each layer were uniform at the middle of the droplet footprint. Peptide fibres fully covered the silk substrate (40 mg/mL) after 1 layer printing with an ink concentration at 3 mg/mL (Figure 3-8), which is similar with previous results (Figure 3-3 e). However, the height of each layer on the edge was higher than that in the middle. This is because of the 'coffee ring effect' of the inkjet printing process that lead more peptide fibres accumulated on the edge of each footprint.⁵⁴⁶ Increase the number of layers resulted in rougher surface in the middle and higher edges (Figure 3-8). PC12 cells showed better attachment on the edge of the printed patterns. (Figure 3-9 a and b).

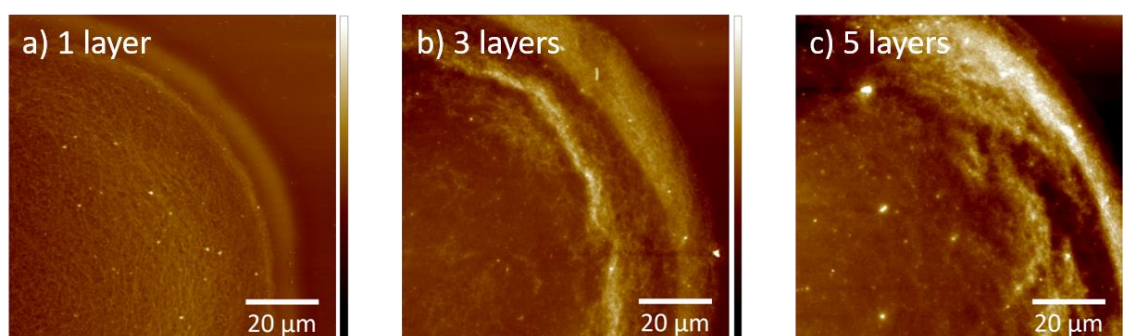


Figure 3-8 AFM topography images indicate peptide I₃QGK droplets (3 mg/ml) were printed at (a) 1 layer, (b) 3 layers and (c) 5 layers on silk substrates (40 mg/ml). These images indicated the “coffee stain effect” of inkjet printing leads more self-assembled nanofibers at the borders. It means the concentration of I₃QGK located in border higher than that in the middle. The Z scale bar for all images is 500 nm.

Peptide lines (Figure 3-9) and more complex structures such as the University of Sheffield logo (Figure 3-11) were fabricated by inkjet printing of I₃QGK (3 mg/mL) nanofibers onto RSF (40 mg/mL) coated substrates. As was demonstrated in Figure 3-9, PC12 cells only grew along the printed patterns. With increasing layers, the number of cells attached to printed lines increased

(Figure 3-10). This indicates PC12 cells proliferation and attachment onto I₃QGK substrates depends on the amount of peptide nanofibers adhered to the surface. The alignment of cells play a dominant role in cell differentiation, cellular microenvironment and cell-cell interactions and therefore, micro-patterning of cells via inkjet printing of peptides may provide a useful tool for future studies of neuronal cell behaviour such as axonal development.^{543, 544, 547} The live/dead assay (Figure 3-4) has demonstrated that the PC12 on the peptide nanofibers showed excellent viability, comparable to that on gelatin methacrylate (GelMA) scaffold.⁵⁴⁸ GelMA contains cell recognized peptide RGD, and has been widely used as 3D hydrogel scaffolds in tissue engineering. Recently, Ye *et al.*⁵⁴⁸ reported GelMA scaffolds fabricated by 3D printing can be used as nerve guidance conduits (NGC) whose aim are regenerate large-gap nerve injuries. Here, peptide I₃QGK has also shown excellent neuronal cell compatibility. Therefore, it has a great potential to be used in the fabrication of NGC in future.

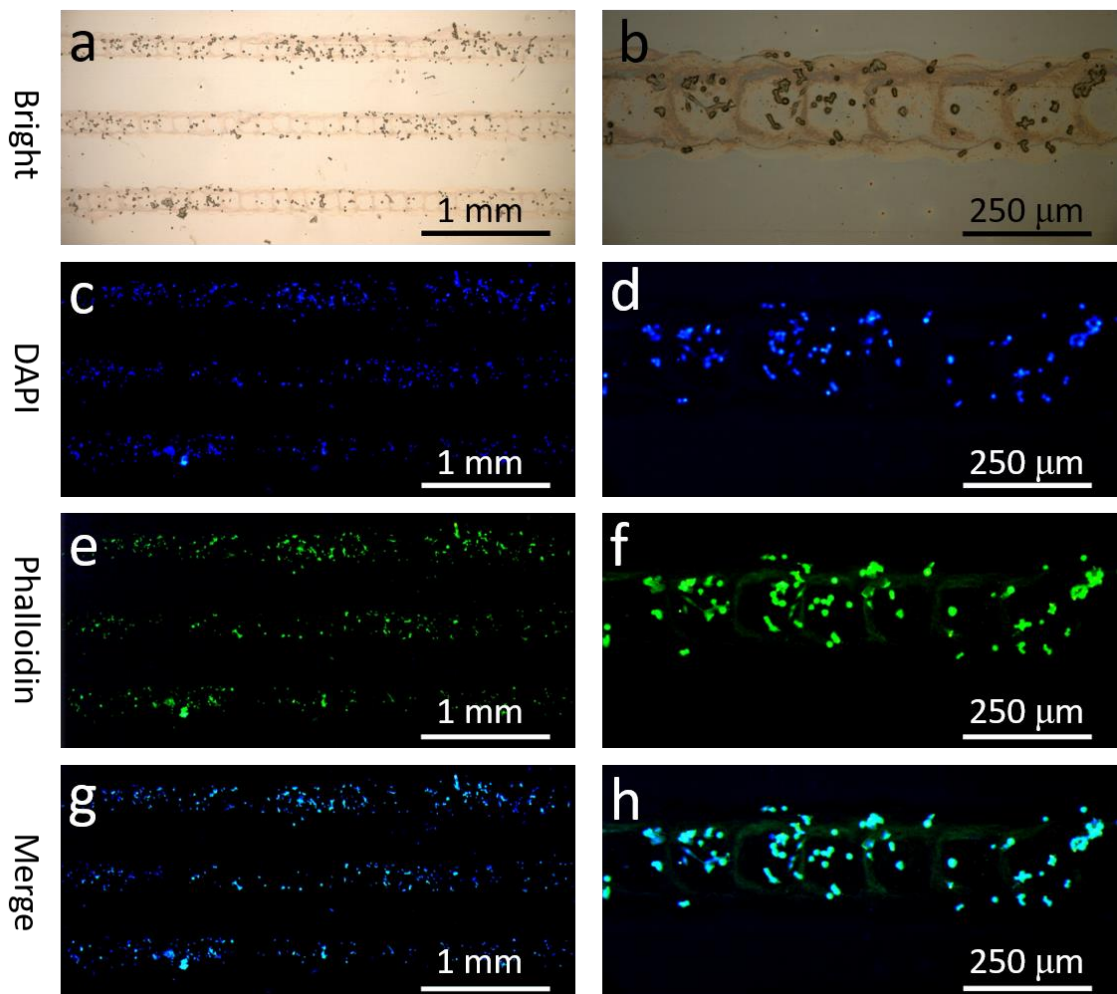


Figure 3-9 Inkjet printing of I₃QGK peptide lines (5 layers) on RSF (40 mg/mL) coated surfaces. PC12 neuronal cells only attached on the printed lines. (a & b) Bright-field microscopy images of printed lines. (c & d) Fluorescent micrographs of PC12 cells on printed lines (DAPI staining of nuclei). (e & f) Phalloidin staining of F-actin. (g & h) are the merged images of c & e, and f & h. For all images, lines were printed with 5 layers of peptides. Scale bars = 1 mm for a, c, e and g and 250 μm for b, d, f and h.

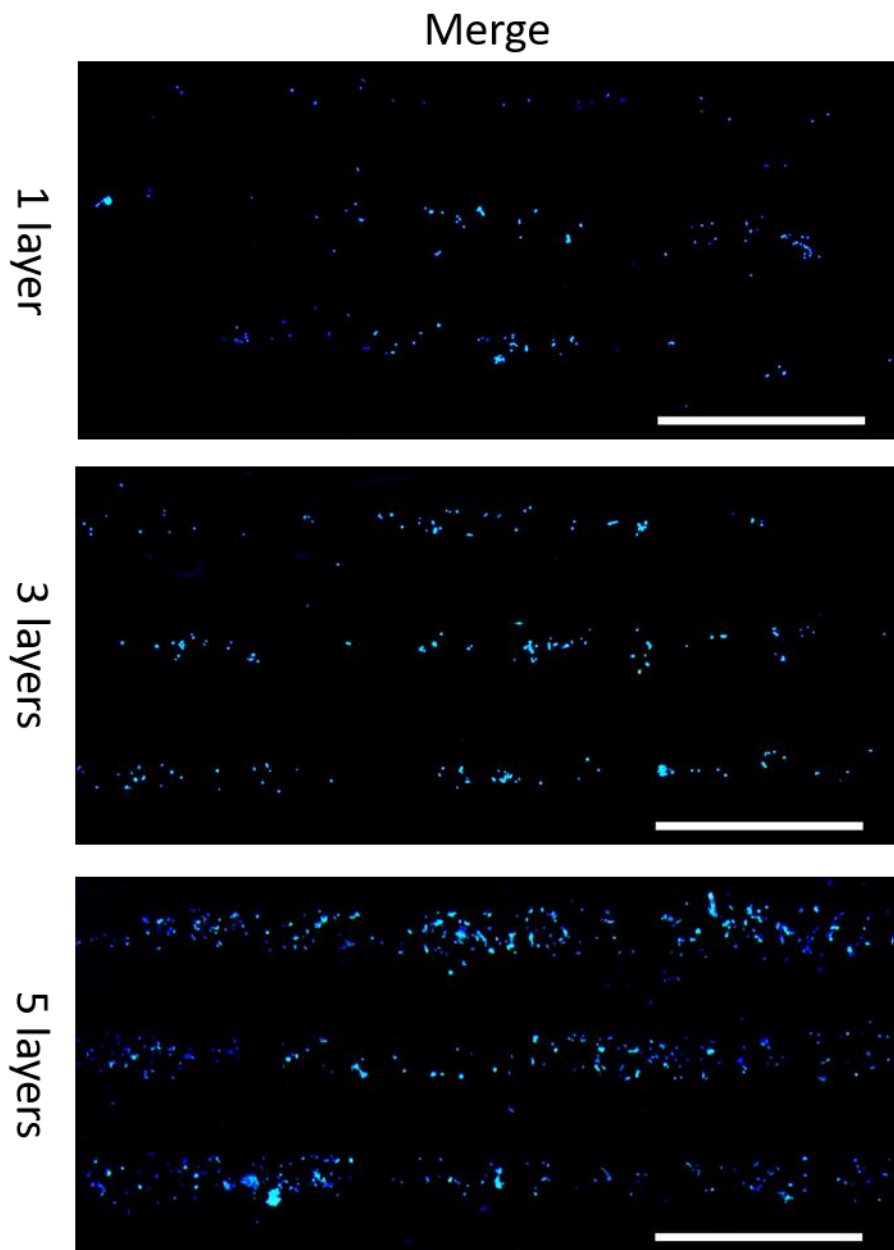


Figure 3-10 Fluorescence microscopy images of PC12 neuronal cells growing along the I₃QGK (3 mg/mL) printed lines on silk substrates (40 mg/ml). Lines were printed with varying layers (1, 3, 5 layers). Scale bars = 1 mm. Images were stained by DAPI and Phalloidin-FITC.

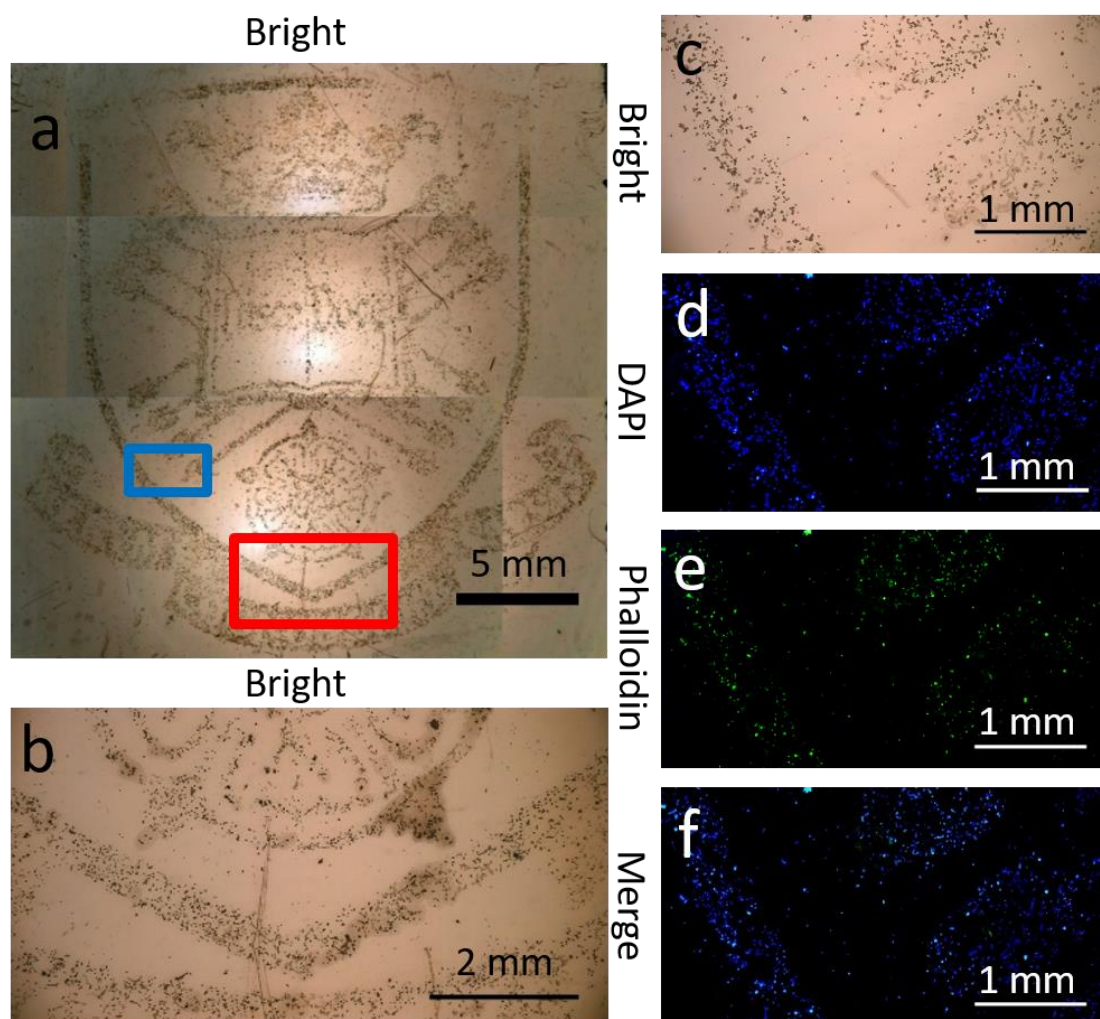


Figure 3-11 (a) Inkjet-printed University of Sheffield logo (on RSF a coated glass surface) using I₃QGK peptide ink, with PC12 neuronal cells growing along the printed pattern. The red and blue box areas are shown in (b) and (c), respectively. Fluorescence microscopy images of the printed logo: (d) DAPI staining for nuclei. (e) Phalloidin staining of F-actin. (f) The merged images of (d) and (e). The logo was printed with 1 layer of peptide (3 mg/mL).

3.3.6. NG108-15 neuronal cells growth on RSF/I₃QGK scaffolds

NG108-15 is a hybrid cell line, obtained from the fusion of mouse neuroblastoma and rat glioma, which can mimic the process of neuronal differentiation for *in-vitro* studies.⁵⁴⁹ RSF and I₃QGK were alternately coated onto glass slides which can also be used as scaffolds for cell culture with NG108-15 neuronal cells. The surface characterization of different ratios of RSF and I₃QGK are shown in [Figure 3-12](#). Comparing RSF/I₃QGK scaffolds used for PC12 cells, RSF/I₃QGK scaffolds for NG108-15 neuronal cells were prepared in different way. Firstly, the spin coating order was changed to RSF solution,

peptide deposition and then ethanol. In addition, the layers of RSF/I₃Q GK deposited were changed from one to two layers. The concentration ratios of RSF and I₃Q GK were also changed. However, the overall tendency where greater amounts of nanofibers resulted in better cell growth was similar to the previous results obtained from RSF/I₃Q GK scaffolds for PC12 cells (Figure 3-3).

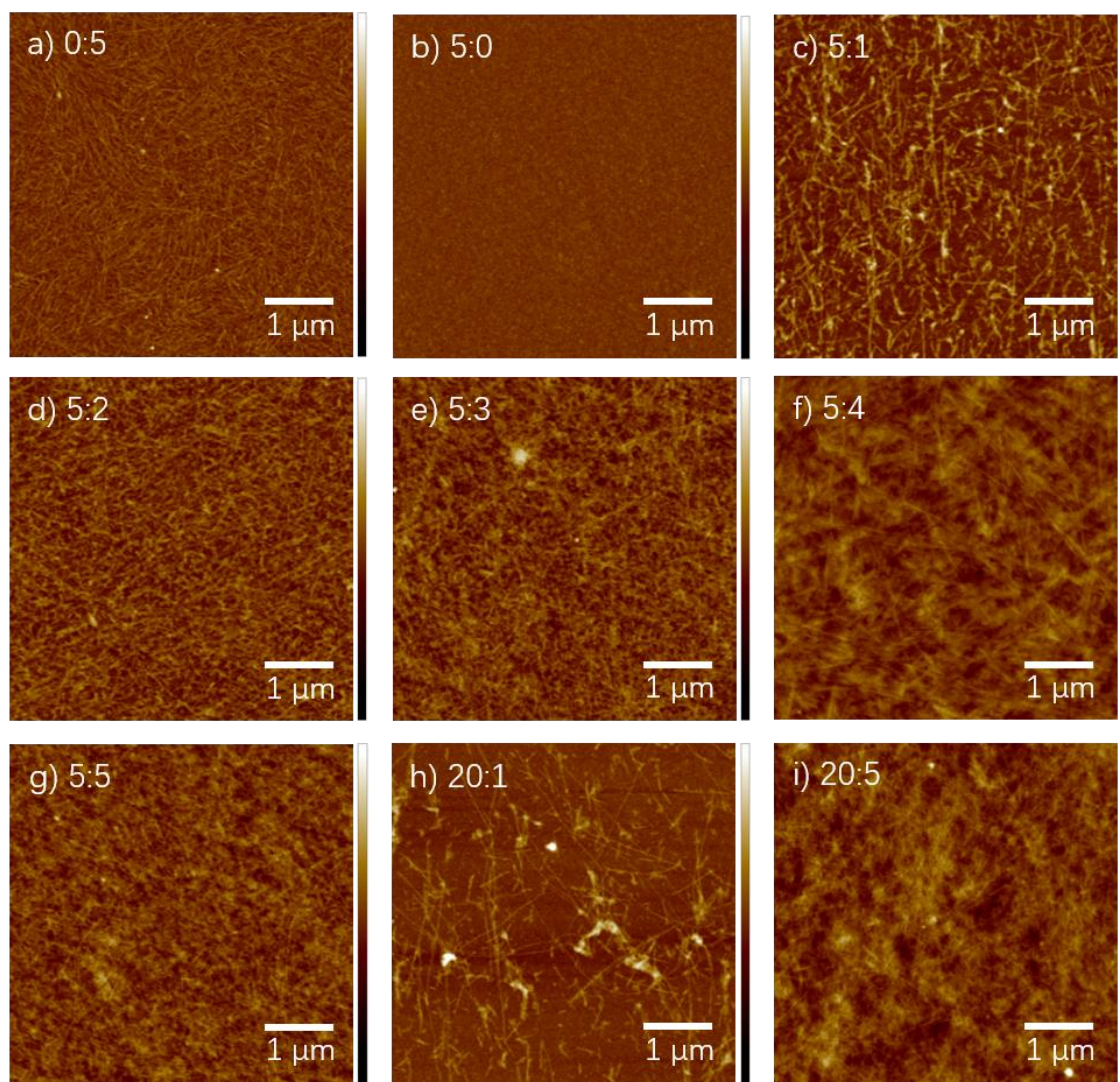


Figure 3-12 AFM topographical images ($25 \mu\text{m}^2$) of RSF/I₃Q GK scaffolds (2-layers). RSF/I₃Q GK scaffolds coated at different ratios: (a) 0:5 (only peptide), (b) 5:0 (only RSF), (c) 5:1, (d) 5:2, (e) 5:3, (f) 5:4, (g) 5:5, and (h) 20:1. (i) 20:5. Note that, the spin coating order was changed to RSF solution, peptide and ethanol respectively. The Z scales (height) of all images are 60 nm.

NG108-15 neuronal cells were cultured on 1 cm^2 spin coated glass samples for 2 days in growth media and 4 days in serum free media. Before staining, cells were imaged under a light microscope, as shown in Figure 3-13. Subsequently, dual fluorescent dyes, consistent of DAPI and Phalloidin, were used to stain nuclei and F-actin of cells (Figure 3-14). This enabled a visualisation of the

degree of morphology of cell adhesion on the RSF/I₃QGK scaffolds. I₃QGK scaffolds showed good cell attachment, but the number of cells present was low. This is assumed to be the case due to a low number of β -sheet structures present in the peptide and thus they were easily washed off during cell culture (Figure 3-14 A (a)). Although NG108-15 cells showed an excellent cell attachment on RSF scaffolds in Figure 3-13 (b), they were present in clusters most of them detached from the scaffold. The cells easily detached during the staining process meaning that NG108-15 cells showed poor attachment on RSF scaffolds (Figure 3-14 A (b)). For scaffolds containing RSF and I₃QGK, increasing the peptide concentration resulted in more cells uniformly adhering onto the surface (Figure 3-14 A (c)-(d)). At a ratio of 5:4 (RSF/ I₃QGK), the cells fully covered the surface however had a tendency to detach (Figure 3-14 A (e)). This is assumed to be the case due to the concentration of I₃QGK being too high resulting in the stacking of nanofibers. The cells adhered and proliferated onto the stacked nanofibers. This in turn led to cells detaching easily during cell culture. Therefore, at concentrations of 5:5 (RSF/ I₃QGK), there were more places without cells adhered to the surface (Figure 3-14 A (f)). Comparison of the concentration ratios of RSF and I₃QGK at 5:1 and 20:1, showed that at increased concentrations of RSF the number of attached cells increased (Figure 3-14 A (c) and (h)). Comparison of the concentration ratios of RSF and I₃QGK at 5:5 and 20:5, the places without cells decreased (Figure 3-14 A (g) and (i)). This gives evidence that the increasing the RSF concentration leads to a cell attachment increase for RSF/I₃QGK scaffolds. This result is different to that obtained from RSF/I₃QGK scaffolds (1 layer) for PC12 cells, where high concentrations of RSF resulted in poor neuronal cell attachment. There are two assumptions can be postulated: 1) as the concentration of RSF is increased, the charge-charge interactions between negatively RSF and positively charged I₃QGK becomes stronger, resulting in nanofibers being adhered on the RSF surface. 2) RSF/I₃QGK scaffolds for NG108-15 neuronal cells are coated with 2 layers, which means that both sides of the second layer of the RSF scaffold are coated with I₃QGK. This is mostly likely to make positive influences on neuronal cell attachment. In addition, as shown by the results in Figure 3-13, neurite outgrowth can be observed, with the exception of pure RSF scaffolds (Figure 3-13 (b)). From this we can deduce that I₃QGK enhances neurite regeneration

of NG108-15 neuronal cells. However, unfortunately the Phalloidin fluorescent dye did not stain the F-actin of cells properly so no neurite could be observed, see [Figure 3-14 B](#). Therefore, for future experiments the Phalloidin fluorescent dye should be replaced by another fluorescent dye that are able to stain neurites. For example, the indirect immunofluorescence technique can be applied, which introduces a mouse anti- β III-tubulin (neurite marker) antibody and a Texas Red-conjugated anti-mouse IgG antibody into cells.

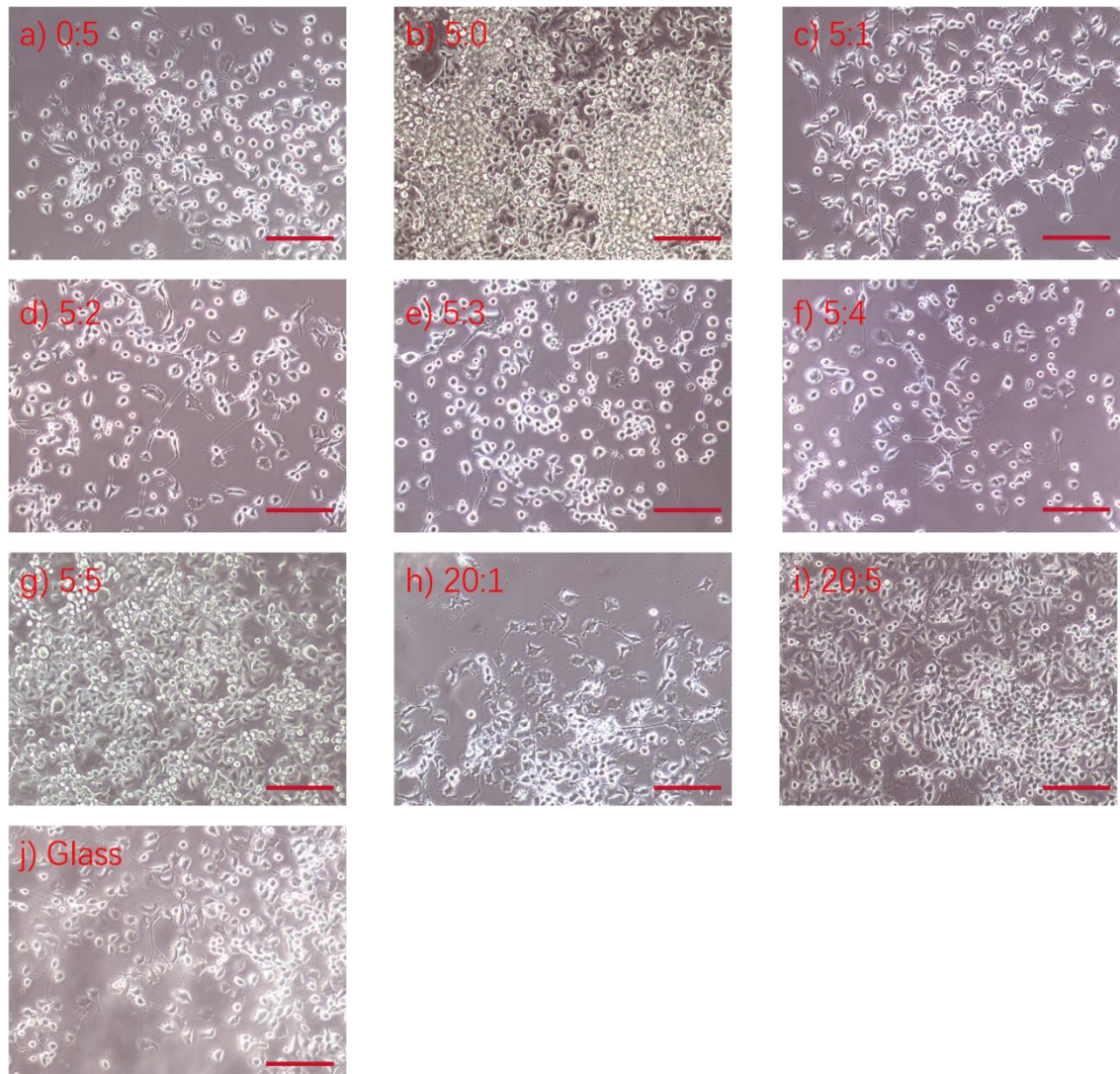


Figure 3-13 The light microscope images of NG108-15 cells adhesion on RSF/I₃QGK scaffolds (2-layers). The concentration ratios between RSF and I₃QGK are (a) 0:5, (b) 5:0, (c) 5:1, (d) 5:2, (e) 5:3, (f) 5:4, (g) 5:5, (h) 20:1, (i) 20:5 and (j) glass. The scale bar is 200 μ m as indicated.

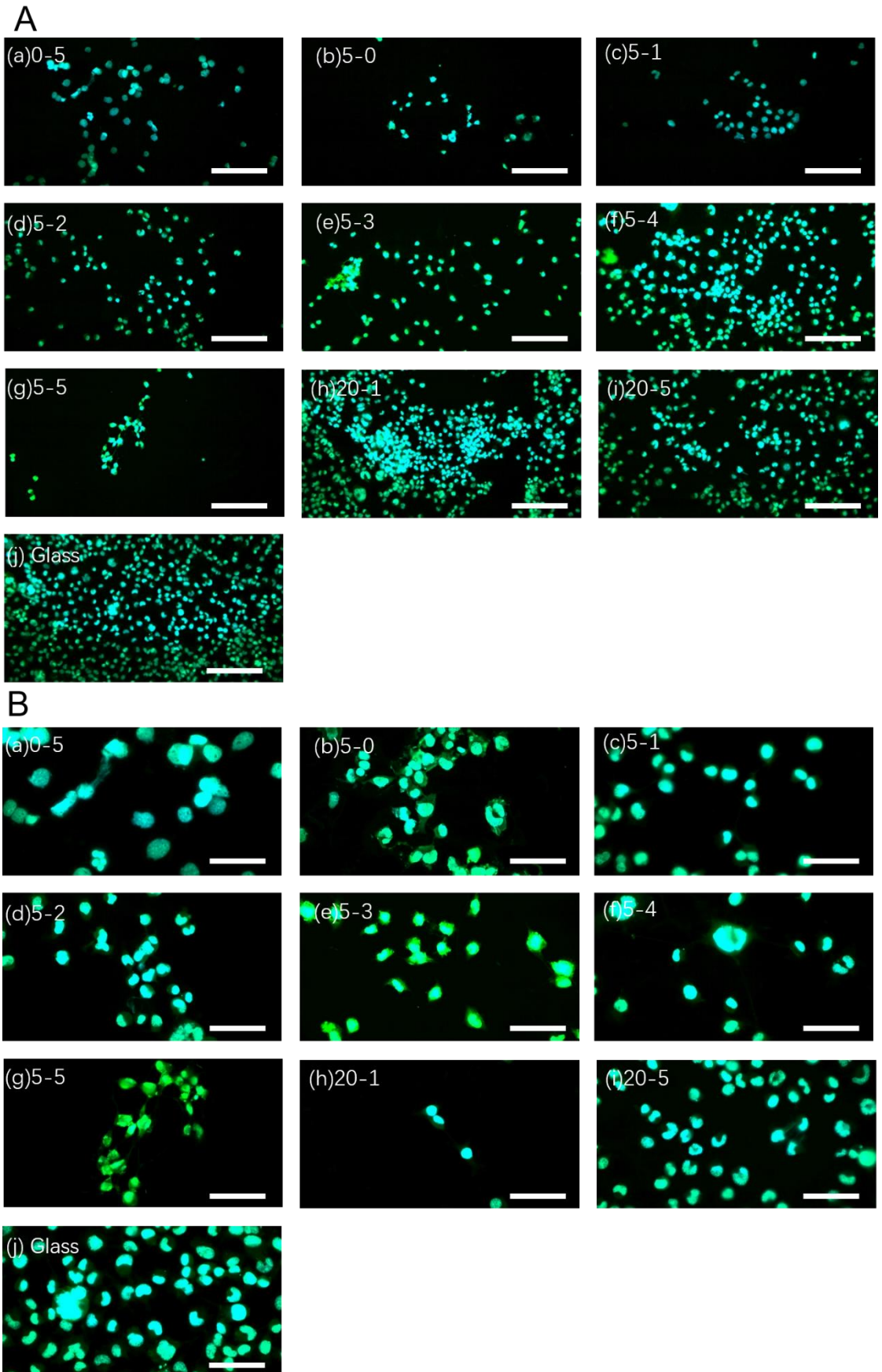


Figure 3-14 A and B show fluorescent microscope images of NG108-15 cells adhesion on RSF/I₃QGK scaffolds (2-layers). They showed the cell number and morphology of NG108-15

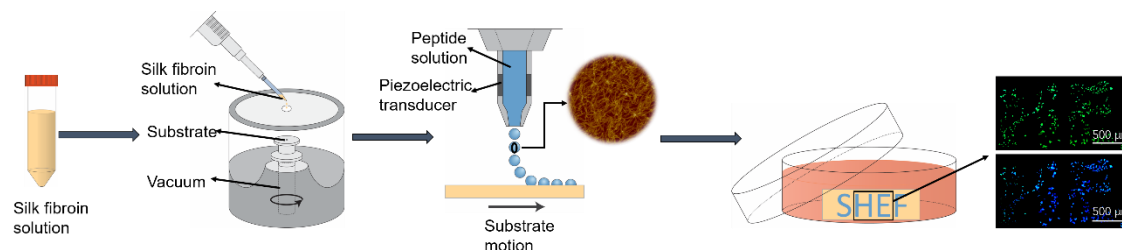
cells on RSF/I₃QGK scaffolds (2-layers). The concentration ratios between RSF and I₃QGK are (a) 0:5, (b) 5:0, (c) 5:1, (d) 5:2, (e) 5:3, (f) 5:4, (g) 5:5, (h) 20:1, (i) 20:5 and (j) glass. (Blue: DAPI staining for nucleus, and green: phalloidin staining for F-actin). The scale bar of A is 300 μm and B is 120 μm as indicated.

3. 4. Conclusions

In summary, the synthetic peptide I₃QGK can dynamically self-assemble into nanofibers, which can be coated or printed onto RSF scaffolds via charge-charge interactions and improve neuronal cell attachment and differentiation as well as neurite outgrowth. The concentration of the I₃QGK used for coating (which affect the nanofiber coverage) has a significant effect to cell attachment and morphology. We find concentrations between 3-4 mg/mL coated on RSF substrates to be the ideal condition for PC12 neuronal cells with best attachment and proliferation. More importantly, it can be used to guide axonal regeneration and promote the growth of axon terminal buttons. In addition, I₃QGK and RSF exhibit low cytotoxicity against PC12 neuronal cells. Inkjet printing is capable of depositing functional peptide nanofiber inks into complex patterns and facilitating cell alignment for tissue engineering applications⁵⁵⁰, providing a way for further analysis of *in vitro* cellular functions⁵⁵¹ such as axonal development.

4. Cell Guidance on Peptide Micropatterned Silk Fibroin Scaffolds

Abstract



Guiding neuronal cell growth is desirable for neural tissue engineering but is very challenging. In this work, a self-assembling ultra-short surfactant-like peptide I₃K which possesses positively charged lysine head groups, and hydrophobic isoleucine tails, was chosen to investigate its potential for guiding neuronal cell growth. The peptides were able to self-assemble into nanofibrous structures and interact strongly with silk fibroin (SF) scaffolds, providing a niche for neural cell attachment and proliferation. SF is an excellent biomaterial for tissue engineering. However neuronal cells, such as rat PC12 cells, showed poor attachment on pure regenerated SF (RSF) scaffold surfaces. Patterning of I₃K peptide nanofibers on RSF surfaces significantly improved cellular attachment, cellular density, as well as morphology of PC12 cells. The live / dead assay confirmed that RSF and I₃K have negligible cytotoxicity against PC12 cells. Atomic force microscopy (AFM) was used to image the topography and neurite formation of PC12 cells, where results revealed that self-assembled I₃K nanofibers can support the formation of PC12 cell neurites. Immunolabelling also demonstrated that coating of I₃K nanofibers onto the RSF surfaces not only increased the percentage of cells that bore neurites but also increased the average maximum neurite length. Therefore, the peptide I₃K could be used as an alternative to poly-L-lysine for cell culture and tissue engineering applications. As micro-patterning of neural cells to guide neurite growth is important for developing nerve tissue engineering scaffolds, inkjet printing was used to pattern self-assembled I₃K peptide nanofibers on RSF surfaces for directional control of PC12 cell growth. The results demonstrated that inkjet-printed peptide

micro-patterns can effectively guide the cell alignment and organization on RSF scaffold surfaces, providing great potential for nerve regeneration applications.

Keywords: Nerve tissue engineering, micro-patterning, inkjet printing, self-assembling peptides, PC12 cells

4. 1. Introduction

The human nervous system is composed of the central nervous system (CNS) and the peripheral nervous system (PNS), which can be easily impaired by injuries, such as trauma and car accidents, as well as diseases, including Alzheimer's disease, Parkinson's disease, strokes and brain tumours.^{1, 552, 553} Although the CNS lacks self-healing ability, the PNS does have regeneration capabilities but regeneration of both damaged CNS and PNS is a big challenge in tissue engineering.^{1, 554, 555} It is therefore vitally important to develop well-defined functional scaffolds for nerve tissue regeneration to help guide neural cell attachment, alignment, spreading and proliferation.⁵⁵⁶⁻⁵⁵⁸

In addition to the above, alignment and interconnection of neuronal cells *in vitro* allows the mimicking of real neuronal architectures *in vivo* and help in understanding the underlying mechanisms needed to promote accelerate nerve tissue regeneration of damaged neural tissue. Micro-patterning technology, which has already attracted significant attention, can enable the geometric control of neuronal cell alignment.⁵⁵⁹⁻⁵⁶² Lithography, including ultraviolet lithography (UVL), soft lithography (SL) and electron-beam lithography (EBL), is a traditional technology for micro-patterning proteins onto substrates.^{20, 147} Compared to UVL and EBL, SL is a convenient technique,¹⁴⁶ which has been widely used to micro-pattern neuronal cells.^{559, 560, 562} For example, micro-patterned polydimethylsiloxane (PDMS) has been shown to enhance the attachment, alignment, spreading, proliferation, neurite formation and elongation of neuronal cells.⁵⁶² However, SL needs to be operated in a high-standard clean room, and samples can be easily contaminated during fabrication.^{143, 497} Inkjet printing, on the other hand, is a cost-effective and flexible micro-patterning technique which is capable of patterning complex geometries at high precision.^{20, 147} Moreover, as inkjet printing is a non-contact technique, cross-contamination of the final product is significantly reduced.

Therefore, Inkjet printing was used as a micro-patterning technique to pattern self-assembled peptide nanofibers on regenerated silk fibroin (RSF) surface to guide the growth of neuronal PC12 cells in this study.

Silk fibroin (SF), extracted from *Bombyx mori* (*B. mori*), has received significant attention due to its biocompatibility, tuneable biodegradability, low immunogenicity and excellent mechanical properties.^{23, 563} RSF possesses tuneable rheological properties and can be used to fabricate different types of scaffolds, such as hydrogels,³¹ films⁹⁶ and sponges.³² These scaffolds have been successfully applied in a variety of tissue engineering, such as skin,²¹⁵ vascular⁵⁶⁴ and musculoskeletal tissue engineering to match the different properties of autologous tissues.¹ However, *B. mori* silk lacks the cell adhesive components, such as arginine-glycine-aspartic acid (RGD) sequence, which promotes cell attachment.^{38, 221, 565} Therefore, without the addition of cell adhesive molecules, such as poly-L-lysine (PLL), and extracellular matrix (ECM) components, silk scaffolds normally have poor cell attachment,^{566, 567} which is particularly significant for neuronal cells.⁵⁶⁸

Cell adhesive molecules have been successfully applied as scaffolding materials in nerve tissue engineering.⁵¹⁵ During the last two decades, peptide sequences such as RGD, YIGSR and IKVAV have been used to promote neuronal cell attachment, proliferation, and neurite outgrowth.^{518, 519} Self-assembled peptide nanofibers are novel biomaterials that can be fabricated through bottom-up approach and have the potential to be used as scaffold materials for tissue engineering.^{250, 284} For example, surfactant-like peptide AC-I₃K-NH₂ (I₃K) has an acetyl group on its N terminal and its C terminal was blocked by an amine group. Three hydrophobic isoleucine (Ile or I) and one hydrophilic lysine residue (Lys or K) causes the peptide to possess the surfactant feature and promote the self-assembly of I₃K into long and uniform nanofibers in aqueous solutions.^{299, 300} Positively charged PLL has been shown to promote neuronal cells attachment.⁵⁶⁹ Therefore, it is anticipated that the self-assembled I₃K peptide nanofibers also have great potential as a cell adhesive matrix for nerve tissue regeneration.

In this study, RSF/I₃K peptide scaffolds were fabricated to guide neuronal cell attachment. The coating and patterning of peptide nanofibers was achieved

through spin coating and inkjet printing, respectively. The glass/silicon wafer substrates were coated with a layer of negatively charged RSF⁵⁷⁰ before the coating, or printing, of peptide nanofiber solutions. The cationic peptide nanofibers adhered onto the RSF surfaces through charge-charge interactions. Rat pheochromocytoma (PC12) cells were cultured onto RSF/I₃K scaffolds to investigate the effect of the I₃K peptide nanofibers on cell attachment, proliferation and viability. Atomic force microscopy (AFM) was used to further analyse cell morphology, height and footprint on the RSF/I₃K scaffold surfaces.⁵⁷¹

4. 2. Methods

4.2.1. Resazurin assay

Metabolic activity of PC12 cells was assessed after 24, 72, and 144 hours in culture. Culture medium was removed, and samples were cultured in a 100 μ M resazurin salt in PBS, and assay dependent culture media for 4 hours at 37°C and 5% CO₂. Triplicates of 100 μ L, of reduced formazan product, were then transferred to a black 96 well plate and the fluorescence was read in a FLx800 fluorescence plate reader (Biotek Instruments Inc.) at 540/635 nm. Background fluorescence readings were measured and subtracted from results.

4.2.2. Immunostaining of the neurites assay

Neuronal cell differentiation, on samples, was assessed by measuring the lengths of neurites extending from cells. PC12 cells were washed with PBS before cells were fixed with 3.7% (v/v) PFA for 20 minutes at room temperature. Following a PBS wash, cells were permeabilized with 0.1% Triton X-100 for 20 minutes, at room temperature and unreactive binding sites were blocked with 3% bovine serum albumin (BSA) in PBS for 30 minutes. PC12 cells were incubated with a mouse anti- β III-tubulin (neurite marker) antibody (1:250 dilution from Promega, Chilworth, United Kingdom) diluted in 1% BSA in PBS and incubated at 4°C for 24 hours. After a PBS wash, PC12 cells were labelled with Texas Red-conjugated anti-mouse IgG antibody (1:200 dilution in 1% BSA from Vector Labs, Burlingame, USA) in 1% BSA, for 90 minutes at room temperature. Samples were imaged with an upright Zeiss LSM 510 confocal microscope,

using a helium-neon laser (543 nm) for Texas Red excitation ($\lambda_{\text{ex}} = 589 \text{ nm} / \lambda_{\text{em}} = 615 \text{ nm}$). Images were analysed, and neurites were measured using the ruler tool on ImageJ software.

4. 3. Result and discussion

4.3.1. Attachment of PC12 neuronal cells on SF films

RSF scaffolds have been extensively used in tissue engineering applications.²¹⁵ However, pure RSF lacks cell recognized molecules, and therefore, it normally has poor cell attachment.^{38, 221, 565} To investigate the attachment of PC12 neuronal cells on the RSF scaffold surfaces, RSF solutions, at different concentrations, were spin coated onto clean cover glasses or silicon wafers. AFM images (Figure 4-1 A) demonstrated different surface topographies, and consequently cell attachment. The RSF coated glass surfaces (both 5 and 40 mg/mL) showed smooth coated layers (Figure 4-1 A (a-b)) with roughness's at the nanoscale ($0.78 \pm 0.02 \text{ nm}$ and $0.93 \pm 0.01 \text{ nm}$). The RSF scaffolds investigated here showed poor performance in cell attachment and spreading using PC12 neuronal cells (Figure 4-1 A (d-e)). A significant decrease in cell density on the surfaces (Figure 4-1B) was observed using RSF coated glasses both at 5 mg/mL ($9600 \pm 700 \text{ cells/cm}^2$) and 40 mg/mL ($900 \pm 600 \text{ cells/cm}^2$) as substrates compared to clean glass ($21900 \pm 1600 \text{ cells/cm}^2$), which demonstrates that PC12 cells have a low binding efficiency to RSF coated substrates. These results indicate that RSF coatings, in particular at high concentrations, can be used as cell-repellent surfaces for PC12 cells. When combined with cell adhesive moieties, surfaces could be used to pattern PC12 cells, to guild the growth of the cells.

To enhance cell attachment, composite RSF scaffolds have been widely used to facilitate the cell affinity.¹ RSF scaffolds are normally combined with cell recognized molecules such as collagen, gelatin and PLL to enhance cell attachment. For example, gelatin was cross-linked with RSF scaffolds for the repair of cartilage injury *in vitro* and *in vivo*.⁵⁷² The scaffolds not only provided a mechanical protection before neo-cartilage formation, but also a suitable 3D microenvironment for BMSC (endogenic bone marrow stem cells) proliferation, differentiation, and ECM production. RSF scaffolds have also been modified

with RGD sequences through the side groups of aspartic and glutamic acids to improve the cell adhesion.¹ While the previous methods mostly involved chemical modification of the SF material through covalently bonding, here we use the electrostatic interaction of self-assembled cationic peptide nanofibers to enhance cell attachment onto SF scaffolds.

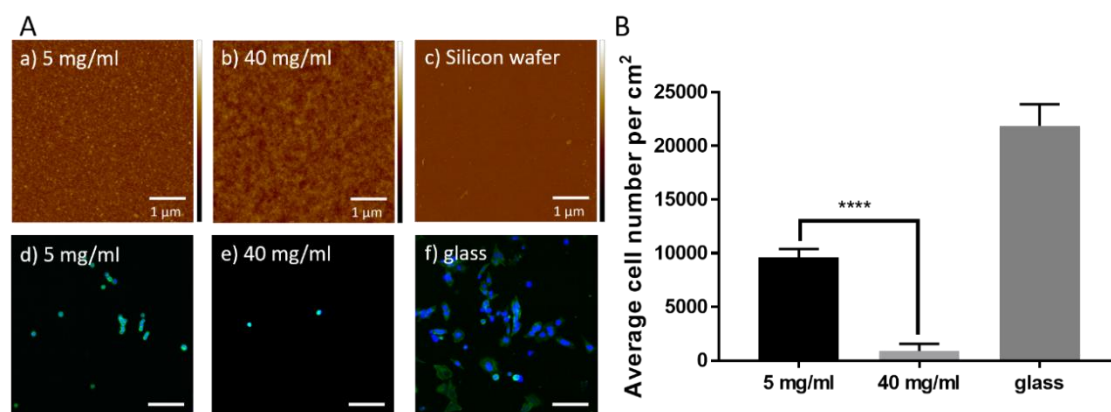


Figure 4-1 **A**, AFM topographical images of RSF coated scaffolds on Si-wafers at (a) 5 mg/mL; (b) 40 mg/mL and (c) bare silicon wafer control, Z scale height = 30 nm. Fluorescence images of PC12 cells attached to (d) 5 mg/mL and (e) 40 mg/mL RSF coated surfaces and (f) glass control. (Blue: DAPI staining for nucleus. Green: FITC-phalloidin staining for F-actin.) Scale bar = 100 μm. **B**, Average cell numbers (per cm²) attached to the RSF coated surfaces at RSF concentrations of 0 (glass control), 5 and 40 mg/mL. $n \geq 3$, **** $p < 0.0001$.

4.3.2. Characterization of RSF/I₃K scaffolds

The peptide I₃K was able to self-assemble into long and uniform nanofibers after two weeks of incubation as previously reported.^{299, 300} According to previous studies²⁹⁹, the self-assembly process of I₃K is a dynamic process via non-covalent interactions. Upon complete dissolution of I₃K molecules, small I₃K fragments form interdigitated bilayers with hydrophobic isoleucine residues kept in the interior, and charged lysine located on the surface of bilayers. Small I₃K fragments then assemble into short stacks through hydrophobic interactions and hydrogen bonding. Subsequently, based on molecular chirality and surface curving, these stacks tend to grow into twisted fibres. Further growth leads to the formation of long and uniform nanofibers. The width of the formed nanofibers was around 50 nm (Figure 4-2) while the length of the nanofibers can reach up to 10 μm. Persistence length is a characteristic length scale that

has been used to determine the conformation of a uniform chain length.⁵⁷³ Cox et al.²⁹⁸ recently measured the contour length (the distance between two ends of I₃K fibres) by AFM and stochastic reconstruction microscopy and then used this value to calculate persistence length of I₃K fibres. Their results indicated that self-assembled I₃K fibres have an average contour length of around 6 μm and persistence length of $10.1 \pm 1.2 \mu\text{m}$.

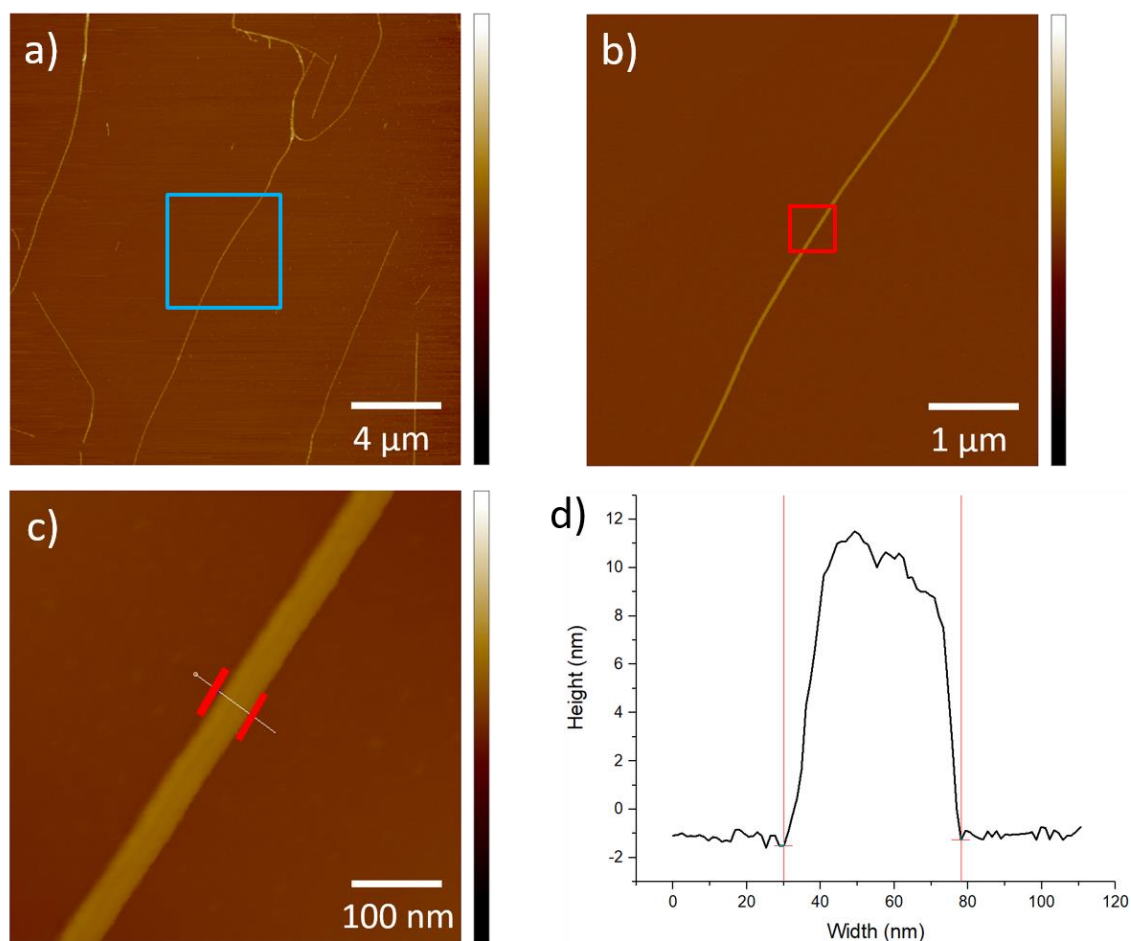


Figure 4-2 AFM topographical images of self-assembled I₃K nanofibers in HEPES buffer (20 mM; pH 6.0) at (a) 1 mg/mL for 2 weeks (20 μm \times 20 μm). The area indicated by the blue and red boxes are shown in (b) (5 μm \times 5 μm) and (c) (500 nm \times 500 nm). The height and width of the cross-section line along a nanofiber are shown in (d). Z scale (height) of all images = 90 nm.

AFM was further used to characterise how concentrations of I₃K affect the surface topography of the I₃K coated RSF scaffolds. As shown in [Figure 4-3 \(a\)](#), only a few self-assembled nanofibers were observed on the 1 mg/mL I₃K coated RSF scaffolds. By increasing the concentration of I₃K, the number of nanofibers increased gradually forming a near full coverage at 3 mg/mL ([Figure 4-3 \(b-c\)](#)). Further increasing the concentration of I₃K resulted in more stacked self-

assembled nanofibers, which can potentially lead to cell detachment during cell culture. No significant difference of surface topography between the multi-material RSF/I₃K scaffold (at concentration ratio 40:5) and I₃K-only scaffold (5 mg/mL coated glass) could be detected. However, I₃K-only scaffolds assembled on blank glass could easily be washed off when immersed in the aqueous solutions due to low adhesion properties to the glass surface (Figure 4-4 and Figure 4-5), hence making it ineffective for cell culture applications. Therefore, the multi-material combination of I₃K and RSF generates a structurally stable scaffold that can easily withstand normal cell culture procedures and thus provides an excellent way to generate peptide-based scaffolds for cell culture applications. The strong adhesion between RSF (negatively charged) and I₃K (positively charged) is a result of the strong electrostatic charge-charge interactions.^{299, 300}

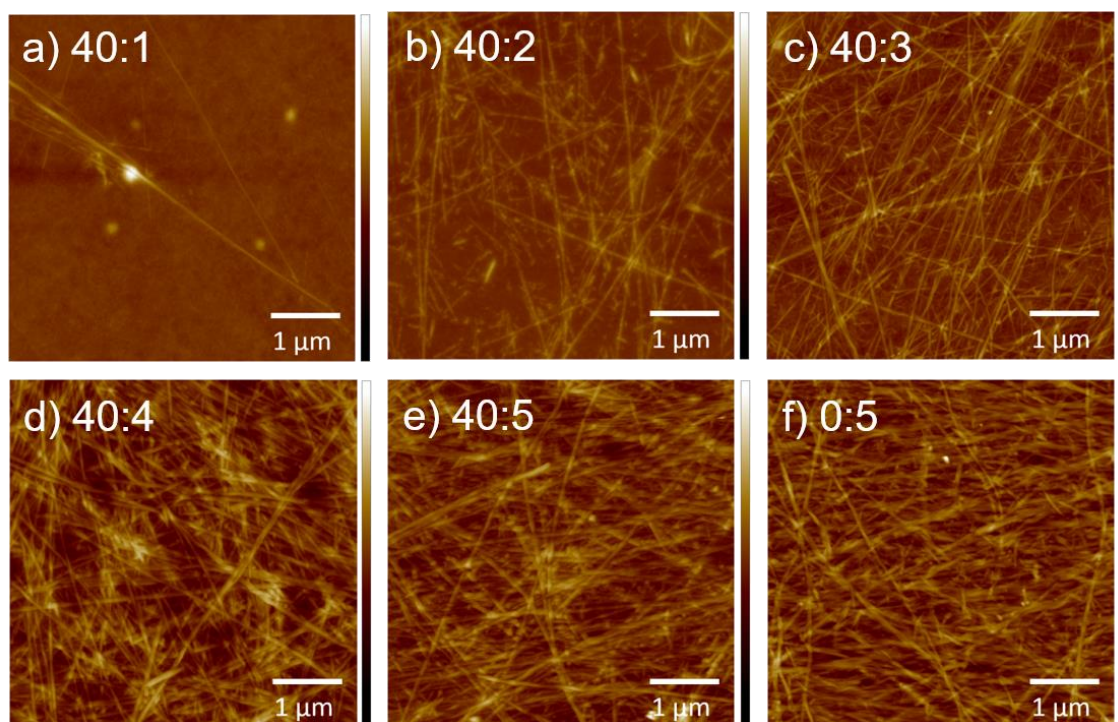


Figure 4-3 AFM topographical images ($25 \mu\text{m}^2$) showing 1-layer RSF/I₃K scaffolds coated at different concentration ratios: (a) 40:1, (b) 40:2, (c) 40:3, (d) 40:4, (e) 40:5, (f) 0:5. The Z scale (height) for all images is 120 nm.

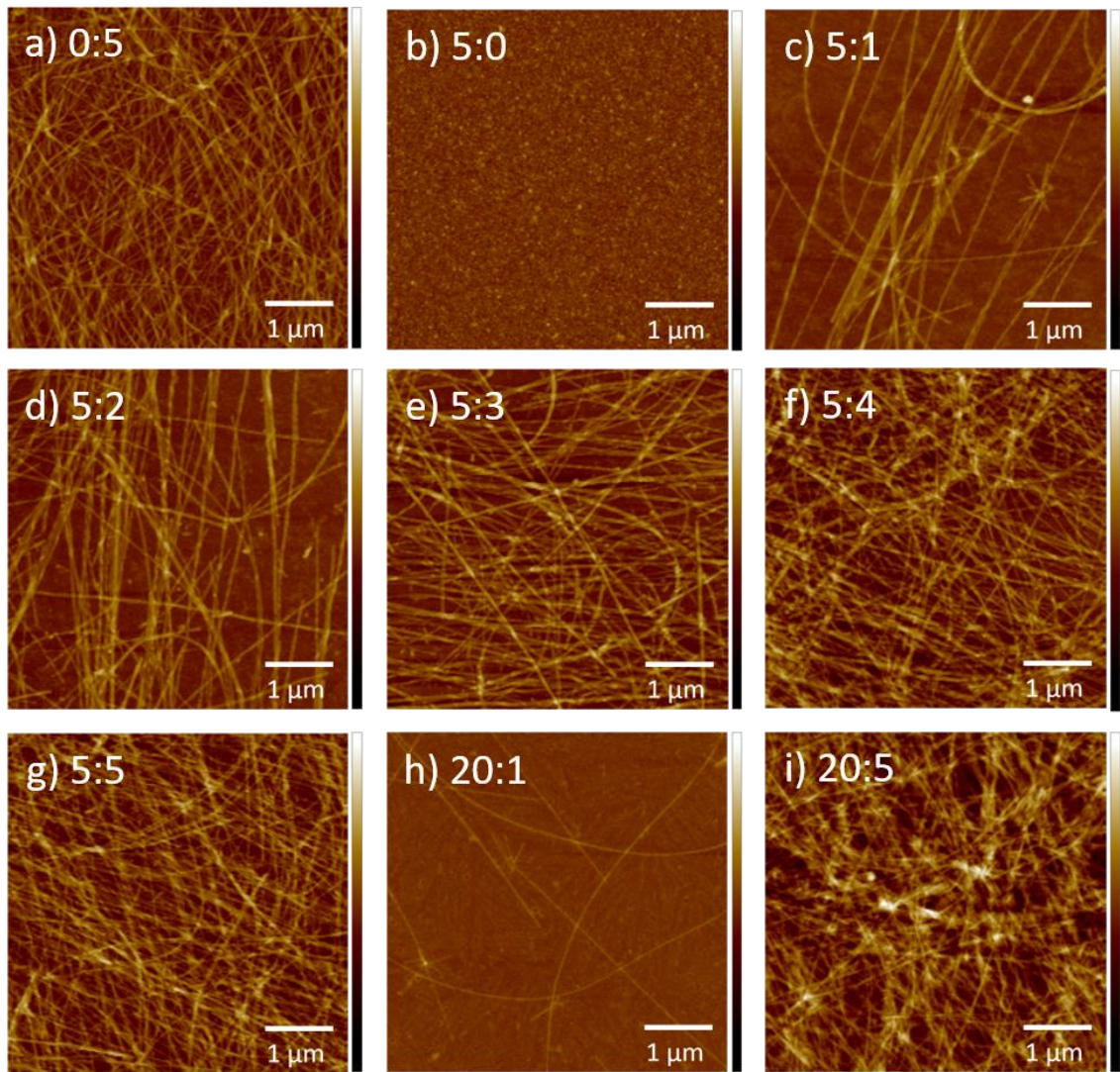


Figure 4-4 AFM topographical images ($25 \mu\text{m}^2$) showing 1-layer RSF/I₃K scaffolds coated at different concentration ratios: (a) 0:5, (b) 5:0, (c) 5:1, (d) 5:2, (e) 5:3, (f) 5:4, (g) 5:5, (h) 20:1 and (i) 20:5 in 1 layer. The Z scale (height) =120 nm (a, c, d, e, f, g, h and i). The Z scale (height) =30 nm (b).

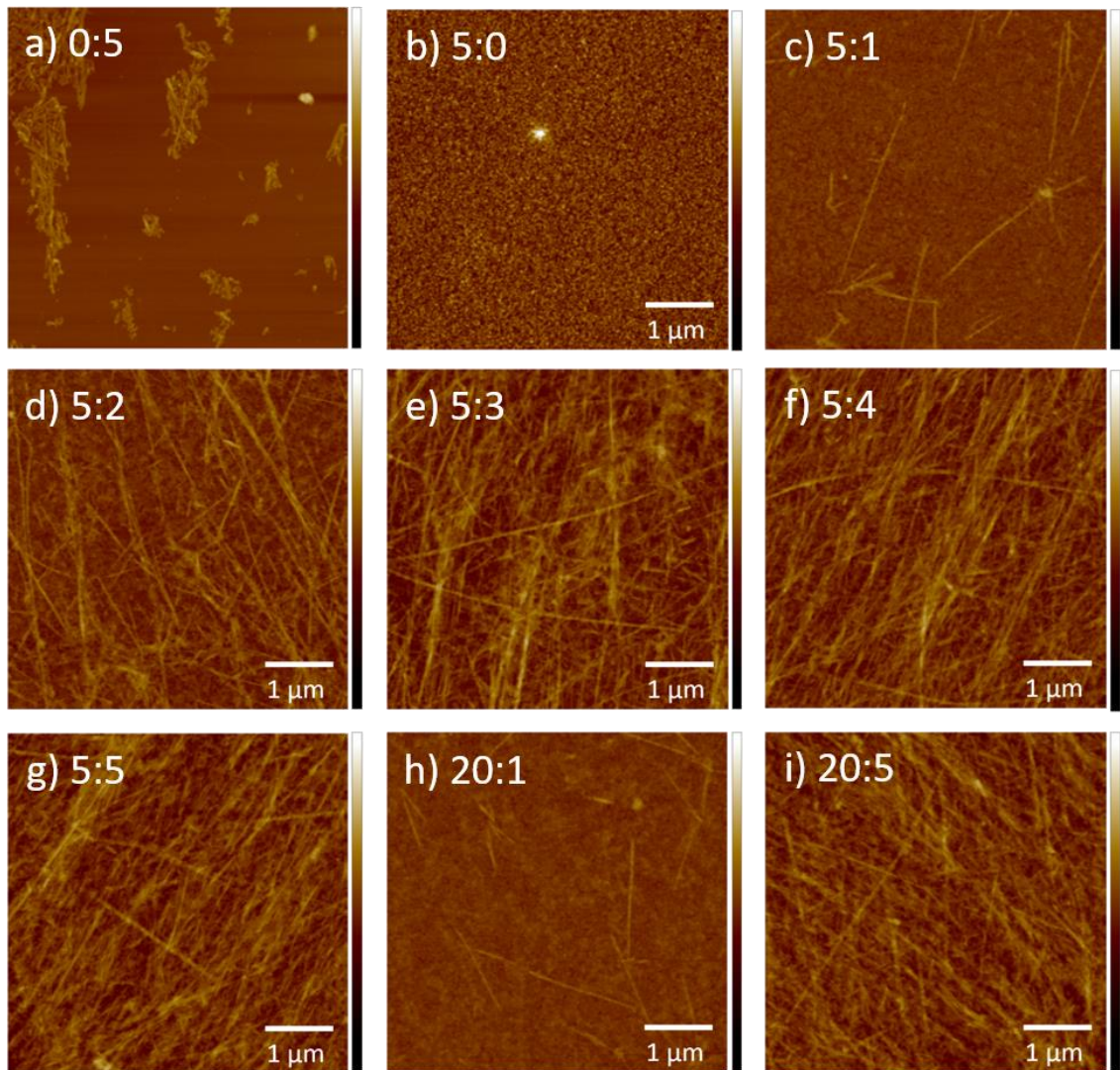


Figure 4-5 AFM topographical images ($25 \mu\text{m}^2$) showing 1-layer RSF/I₃K scaffolds after immersion in deionized water and incubation under a 5% CO₂ atmosphere at 37 °C for 6 days. The concentration ratios of RSF/I₃K scaffolds are: (a) 0:5, (b) 5:0, (c) 5:1, (d) 5:2, (e) 5:3, (f) 5:4, (g) 5:5, (h) 20:1 and (i) 20:5 in 1 layer. The Z scale (height) =120 nm (a, c, d, e, f, g, h and i). The Z scale (height) =30 nm.

4.3.3. Neuronal cell attachment and morphology on RSF/I₃K scaffolds

To investigate PC12 neuronal cell attachment and viability on different RSF/I₃K scaffold surfaces, a live / dead assay was carried out as shown in [Figure 4-6](#). RSF-only scaffolds showed very low cell adhesion due to a lack of cell recognizable groups such as RGD. Furthermore, they are negatively charged, which has been known to have negative effects on cell attachment.^{22, 98} Therefore, by adding positively charged I₃K peptide nanofibers onto the

negatively charged RSF substrates, the positively charged lysine residues deposited on the scaffold surface promoted PC12 cell binding.⁵¹⁴ PC12 cells showed poor attachment on I₃K-only and RSF/I₃K scaffolds at low I₃K concentrations (< 3 mg/mL) compared with RSF/I₃K scaffolds with high I₃K concentrations (3-5 mg/mL). This is most likely because I₃K nanofibers are easily washed off without RSF base during cell culture as shown in the AFM images in [Figure 4-4](#) and [Figure 4-5](#), and the RSF/I₃K scaffolds with low concentrations of I₃K provide insufficient anchoring points for cell attachment. A significant difference in cell density was observed between RSF-only and RSF/I₃K (3-5 mg/mL) scaffolds, indicating the promotion of PC12 neuronal cell attachment on RSF/I₃K scaffolds through the addition of positively charged I₃K nanofibers. However, with an I₃K concentration of 5 mg/mL, the number of cells decreased slightly, where no cell attachment in some areas was observed. This was possibly due to some detachment of stacked I₃K nanofibers occurring at this and higher concentrations, as previously discussed in section 3.2. The stacked I₃K nanofibers promoted excessive cell attachment and cells grew quickly becoming over confluent during the incubation time, thus detaching from the scaffold surface. Additionally, the live / dead assay indicated that RSF/I₃K scaffolds have excellent biocompatibility. The results indicated that I₃K is a promising candidate which can be used as a functional scaffold material similar to other peptides (such as PLL⁵¹⁴ or gelatin⁵⁵⁴) previously reported for tissue engineering.

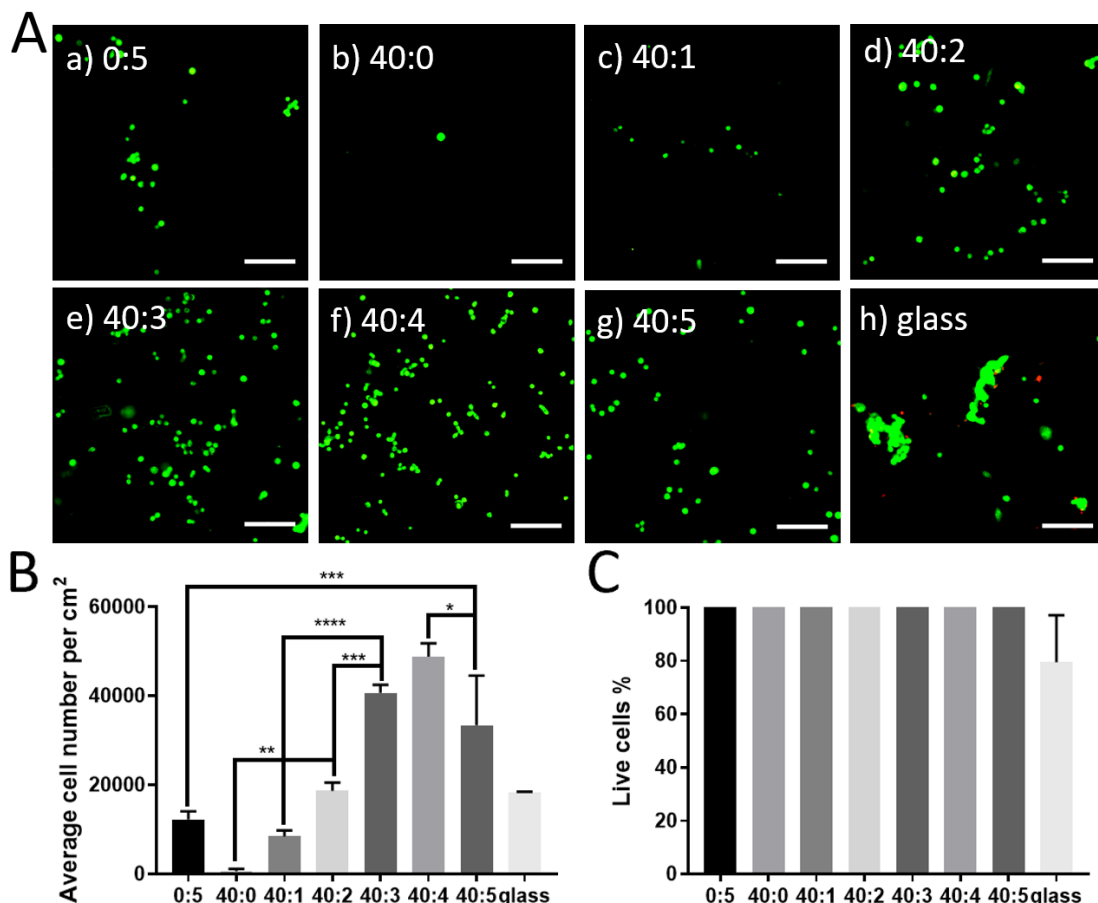


Figure 4-6 **A**, Live / dead assay of PC12 neuronal cells adhered on RSF/I₃K scaffold surfaces. The live cells (green) were stained by Syto-9TM and dead cells (red) were stained by propidium iodide. The concentration ratio of RSF and I₃K are (a) 0:5; (b) 40:0; (c) 40:1; (d) 40:2; (e) 40:3; (f) 40:4; (g) 40:5 and (h) blank glass (control). (Scale bar = 100 μm) **B**, Average cell numbers (per cm²) adhered on RSF/I₃K scaffold surfaces. **C**, Percentage of live cells adhered on RSF/I₃K scaffold surfaces. n ≥ 3. (**** p < 0.0001; *** p < 0.001; ** p < 0.01 and * p < 0.05).

The investigation of cell morphology attached on different ratios of RSF/I₃K scaffolds was carried out via AFM (Figure 4-7 and Figure 4-8). As previously noted, cells spread out well on I₃K-only coated surfaces but showed patchy attachment due to the peptide being washed off during cell culture. Cells showed an excellent spreading on I₃K-only coated surfaces (Figure 4-7 **A(a)**) whereas cells barely spread out their terminals on RSF-only coated surfaces (Figure 4-7 **A(b)**). Cells started to attach on RSF/I₃K coated surfaces at concentration ratio 40:1 (Figure 4-7 **A(c)**). By increasing the concentration of I₃K from 2 to 4 mg/mL deposited onto RSF (40 mg/mL) coated surfaces, cellular spreading improved drastically (Figure 4-7 **A(d-g)**), indicating a peptide

concentration dependence of cell spreading. Additionally, FITC-phalloidin and DAPI was used to stain actin filaments and cell nuclei respectively to further characterize the morphology of cells adhered on RSF/I₃K scaffolds (Figure 4-9). Cells on RSF/I₃K coated substrates also showed excellent spreading and flattening with this being enhanced as the concentration of coated I₃K increased. These results are consistent with previous AFM results shown in Figure 4-7 A.

The first step of the cell adhesion process is the cell-polymer interactions, which is essential for cell communication, regulation, tissue development and maintenance.^{494, 538} Cell-polymer interactions can be divided into three types, i.e. non-adhesion, passive adhesion and active adhesion.⁴⁹⁴ The interactions between cells and RSF surfaces corresponds to passive adhesion, which means cells attach easily but can also easily detach from surfaces.⁵⁷⁴ Cells attached on RSF/I₃K scaffolds on the other hand undergo active adhesion, in which cells spontaneously adhere onto the surface and the adhesion is tight, therefore, it is difficult for cells to detach.⁵⁷⁵ Additionally, the positively charged lysine residues in I₃K activates cell changing morphology and causes spreading for attachment-dependent phenotypes. Furthermore, there are three phases that can describe the process of cell adhesion onto cell-active polymer surfaces. Cells adhere onto the RSF-only scaffolds via complex physicochemical interactions including van der Waals, coulombic and hydrophobic forces, known as Phase I cell attachment.⁵³⁹ The action of the cells starting to spread and become flattened on the RSF/I₃K scaffold surface (Figure 4-7 A(c-d)), due to integrin binding, is known as Phase II. Full spreading and formation of focal adhesions for the cytoskeleton of PC12 neuronal cells on the RSF/I₃K (Figure 4-7 A(e-g)) is regarded as Phase III. Therefore, RSF/I₃K scaffolds, where I₃K can be considered a cell-adhesive polymer, are able to activate the cell adhesion process inducing spreading and flattening. Increasing the concentration of I₃K resulted in improved and expedited cell adhesive properties.

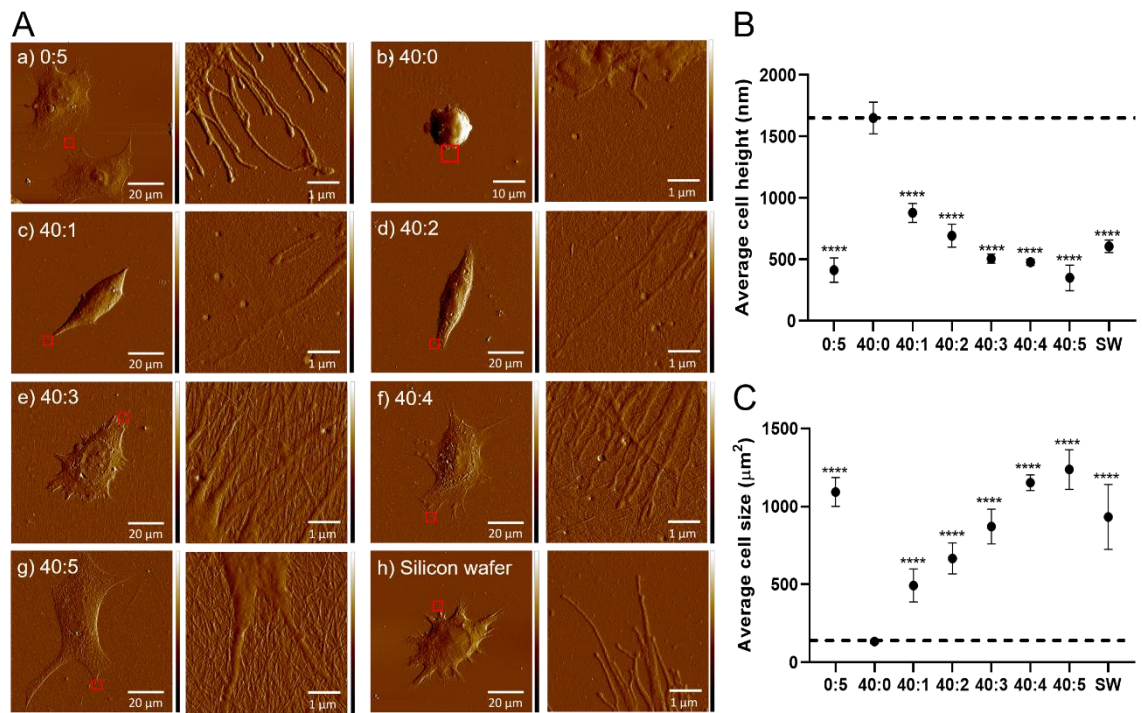


Figure 4-7 **A**, AFM Peak Force Error images of PC12 neuronal cells attached on a series of RSF and I₃K coated surfaces. In addition, enlarged AFM images of red box areas are shown in right of each image. The concentration ratios of RSF and I₃K were: **(a)** 0:5, **(b)** 40:0, **(c)** 40:1, **(d)** 40:2, **(e)** 40:3, **(f)** 40:4, **(g)** 40:5 and **(h)** silicon wafer control. The force setpoint constant is 30 nN for images of cells and 5 nN for enlarged areas. **B** and **C** indicate average cell heights and sizes in all scenarios. ($n \geq 3$; **** $p < 0.0001$; *** $p < 0.001$; and * $p < 0.05$).

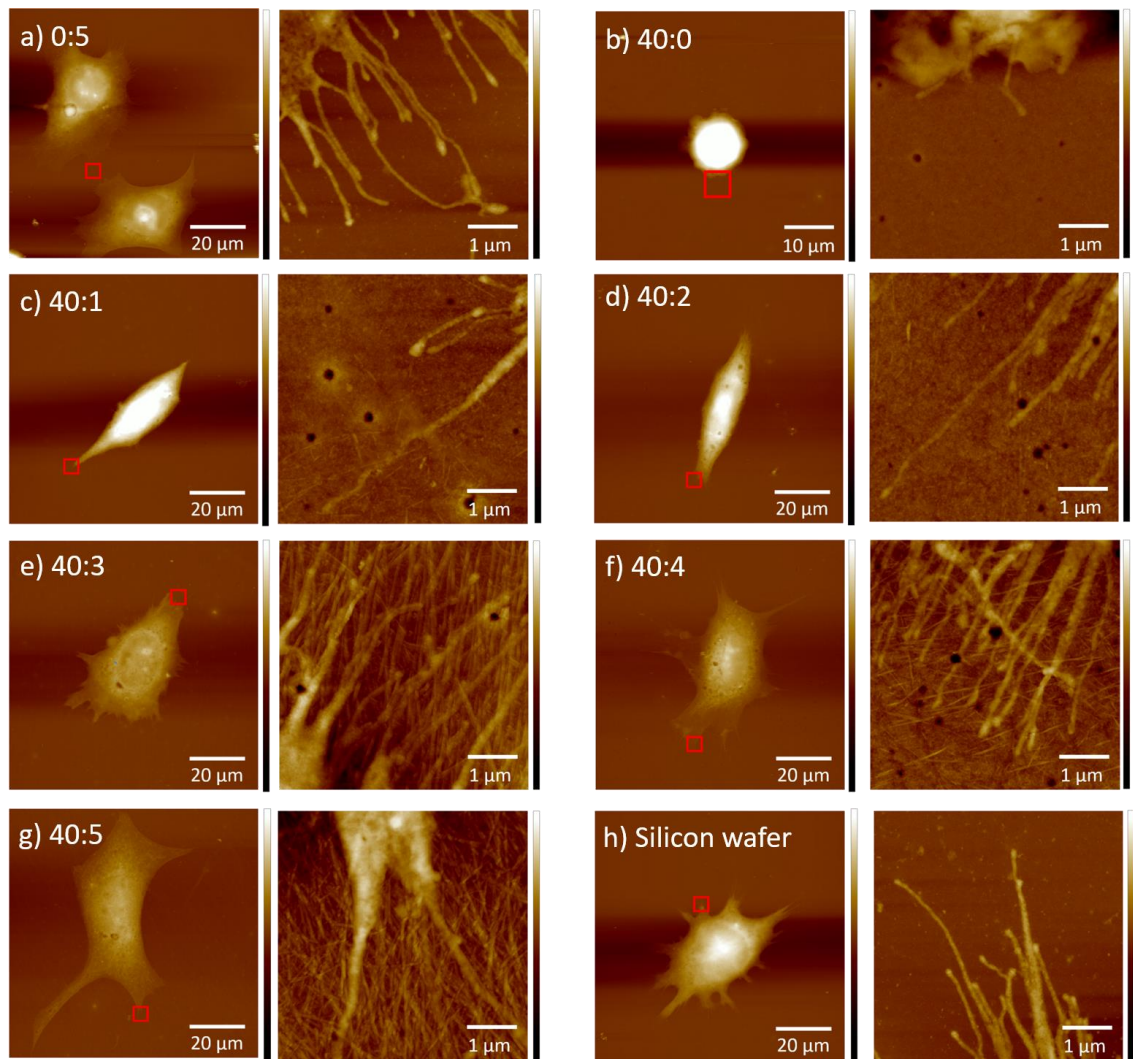


Figure 4-8 AFM topographical images of PC12 neuronal cells attached on various coated surfaces. Enlarged AFM topographical images of red box areas shown in right of each image of cells. The concentration ratios of RSF and I₃K were: (a) 0:5, (b) 40:0, (c) 40:1, (d) 40:2, (e) 40:3, (f) 40:4, (g) 40:5 and (h) silicon wafer. The Z scale bar is 1.5 μm for images of cells and 150 nm for enlarged areas.

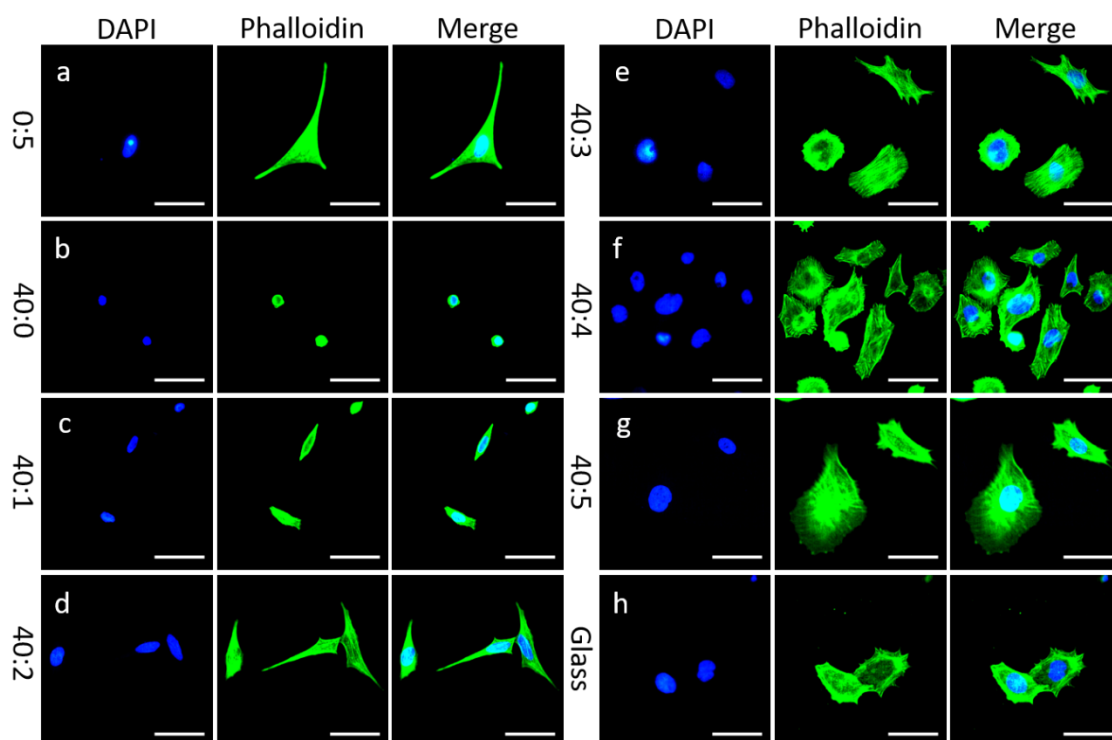


Figure 4-9 F-actin staining of PC12 neuronal cells attached on different ratios of RSF/I₃K coated surfaces: (a) 0:5; (b) 40:0; (c) 40:1; (d) 40:2; (e) 40:3; (f) 40:4; (g) 40:5 and (h) blank glass (control). The nucleus was stained by DAPI (blue) and F-actin was stained by FITC-phalloidin, scale bar = 50 μm .

Further AFM analysis revealed the average cell height (Figure 4-7 B) on RSF-only scaffolds was 1650 ± 110 nm. In the case of I₃K-only scaffolds, an average cell height of 410 ± 80 nm was measured. The average height of cells on RSF/I₃K peptide scaffolds decreased with increasing I₃K concentrations (1 to 5 mg/mL) from 880 ± 60 nm to 350 ± 90 nm. For the blank silicon wafer, the average cell height was 600 ± 40 nm, which was similar to (but slight lower than) that of the RSF/I₃K (ratio 40:2) samples. The average size of attached cells (Figure 4-7 C) on RSF-only scaffolds was found to be 140 ± 10 μm^2 . A gradual size increase (up to 9-fold at 5 mg/mL I₃K) was observed as I₃K concentration was increased. Both average cell height and size on the silicon wafer substrates were similar to the RSF/I₃K scaffold at a concentration ratio of 40:3. The results indicated that RSF/I₃K scaffolds with I₃K concentrations above 3 mg/mL are ideal for PC12 cell adhesion and spreading, outperforming the cell behaviour on RSF-only scaffolds. The red boxes in Figure 4-7 A also indicate areas of interest that were enlarged to further investigate the cell morphology. The AFM images show neurites of PC12 cells adhering to the RSF-only or RSF/I₃K

coated surfaces (Figure 4-7 A(b-g)). In contrast to I₃K-only scaffolds, Figure 4-7A(h) shows the neurites of PC12 cells adhering on exposed bare silicon wafer substrate. The results were similar to those reported by Gupta et al.⁵⁷⁶ who indicated that neural cells can adhere and differentiate on chitosan-based scaffolds. We conclude that I₃K can promote PC12 cell attachment, spreading and neurite formation.

4.3.4. Differences between RSF/I₃K scaffolds and collagen scaffolds on the function of PC12 cells

Collagen is one of the basic components of the ECM that can provide a natural environment for cell growth, and proliferation, and is widely used in nerve tissue repair.^{577, 578} In addition, collagen has been proven to possess a good adherence and proliferation ability for PC12 cells.⁵⁷⁹ Therefore, the following experiments, including resazurin assay, live / dead assay and immunostaining of the neurites, were carried out comparing the differences in PC12 cell functions on RSF/I₃K scaffolds and collagen scaffolds. Note that, three types of RSF/I₃K scaffolds were chosen, where the RSF scaffold concentration was 40 mg/mL and RSF/I₃K scaffold concentration ratios were 40:3 and 40:4 (represented as RSF/I₃K 40:3 and RSF/I₃K 40:4).

The metabolic activity of PC12 cells on sample surfaces (Type I collagen; RSF; RSF/I₃K 40:3 and RSF/I₃K 40:4) were determined after 24, 72 and 144 hours in culture using a resazurin assay, and control groups performed on bare glass and TCP (tissue culture plastic) substrates (Figure 4-10). Resazurin possesses poor fluorescence, which can be reduced by viable cells to form the strong-fluorophore resorufin. The results of resazurin assay can be measured by fluorescence reading of the reduced resorufin product. The fluorescence output is proportional to the population of viable cells. Metabolic activity was observed to increase gradually between 24 and 144 hours on all surfaces. Cells adhered on RSF coated surfaces showed the lowest metabolic activity among all test surfaces at 24 and 144 hours, while for RSF/I₃K scaffolds, the metabolic activity increased more, indicating I₃K can promote PC12 cell proliferation. RSF/I₃K scaffolds at a ratio of 40:4 showed the highest metabolic activity which surpassed that of Type I collagen scaffolds (between 24 and 144 hours), indicating a difference proliferation on the surfaces. For control groups, cells on

glass had a lower metabolic activity at all time points which in contrast to TCP. Highest cell metabolic activity was observed on TCP samples compared to test surfaces at 24 hours. However, the increase in metabolic activity observed on the TCP surface between 72 and 144 hours was similar to that of the other surfaces. This indicates excellent cell proliferation on the coated surfaces.

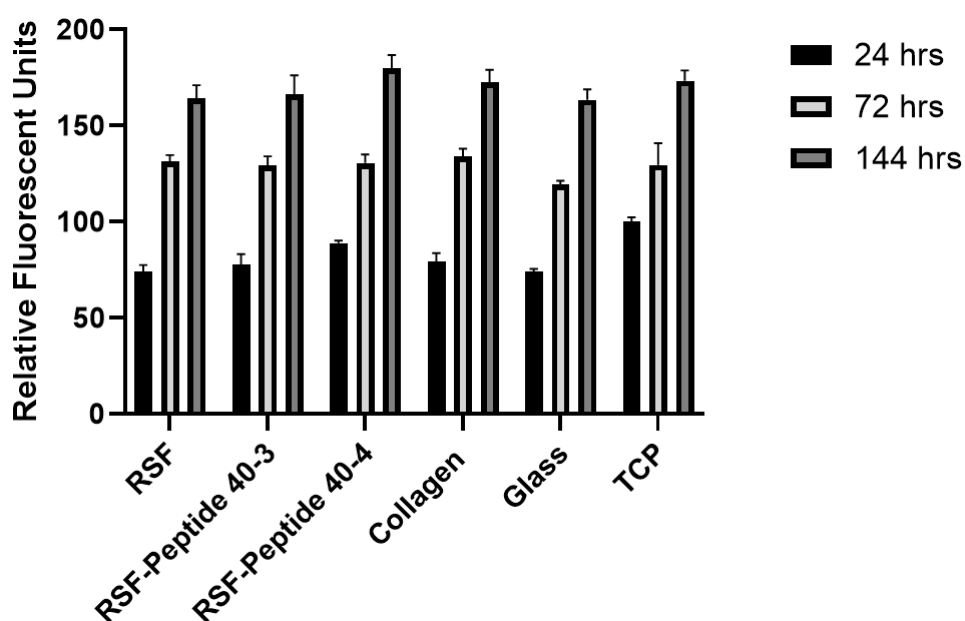


Figure 4-10 Metabolic activity of PC12 cells adhered on different surfaces assessed using resazurin assay after 24-, 72-, and 144-hours culture. TCP represents tissue culture plastic. ($n \geq 3$; **** $p < 0.0001$).

Live / dead assay results (Figure 4-11) indicated a low rate of cell mortality on all surfaces after 6 days of culture. As can be seen from Figure 4-11 B, there was a slightly lower proportion of live cells on type I collagen ($96.7\% \pm 0.3\%$) compared to RSF (100%), RSF/I₃K 40:3 ($99.3\% \pm 0.1\%$) and RSF/I₃K 40:4 ($98.4\% \pm 0.2\%$) scaffolds. Although collagen is a well-known biocompatible material⁵⁸⁰, RSF/I₃K showed better cell growth and proliferation overall. The population of cells adhered onto uncoated RSF surfaces was poor (Figure 4-11 C), only 34 ± 28 cells were observed, which is much lower than the adherence onto RSF/I₃K 40:3 (180 ± 50) and RSF/I₃K 40:4 (290 ± 50). Please note that, I₃K coated on RSF surfaces, resulted in a significant difference in observed percentage of live cells. That is due to RSF surfaces having a poor cell attachment, resulting in cells easily detaching from the RSF surfaces during cell culture, and only a few cells remaining. The results demonstrated that I₃K

coated on RSF scaffolds can increase neuronal cell proliferation and attachment. Furthermore, the population of cells increased with increasing I₃K concentration, which is consistent with the results reported in section 3.3. According to Wiatrak *et al.*⁵⁷⁹, PC12 Adh cells show good attachment on plastic surfaces. As can be seen in Figure 4-11 C (results obtained from much larger areas than showed in Figure 4-11 A), there is no significant difference between RSF/I₃K 40:4 and TCP (note that cells on TCP showed patches with some areas having more cells (e.g., Figure 4-11 A(f)) and some areas having less). Therefore, RSF/I₃K 40:4 scaffold also promotes good PC12 cell attachment. However, there was still a significant higher cell population (650 ± 30) on type I collagen than RSF/I₃K 40:4 scaffolds, indicating that peptides with multiple amino acids / functional groups are required to increase cell densities. The main amino acids in the collagen peptide are glycine, proline and alanine,⁵⁸⁰ which can be used as building blocks to further design a modified self-assembled peptide based on I₃K to improve the performance in nerve tissue engineering.²⁴⁶

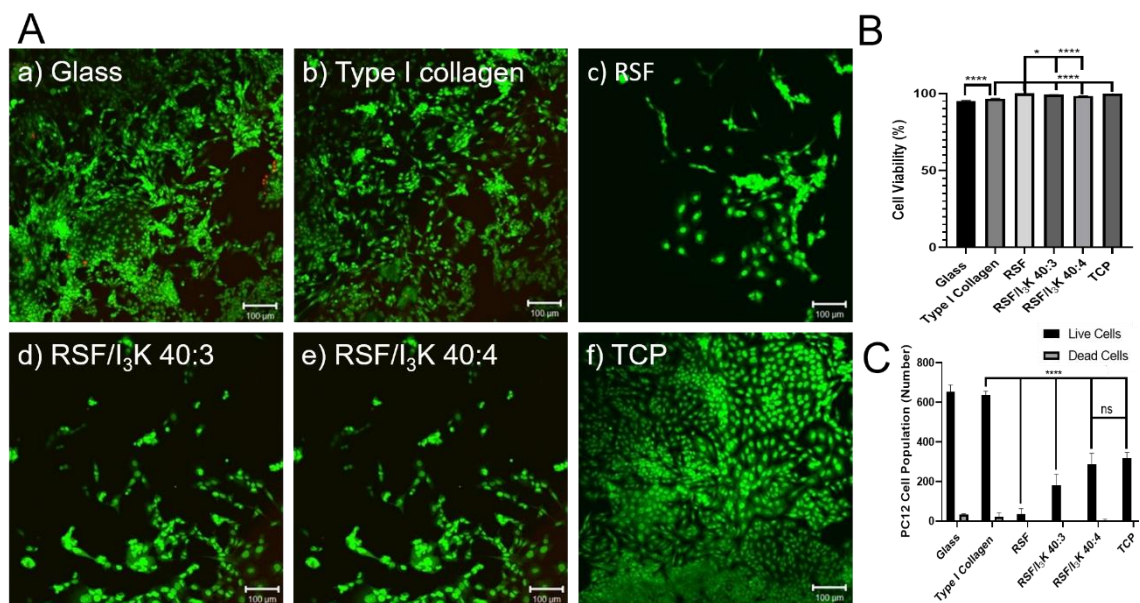


Figure 4-11 **A**, Representative confocal images of live / dead analysis from PC12 neuronal cell culture on different surfaces, (a) Glass (control); (b) Type I collagen; (c) RSF; (d) RSF/I₃K 40:3; (e) RSF/I₃K 40:4 and (f) TCP (control). The live cells (green) were stained by Syto-9TM and dead cells (red) were stained by propidium iodide, scale bar = 100 μm. **B**, Percentage of cell viability. **C**, The population of live and dead cells. The percentage of live cells on glass surface was $95.1 \pm 0.4\%$; on type I collagen surface was $96.7 \pm 0.3\%$; on RSF surface was 100%; on RSF/I₃K 40:3

surface was $99.3 \pm 0.1\%$; on RSF/I₃K 40:4 surface was $98.4 \pm 0.2\%$ and on TCP surface was $99.9 \pm 0.1\%$. TCP represents tissue culture plastic. ($n \geq 3$; **** $p < 0.0001$).

PC12 neuronal cells were labelled for β III-tubulin, a specific neurite formation marker (Figure 4-12 A). Short neurite outgrowth was observed for cells adhered to uncoated RSF surfaces and on glass substrates. However, at an I₃K concentration of 3 mg/mL coated onto RSF surfaces, neurite formations were observed, but slightly shorter than those on cells grown on type I collagen. With increasing concentration of I₃K to 4 mg/mL, longer neurite formation was observed, which indicated that the concentration of I₃K directly affects the length of neurites (Figure 4-12 B), which is consistent with the previous AFM images (Figure 4-7). The measurement of average maximum neurite lengths per neuronal cell revealed no significant difference between cells grown on type I collagen ($25 \pm 8 \mu\text{m}$) and RSF/I₃K 40:4 surfaces (Figure 4-12 B). Experiments were terminated after 6 days, due to long neurite lengths being physically impaired at high cell density.⁵⁸¹ Comparison to glass and RSF surfaces, type I collagen and RSF/I₃K 40:4 surfaces had significantly higher percentage of cells bearing neurites (Figure 4-12 C). However, no significant difference was observed between type I collagen and RSF/I₃K 40:4 surfaces, suggesting that I₃K at a concentration of 4 mg/mL possesses similar neuronal cell differentiation to type I collagen.

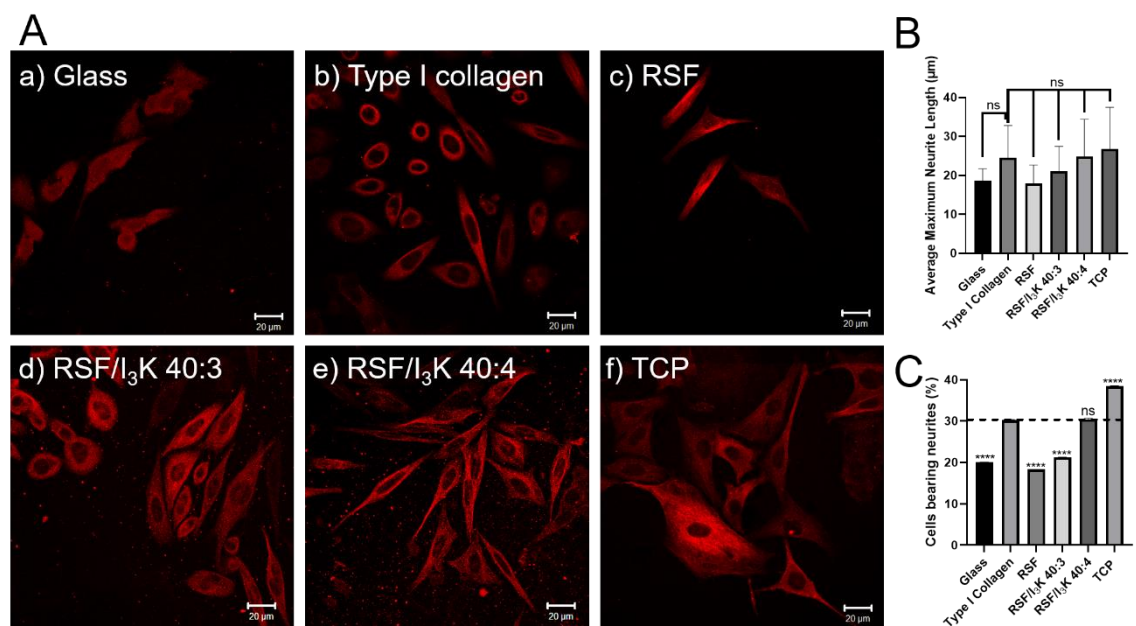


Figure 4-12 **A**, confocal images of PC12 neuronal cells adhered onto different surfaces, including (a) Glass (control); (b) Type I collagen; (c) RSF; (d) RSF/I₃K 40:3; (e) RSF/I₃K 40:4 and (f) TCP (control). Neurites (red) were stained by anti- β III-tubulin, scale bar = 20 μ m. **B** and **C** indicate average neurite lengths and the percentage of cells bearing neurites in all scenarios. TCP represents tissue culture plastic. ($n \geq 3$; **** $p < 0.0001$).

4.3.5. Micropatterning PC12 cells on RSF scaffolds via inkjet printing of peptide nanofibers

The micro-patterning of complex biomaterial structures plays an essential role in guiding cell adhesion, migration, differentiation and proliferation.^{140, 142} Inkjet printing can be used as an effective tool to micro-pattern complex structures of biomaterials onto a vast variety of bio-substrates including protein scaffolds.⁵⁴⁴ Therefore, it has been deployed here to print I₃K (3 mg/mL) peptide nanofibers as the letters “SHEF” onto RSF (40 mg/mL) coated substrates. Cell culture studies revealed cells grew almost exclusively along the printed I₃K letters as shown in [Figure 4-13](#). The results were consistent with those reported by Poudel et al.⁵⁶¹ who used photolithography to pattern collagen type I on cell-repellent surfaces and demonstrated neural cell growth along the patterns. It was noticed that PC12 cells prefer to grow on the edge of the letter lines rather than their central areas. This is attributed to the so-called ‘coffee ring effect’ resulting from the inkjet printing process, thus resulting in more I₃K nanofibers accumulating on the edge of the letters.^{546, 582} It is possible to reduce this effect by the addition of additives to alter the surface tension and spreading of the I₃K ink during the printing process, which might be deemed beneficial in the future. In nerve tissue engineering, the alignment of cells is important in axonal regeneration and direction⁵⁸³. Therefore, we have shown here the micro-patterning of PC12 cells via inkjet printing of the self-assembled I₃K peptide nanofibers onto RSF substrates may provide an excellent approach to enable the analysis of axonal development *in vitro*.^{544, 584}

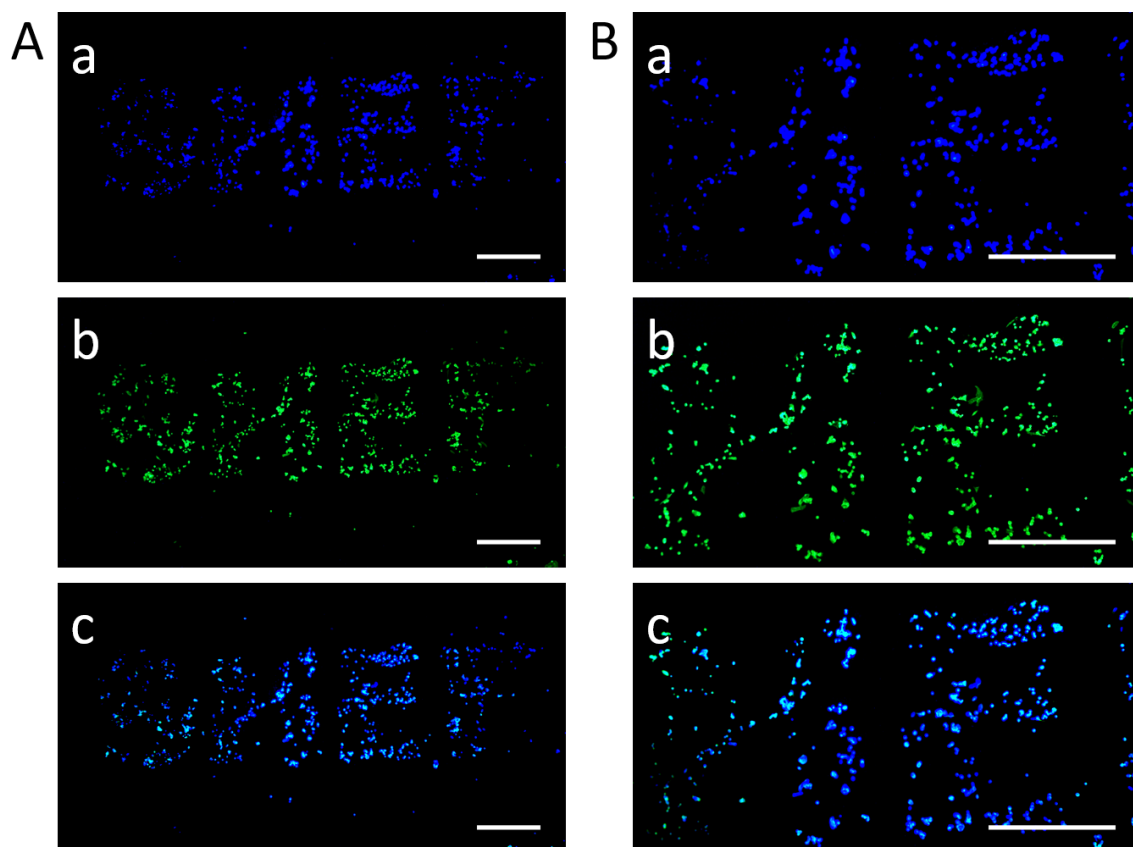


Figure 4-13 **A**, Inkjet-printing of 1 layer of “SHEF” letters onto RSF coated glass surfaces (40 mg/mL) using I₃K peptide (3 mg/mL) as the ink, with PC12 neuronal cells growing along the printed letters. **B**, Enlarged letters (“HE”). (a, DAPI staining for nucleus; b, FITC-phalloidin staining for F-actin; c, merged images of a & b), scale bar = 500 μm.

4.3.6. Investigation of topographical and thickness of RSF/I₃K scaffolds with different layers

AFM was further used to characterise the different number of layers of RSF/I₃K scaffolds, where 1 layer (Figure 4-4), 2 layers (Figure 4-14) and 3 layers (Figure 4-15) coated onto silicon wafer were investigated. Firstly, different concentration ratios between RSF and I₃K of 1 layer coating was characterised. Figure 4-4 (a) shows the long nanofibers of self-assembled I₃K in 20 mM HEPES buffer (pH 6) at 5 mg/ml without RSF. A blank sample only containing RSF is shown in Figure 4-4 (b), where the nanofibrillar structure of pure RSF with a sequence of associated segments can be seen. For samples containing RSF and I₃K mixtures, increasing the peptide concentration resulted in more nanofibers adhering to the RSF surface. Further increase of peptide concentration of I₃K resulted in stacking behaviour (Figure 4-4 (c)-(g)). At a concentration ratio of 5:3

(RSF/I₃K), the nanofibers fully covered on RSF surface. Nanofiber stacking can be considered unfavourable for cell culture as this might lead to cell detachment when stacked fibres detach. Comparison of the concentration ratios of RSF and I₃K at 20:1 and 20:5, showed that they had a similar trend with 5:1 and 5:5. Comparison between 20:1 and 20:5 ratios as shown in [Figure 4-4 \(g\) and \(i\)](#) respectively, showed that there were very few nanofibers at a ratio of 20:1. Increasing the ratio to 20:5 resulted however in an increase to the order of few hundreds.

As shown in the AFM images ([Figure 4-4](#), [Figure 4-14](#) and [Figure 4-15](#)), different amount of layers spin coated (1-3 layers) onto silicon wafer showed similar surface characterization.

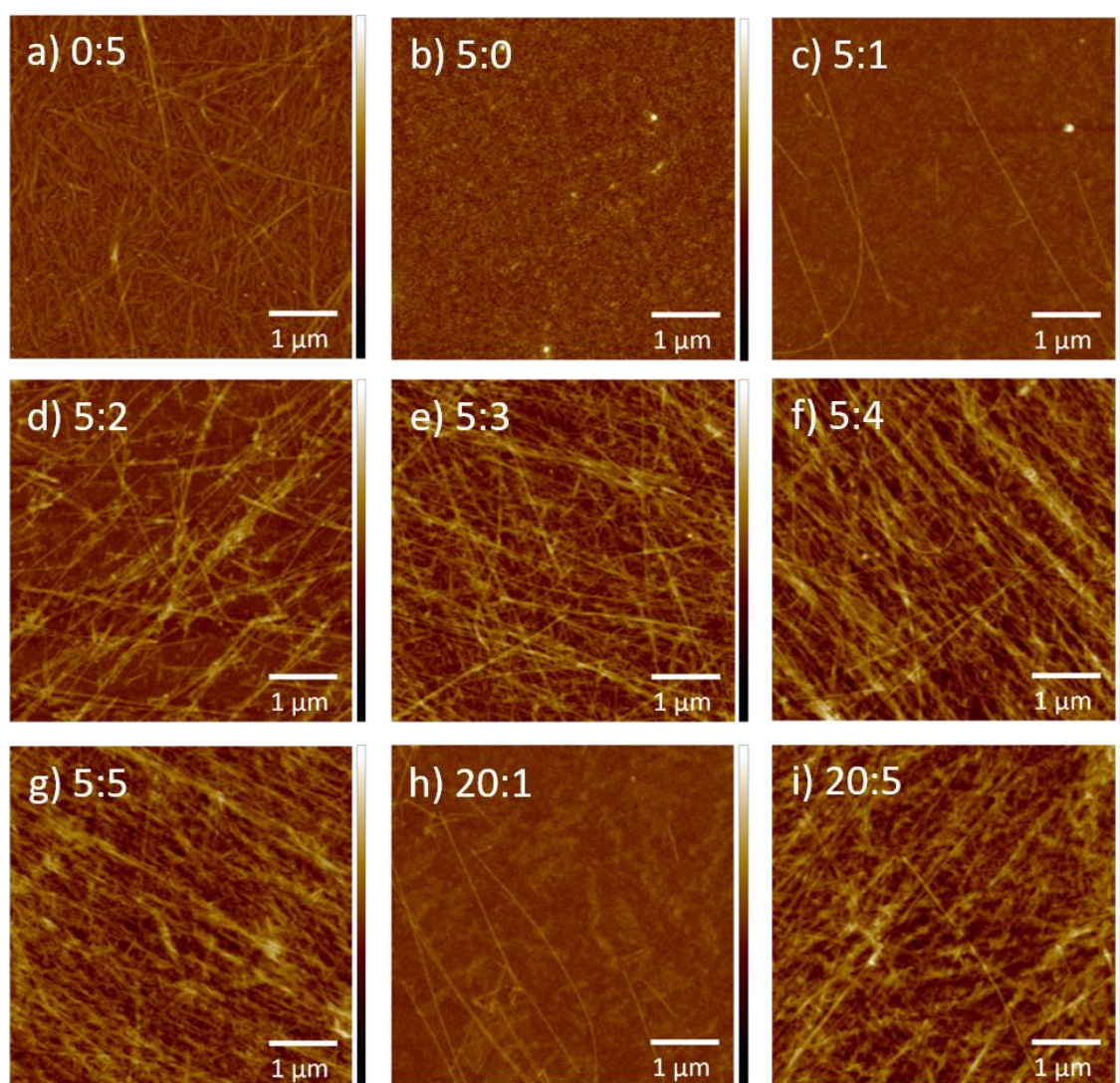


Figure 4-14 AFM topographical images ($25 \mu\text{m}^2$) showing 2-layers RSF/I₃K scaffolds coated at different concentration ratios: (a) 0:5, (b) 5:0, (c) 5:1, (d) 5:2, (e) 5:3, (f) 5:4, (g) 5:5, (h) 20:1

and (i) 20:5 in 1 layer. The Z scale (height) =120 nm (a, c, d, e, f, g, h and i). The Z scale (height) =30 nm (b).

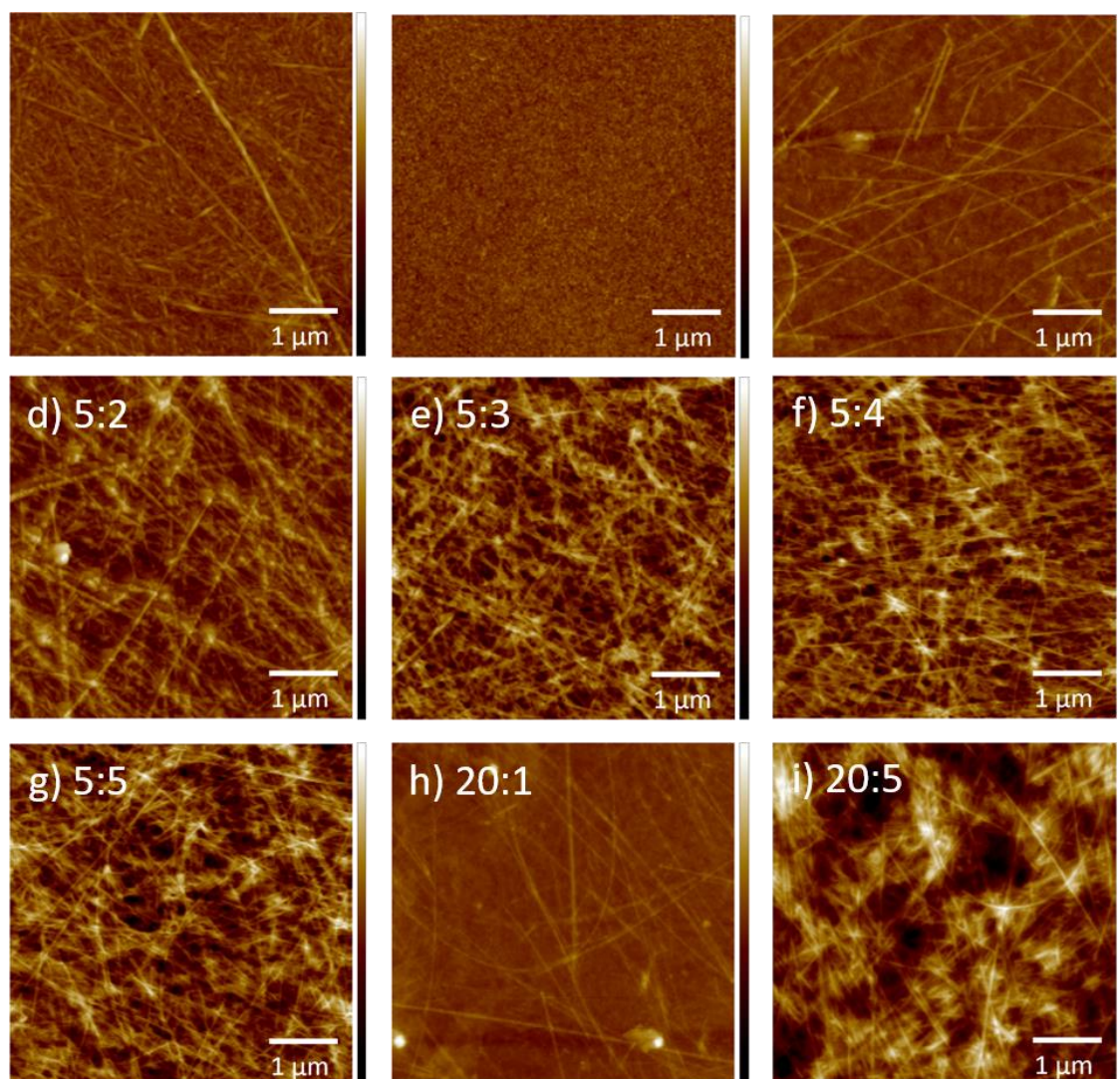


Figure 4-15 AFM topographical images ($25 \mu\text{m}^2$) showing 3-layers RSF/I₃K scaffolds coated at different concentration ratios: (a) 0:5, (b) 5:0, (c) 5:1, (d) 5:2, (e) 5:3, (f) 5:4, (g) 5:5, (h) 20:1 and (i) 20:5 in 1 layer. The Z scale (height) =120 nm (a, c, d, e, f, g, h and i). The Z scale (height) =30 nm (b).

In conclusion, RSF/I₃K scaffolds at a concentration ratio of 5:3 resulted in a desirable amount and distribution of nanofibers adhering to the RSF surface, which might show best properties for cell culture (Figure 4-4 (e), Figure 4-14 (e) and Figure 4-15 (e)).

Despite the surface morphology appearing to be similar regardless of the number of layers coated, it is important to investigate any possible effects the

layer number might have in cell culture studies (Figure 4-16). The depth of the 'dark holes' in Figure 4-16 showed a significant increase with increasing number of layers. This might give rise to an attraction of lots of cells on the scaffold surface, however, most likely will lead to cell detachment when media is changed as fibres might detach from the surface more readily.

It is possible to seed cells onto these scaffolds with different layer amounts, to investigate how the layers affect cell proliferation and attachment. If the amounts of layers have a positive influence on cells, inkjet printing can be applied to alternately print RSF and I₃K for many layers (e.g., 50 layers) with ease. This could pave the way to 3D RSF/I₃K scaffold providing a better opportunity to further investigate the properties of neural cells in 3D.

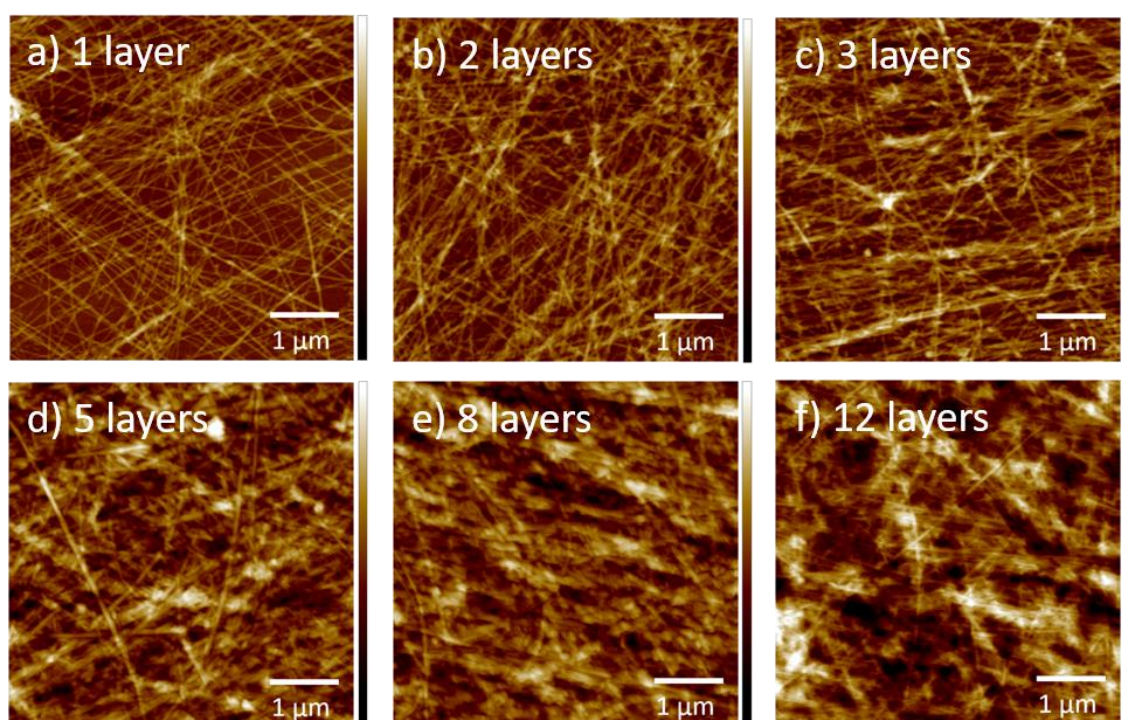


Figure 4-16 AFM topographical images ($25 \mu\text{m}^2$) showing RSF/I₃K scaffolds coated at the ratio 5:3 in different layers (a) 1 layer, (b) 2 layers, (c) 3 layers, (d) 5 layers, (e) 8 layers, (f) 12 layers. The Z scale for all images is 120 nm as indicated.

Spectroscopic ellipsometry was used to test the thickness of RSF/I₃K layers on silicon wafers after spin coating. The results of RSF/I₃K for 1 and 3 layers are shown in (Figure 4-17). Both samples show the same tendency, after mixing RSF with 1 mg/ml I₃K, the thickness showed a slight decrease in thickness. Following a further increase of I₃K, the thickness increased in a linear manner.

The thickness difference between the two samples (Figure 4-17 A) mostly likely originates from two silicon wafers not having been cleaned in exactly the same way, however a thickness of 20 Å was assumed for the ellipsometry measurements. RSF and I3K contain negative and positive charges, respectively, which might explain the decrease in thickness between pure RSF (5:0) and RSF/I3K (5:1) due to attractive forces.

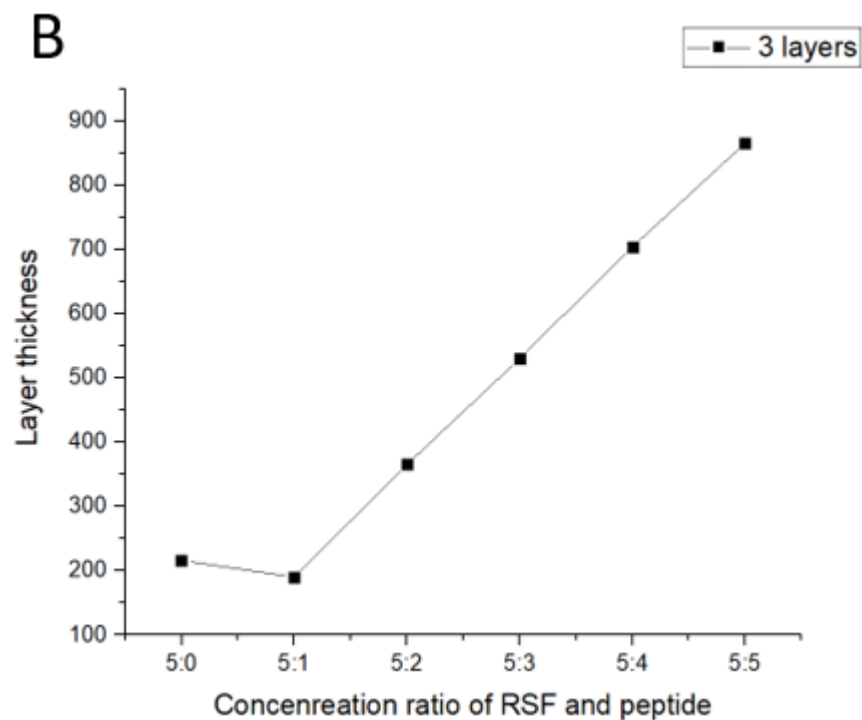
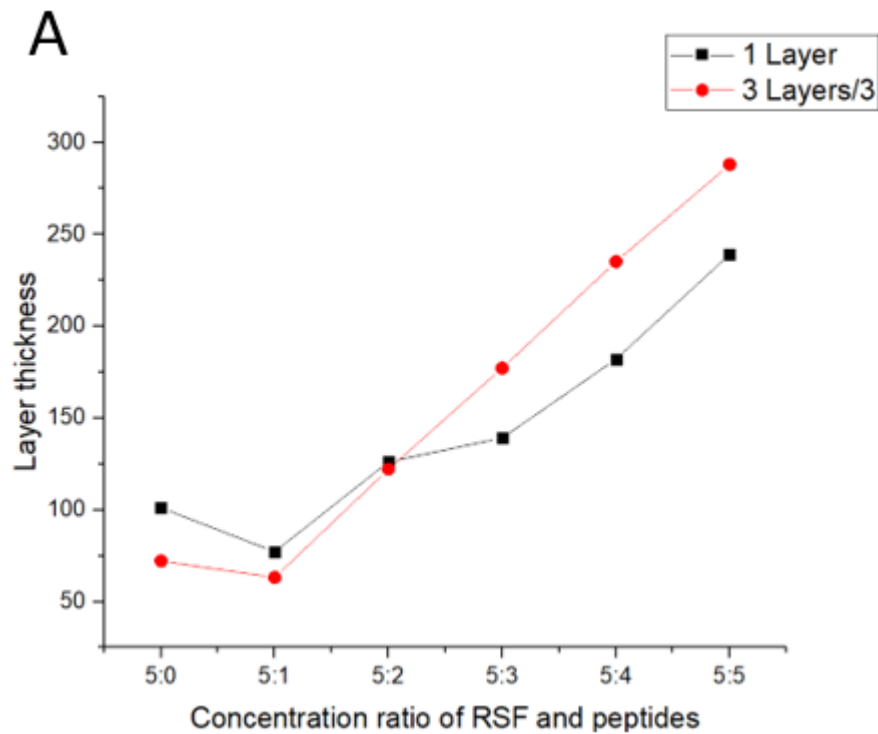


Figure 4-17 Layer thickness of RSF/I₃K coated surface (5:0, 5:1, 5:2, 5:3, 5:4, 5:5). (A) 1 layer (black line) and 3 layers/3 (red line). (B) 3 layers. The unit of thickness is Å.

4. 4. Conclusions

The surfactant-like ultrashort peptide I₃K is able to self-assemble into nanofibrillar structures with a hydrophobic isoleucine tailed fibre core, and positively charged lysine residues located outside the fibres.^{298, 585} The self-assembled I₃K peptide nanofibers have been successfully used as templates for the fabrication of silica nanotubes.²⁹⁹ In this study, I₃K peptide nanofibers were used as a cell-attractive agent to modify RSF scaffold surfaces to encourage neuronal cell (PC12 cell) attachment and growth. Commonly, positively charged PLL has been used for facilitating cell attachment and proliferation^{586, 587}. However, it can be cytotoxic, especially due to the high-molecular-weight of PLL.⁵⁸⁸ Therefore, the structure of PLL should be modified via incorporation of segments that can reduce toxicity.⁵⁸⁹ In addition, the I₃K peptide is more cost-effectively than PLL due to its short sequence. Overall, we speculate that the positively charged I₃K peptide nanofibers could be used as an alternative to PLL for cell culture and tissue engineering applications.

It was found in our study that RSF-only coated surfaces had poor PC12 cell attachment, due to a lack of cell binding functional groups. However, this could be counteracted by introducing I₃K peptides nanofibers onto the scaffolds during the fabrication process. The peptide nanofibers naturally immobilise onto the RSF scaffold surfaces via charge-charge interactions, where the RSF-only scaffold surface is negatively charged and the I₃K peptide nanofibers are positively charged. The results showed that the presence of I₃K peptides promoted PC12 cell binding efficiency as the positively charged lysine residues facilitate cell attachment, which is equivalent to PLL.⁵⁶⁹

Two methods (spin coating and inkjet printing) were applied to prepare scaffolds, with a series of different concentration ratios of RSF and I₃K onto glass and silicon wafer as substrates. Cells grown on the prepared scaffolds showed variable attachment, proliferation, and morphology including the formation of neurites. Additionally, the live and dead assay demonstrated that both RSF and I₃K demonstrated negligible cytotoxicity toward PC12 neuronal cells, indicating

that both materials are promising scaffold materials for neural tissue engineering. In addition, the RSF/I₃K (ratio 40:4) produced scaffolds that optimally supported cell adhesion indicating excellent biocompatibility and differentiation. This also demonstrates that the ultra-short peptide I₃K could be used as an alternative to PLL for cell culture and tissue engineering applications.

Inkjet printing has been shown to be an excellent micro-patterning method for the guidance of cell attachment.⁵⁹⁰ The charge-charge interactions between positively charged I₃K peptide nanofibers and negatively charged RSF coated surfaces facilitated the robustness of the scaffold system during fabrication and cell culture work. Thus, enabling excellent cell growth along the printed patterns. This patterning method is a strength of inkjet printing offering a promising approach for analysing and understanding fundamental cellular functions such as neurite development and cell-cell interaction *in vitro*.^{551, 591}

5. Short peptides induce neurite outgrowth of neuronal cells

Abstract:

Control of polymer-cell interactions is an essential factor to be considered for the design and fabrication of scaffolds for tissue engineering applications. In this work, the hydrophobic isoleucine tail (I₃) was modified with laminin or fibronectin derived peptides with the sequence of IKVAV, PDSGR, YIGSR, RGDS and PHSRN, respectively. The resulting designed short peptides I₃KVAV, I₃RGDS and I₃YIGSR were able to dynamically self-assemble into nanofibers, while the remainder were unable to. Pure regenerated silk fibroin (RSF) substrates showed poor cell attachment of neuron cells, such as rat PC12 cells. Therefore, this property was used as a cell-repellent agent. On this other hand, RSF substrates allowed the designed short peptides to strongly adhere to its surface via hydrogen bonding. Live / dead assays revealed that the peptides I₃KVAV, I₃RGDS and I₃YIGSR exhibited negligible cytotoxicity against PC12 cells. The specific interaction between PC12 cells and the short peptides were investigate using atomic of microscopy (AFM). The results indicted the presence of a synergistic effect in the designed short peptides enabling them to promote cellular attachment, cellular proliferation and morphology change of PC12 cells. In addition, AFM results showed the presence of both peptides I₃KVAV and I₃YIGSR possesses the best regulation of proliferation and attachment of PC12 cells, consistent with those obtained from the immunofluorescence staining technology. The approach of combining two different self-assembling short peptides has great potential for nerve regeneration applications.

Keywords: Nerve tissue engineering, polymer-cell interaction, RGDS; YIGSR; IKVAV; self-assembling peptides, PC12 cells

5. 1. Introduction

The peripheral nervous systems (PNS), which includes cranial nerves, peripheral nerves, spinal nerves and neuromuscular junctions, as well as the central nervous system (CNS), consisting of the brain and spinal cord, are the

two major components of the human nervous system.¹ After injury, nerves are capable to spontaneously regenerate in the PNS, however are unable to regenerate in the CNS. Despite the peripheral nerve self-repair ability, the nerve regeneration and functional recovery depends on the injury gap length. If the gap length is too long above the critical gap length nerve regeneration is limited.⁵⁹²⁻⁵⁹⁴ In addition, nerve injuries for both PNS and CNS are a serious problem that affects millions of people worldwide, leaving a large social and economic burden on society.¹ Therefore, it is of strong interest to design biomaterial scaffolds to promote nerve regeneration and functional recovery.

The extracellular matrix (ECM) is a non-cellular component located within all tissue and organs, and can be recognized as a scaffold to modulate cellular behaviours, such as differentiation, proliferation, adhesion and migration. The major components of ECM are glycosaminoglycans, proteoglycans and fibrous proteins that contain collagen, fibronectin, laminin, elastin and so forth.^{517, 595, 596} In the last decades, ECM components have been used as biomaterial scaffolds in nerve tissue engineering (TE).^{597, 598} Collagen is the major component of ECM in living tissue, making it the most studied scaffold material to date.^{599, 600} Until now, at least 28 different types of collagen have been discovered and classified into different families based on their structure and distribution within the human body.⁶⁰¹ Type I collagen has a strong positive effect on nerve cells, enable it as the gold standard in nerve TE.^{578, 602} In addition to collagen, laminin and fibronectin have also been successfully applied in nerve TE.⁴²⁸ This is because of active peptide sequences present within laminin and fibronectin. These include the peptide sequences IKVAV, PDSGR and YIGSR present within laminin, as well as RGDS and PHSRN in fibronectin.⁶⁰³⁻⁶⁰⁵ Although these active sequences have been successfully synthesised, they have been unable to form suitable 2D/3D scaffolds, allowing to provide more suitable cellular microenvironment in the development of TE applications.

Peptide self-assembly is a “bottom-up” approach, in which the 20 natural amino acids are used as building blocks, enabling the ability to form well-ordered nanoarchitectures under certain conditions, leading to the formation of hydrogels.^{250, 293} Peptide amphiphiles are one essential category of peptide self-assembly, which can emulate nanoscale fibres and pore morphology of

natural ECM. Therefore, these have been widely applied for use as biomaterial scaffolds for bone, skin and nerve repair applications.^{259, 606, 607} Peptide amphiphiles can be further divided into several sub-types, of which the surfactant-like peptide sub-type, structurally the simplest, have been successfully applied in nerve TE. These peptides are normally consisting of several repeated hydrophilic amino acid residues as the head and one or two hydrophobic amino acid residues functioning as the tail.^{26, 246, 608} The short peptide AC-I₃K-NH₂ (I₃K) is a typical example of surfactant-like peptide, which contains a hydrophobic tail made of three isoleucine residues (Ile or I) and a hydrophilic head composed of lysine (Lys or K).^{298, 299} In addition to this, the terminal charges on the N terminal are blocked by acetyl groups and the carboxyl groups of the C terminals are blocked by amine groups, thus promoting the self-assembling of I₃K. Inspired by active peptide sequences from laminin and fibronectin there is a great potential to design self-assembling peptides via the addition of a hydrophobic tail such as I₃.

Another inexpensive biomaterial is silk fibroin (SF), which has been extensively researched owing to its strong mechanical properties, biocompatibility, low immunogenicity, and biodegradability, can be extracted from the silk worm *Bombyx mori* (*B. mori*).^{1, 563} Over the last two decades, SF has been widely applied in different categories of TE as a scaffold material, ranging from bone, skin, vascular and so forth.^{25, 38} However, pure SF lacks specific domains (e.g., adhesion motifs contained in laminin and fibronectin) beneficial for neural cell adhesion, and thus has been shown to have poor cell attachment and differentiation of neuron cells.^{563, 609} Therefore, SF can be utilised as a cell-repellent surface, allowing the design of short peptides coated on SF surfaces.

In this study, short peptides were designed and their solubility and self-assembly was tested and characterised via atomic force microscopy (AFM). Subsequently, RSF/peptide scaffolds were fabricated via spin coating, and were further used to culture rat pheochromocytoma (PC12) cells. This allowed the investigation of how the designed short peptides affected the response of PC12 cells, including cell attachment, differentiation and viability. AFM was also used to further analyse the phenotype of PC12 cells in respect to their size and height as well as their neurite formation.

5. 2. Methods

5.2.1. Peptide solution preparation

It was attempted to dissolve the designed peptides AC-I₃RGDS-COOH (I₃RGDS), AC-I₃KVAV-COOH (I₃KVAV), AC-I₃YIGSR-COOH (I₃YIGSR), AC-I₃PDSGR-COOH (I₃PDSGR) and AC-I₃PHSRN-COOH (I₃PHSRN), in 20 mM HEPES buffer at 1 mg/mL. The peptide solutions were influenced by means of a variety of external environmental conditions including temperature and pH in an attempt to fully dissolve the peptides and promote self-assembly.

5.2.2. Investigation of time dependent peptide self-assembly

The synthetic peptide I₃RGDS was dissolved in 20 mM HEPES buffer (pH 7.5) at 1 mg/mL. The synthetic peptides I₃KVAV and I₃YIGSR were dissolved in 20 mM HEPES buffer (pH 12.5) at 1 mg/mL. After this, samples of the peptide solutions were dripped (around 20 μ L) onto fresh mica at different time intervals (0 h, 3 h, 6 h, 9 h and 3 days) and then dried under ambient conditions prior to AFM characterization.

5.2.3. Preparation of RSF/peptide bilayer scaffolds

The synthetic peptide I₃RGDS was dissolved in 20 mM HEPES buffer (pH 7.5) at 1 mg/mL. The synthetic peptides I₃KVAV and I₃YIGSR were dissolved in 20 mM HEPES buffer (pH 12.5) at 1 mg/mL. After complete dissolution, a mixture of two peptide solutions at 1:1 volume ratio was done. These peptide solutions were then incubated for 1 week under ambient conditions for self-assembly to commence.

The RSF/peptide bilayer scaffolds were prepared by following a previously described method. RSF/peptide bilayer scaffolds were fabricated through spin coating (Laurell Technologies Corporation, USA) onto 1 cm² glass slides or silicon wafers. The first layer of RSF (30 μ L, 8000 rpm, 25 s) was coated followed by 95% ethanol (20 μ L, 8000 rpm, 25 s) to convert the structure of RSF from soluble silk I to insoluble silk II.¹⁴⁸ Then, the peptide solution (30 μ L, 8000 rpm, 25 s) was spin coated onto RSF substrate to form second layer. The concentration of RSF was diluted to 40 mg/mL and the concentration of either of

peptide solution or mixed peptide solution was 1 mg/mL. The samples were designed as RSF and peptide solution or mixed peptide solution. For example, RSF/I₃KVAV/I₃YGSR means 1mL peptide I₃KVAV solution at 1 mg/mL mixed with 1mL peptide I₃YGSR solution at 1 mg/mL were coated onto RSF (40 mg/mL) surface.

5. 3. Results and discussion

5.3.1. Investigation of the properties of designed short peptides

The chemical structures of the designed short peptides are shown in [Figure 5-1 A](#). Structurally the N terminal connected I₃ tail is blocked by an acyl group to increase tendency for aggregation, whilst the C terminal connected hydrophilic head (active sequence) is left open. The hydrophilic head of the designed short peptides contains hydrophobic or polar uncharged amino acid residues, so that they do not need an amine group to increase their self-assembly ability. To test their solubility and self-assembly ability, the designed short peptides were dissolved in 20 mM HEPES buffer at various pH values prior to AFM characterization. HEPES buffer rather than pure water was chosen as it promotes the dissolution of peptides, this is due to the fact that HEPES buffer is negatively charge when the pH is over 9.5 and positively charged at pH's below 5.5.⁶¹⁰ In addition, it can reduce the electrostatic repulsion between the peptide monomers of peptides during self-assembly process.

Unlike the peptide I₃QGK that has been previously reported,²⁶ our peptide I₃RGDS was unable to completely dissolve in HEPES buffer at pH 6.0 which we assume is due to the arginine (Ala) residues present with a hydrophobicity value of 0.31. In addition to this, when the peptide I₃RGDS was dissolved in HEPES buffer (pH 6.0), the pH of the mixture decreased below pH 4.0 almost reaching the peptides isoelectric point (PI). Therefore, I₃RGDS could not be completely dissolved under this condition. Increasing the pH of peptide I₃RGDS solution to around pH 5.0 enabled the complete dissolution. Therefore, the best condition for I₃RGDS was 20 mM HEPES buffer at a pH of 7.5. According to [Figure 5-1 B \(a\) and \(b\)](#), although the dissolving part of peptide I₃RGDS in 20 mM HEPES buffer can form nanofibers (pH 6.0), the amounts of nanofibers increased significantly when I₃RGDS was dissolved in 20 mM HEPES buffer at an initial

pH of 7.5. Therefore, increasing the pH value of the peptide I₃RGDS solution could increase its solubility, allowing more peptides available for self-assembly, hence the more fibres formed.

Compared to I₃RGDS, there are more hydrophobic residues present in the peptides I₃KVAV and I₃YIGSR. Therefore, these show a stronger self-assembly ability, but are also less soluble. Adding I₃KVAV and I₃YIGSR into 20 mM HEPES buffer at an initial pH of 6.0, the pH of the mixture decreased to around pH 4.0, where the PI of I₃KVAV and I₃YIGSR are 5.68 and 5.12 respectively. Therefore, both peptides showed very poor solubility in this buffer, but the dissolved part could still form nanofibers (Figure 5-1 B (c) and (e)). When the pH value was increased to reach pH 6.0, both peptides could be completely dissolved. However, partial aggregation and precipitation of both short peptides could be observed. That is because of the positive charged lysine (Lys) and Ala residues in the peptides, which can connect with carboxyl groups via charge-charge interactions. When the pH value of peptide solution was increased to over pH 9.5, the positive charge of Lys and Ala forms water by hydroxide. Therefore, the best dissolution condition for the peptides I₃KVAV and I₃YIGSR were in 20 mM HEPES buffer at an initial pH 12.5, which showed excellent solubility and self-assembly capabilities (Figure 5-1 B (d) and (f)).

Compared to the peptide sequence I₃RGDS, the peptide I₃PDSGR has an added proline (Pro) residue in its sequence. The hydrophobicity value of Pro is 0.72, resulting in a poor solubility in HEPES buffer (pH 6). In addition, as can be seen from Figure 5-1 B (g), the self-assembly ability of I₃PDSGR was also poor for the dissolved part, only a few small peptide segments were formed. That is because of Pro residue is the most destabilizing group, which may inhibit the backbone to form a secondary structure, such as a β -sheet conformation.⁶¹¹

The peptide sequence I₃PHSRN showed good solubility in 20 mM HEPES buffer at pH 6.0 but could not self-assemble (Figure 5-1 B (h)). Therefore, we find that I₃PHSRN lacks self-assembly ability. Its self-assembly capabilities could be improved by blocking with an amine group on its C terminal.

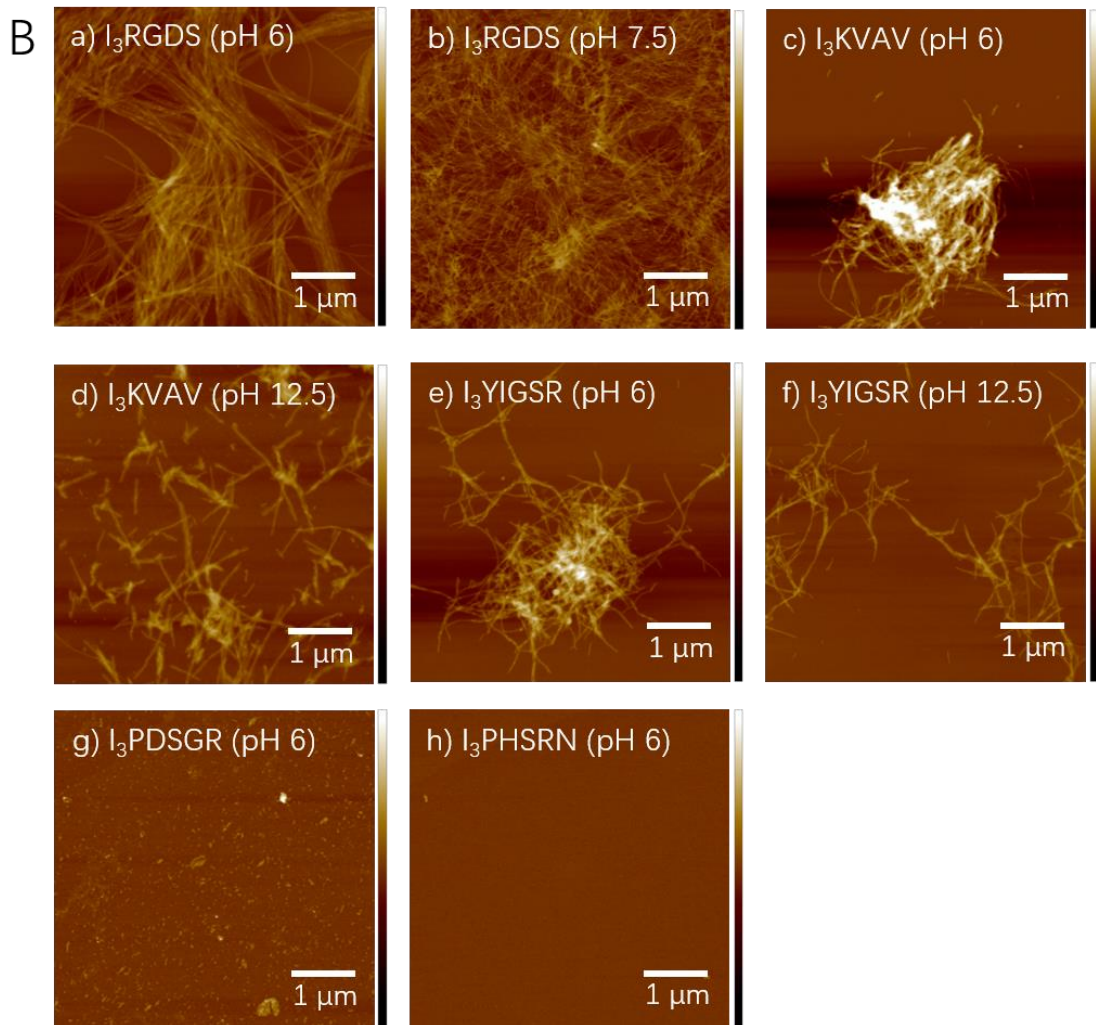
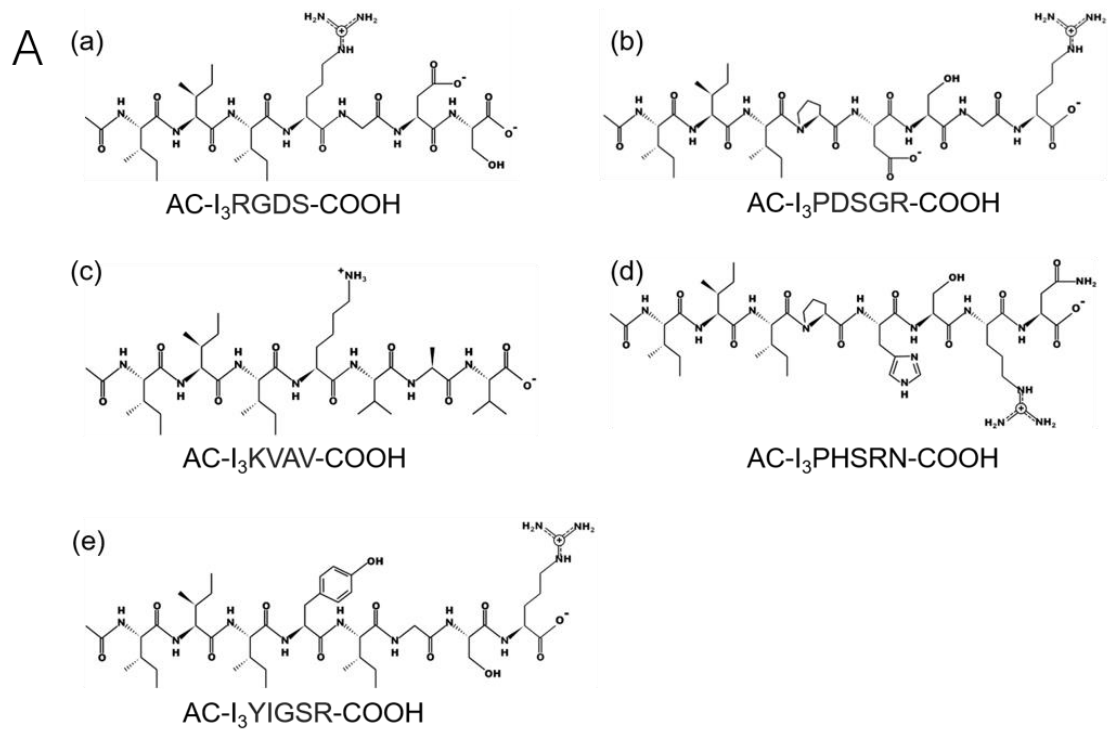


Figure 5-1 A, Chemical structures of the designed short peptides. (a) I₃RGDS; (b) I₃PDSGR; (c) I₃KVAV; (d) I₃PHSRN and (e) I₃YIGSR. B, AFM topographical images (25 μm²) showing short designed peptides (1 mg/mL in 20 mM HEPES buffer) self-assembles 3 days at different initial pH value. Peptide I₃RGDS self-assembles at (a) pH 6.0 and (b) pH 7.5. Peptide I₃KVAV self-assembling at (c) pH 6.0 and (d) pH 12.5. Peptide I₃YIGSR self-assembles at (e) pH 6.0 and (f) pH 12.5. (g) Peptide I₃PDSGR assembles at pH 6.0 and (h) Peptide I₃PHSRN assembles at pH 6.0. The Z scales (height) of image (a) to (d) are 100 nm; (e) and (f) are 80 nm; (g) and (h) are 30 nm.

5.3.2. Time effect of peptides self-assembly

The dynamic self-assembly process of the peptide I₃RGDS was similar to that of I₃K and I₃QGK.^{26, 299} After dissolution of I₃RGDS, small short stacks are immediately formed through hydrophobic interactions between the I₃ tails (Figure 5-2 (a)). These stacks continued to grow, resulting in the formation of nanoribbons (Figure 5-2 (b)). Furthermore, as nanoribbons grow, they tend to twist due to electrostatic repulsion and molecular chirality (Figure 5-2 (c)). At the later stage of self-assembly, long and uniform nanofibers are formed (Figure 5-2 (d)).

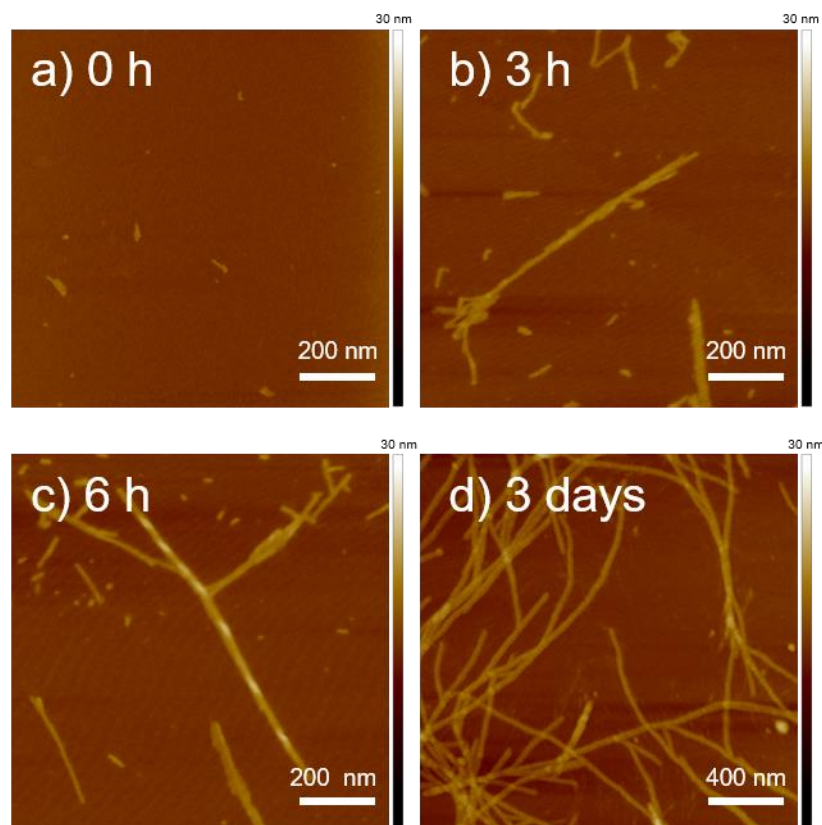


Figure 5-2 AFM topographical images of peptide I₃RGDS dynamic self-assembly (1 mg/ml in 20 mM HEPES buffer at pH 7.5) at different time scales. (a) 0 h; (b) 3 h; (c) 6 h and (d) 3 days. The Z scales for all images are 30 nm as indicated.

The peptide I₃KVAV also can self-assemble into long and uniform nanofibers (Figure 5-3 (d)), with a dynamic self-assembly process similar to that of I₃RGDS. Here the hydrophobic interactions and hydrogen bonding play a dominant role during the initial stage of self-assembly, forming anti-parallel β -sheets (Figure 5-3 (a) and (b)). Subsequently, long-range interactions become dominant, leads to a twist occurs (Figure 5-3 (c)). Continued growth eventually develops into long and uniform nanofibers (Figure 5-3 (d)). It is worthy to note that, the speed at which the peptide I₃KVAV self-assembles is faster than that of I₃RGDS, especially in later stage of the self-assembly process. This is most likely due to the Lys residues in the middle of backbone. The electrostatic repulsion amongst the side chains of the Lys residues has a strong hydrophobic attraction towards the side chains of the I₃ tails as well as sides chains of the Val and Ala residues. This enables the formation of nanofibers with greater speed.

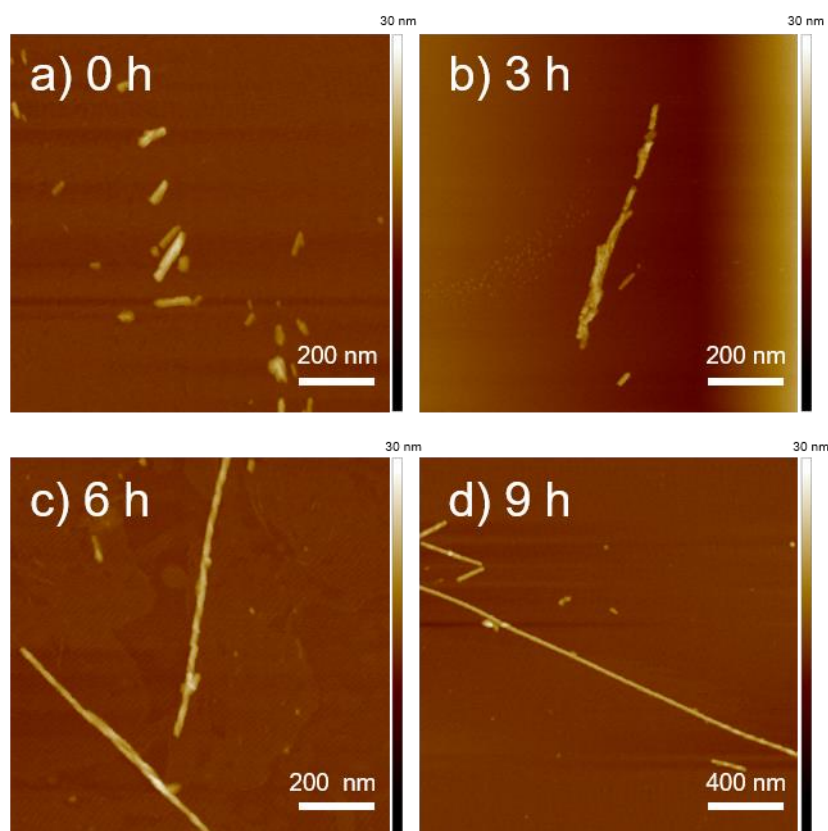


Figure 5-3 AFM topographical images of peptide I₃KVAV dynamic self-assembly (1 mg/ml in 20 mM HEPES buffer at pH 12.5) at different time scales. (a) 0 h; (b) 3 h; (c) 6 h and (d) 9 h. The Z scales for all images are 30 nm as indicated.

After complete dissolution of I₃YIGSR in HEPES buffer at 20 mM and a pH of 12.5, the self-assembly had already completed, evident from long and uniform nanofibers formed (Figure 5-4). The self-assembly process of I₃YIGSR is also a dynamic process. Because small and short stacks and twisted nanoribbons could be observed at 0 hour (Figure 5-4 (a)). Tyrosine (Tyr) residues present in the peptide I₃YIGSR can form π - π stacking to structurally facilitate the peptide self-assembly. In addition, the tendency for aggregation is increased due to long hydrophobic tails present in I₃YIGSR. Due to these features I₃YIGSR has the fastest self-assembly among the three designed short peptides.

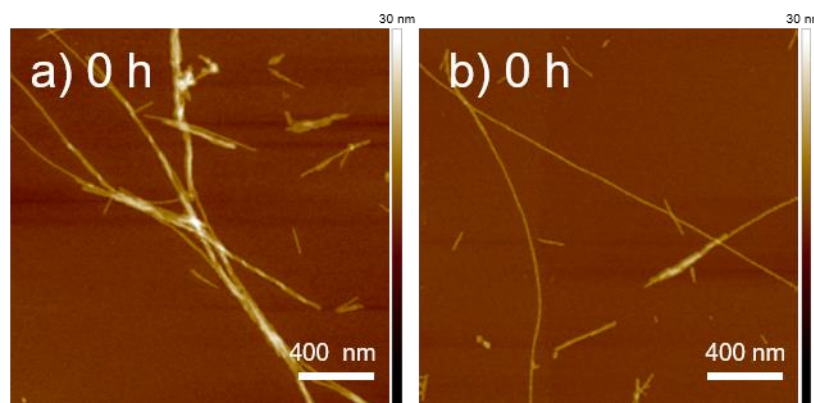


Figure 5-4 AFM topographical images of peptide I₃YIGSR self-assembly (1 mg/ml in 20 mM HEPES buffer at pH 12.5) at 0 h (a) and (b). The Z scales for all images are 30 nm as indicated.

5.3.3. Further characterize designed short peptides

AFM was used to characterize the width and height of the designed short peptides after incubation for 3 days during self-assembly into nanofibers (Figure 5-5 A). As can be seen from Figure 5-5 B, there was a significant greater width of I₃YIGSR nanofibers (58.3 ± 3.9 nm) compared to those of I₃RGDS nanofibers (45.7 ± 4.0 nm) and I₃KVAV nanofibers (47.7 ± 2.6 nm), which demonstrates that I₃YIGSR possesses a stronger self-aggregation ability. This result was further confirmed due to the Tyr residues and long hydrophobic tails that can help in the self-aggregation of short peptides. According to previously reported works,^{304, 612} hydrogen bonding is mainly responsible for the 1-D growth of the

assembly, and hydrophobic interactions amongst the side chains of hydrophobic amino acids can drive lateral growth. Therefore, there was no significant difference of width between I₃RGDS nanofibers and I₃KVAV nanofibers, but the height of I₃RGDS nanofibers (5.12 ± 0.54 nm) was significantly lower than that of I₃KVAV nanofibers (8.34 ± 0.43 nm). Although there was no significant difference in height between I₃KVAV nanofibers and I₃YIGSR nanofibers (6.44 ± 1.44 nm), the formed I₃KVAV nanofibers showed more entangled tendency. The peptide nanofibers tend to entangle is due to the nonspecific inter fibre attractive forces exceed repulsive force.⁶¹³ Therefore, the inter fibre force (between attractive forces and repulsive force) of I₃KVAV nanofibers is larger than inter fibre force of I₃YIGSR nanofibers. This means peptide I₃KVAV at high concentration is easier to self-assemble into hydrogel.

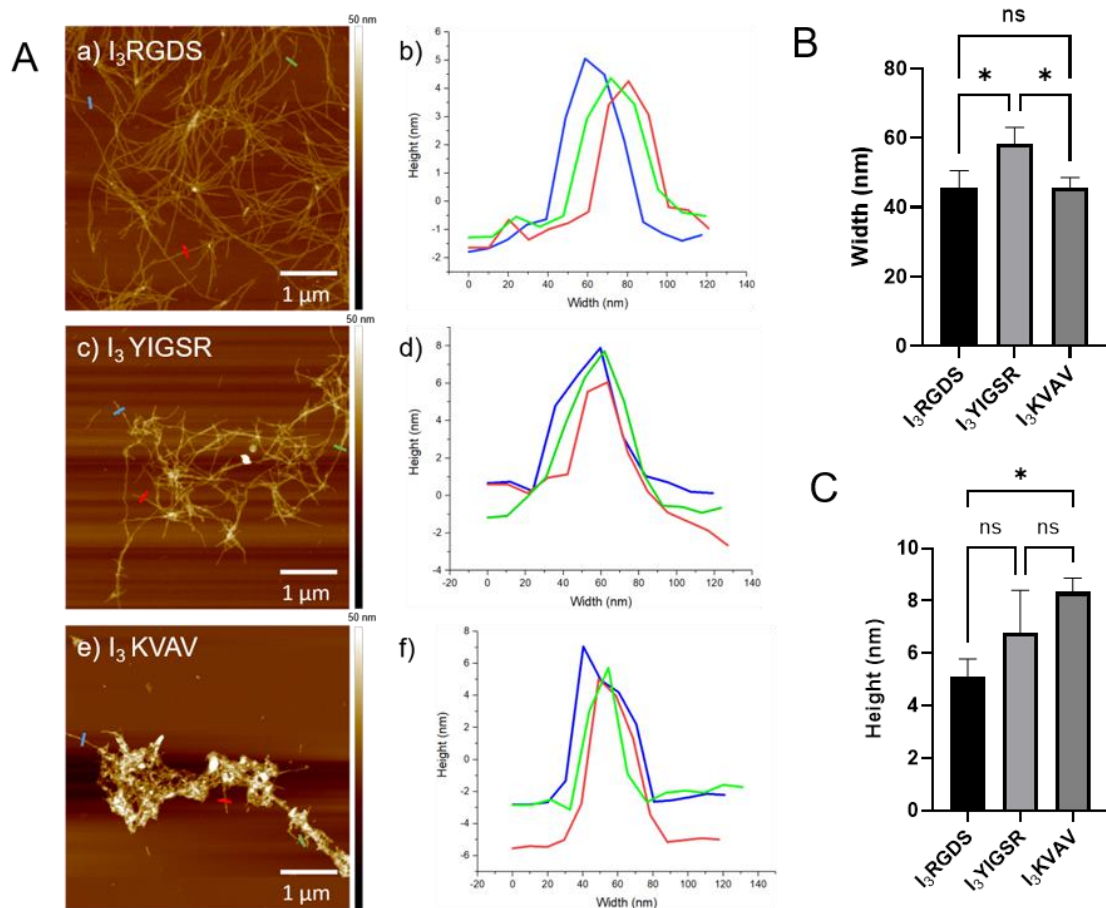


Figure 5-5 A, AFM topographical images ($25 \mu\text{m}^2$) of self-assembled short peptides in HEPES buffer (20 mM; 1 mg/mL) for 3 days, in which (a) peptide I₃RGDS self-assembled in HEPES buffer at pH 7.5, (c) peptide I₃YIGSR and (e) peptide I₃KVAV self-assembled in HEPES buffer at pH 12.5. Z scale height of all images = 50 nm. The areas labelled by blue, red and green colour in (a), (c) and (e) were analysed in (b), (d) and (f), including their height and width of cross-

section line along a nanofiber. B and C, Average width, and height of cross-section lines along nanofibers (n=3).

5.3.4. Characterization of RSF/peptide bilayer scaffolds

The surface topography of scaffolds has a real impact on cell biology behaviour, such as cell adhesion, proliferation and migration.⁶¹⁴ Therefore, it is necessary to investigate whether the self-assembled peptide can be washed off from the surface when immersed in an aqueous solution. AFM was used to characterize the topography of RSF/peptides scaffolds after immersion in deionized water and incubation under a 5% CO₂ atmosphere at 37 °C for 6 days (Figure 5-6). The results indicated that the self-assembled peptides possess a good adhesion to RSF substrates. In detail, RSF-only scaffolds formed a stable structure after the conformational change converting the soluble silk I to insoluble silk II by treatment with ethanol was done (Figure 5-6 (a)).¹⁴⁸ In addition, RSF proteins contain lots of amino acids such as serine (Ser) and Tyr residues. Their side chains are capable to form hydrogen bonds with biological substrates.⁶¹⁵ This is reason why self-assembled peptides are highly adhesive to RSF surfaces (Figure 5-6 (b)-(h)). It has been widely shown that type I collagen can promote the cells adhesion of PC 12 as well as differentiation and neurite outgrowth,⁶¹⁶ hence it was used as a control group in this study. As shown in Figure 5-6 (i), a coating of type I collagen resulted in a smooth layer on glass substrates.

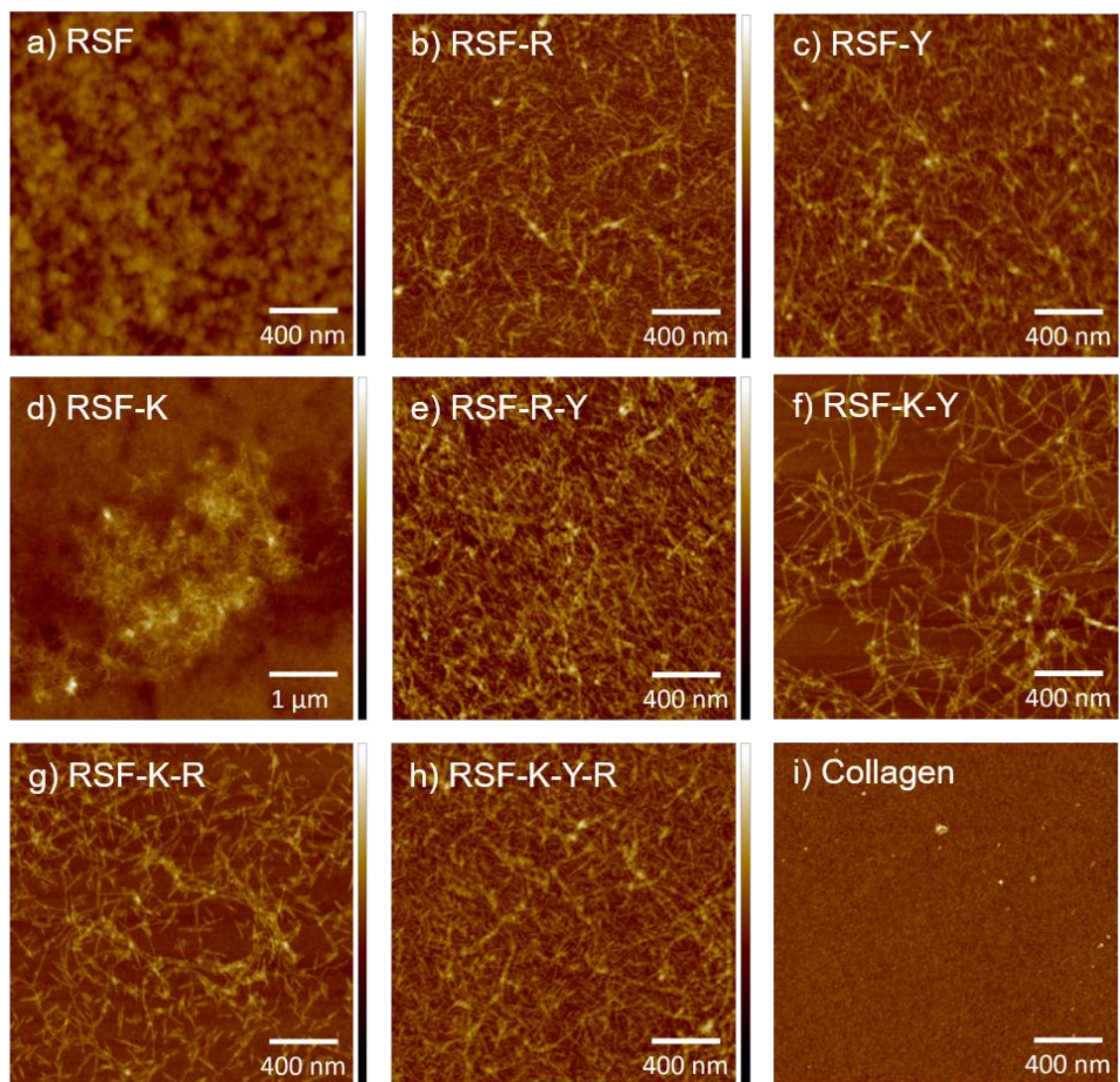


Figure 5-6 AFM topographical images of RSF/peptides scaffolds after immersion in deionized water and incubation under a 5% CO₂ atmosphere at 37 °C for 6 days. (a) RSF scaffold; (b) RSF/I₃RGDS scaffold, (c) RSF/I₃YIGSR scaffold, (d) RSF/I₃KVAV scaffold, (e) RSF/I₃RGDS/I₃YIGSR scaffold, (f) RSF/I₃KVAV/I₃YIGSR scaffold (g) RSF/I₃KVAV/I₃RGDS scaffold, (h) RSF/I₃KVAV/I₃YIGSR/I₃RGDS scaffold; and (i) Type I collagen. The Z scales for images (a)-(c) and (e)-(h) are 30 nm; (d) is 90 nm and (i) is 10 nm as indicated.

5.3.5. Cellular adhesion and viability

The Live/dead assay was carried out to investigate PC12 neuronal cell adhesion and viability adhered on different RSF/peptide scaffold surfaces (Figure 5-7). As can be seen from Figure 5-7 A (a), pure RSF scaffold surfaces showed poor PC12 cell attachment (800 ± 632 cells/cm²). That is because pure RSF lacks cell recognized active sequences, leading to easy cell detachment during cell culture. When the designed short peptides sequences were coated

onto RSF surfaces however, all surfaces supported excellent PC12 cell attachment, with no notable dead cells to be observed (Figure 5-7 A (b)-(h)). This is due to the adhesion motifs RGDS, IKVAV and YIGSR present in the designed short peptides enabling the promotion of proliferation and attachment of the cells.^{617, 618} Type I collagen, a famous biocompatibility material, is currently the gold standard for nerve cells.^{578, 602} There was a significant higher cell population on type I collagen surfaces (37600 ± 1600 cells/cm²) compared to those on RSF/I₃RGDS surfaces (26000 ± 4850 cells/cm²; Figure 5-7 B; **p <0.01). However, on I₃KVAV or I₃YIGSR nanofiber coated RSF surfaces no significant difference could be observed compared to that of type I collagen. The highest number of PC12 cells were identified when grown on RSF/I₃KVAV/I₃YGSR surfaces (50267 ± 2948 cells/cm²), which showed a significantly higher cell population compared to that of type I collagen (Figure 5-7 B; **p <0.01). In addition, the live/dead assay revealed RSF/peptide scaffolds possess excellent biocompatibility, which similar values to type I collagen (Figure 5-7 C). These results demonstrated that our designed short peptides sequences can provide similar efficacy to other short peptides (such as Fmoc-IKVAV and Fmoc-YIGSR) previously reported in literature, making them promising candidates for nerve tissue engineering applications.⁶¹⁸

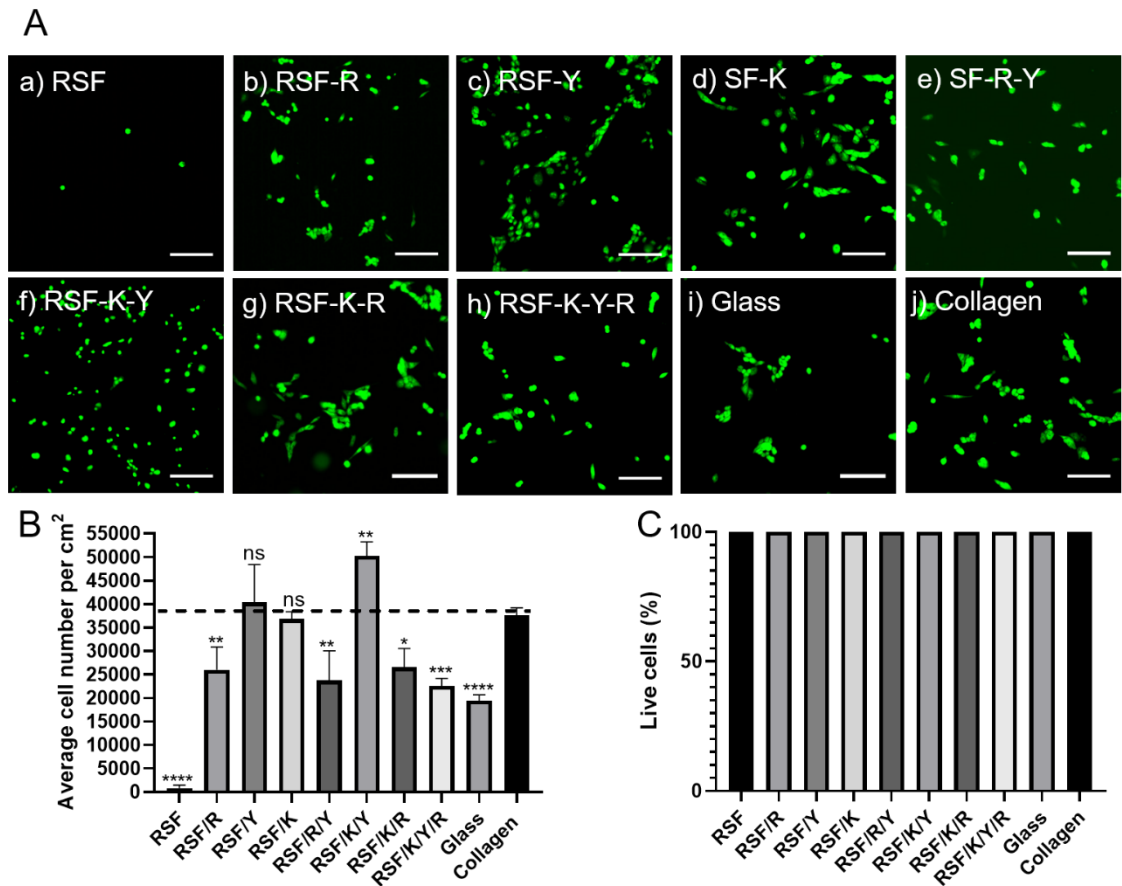


Figure 5-7 A, Live/dead assay of PC12 neuronal cells adhered on various RSF/peptides scaffolds surfaces. (a) RSF scaffold; (b) RSF/I₃RGDS scaffold, (c) RSF/I₃YIGSR scaffold, (d) RSF/I₃KVAV scaffold, (e) RSF/I₃RGDS/I₃YIGSR scaffold, (f) RSF/I₃KVAV/I₃YIGSR scaffold (g) RSF/I₃KVAV/I₃RGDS scaffold, (h) RSF/I₃KVAV/I₃YIGSR/I₃RGDS scaffold; (i) glass control and (j) Type I collagen (control). Syto-9TM was used to stain live cells (green) and propidium iodide was used to stain dead cells (red). The scale bar for all images is 100 μ m as indicated. B, Average cell number (per cm²) adhered on various RSF/peptides scaffolds surfaces. All values are compared to Type I collagen coated surface. C, Percentage of lives adhered on various RSF/peptides scaffolds surfaces. $n \geq 3$. (**** $p < 0.0001$; *** $p < 0.001$; ** $p < 0.01$ and * $p < 0.05$).

5.3.6. Cell morphology

The investigation of PC12 cell morphology adhered onto different RSF/peptides scaffolds was carried out by immunofluorescence staining technology (Figure 5-8), in which the cell nucleus was stained by DAPI and F-actin was stained by FITC-phalloidin. Pure RSF surfaces showed poor performance in cell spreading (Figure 5-8 (a)), similar to previously reported works.^{26, 608} When I₃KVAV nanofibers or I₃YIGSR nanofibers were coated onto RSF surfaces, extended

cell morphologies were observed (Figure 5-8 (b) and (d)). However, this effect appeared not to be significant on RSF/I₃RGDS scaffolds (Figure 5-8 (c)), indicating the presence of I₃RGDS nanofibers was not able to active good cell adhesion, such as spreading and flattening. The scaffold surfaces containing equimolar concentrations of peptide I₃RGDS and peptide I₃KVAV or peptide I₃YIGSR showed improved spreading (Figure 5-8 (e) and (g)). This result was similar to those reported by Lee et al.⁶⁰⁴ who indicated the combination of the peptides RGD and YIGSR showed a synergistic effect on the spreading of PC12 cells. Laminin based peptides I₃KVAV and I₃YIGSR also showed a synergistic regulatory effect on cell morphology for which the cell adhesion properties even better than those growth on type I collagen (Figure 5-8 (f) and (j)). The results indicated RSF/I₃KVAV/I₃YIGSR scaffolds were the best for the positive regulation of morphology of PC12 cells.

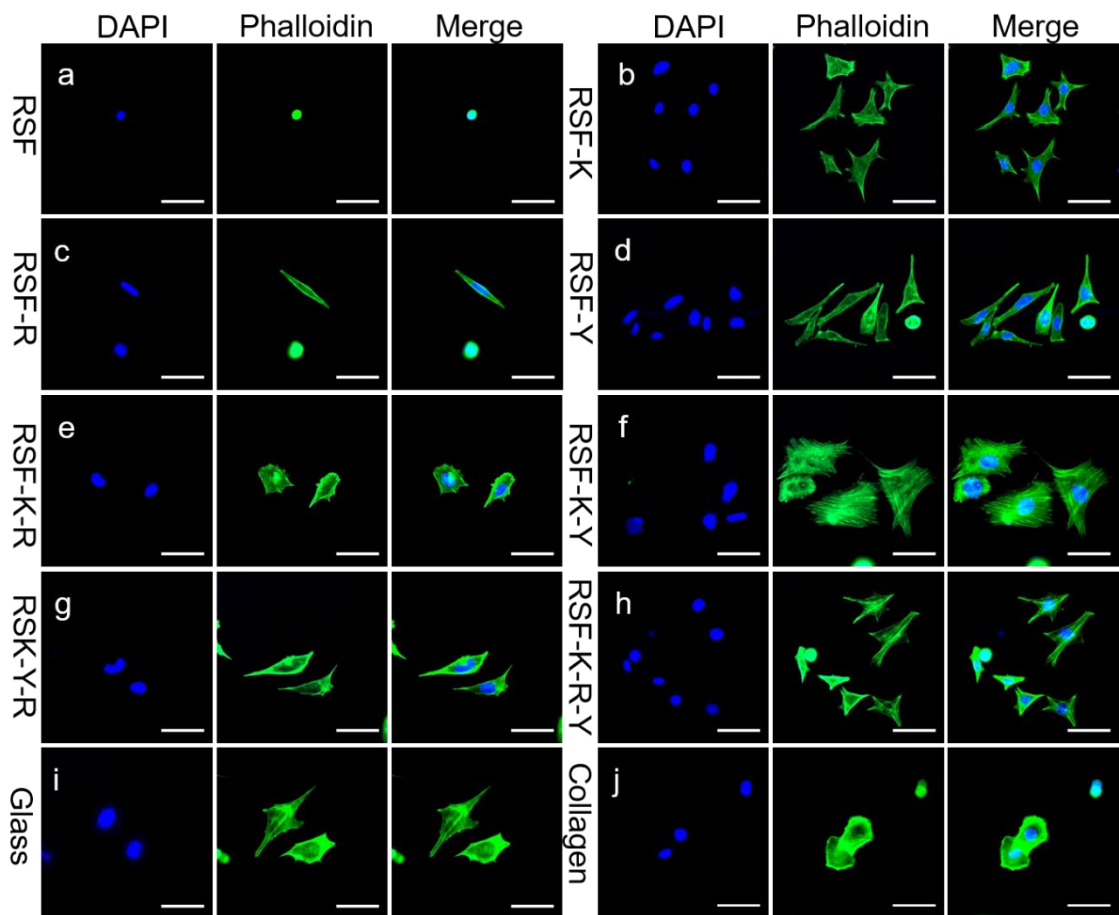


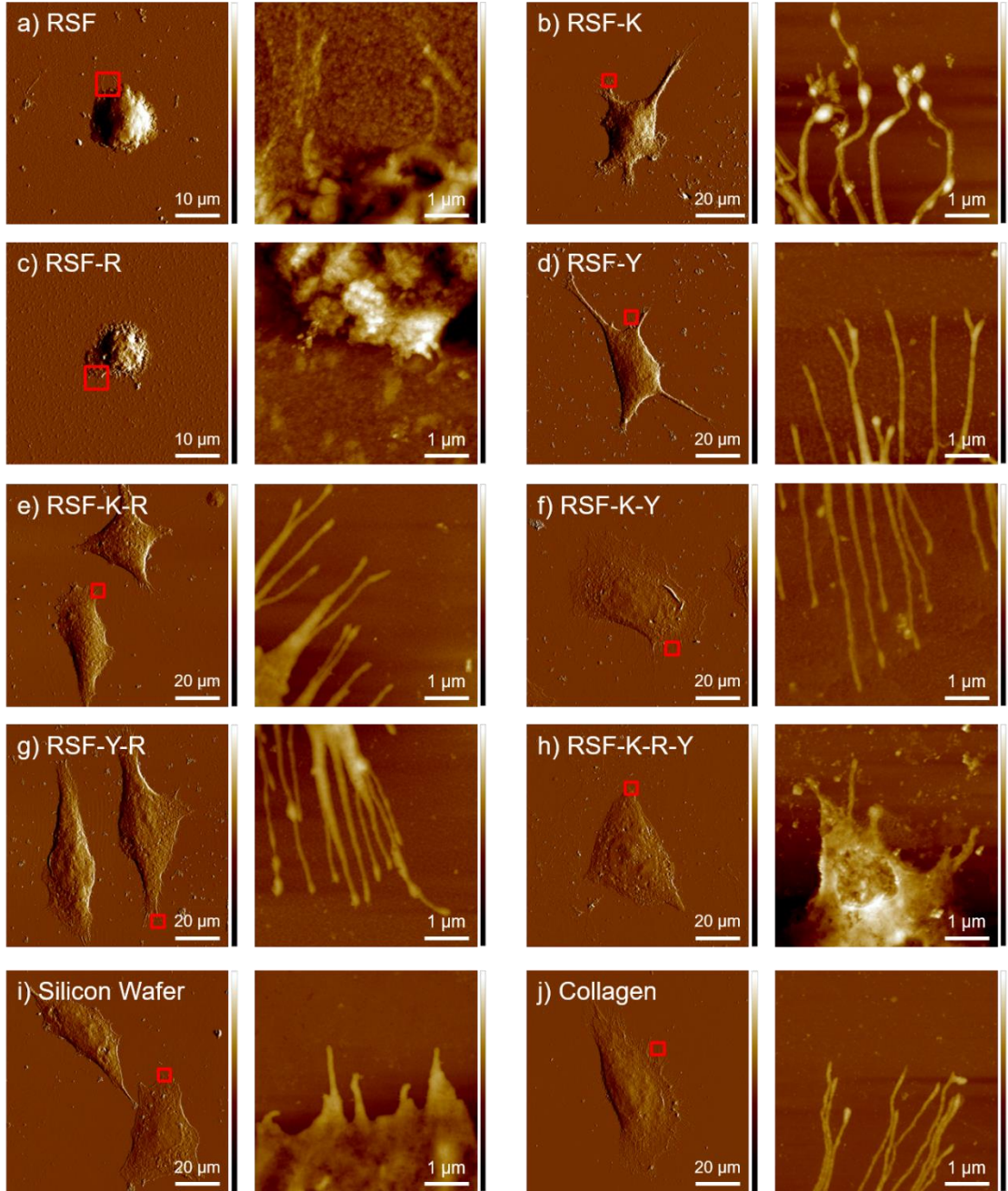
Figure 5-8 F-actin staining of PC12 neuronal cells attached to various RSF/peptides scaffolds. (a) RSF scaffold; (b) RSF/I₃KVAV scaffold, (c) RSF/I₃RGDS scaffold, (d) RSF/I₃YIGSR scaffold, (e) RSF/I₃KVAV/I₃RGDS scaffold, (f) RSF/I₃KVAV/I₃YIGSR scaffold, (g) RSF/I₃YIGSR/I₃RGDS scaffold, (h) RSF/I₃KVAV/I₃RGDS/I₃YIGSR scaffold; (i) blank glass and (j) Type I collagen. The nucleus was

stained by DAPI (blue) and F-actin was stained by FITC-phalloidin. The scale bar for all images is 50 μm .

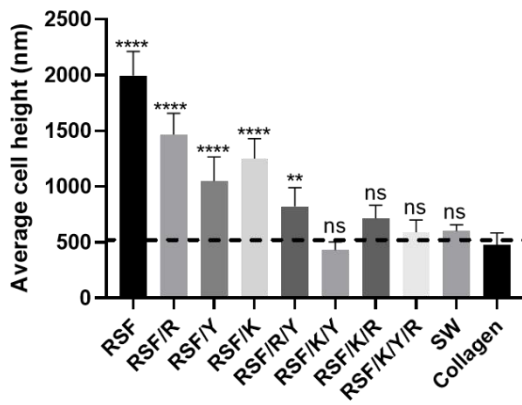
AFM was also applied to continue to investigate the PC12 cell morphologies adhered to different RSF/peptide scaffolds (Figure 5-9 and Figure 5-10). The average cell height on pure RSF scaffolds was measured at 1745 ± 165 nm, which had no significant difference compared to that on RSF/I₃RGDS scaffolds (1465 ± 192 nm). In addition, as shown in Figure 5-9 C, the average cell size on pure RSF (149 ± 7.9 μm^2) and RSF/I₃RGDS scaffolds (125 ± 4.9 μm^2) had no significant difference. These results indicated I₃RGDS nanofibers do not promote differentiation into neuronal phenotypes, which was consistent with immunofluorescence staining analysis shown in Figure 5-8 (b). In contrast however, the peptides I₃RGDS simply mixed with I₃YIGSR or I₃KVAV at a ratio of 1:1, keeping the overall concentration at the same 1 mg/mL, resulted in a significant increase in observed average cell height and area of PC12 cells (Figure 5-8 (e) and (g)). Interestingly, there was no significant difference of average cell height between the RSF/I₃KVAV/I₃RGDS scaffold (714 ± 118 nm) and collagen (473 ± 111 nm). In addition, no significant difference of average cell area between the RSF/I₃RGDS/I₃YIGSR scaffold (777.4 ± 142 μm^2) and collagen (1075 ± 251 μm^2) could be observed. However, both RSF/I₃YIGSR (1049.5 ± 216 nm; 552.3 ± 47 μm^2) and RSF/I₃KVAV scaffolds (1250 ± 180 nm; 594.9 ± 40 μm^2) had a significant difference in average cell height and the cell surface area compared to those grown on collagen. This implies that I₃RGDS had a synergistic effect when combined with I₃YIGSR or I₃KVAV in terms of PC12 cells active adhesion. Furthermore, the peptides I₃YIGSR and I₃KVAV also showed a synergistic effect on the spreading of PC12 cells (429.6 ± 74.2 nm; 1200.2 ± 308 μm^2), which however had no significant difference to the average cell height and area compared to those grown on collagen. In addition to these dual-peptide presenting scaffold, triple-peptide scaffolds also showed a synergistic effect on the spreading of PC12 cells. The areas of interest indicated with red boxes on the figures were enlarged to further investigate the structure of neurites. As can be seen from Figure 5-9 and Figure 5-10, dendrites did not grow well on pure silicon wafer samples, pure RSF, RSF/I₃RGDS and RSF/I₃RGDS/I₃YIGSR/I₃KVAV scaffolds. Although the cells adhered on dual-peptide presenting scaffolds had long axons, terminal buttons could be only

clearly seen on RSF/I₃KVAV scaffolds, indicating I₃KVAV nanofibers promoted the growth of axon terminal buttons the best. Therefore, the molar ratio of the peptides I₃KVAV and I₃YIGSR could be regulated to over 1, such as 2:1, which may strongly promote neurite formation. Overall, laminin derived self-assembled peptides (I₃YIGSR and I₃KVAV) provided a synergistic effect, enabling cells to fully spread and promote the formation of long neurites. This result was similar to that of collagen. Therefore, this peptide combination it has a great potential to be used instead of collagen for the regeneration of neural tissue.

A



B



C

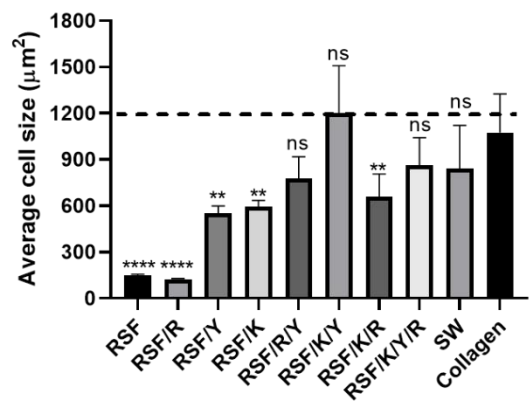


Figure 5-9 A, AFM peak force images (left) and topographical images (right) of PC 12 neuronal cells attached to different RSF/peptides scaffolds, in which enlarged areas of red box in right images are shown in right of images. (a) RSF scaffold; (b) RSF/I₃KVAV scaffold, (c) RSF/I₃RGDS scaffold, (d) RSF/I₃YIGSR scaffold, (e) RSF/I₃KVAV/I₃RGDS scaffold, (f) RSF/I₃KVAV/I₃YIGSR scaffold, (g) RSF/I₃YIGSR/I₃RGDS scaffold, (h) RSF/I₃KVAV/I₃RGDS/I₃YIGSR scaffold; (i) blank silicon wafer (SW) and (j) Type I collagen. The force setpoint constant is 30 nN in all left images. The Z scale (height) bars are 150 nm in all right images. B and C indicated average cell height and size of PC12 cells in all scenarios. All values are compared to Type I collagen coated surface. (n ≥ 3; **** p < 0.0001; *** p < 0.001; ** p < 0.01 and * p < 0.05).

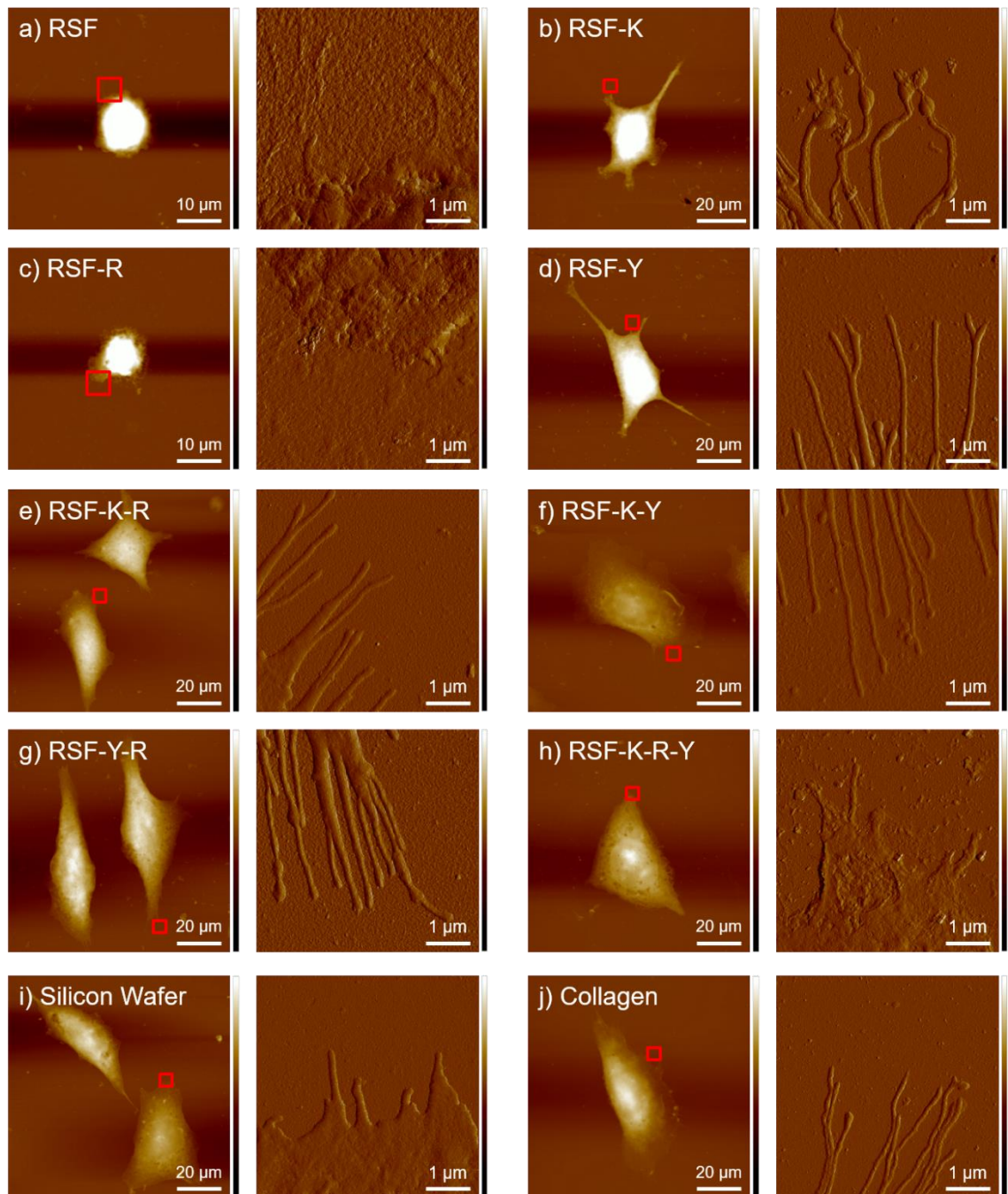


Figure 5-10 AFM topographical images (left) and peak force images (right) of PC 12 neuronal cells attached to different RSF/peptides scaffolds, in which enlarged areas of red box in right images are shown in right of images. (a) RSF scaffold; (b) RSF/I₃KVAV scaffold, (c) RSF/I₃RGDS scaffold, (d) RSF/I₃YIGSR scaffold, (e) RSF/I₃KVAV/I₃RGDS scaffold, (f) RSF/I₃KVAV/I₃YIGSR scaffold, (g) RSF/I₃YIGSR/I₃RGDS scaffold, (h) RSF/I₃KVAV/I₃RGDS/I₃YIGSR scaffold; (i) blank silicon wafer (SW) and (j) Type I collagen. The Z scale (height) bars are 1.5 μ m in all left images. The force setpoint constant is 5 nN in all right images.

5. 4. Conclusions

In this study, five different short peptides were designed based on the active sequences found in the natural ECM. It was found that the peptides I₃RGDS, I₃KVAV and I₃YIGSR could dynamically self-assemble into long and uniform nanofibers in aqueous solutions, while the peptides I₃PDSGR and I₃PHSRN were unable to self-assemble. It is believed this is due to I₃PDSGR containing pro residues, which can inhibit the formation of the secondary structure. The peptide I₃PHSRN was found to lack self-assembly capabilities. Subsequently the peptides I₃RGDS, I₃KVAV, I₃YIGSR and their mixtures were coated onto RSF substrates by spin coating and attached firmly via hydrogen bonding.⁶¹⁵

In vitro cell culture experiments with PC12 cells showed that I₃RGDS could promote proliferation, but was unable to regulate a morphological change of PC12 cells. However, the peptide I₃RGDS provided a synergistic effect when combined with the peptides I₃YIGSR or I₃KVAV, and resulted in a significantly improved morphology change of neuron cells. In addition, the presence of both peptide I₃KVAV and peptide I₃YIGSR also showed synergistic effects on PC12 cells, indicating the best attachment, proliferation and spreading that was similar to those grown on collagen substrates. Moreover, the live/dead assay revealed that the RSF substrates coated with I₃KVAV, I₃RGDS and I₃YIGSR exhibited negligible cytotoxicity against PC12 cells. As such, the presence of both the peptides I₃KVAV and I₃YIGSR was able to better regulate neuron cell proliferation and attachment, which gives rise to a great potential to valuable applications for future nerve tissue engineering applications.

6. Conclusions and future work

6. 1. Conclusions

In this thesis, two variety of attractive biomaterials, silk fibroin (SF) and peptide amphiphiles (PAs), have been fully investigated and discussed relating to their performance for tissue engineering (TE) applications. Although SF-based scaffolds have been successfully applied in most TE applications, such as musculoskeletal, skin and wound, they showed poor performance for nerve TE, due to lack of cell recognized peptide segments. PAs can be further divided into few sub-classes, in which ionic self-complementary peptides and lipidated PAs which have been widely studied for use in nerve TE. However, surfactant-like peptides are another sub-class of PAs, which have not been applied to nerve TE to date. Therefore, surfactant-like peptides were used here to improve the performance of SF for nerve TE applications.

The peptides I₃K and I₃QGK are typical examples of surfactant-like peptides, which can self-assemble into long and uniform nanofibers as previously reported. The successfully self-assembly was characterised by atomic force microscopy (AFM). It was demonstrated that the formed nanofibers, with strong positive charges due to lysine residues strongly adhered to SF coated substrate via charge-charge interaction. Furthermore, results indicated that nearly no neuron cells adhere onto pure SF scaffold. However, when peptide nanofibers were coated onto SF surfaces morphology and amount of neuron cells significant increased. For both I₃K and I₃QGK concentrations between 3 and 4 mg/mL showed the best cell attachment, proliferation and neurite outgrowth of neuron cells. In addition, according to AFM results, the peptide I₃QGK can foster growth of axon terminal buttons while I₃K was unable to. This might be due to the glutamine residues present in I₃QGK. The live/dead assay showed SF, I₃K and I₃QGK possess negligible cytotoxicity against neuron cells. In addition to this, inkjet printing was used to print peptide nanofibers into complex patterns (e.g., the university icon and words) onto SF surfaces, enabling cell guidance of neuron cells. This approach to micro-pattern neural cells might provide a way to further analysis and understand neurite development and cell-cell interactions *in vitro*.

Inspired from the typical examples of surfactant-like peptides, five different short peptides were designed focused on active sequences present in the extracellular matrix, including I₃KVAV, I₃RGDS, I₃YIGSR, I₃PDSGR and I₃PHSRN. Unfortunately, the peptides I₃PDSGR and I₃PHSRN were found to be unable to self-assemble into long and uniform nanofibers. This is most likely due to proline residues present in the backbone, which can inhibit the formation of secondary structures. The peptide I₃PHSRN also lacked self-assembly capabilities. The peptides I₃KVAV, I₃RGDS and I₃YIGSR were able to self-assemble into nanofibrillar structures after incubation and were further investigated. It was found that pure SF substrates could serve as a cell-repellent agent, however, it also allows for strong adhesion of peptides via hydrogen bonding with I₃KVAV, I₃RGDS and I₃YIGSR. Although the peptide I₃RGDS could improve the proliferation of neuron cells, it could not control the phenotype of neuron cells. However, I₃RGDS provided a synergistic effect together with I₃YIGSR or I₃KVAV or both, resulting in a significantly improved morphology change of neuron cells. The presence of both peptides I₃YIGSR and I₃KVAV showed the best synergistic regulatory effect on the response of neuron cells, including cell attachment, differentiation and spreading. This result was similar to those grown on collagen. In addition, I₃KVAV, I₃RGDS and I₃YIGSR showed low cytotoxicity towards neuron cells. The combination of the peptides I₃KVAV and I₃YIGSR indicates a great potential for use instead of collagen for nerve regeneration applications.

These results strongly indicate that surfactant-like peptides can also serve as successful biomaterial for scaffolds in nerve TE.

6. 2. Future work

6.2.1. Based on this thesis

The results collected and analysed in this thesis indicated that self-assembled peptides could promote proliferation, morphological change, differentiation of neuron cells, *in vitro*. However, *in vivo* studies should be investigated before commercial applications can be considered. Hydrogels are one of the most attractive scaffolds to provide a suitable three-dimension (3D) microenvironment for neuron cells. In addition, these can better mimic the extracellular matrix (ECM) of the human body over two-dimensional (2D) models. Therefore, the fabrication of 3D hydrogels is very important and necessary for future studies. Although self-assembled peptides can eventually lead to the formation of hydrogels, a huge amount of self-assembled peptides will need to be used to achieve this. In addition, pure peptide formed hydrogels have poor mechanical properties.

The RSF hydrogel scaffolds can be made by the introduction of crosslinkers and catalysts to the RSF solution at sub-zero temperatures.^{619, 620} This was tested by using glutaraldehyde as the crosslinker and N,N,N',N'-Tetramethylethylenediamine (TEMED) as the catalyst. As shown in [Figure 6-1 A](#), the crosslinker (glutaraldehyde) and catalyst (TEMED) were added to the RSF solution at 120 mg/mL, which formed hydrogels at -16 °C within 1 day. Interestingly, only mixtures containing glutaraldehyde and TEMED added into RSF the solution at equal volumes formed hydrogels. Despite quantitatively evaluating the reaction with RSF, glutaraldehyde and TEMED is difficult, the mechanical performance of these hydrogels fabricated is impressive. RSF/peptide hydrogels were successfully fabricated using this approach as shown in [Figure 6-1 B](#). The RSF/peptide hydrogels could potentially be implanted in nerve defects in small animals (e.g., sciatic nerve defects in rat and acute spinal cord injury in rabbit), which will have a great potential to promote regeneration of defect sites.

The short peptides, discussed in chapter 3 and 4 (I₃K or I₃QGK) also can be mixed with the designed short peptides from chapter 5, to investigate how they might influence the response of nerve cells. As shown in [Figure 6-2](#), all mixed

short peptides could self-assemble into long and uniform nanofibers. These combinations might also provide a synergistic effect on the adhesion and spreading of neuron cells.

In addition to this, the technologies to fabricate 3D scaffolds should be further studied. For example, the fabrication of RSF/peptide scaffolds crosslinked with glutaraldehyde vapour via electrospinning;⁶²¹ using inkjet printing to print RSF and peptides layer-by-layer to fabricate porous RSF/peptides scaffold; using extrusion bioprinting to print 3D scaffold that contain the mixture of living cells, RSF and peptides.⁶²²

Overall, the combination of short peptides and RSF should give a better regulation for the proliferation and differentiation of neuron cells and offer a significant cost savings. This should be considered for future work and its use in nerve tissue engineering.

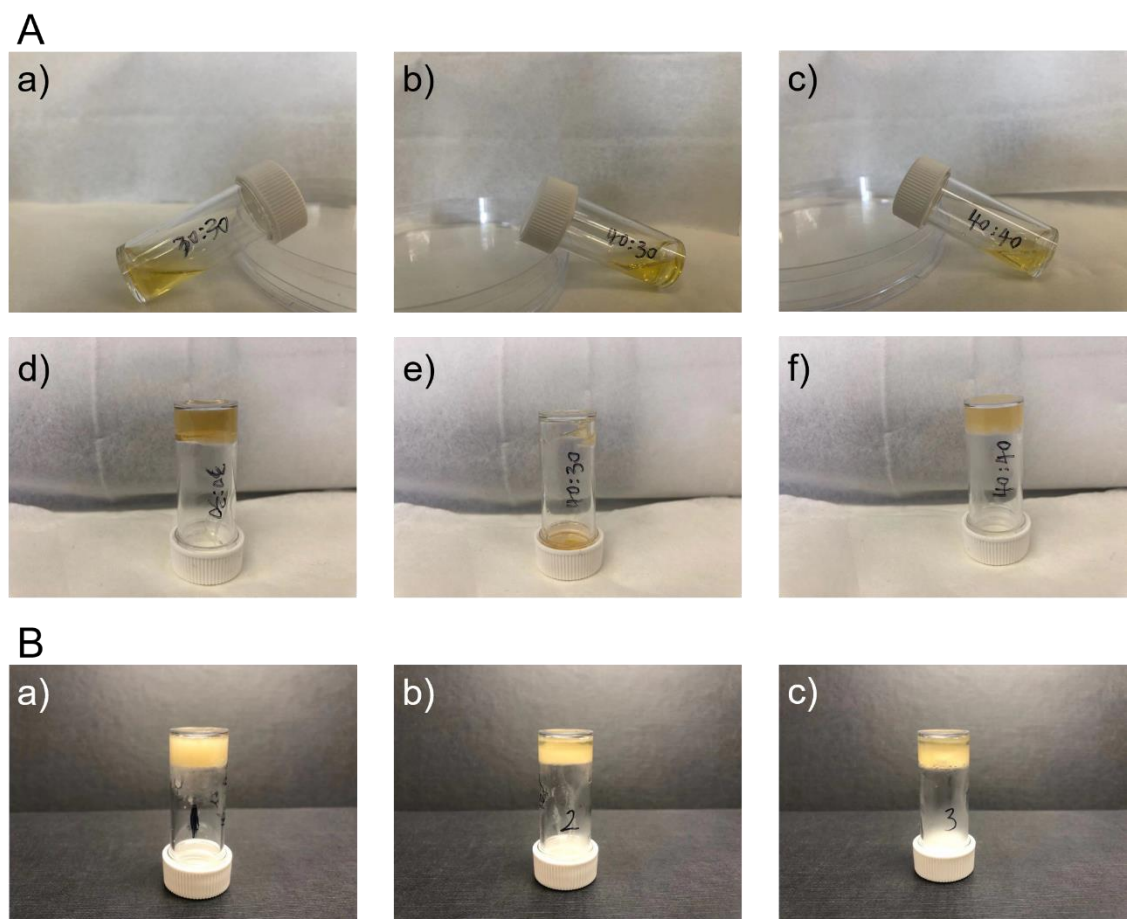


Figure 6-1 A, the addition of glutaraldehyde and TEMED at various volume ratios into RSF solutions (120 mg/mL), in which (a) and (d) at volume ratio 30:30; (b) and (e) at volume ratio

40:30; (c) and (f) at volume ratio 40:40. In addition, digital images (a)-(c) showing the mixed solution before incubating at sub-zero temperature. Digital images (d)-(f) showing the mixed solution formed hydrogels after incubation at -16 °C for 1 day. B, the fabrication of RSF/peptides hydrogels. In details, peptide solution (I₃KVAV/I₃YIGSR; 1 mg/mL) was added into RSF solution at different volume (a) 100 mL, (b) 200 mL and (c) 300 mL, then mixed with glutaraldehyde and TEMED at volume ratio 30:30, followed by incubating at -16 °C for 1 day.

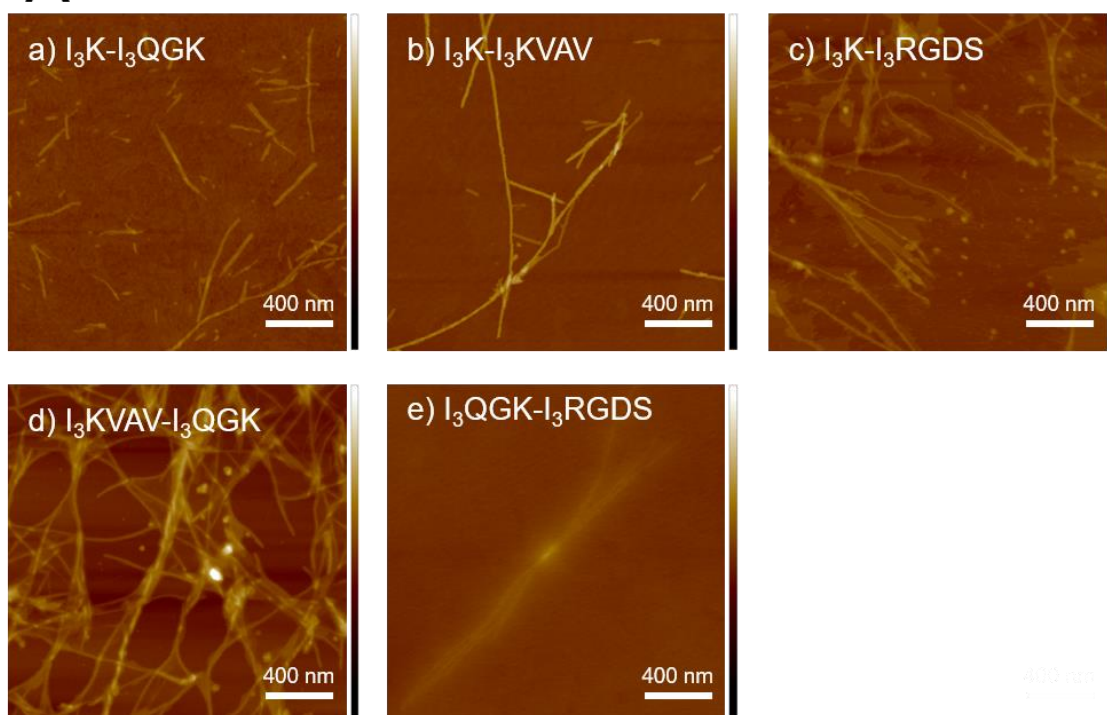
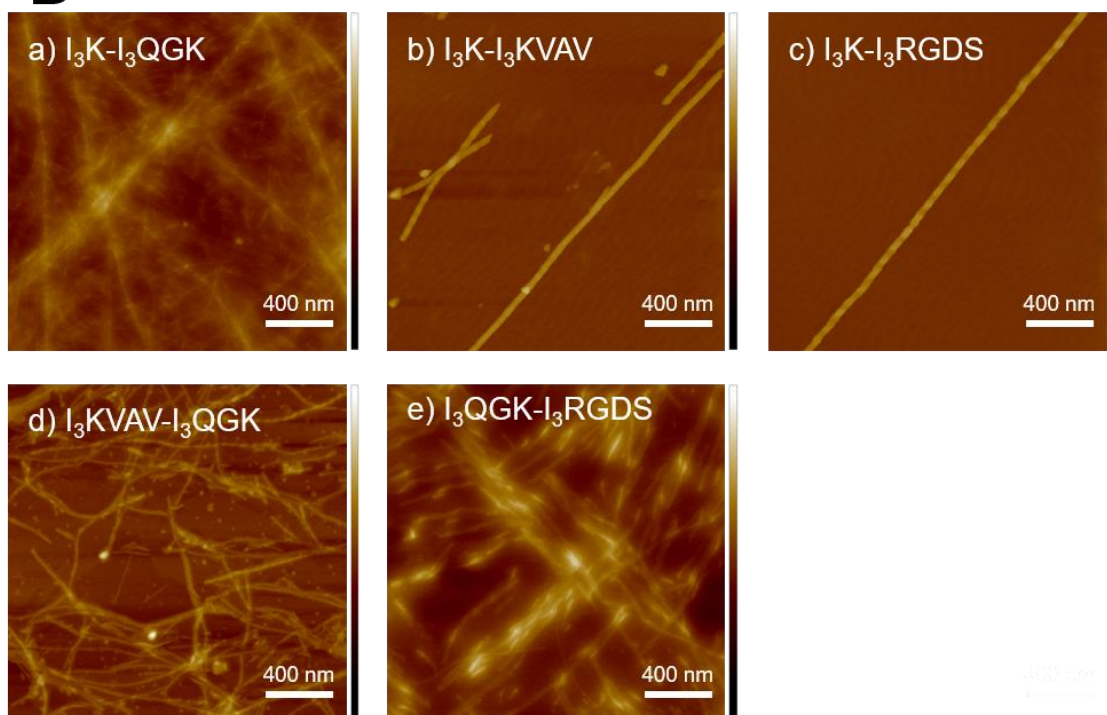
A**B**

Figure 6-2 AFM topographical images of the mixed short peptides at equimolar concentrations self-assembled at A, 1 day and B, 7 days. (a) I_3K mixed with I_3QGK ; (b) I_3K mixed with I_3KVAV ; (c) I_3K mixed with I_3RGDS ; (d) I_3KVAV mixed with I_3QGK ; (e) I_3QGK mixed with I_3RGDS . The Z scales for all images = 50 nm as indicated.

6.2.2. Silk fibroin

As was reported by Thakur *et al.*,⁶²³ 2D nanomaterials possessing high aspect ratios and ultrathin structures could interact with the polymers to enhance their mechanical properties. Additionally, some specific patterned 2D nanomaterials could have similar effects to growth factors on the enhancement of cell differentiation.⁶²⁴ SF has shown great potential together with 2D nanomaterials to increase its mechanical properties for future bone, cartilage ligament and tendon tissue engineering applications. In skin and wound applications, the production of SF matrices built on particular morphologies has demonstrated promise in decreasing the risk of scar tissue in patients. However, at present, their clinical applications are still scarce and therefore more research needs to be conducted to move towards clinical trials and FDA approved products based on this excellent biomaterial.

In addition, four-dimensional (4D) printing (when 3D printing combined with 'Time') has emerged and became an emerging technology and attractive topic, which can overcome some limitations of 3D printing, such as the creation of the sophisticated dynamics of native tissues⁶²⁵ and optimize the functional responses of cell-constructs interactions⁶²⁶. 'Time' is defined as printed 3D biocompatible scaffolds that continue to evolve over time while they are printed.⁶²⁷ The materials chosen for 4D printing should possess biocompatibility and reshape or change their function by means of external stimuli including temperature, water, magnetic fields, osmotic pressure and light.⁶²⁷ Very recently, Kim *et al.*⁶²⁸ described a 4D printing system based on Sil-MA hydrogels and DLP, which has been successfully applied in the regeneration of damaged trachea of rabbits. Therefore, RSF could be a key biomaterial that can be used in bioink formulations, illustrating its great potential in future 4D bioprinting.

6.2.3. Peptide amphiphiles

Although PAs have demonstrated significant advantages in TE applications, one main disadvantage that urgently need to be addressed is their low mechanical strength and stability to enable their usefulness in clinical applications. We believe this can be solved by targeted design of the peptide backbone with an aim to increase their intermolecular forces during the self-

assembly process. Furthermore, the peptide self-assembly can be enhanced via chemically-induced crosslinkers, catalysing enzymes or by physically-induced parameters such as temperature and pH and CMC concentration. A striking example for this was described by Singha et al.⁶²⁹ where the designed lipopeptide contained pyrene butanoic acid connected to lysine and cysteine, which formed hydrogels with a high insolubility and excellent confinement properties. The strong π - π stacking of pyrene rings and intramolecular hydrogen bonds endow the insolubility of this hydrogel giving it an excellent stability for over 1 year.

Furthermore, chemical peptide synthesis can ensure batch-to-batch consistency of PAs for TE applications.³⁶⁷ However, at present the commercial fabrication of PAs hydrogels is still a challenge. This is because there is a need to make to ensure reproducibility and functionality of PAs hydrogels for high speed and large-scale fabrications methodologies, particularly to produce cell-encapsulated PA hydrogels. Another challenge is the sterilization process of PAs-based hydrogels, but standard irradiation and heat methods can deactivate bioactive macromolecules⁶³⁰ and freeze-drying methods might affect the porosity, morphology and mechanical properties of the hydrogels. Therefore, more research is needed in this area.

7. References

- *1. Singh, D.; Harding, A. J.; Albadawi, E.; Boissonade, F. M.; Haycock, J. W.; Claeysens, F., Additive manufactured biodegradable poly(glycerol sebacate methacrylate) nerve guidance conduits. *Acta Biomaterialia* **2018**, *78*, 48-63.
2. Cheng, G.; Davoudi, Z.; Xing, X.; Yu, X.; Cheng, X.; Li, Z.; Deng, H.; Wang, Q., Advanced Silk Fibroin Biomaterials for Cartilage Regeneration. *ACS Biomaterials Science & Engineering* **2018**, *4* (8), 2704-2715.
3. Yodmuang, S.; McNamara, S. L.; Nover, A. B.; Mandal, B. B.; Agarwal, M.; Kelly, T.-A. N.; Chao, P.-h. G.; Hung, C.; Kaplan, D. L.; Vunjak-Novakovic, G., Silk microfiber-reinforced silk hydrogel composites for functional cartilage tissue repair. *Acta Biomaterialia* **2015**, *11*, 27-36.
4. Gui, L.; Niklason, L. E., Vascular Tissue Engineering: Building Perfusable Vasculature for Implantation. *Curr Opin Chem Eng* **2014**, *3*, 68-74.
- **5. O'Brien, F. J., Biomaterials & scaffolds for tissue engineering. *Materials Today* **2011**, *14* (3), 88-95.
6. Howard, D.; Buttery, L. D.; Shakesheff, K. M.; Roberts, S. J., Tissue engineering: strategies, stem cells and scaffolds. *J Anat* **2008**, *213* (1), 66-72.
7. Dhar, P.; Fischer, T. M.; Wang, Y.; Mallouk, T. E.; Paxton, W. F.; Sen, A., Autonomously moving nanorods at a viscous interface. *Nano Letters* **2006**, *6* (1), 66-72.
8. Brown, B. N.; Badylak, S. F., Extracellular matrix as an inductive scaffold for functional tissue reconstruction. *Translational Research* **2014**, *163* (4), 268-285.
9. Glowacki, J.; Mizuno, S., Collagen scaffolds for tissue engineering. *Biopolymers* **2008**, *89* (5), 338-44.
10. Koide, A.; Bailey, C. W.; Huang, X.; Koide, S., The fibronectin type III domain as a scaffold for novel binding proteins. *Journal of molecular biology* **1998**, *284* (4), 1141-51.
11. Tate, C. C.; Shear, D. A.; Tate, M. C.; Archer, D. R.; Stein, D. G.; LaPlaca, M. C., Laminin and fibronectin scaffolds enhance neural stem cell transplantation into the injured brain. *Journal of tissue engineering and regenerative medicine* **2009**, *3* (3), 208-17.
12. Daamen, W. F.; Veerkamp, J. H.; van Hest, J. C. M.; van Kuppevelt, T. H., Elastin as a biomaterial for tissue engineering. *Biomaterials* **2007**, *28* (30), 4378-4398.
13. Farrell, E.; O'Brien, F. J.; Doyle, P.; Fischer, J.; Yannas, I.; Harley, B. A.; O'Connell, B.; Prendergast, P. J.; Campbell, V. A., A collagen-glycosaminoglycan scaffold supports adult rat mesenchymal stem cell differentiation along osteogenic and chondrogenic routes. *Tissue engineering* **2006**, *12* (3), 459-68.
14. Lee, K. Y.; Mooney, D. J., Alginate: Properties and biomedical applications. *Progress in Polymer Science* **2012**, *37* (1), 106-126.
15. Hickey, R. J.; Pelling, A. E., Cellulose Biomaterials for Tissue Engineering. *Front Bioeng Biotechnol* **2019**, *7*, 45-45.
16. Croisier, F.; Jérôme, C., Chitosan-based biomaterials for tissue engineering. *European Polymer Journal* **2013**, *49* (4), 780-792.
17. Sionkowska, A., Current research on the blends of natural and synthetic polymers as new biomaterials: Review. *Progress in Polymer Science* **2011**, *36* (9), 1254-1276.
18. Nair, L. S.; Laurencin, C. T., Biodegradable polymers as biomaterials. *Progress in Polymer Science* **2007**, *32* (8), 762-798.
19. Gagner, J. E.; Kim, W.; Chaikof, E. L., Designing protein-based biomaterials for medical applications. *Acta Biomaterialia* **2014**, *10* (4), 1542-1557.
20. Huang, W.; Ling, S.; Li, C.; Omenetto, F. G.; Kaplan, D. L., Silkworm silk-based materials and devices generated using bio-nanotechnology. *Chem Soc Rev* **2018**, *47* (17), 6486-6504.
21. Chen, F.; Porter, D.; Vollrath, F., Morphology and structure of silkworm cocoons. *Materials Science and Engineering: C* **2012**, *32* (4), 772-778.

22. Panilaitis, B.; Altman, G. H.; Chen, J.; Jin, H.-J.; Karageorgiou, V.; Kaplan, D. L., Macrophage responses to silk. *Biomaterials* **2003**, *24* (18), 3079-3085.
23. Zhang, C.; Zhang, Y.; Shao, H.; Hu, X., Hybrid Silk Fibers Dry-Spun from Regenerated Silk Fibroin/Graphene Oxide Aqueous Solutions. *ACS Applied Materials & Interfaces* **2016**, *8* (5), 3349-3358.
24. Song, W.; Muthana, M.; Mukherjee, J.; Falconer, R. J.; Biggs, C. A.; Zhao, X., Magnetic-Silk Core–Shell Nanoparticles as Potential Carriers for Targeted Delivery of Curcumin into Human Breast Cancer Cells. *ACS Biomaterials Science & Engineering* **2017**, *3* (6), 1027-1038.
25. Melke, J.; Midha, S.; Ghosh, S.; Ito, K.; Hofmann, S., Silk fibroin as biomaterial for bone tissue engineering. *Acta Biomaterialia* **2016**, *31*, 1-16.
26. Sun, W.; Zhang, Y.; Gregory, D. A.; Jimenez-Franco, A.; Tomeh, M. A.; Lv, S.; Wang, J.; Haycock, J. W.; Lu, J. R.; Zhao, X., Patterning the neuronal cells via inkjet printing of self-assembled peptides on silk scaffolds. *Progress in Natural Science: Materials International* **2020**, *30* (5), 686-696.
27. He, P.; Sahoo, S.; Ng, K. S.; Chen, K.; Toh, S. L.; Goh, J. C. H., Enhanced osteoinductivity and osteoconductivity through hydroxyapatite coating of silk-based tissue-engineered ligament scaffold. *Journal of Biomedical Materials Research Part A* **2013**, *101A* (2), 555-566.
28. Cai, Z.-x.; Mo, X.-m.; Zhang, K.-h.; Fan, L.-p.; Yin, A.-l.; He, C.-l.; Wang, H.-s., Fabrication of Chitosan/Silk Fibroin Composite Nanofibers for Wound-dressing Applications. *International Journal of Molecular Sciences* **2010**, *11* (9), 3529-3539.
29. Wang, J.; Yang, Q.; Cheng, N.; Tao, X.; Zhang, Z.; Sun, X.; Zhang, Q., Collagen/silk fibroin composite scaffold incorporated with PLGA microsphere for cartilage repair. *Materials Science and Engineering: C* **2016**, *61*, 705-711.
30. Zhang, F.; Zuo, B.; Fan, Z.; Xie, Z.; Lu, Q.; Zhang, X.; Kaplan, D. L., Mechanisms and Control of Silk-Based Electrospinning. *Biomacromolecules* **2012**, *13* (3), 798-804.
31. Floren, M.; Migliaresi, C.; Motta, A., Processing Techniques and Applications of Silk Hydrogels in Bioengineering. *J Funct Biomater* **2016**, *7* (3), 26.
32. Yan, L.-P.; Oliveira, J. M.; Oliveira, A. L.; Caridade, S. G.; Mano, J. F.; Reis, R. L., Macro/microporous silk fibroin scaffolds with potential for articular cartilage and meniscus tissue engineering applications. *Acta Biomaterialia* **2012**, *8* (1), 289-301.
33. A., G. D.; Yu, Z.; J., S. P.; Xiubo, Z.; J., E. S., Reactive Inkjet Printing of Biocompatible Enzyme Powered Silk Micro-Rockets. *Small* **2016**, *12* (30), 4048-4055.
34. Craig, C. L., EVOLUTION OF ARTHROPOD SILKS. *Annual Review of Entomology* **1997**, *42* (1), 231-267.
35. Kundu, B.; Rajkhowa, R.; Kundu, S. C.; Wang, X., Silk fibroin biomaterials for tissue regenerations. *Adv Drug Deliv Rev* **2013**, *65* (4), 457-70.
36. von Byern, J.; Chandler, P.; Merritt, D.; Adlassnig, W.; Stringer, I.; Meyer-Rochow, V. B.; Kovalev, A.; Dorrer, V.; Dimartino, S.; Marchetti-Deschmann, M.; Gorb, S., Biomechanical properties of fishing lines of the glowworm *Arachnocampa luminosa* (Diptera; Keroplatidae). *Scientific Reports* **2019**, *9* (1), 3082.
37. Yoshioka, T.; Tsubota, T.; Tashiro, K.; Jouraku, A.; Kameda, T., A study of the extraordinarily strong and tough silk produced by bagworms. *Nature Communications* **2019**, *10* (1), 1469.
- **38. Qi, Y.; Wang, H.; Wei, K.; Yang, Y.; Zheng, R.-Y.; Kim, I. S.; Zhang, K.-Q., A Review of Structure Construction of Silk Fibroin Biomaterials from Single Structures to Multi-Level Structures. *International Journal of Molecular Sciences* **2017**, *18* (3), 237.
- *39. Tomeh, M. A.; Hadianamrei, R.; Zhao, X., Silk Fibroin as a Functional Biomaterial for Drug and Gene Delivery. *Pharmaceutics* **2019**, *11* (10), 494.

40. Kiseleva, A. P.; Krivoschapkin, P. V.; Krivoschapkina, E. F., Recent Advances in Development of Functional Spider Silk-Based Hybrid Materials. *Frontiers in Chemistry* **2020**, *8* (554).
41. Lewis, R., Unraveling the weave of spider silk: One of nature's wondrous chemical structures is being dissected so that it can be used in human inventions. *BioScience* **1996**, *46* (9), 636-638.
42. Blamires, S. J.; Spicer, P. T.; Flanagan, P. J., Spider Silk Biomimetics Programs to Inform the Development of New Wearable Technologies. *Frontiers in Materials* **2020**, *7* (29).
43. Andersson, M.; Jia, Q.; Abella, A.; Lee, X.-Y.; Landreh, M.; Purhonen, P.; Hebert, H.; Tenje, M.; Robinson, C. V.; Meng, Q.; Plaza, G. R.; Johansson, J.; Rising, A., Biomimetic spinning of artificial spider silk from a chimeric minispidroin. *Nature Chemical Biology* **2017**, *13* (3), 262-264.
44. Hwang, J. S.; Lee, J. S.; Goo, T. W.; Kang, H. A.; Sohn, H. R.; Kim, H. R.; Kwon, O. Y., The comparative molecular study between Bombycidae and Saturniidae based on mtDNA RFLP and cytochrome oxidase I gene sequences: implication for molecular evolution. *Zeitschrift fur Naturforschung. C, Journal of biosciences* **1999**, *54* (7-8), 587-94.
45. Fang, G.; Sapru, S.; Behera, S.; Yao, J.; Shao, Z.; Kundu, S. C.; Chen, X., Exploration of the tight structural–mechanical relationship in mulberry and non-mulberry silkworm silks. *Journal of Materials Chemistry B* **2016**, *4* (24), 4337-4347.
46. Kawamoto, M.; Jouraku, A.; Toyoda, A.; Yokoi, K.; Minakuchi, Y.; Katsuma, S.; Fujiyama, A.; Kiuchi, T.; Yamamoto, K.; Shimada, T., High-quality genome assembly of the silkworm, *Bombyx mori*. *Insect Biochemistry and Molecular Biology* **2019**, *107*, 53-62.
47. Liu, B.; Song, Y.-w.; Jin, L.; Wang, Z.-j.; Pu, D.-y.; Lin, S.-q.; Zhou, C.; You, H.-j.; Ma, Y.; Li, J.-m.; Yang, L.; Sung, K. L. P.; Zhang, Y.-g., Silk structure and degradation. *Colloids and Surfaces B: Biointerfaces* **2015**, *131*, 122-128.
48. Malay, A. D.; Sato, R.; Yazawa, K.; Watanabe, H.; Ifuku, N.; Masunaga, H.; Hikima, T.; Guan, J.; Mandal, B. B.; Damrongsakkul, S.; Numata, K., Relationships between physical properties and sequence in silkworm silks. *Scientific Reports* **2016**, *6*, 27573.
49. Vepari, C.; Kaplan, D. L., Silk as a biomaterial. *Progress in Polymer Science* **2007**, *32* (8), 991-1007.
50. Nguyen, T. P.; Nguyen, Q. V.; Nguyen, V. H.; Le, T. H.; Huynh, V. Q. N.; Vo, D. N.; Trinh, Q. T.; Kim, S. Y.; Le, Q. V., Silk Fibroin-Based Biomaterials for Biomedical Applications: A Review. *Polymers (Basel)* **2019**, *11* (12).
51. Aramwit, P.; Kanokpanont, S.; De-Eknamkul, W.; Srichana, T., Monitoring of inflammatory mediators induced by silk sericin. *Journal of bioscience and bioengineering* **2009**, *107*, 556-61.
52. Sahu, N.; Pal, S.; Sapru, S.; Kundu, J.; Talukdar, S.; Singh, N. I.; Yao, J.; Kundu, S. C., Non-Mulberry and Mulberry Silk Protein Sericins as Potential Media Supplement for Animal Cell Culture. *Biomed Res Int* **2016**, *2016*, 7461041-7461041.
53. Chopra, S.; Gulrajani, M., *Comparative evaluation of the various methods of degumming silk*. 1994; Vol. 19, p 76-83.
54. Dou, H.; Zuo, B., Effect of sodium carbonate concentrations on the degumming and regeneration process of silk fibroin. *The Journal of The Textile Institute* **2015**, *106* (3), 311-319.
55. Shao, Z.; Vollrath, F., Surprising strength of silkworm silk. *Nature* **2002**, *418* (6899), 741-741.
56. Mori, K.; Tanaka, K.; Kikuchi, Y.; Waga, M.; Waga, S.; Mizuno, S., Production of a Chimeric Fibroin Light-chain Polypeptide in a Fibroin Secretion-deficient Naked Pupa Mutant of the Silkworm *Bombyx mori*. *Journal of molecular biology* **1995**, *251* (2), 217-228.
57. Wongpinyochit, T.; Johnston, B. F.; Seib, F. P., Degradation Behavior of Silk Nanoparticles—Enzyme Responsiveness. *ACS Biomaterials Science & Engineering* **2018**, *4* (3), 942-951.

58. Tanaka, K.; Inoue, S.; Mizuno, S., Hydrophobic interaction of P25, containing Asn-linked oligosaccharide chains, with the H-L complex of silk fibroin produced by *Bombyx mori*. *Insect Biochemistry and Molecular Biology* **1999**, *29* (3), 269-276.
59. Inoue, S.; Tanaka, K.; Arisaka, F.; Kimura, S.; Ohtomo, K.; Mizuno, S., Silk fibroin of *Bombyx mori* is secreted, assembling a high molecular mass elementary unit consisting of H-chain, L-chain, and P25, with a 6:6:1 molar ratio. *The Journal of biological chemistry* **2000**, *275* (51), 40517-28.
60. Cong-Zhao, Z.; Fabrice, C.; Michel, J.; Roland, P.; Zhen-Gang, L.; Joel, J., Silk fibroin: Structural implications of a remarkable amino acid sequence. *Proteins: Structure, Function, and Bioinformatics* **2001**, *44* (2), 119-122.
61. Asakura, T.; Ito, T.; Okudaira, M.; Kameda, T., Structure of Alanine and Glycine Residues of *Samia cynthia ricini* Silk Fibers Studied with Solid-State ¹⁵N and ¹³C NMR. *Macromolecules* **1999**, *32* (15), 4940-4946.
62. Gage, L. P.; Manning, R. F., Internal structure of the silk fibroin gene of *Bombyx mori*. I The fibroin gene consists of a homogeneous alternating array of repetitious crystalline and amorphous coding sequences. *The Journal of biological chemistry* **1980**, *255* (19), 9444-50.
63. Fedic, R.; Zurovec, M.; Sehnal, F., Correlation between fibroin amino acid sequence and physical silk properties. *The Journal of biological chemistry* **2003**, *278* (37), 35255-64.
64. Cho, S. Y.; Yun, Y. S.; Lee, S.; Jang, D.; Park, K.-Y.; Kim, J. K.; Kim, B. H.; Kang, K.; Kaplan, D. L.; Jin, H.-J., Carbonization of a stable β -sheet-rich silk protein into a pseudographitic pyroprotein. *Nature Communications* **2015**, *6*, 7145.
65. Cebe, P.; Partlow, B. P.; Kaplan, D. L.; Wurm, A.; Zhuravlev, E.; Schick, C., Silk I and Silk II studied by fast scanning calorimetry. *Acta Biomaterialia* **2017**, *55*, 323-332.
66. Jaramillo-Quiceno, N.; Álvarez-López, C.; Restrepo-Osorio, A., Structural and thermal properties of silk fibroin films obtained from cocoon and waste silk fibers as raw materials. *Procedia Engineering* **2017**, *200*, 384-388.
67. Valluzzi, R.; Gido, S. P.; Muller, W.; Kaplan, D. L., Orientation of silk III at the air-water interface. *International journal of biological macromolecules* **1999**, *24* (2-3), 237-42.
68. Sirichaisit, J.; Brookes, V. L.; Young, R. J.; Vollrath, F., Analysis of structure/property relationships in silkworm (*Bombyx mori*) and spider dragline (*Nephila edulis*) silks using Raman spectroscopy. *Biomacromolecules* **2003**, *4* (2), 387-94.
69. Koh, L.-D.; Cheng, Y.; Teng, C.-P.; Khin, Y.-W.; Loh, X.-J.; Tee, S.-Y.; Low, M.; Ye, E.; Yu, H.-D.; Zhang, Y.-W.; Han, M.-Y., Structures, mechanical properties and applications of silk fibroin materials. *Progress in Polymer Science* **2015**, *46*, 86-110.
70. Gosline, J. M.; Guerette, P. A.; Ortlepp, C. S.; Savage, K. N., The mechanical design of spider silks: from fibroin sequence to mechanical function. *Journal of Experimental Biology* **1999**, *202* (23), 3295-3303.
71. Altman, G. H.; Horan, R. L.; Lu, H. H.; Moreau, J.; Martin, I.; Richmond, J. C.; Kaplan, D. L., Silk matrix for tissue engineered anterior cruciate ligaments. *Biomaterials* **2002**, *23* (20), 4131-4141.
72. Nazarov, R.; Jin, H.-J.; Kaplan, D. L., Porous 3-D Scaffolds from Regenerated Silk Fibroin. *Biomacromolecules* **2004**, *5* (3), 718-726.
73. Sakabe, H.; Ito, H.; Miyamoto, T.; Noishiki, Y.; Ha, W. S., IN VIVO BLOOD COMPATIBILITY OF REGENERATED SILK FIBROIN. *Sen'i Gakkaishi* **1989**, *45* (11), 487-490.
74. Minoura, N.; Aiba, S. I.; Higuchi, M.; Gotoh, Y.; Tsukada, M.; Imai, Y., Attachment and Growth of Fibroblast Cells on Silk Fibroin. *Biochemical and Biophysical Research Communications* **1995**, *208* (2), 511-516.
75. Kim, J.-Y.; Yang, B.-E.; Ahn, J.-H.; Park, S. O.; Shim, H.-W., Comparable efficacy of silk fibroin with the collagen membranes for guided bone regeneration in rat calvarial defects. *J Adv Prosthodont* **2014**, *6* (6), 539-546.
76. Santin, M.; Motta, A.; Freddi, G.; Cannas, M., In vitro evaluation of the inflammatory potential of the silk fibroin. *Journal of Biomedical Materials Research* **1999**, *46* (3), 382-389.

77. Meinel, L.; Hofmann, S.; Karageorgiou, V.; Kirker-Head, C.; McCool, J.; Gronowicz, G.; Zichner, L.; Langer, R.; Vunjak-Novakovic, G.; Kaplan, D. L., The inflammatory responses to silk films in vitro and in vivo. *Biomaterials* **2005**, *26* (2), 147-155.
78. Babensee, J. E.; Anderson, J. M.; McIntire, L. V.; Mikos, A. G., Host response to tissue engineered devices. *Advanced Drug Delivery Reviews* **1998**, *33* (1), 111-139.
79. Cao, Y.; Wang, B., Biodegradation of silk biomaterials. *Int J Mol Sci* **2009**, *10* (4), 1514-24.
80. Arai, T.; Freddi, G.; Innocenti, R.; Tsukada, M., Biodegradation of Bombyx mori silk fibroin fibers and films. *Journal of Applied Polymer Science* **2004**, *91* (4), 2383-2390.
81. Lu, Q.; Zhang, B.; Li, M.; Zuo, B.; Kaplan, D. L.; Huang, Y.; Zhu, H., Degradation mechanism and control of silk fibroin. *Biomacromolecules* **2011**, *12* (4), 1080-1086.
82. Li, M.; Ogiso, M.; Minoura, N., Enzymatic degradation behavior of porous silk fibroin sheets. *Biomaterials* **2003**, *24* (2), 357-365.
83. Horan, R. L.; Antle, K.; Collette, A. L.; Wang, Y.; Huang, J.; Moreau, J. E.; Volloch, V.; Kaplan, D. L.; Altman, G. H., In vitro degradation of silk fibroin. *Biomaterials* **2005**, *26* (17), 3385-3393.
84. Wang, Y.; Rudym, D. D.; Walsh, A.; Abrahamsen, L.; Kim, H. J.; Kim, H. S.; Kirker-Head, C.; Kaplan, D. L., In vivo degradation of three-dimensional silk fibroin scaffolds. *Biomaterials* **2008**, *29* (24-25), 3415-28.
85. Hu, Y.; Zhang, Q.; You, R.; Wang, L.; Li, M., The Relationship between Secondary Structure and Biodegradation Behavior of Silk Fibroin Scaffolds. *Advances in Materials Science and Engineering* **2012**, *2012*, 1-5.
86. Jin, H. J.; Park, J.; Karageorgiou, V.; Kim, U. J.; Valluzzi, R.; Cebe, P.; Kaplan, D. L., Water-Stable Silk Films with Reduced β -Sheet Content. *Advanced Functional Materials* **2005**, *15* (8), 1241-1247.
87. Lu, Q.; Hu, X.; Wang, X.; Kluge, J. A.; Lu, S.; Cebe, P.; Kaplan, D. L., Water-insoluble silk films with silk I structure. *Acta Biomater* **2010**, *6* (4), 1380-7.
88. Wang, J.-N.; Liu, Z.-W.; Yang, Y.-X.; Huang, H.-Y., Enzymatic degradation behavior of silk fibroin fiber treated by γ -ray irradiation. *Textile Research Journal* **2012**, *82* (17), 1799-1805.
89. Cheng, G.; Wang, X.; Tao, S.; Xia, J.; Xu, S., Differences in regenerated silk fibroin prepared with different solvent systems: From structures to conformational changes. *Journal of Applied Polymer Science* **2015**, *132* (22), 41959.
90. Vadim, V.; V., F. A.; Artur, C. P., On the Routines of Wild-Type Silk Fibroin Processing Toward Silk-Inspired Materials: A Review. *Macromolecular Materials and Engineering* **2015**, *300* (12), 1199-1216.
91. Rockwood, D. N.; Preda, R. C.; Yücel, T.; Wang, X.; Lovett, M. L.; Kaplan, D. L., Materials fabrication from Bombyx mori silk fibroin. *Nature Protocols* **2011**, *6*, 1612.
92. Ajisawa, A., Dissolution of silk fibroin with calciumchloride/ethanol aqueous solution. *The Journal of Sericultural Science of Japan* **1998**, *67* (2), 91-94.
93. Sashina, E. S.; Bochek, A. M.; Novoselov, N. P.; Kirichenko, D. A., Structure and solubility of natural silk fibroin. *Russian Journal of Applied Chemistry* **2006**, *79* (6), 869-876.
94. N., A.; A., H. D.; J., F. R., Effect of moisture absorption on the thermal properties of Bombyx mori silk fibroin films. *Journal of Applied Polymer Science* **1997**, *63* (3), 401-410.
95. Zheng, Z.; Guo, S.; Liu, Y.; Wu, J.; Li, G.; Liu, M.; Wang, X.; Kaplan, D., Lithium-free processing of silk fibroin. *Journal of biomaterials applications* **2016**, *31* (3), 450-63.
96. Zhang, W.; Chen, L.; Chen, J.; Wang, L.; Gui, X.; Ran, J.; Xu, G.; Zhao, H.; Zeng, M.; Ji, J.; Qian, L.; Zhou, J.; Ouyang, H.; Zou, X., Silk Fibroin Biomaterial Shows Safe and Effective Wound Healing in Animal Models and a Randomized Controlled Clinical Trial. *Advanced Healthcare Materials* **2017**, *6* (10), 1700121.
97. Yin, Y.; Xiong, J., Finite Element Analysis of Electrospun Nanofibrous Mats under Biaxial Tension. *Nanomaterials* **2018**, *8*, 348.

98. Jacobsen, M. M.; Li, D.; Gyune Rim, N.; Backman, D.; Smith, M. L.; Wong, J. Y., Silk-fibronectin protein alloy fibres support cell adhesion and viability as a high strength, matrix fibre analogue. *Scientific Reports* **2017**, *7*, 45653.
99. Li, Z.; Zheng, Z.; Yang, Y.; Fang, G.; Yao, J.; Shao, Z.; Chen, X., Robust Protein Hydrogels from Silkworm Silk. *ACS Sustainable Chemistry & Engineering* **2016**, *4* (3), 1500-1506.
- *100. Tao, H.; Marelli, B.; Yang, M.; An, B.; Onses, M. S.; Rogers, J. A.; Kaplan, D. L.; Omenetto, F. G., Inkjet Printing of Regenerated Silk Fibroin: From Printable Forms to Printable Functions. *Adv Mater* **2015**, *27* (29), 4273-9.
101. Rodriguez, M. J.; Dixon, T. A.; Cohen, E.; Huang, W.; Omenetto, F. G.; Kaplan, D. L., 3D freeform printing of silk fibroin. *Acta Biomater* **2018**, *71*, 379-387.
102. Terada, D.; Yokoyama, Y.; Hattori, S.; Kobayashi, H.; Tamada, Y., The outermost surface properties of silk fibroin films reflect ethanol-treatment conditions used in biomaterial preparation. *Materials Science and Engineering: C* **2016**, *58*, 119-126.
103. Sagnella, A.; Pistone, A.; Bonetti, S.; Donnadio, A.; Saracino, E.; Nocchetti, M.; Dionigi, C.; Ruani, G.; Muccini, M.; Posati, T.; Benfenati, V.; Zamboni, R., Effect of different fabrication methods on the chemo-physical properties of silk fibroin films and on their interaction with neural cells. *RSC Advances* **2016**, *6* (11), 9304-9314.
104. Liu, W.; Thomopoulos, S.; Xia, Y., Electrospun Nanofibers for Regenerative Medicine. *Advanced Healthcare Materials* **2012**, *1* (1), 10-25.
105. Zhang, X.; Reagan, M. R.; Kaplan, D. L., Electrospun silk biomaterial scaffolds for regenerative medicine. *Advanced Drug Delivery Reviews* **2009**, *61* (12), 988-1006.
106. Jin, H.-J.; Chen, J.; Karageorgiou, V.; Altman, G. H.; Kaplan, D. L., Human bone marrow stromal cell responses on electrospun silk fibroin mats. *Biomaterials* **2004**, *25* (6), 1039-1047.
107. Huang, J.; Liu, L.; Yao, J., Electrospinning of Bombyx mori silk fibroin nanofiber mats reinforced by cellulose nanowhiskers. *Fibers and Polymers* **2011**, *12* (8), 1002-1006.
108. Lee, H.; Jang, C. H.; Kim, G. H., A polycaprolactone/silk-fibroin nanofibrous composite combined with human umbilical cord serum for subacute tympanic membrane perforation; an in vitro and in vivo study. *Journal of Materials Chemistry B* **2014**, *2* (18), 2703-2713.
109. Uttayarat, P.; Jetawattana, S.; Suwanmala, P.; Eamsiri, J.; Tangthong, T.; Pongpat, S., Antimicrobial electrospun silk fibroin mats with silver nanoparticles for wound dressing application. *Fibers and Polymers* **2012**, *13* (8), 999-1006.
110. Win-Chun, J.; Ming-Chien, Y.; Chien-Hong, L.; Chi-Chuan, H., Fabrication and characterization of electrospun silk fibroin/TiO₂ nanofibrous mats for wound dressings. *Polymers for Advanced Technologies* **2012**, *23* (7), 1066-1076.
111. Ha, S.-W.; Tonelli, A. E.; Hudson, S. M., Structural Studies of Bombyx mori Silk Fibroin during Regeneration from Solutions and Wet Fiber Spinning. *Biomacromolecules* **2005**, *6* (3), 1722-1731.
112. Liu, C.; Sun, J.; Shao, M.; Yang, B., A comparison of centrifugally-spun and electrospun regenerated silk fibroin nanofiber structures and properties. *RSC Advances* **2015**, *5* (119), 98553-98558.
113. Müller, F.; Jokisch, S.; Bargel, H.; Scheibel, T., Centrifugal Electrospinning Enables the Production of Meshes of Ultrathin Polymer Fibers. *ACS Applied Polymer Materials* **2020**, *2* (11), 4360-4367.
114. Muller, F.; Zainuddin, S.; Scheibel, T., Roll-to-Roll Production of Spider Silk Nanofiber Nonwoven Meshes Using Centrifugal Electrospinning for Filtration Applications. *Molecules* **2020**, *25* (23).
115. Ahmed, E. M., Hydrogel: Preparation, characterization, and applications: A review. *Journal of Advanced Research* **2015**, *6* (2), 105-121.
116. Matsumoto, A.; Chen, J.; Collette, A. L.; Kim, U.-J.; Altman, G. H.; Cebe, P.; Kaplan, D. L., Mechanisms of Silk Fibroin Sol-Gel Transitions. *The Journal of Physical Chemistry B* **2006**, *110* (43), 21630-21638.

117. Lu, Q.; Huang, Y.; Li, M.; Zuo, B.; Lu, S.; Wang, J.; Zhu, H.; Kaplan, D. L., Silk fibroin electrogelation mechanisms. *Acta Biomaterialia* **2011**, *7* (6), 2394-2400.
118. Leisk, G. G.; Lo, T. J.; Yucel, T.; Lu, Q.; Kaplan, D. L., Electrogelation for Protein Adhesives. *Advanced Materials* **2010**, *22* (6), 711-715.
119. Zhang, W.; Wang, X.; Wang, S.; Zhao, J.; Xu, L.; Zhu, C.; Zeng, D.; Chen, J.; Zhang, Z.; Kaplan, D. L.; Jiang, X., The use of injectable sonication-induced silk hydrogel for VEGF165 and BMP-2 delivery for elevation of the maxillary sinus floor. *Biomaterials* **2011**, *32* (35), 9415-9424.
120. Wang, X.; Kluge, J. A.; Leisk, G. G.; Kaplan, D. L., Sonication-induced gelation of silk fibroin for cell encapsulation. *Biomaterials* **2008**, *29* (8), 1054-64.
121. McPherson, A., Introduction to protein crystallization. *Methods* **2004**, *34* (3), 254-265.
122. Kim, U.-J.; Park, J.; Li, C.; Jin, H.-J.; Valluzzi, R.; Kaplan, D. L., Structure and Properties of Silk Hydrogels. *Biomacromolecules* **2004**, *5* (3), 786-792.
123. Cynthia, L. S., Characterization of Protein and Peptide Stability and Solubility in Non-Aqueous Solvents. *Current Pharmaceutical Biotechnology* **2000**, *1* (2), 165-182.
124. Wang, W.; Nema, S.; Teagarden, D., Protein aggregation—Pathways and influencing factors. *International Journal of Pharmaceutics* **2010**, *390* (2), 89-99.
125. Hanawa, T.; Watanabe, A.; Tsuchiya, T.; Ikoma, R.; Hidaka, M.; Sugihara, M., New Oral Dosage Form for Elderly Patients : Preparation and Characterization of Silk Fibroin Gel. *CHEMICAL & PHARMACEUTICAL BULLETIN* **1995**, *43* (2), 284-288.
126. Motta, A.; Migliaresi, C.; Faccioni, F.; Torricelli, P.; Fini, M.; Giardino, R., Fibroin hydrogels for biomedical applications: preparation, characterization and in vitro cell culture studies. *Journal of Biomaterials Science, Polymer Edition* **2004**, *15* (7), 851-864.
127. Ayub, Z. H.; Arai, M.; Hirabayashi, K., Mechanism of the Gelation of Fibroin Solution. *Bioscience, Biotechnology, and Biochemistry* **1993**, *57* (11), 1910-1912.
128. Floren, M. L.; Spilimbergo, S.; Motta, A.; Migliaresi, C., Carbon Dioxide Induced Silk Protein Gelation for Biomedical Applications. *Biomacromolecules* **2012**, *13* (7), 2060-2072.
129. Partlow, B. P.; Hanna, C. W.; Rnjak-Kovacina, J.; Moreau, J. E.; Applegate, M. B.; Burke, K. A.; Marelli, B.; Mitropoulos, A. N.; Omenetto, F. G.; Kaplan, D. L., Highly Tunable Elastomeric Silk Biomaterials. *Advanced Functional Materials* **2014**, *24* (29), 4615-4624.
130. Murphy, A. R.; John, P. S.; Kaplan, D. L., Modification of silk fibroin using diazonium coupling chemistry and the effects on hMSC proliferation and differentiation. *Biomaterials* **2008**, *29* (19), 2829-2838.
131. Ji, H.; Helfand, E., Concentration Fluctuations in Sheared Polymer Solutions. *Macromolecules* **1995**, *28* (11), 3869-3880.
132. Rangel-Nafaile, C.; Metzner, A. B.; Wissbrun, K. F., Analysis of stress-induced phase separations in polymer solutions. *Macromolecules* **1984**, *17* (6), 1187-1195.
133. Yucel, T.; Cebe, P.; Kaplan, D. L., Vortex-Induced Injectable Silk Fibroin Hydrogels. *Biophysical Journal* **2009**, *97* (7), 2044-2050.
134. Paulusse, J. M. J.; Sijbesma, R. P., Ultrasound in polymer chemistry: Revival of an established technique. *Journal of Polymer Science Part A: Polymer Chemistry* **2006**, *44* (19), 5445-5453.
135. Kim, U.-J.; Park, J.; Joo Kim, H.; Wada, M.; Kaplan, D. L., Three-dimensional aqueous-derived biomaterial scaffolds from silk fibroin. *Biomaterials* **2005**, *26* (15), 2775-2785.
136. Tsukada, M.; Freddi, G.; Minoura, N.; Allara, G., Preparation and application of porous silk fibroin materials. *Journal of Applied Polymer Science* **1994**, *54* (4), 507-514.
137. Mandal, B. B.; Kundu, S. C., Cell proliferation and migration in silk fibroin 3D scaffolds. *Biomaterials* **2009**, *30* (15), 2956-2965.
138. Bütün, V.; Armes, S. P.; Billingham, N. C., Synthesis and aqueous solution properties of near-monodisperse tertiary amine methacrylate homopolymers and diblock copolymers. *Polymer* **2001**, *42*, 5993-6008.

139. Meinel, L.; Fajardo, R.; Hofmann, S.; Langer, R.; Chen, J.; Snyder, B.; Vunjak-Novakovic, G.; Kaplan, D., Silk implants for the healing of critical size bone defects. *Bone* **2005**, *37* (5), 688-698.
140. Du, X.; Wang, Y.; Yuan, L.; Weng, Y.; Chen, G.; Hu, Z., Guiding the behaviors of human umbilical vein endothelial cells with patterned silk fibroin films. *Colloids and Surfaces B: Biointerfaces* **2014**, *122*, 79-84.
141. Li, X.; You, R.; Luo, Z.; Chen, G.; Li, M., Silk fibroin scaffolds with a micro-/nano-fibrous architecture for dermal regeneration. *Journal of Materials Chemistry B* **2016**, *4* (17), 2903-2912.
142. Park, J.; Lee, S.-G.; Marelli, B.; Lee, M.; Kim, T.; Oh, H.-K.; Jeon, H.; Omenetto, F. G.; Kim, S., Eco-friendly photolithography using water-developable pure silk fibroin. *RSC Advances* **2016**, *6* (45), 39330-39334.
143. Gupta, M. K.; Khokhar, S. K.; Phillips, D. M.; Sowards, L. A.; Drummy, L. F.; Kadakia, M. P.; Naik, R. R., Patterned Silk Films Cast from Ionic Liquid Solubilized Fibroin as Scaffolds for Cell Growth. *Langmuir* **2007**, *23* (3), 1315-1319.
144. Kim, S.; Marelli, B.; Brenckle, M. A.; Mitropoulos, A. N.; Gil, E.-S.; Tsioris, K.; Tao, H.; Kaplan, D. L.; Omenetto, F. G., All-water-based electron-beam lithography using silk as a resist. *Nature Nanotechnology* **2014**, *9*, 306.
145. Zhong, J.; Ma, M.; Zhou, J.; Wei, D.; Yan, Z.; He, D., Tip-Induced Micropatterning of Silk Fibroin Protein Using In Situ Solution Atomic Force Microscopy. *ACS Applied Materials & Interfaces* **2013**, *5* (3), 737-746.
146. Whitesides, G. M.; Ostuni, E.; Takayama, S.; Jiang, X.; Ingber, D. E., Soft Lithography in Biology and Biochemistry. *Annual Review of Biomedical Engineering* **2001**, *3* (1), 335-373.
147. Zhou, Z.; Zhang, S.; Cao, Y.; Marelli, B.; Xia, X.; Tao, T. H., Engineering the Future of Silk Materials through Advanced Manufacturing. *Adv Mater* **2018**, e1706983.
- **148. Gregory, D. A.; Zhang, Y.; Smith, P. J.; Ebbens, S. J.; Zhao, X., Reactive Inkjet Printing of Biocompatible Enzyme Powered Silk Micro-Rockets. *Small* **2016**, *12*, 4048-4055.
149. Dababneh, A. B.; Ozbolat, I. T., Bioprinting Technology: A Current State-of-the-Art Review. *Journal of Manufacturing Science and Engineering* **2014**, *136* (6), 061016-061016-11.
150. Murphy, S. V.; Atala, A., 3D bioprinting of tissues and organs. *Nat Biotechnol* **2014**, *32* (8), 773-85.
151. Suntivich, R.; Drachuk, I.; Calabrese, R.; Kaplan, D. L.; Tsukruk, V. V., Inkjet printing of silk nest arrays for cell hosting. *Biomacromolecules* **2014**, *15* (4), 1428-35.
152. Das, S.; Pati, F.; Choi, Y.-J.; Rijal, G.; Shim, J.-H.; Kim, S. W.; Ray, A. R.; Cho, D.-W.; Ghosh, S., Bioprintable, cell-laden silk fibroin-gelatin hydrogel supporting multilineage differentiation of stem cells for fabrication of three-dimensional tissue constructs. *Acta Biomaterialia* **2015**, *11*, 233-246.
153. Sommer, M. R.; Schaffner, M.; Carnelli, D.; Studart, A. R., 3D Printing of Hierarchical Silk Fibroin Structures. *ACS Appl Mater Interfaces* **2016**, *8* (50), 34677-34685.
154. Kim, S. H.; Yeon, Y. K.; Lee, J. M.; Chao, J. R.; Lee, Y. J.; Seo, Y. B.; Sultan, M. T.; Lee, O. J.; Lee, J. S.; Yoon, S.-i.; Hong, I.-S.; Khang, G.; Lee, S. J.; Yoo, J. J.; Park, C. H., Precisely printable and biocompatible silk fibroin bioink for digital light processing 3D printing. *Nature Communications* **2018**, *9* (1), 1620 <https://doi.org/10.1038/s41467-018-03759-y>.
155. Hong, H.; Seo, Y. B.; Kim, D. Y.; Lee, J. S.; Lee, Y. J.; Lee, H.; Ajiteru, O.; Sultan, M. T.; Lee, O. J.; Kim, S. H.; Park, C. H., Digital light processing 3D printed silk fibroin hydrogel for cartilage tissue engineering. *Biomaterials* **2020**, *232*, 119679.
156. Ajiteru, O.; Sultan, M. T.; Lee, Y. J.; Seo, Y. B.; Hong, H.; Lee, J. S.; Lee, H.; Suh, Y. J.; Ju, H. W.; Lee, O. J.; Park, H. S.; Jang, M.; Kim, S. H.; Park, C. H., A 3D Printable Electroconductive Biocomposite Bioink Based on Silk Fibroin-Conjugated Graphene Oxide. *Nano Letters* **2020**, *20* (9), 6873-6883.
157. Buckwalter, J. A.; Glimcher, M. J.; Cooper, R. R.; Recker, R., Bone biology. I: Structure, blood supply, cells, matrix, and mineralization. *Instructional course lectures* **1996**, *45*, 371-386.

158. Roach, H. I., Why does bone matrix contain non-collagenous proteins? The possible roles of osteocalcin, osteonectin, osteopontin and bone sialoprotein in bone mineralisation and resorption. *Cell Biology International* **1994**, *18* (6), 617-628.
159. Olszta, M. J.; Cheng, X.; Jee, S. S.; Kumar, R.; Kim, Y.-Y.; Kaufman, M. J.; Douglas, E. P.; Gower, L. B., Bone structure and formation: A new perspective. *Materials Science and Engineering: R: Reports* **2007**, *58* (3), 77-116.
160. Frantz, C.; Stewart, K. M.; Weaver, V. M., The extracellular matrix at a glance. *Journal of Cell Science* **2010**, *123* (24), 4195-4200.
161. Kasoju, N.; Bora, U., Silk fibroin in tissue engineering. *Adv Healthc Mater* **2012**, *1* (4), 393-412.
162. Meinel, L.; Hofmann, S.; Betz, O.; Fajardo, R.; Merkle, H. P.; Langer, R.; Evans, C. H.; Vunjak-Novakovic, G.; Kaplan, D. L., Osteogenesis by human mesenchymal stem cells cultured on silk biomaterials: Comparison of adenovirus mediated gene transfer and protein delivery of BMP-2. *Biomaterials* **2006**, *27* (28), 4993-5002.
163. Guodong, L.; Fuqiang, Z.; Lijiao, Z.; Yanli, W.; Liubin, F., Glass Transition Temperature of Polystyrene Determined by DSC Revisited. *Acta Polymerica Sinica* **2010**, *1* (9), 1065-1069.
164. Bhumiratana, S.; Grayson, W. L.; Castaneda, A.; Rockwood, D. N.; Gil, E. S.; Kaplan, D. L.; Vunjak-Novakovic, G., Nucleation and growth of mineralized bone matrix on silk-hydroxyapatite composite scaffolds. *Biomaterials* **2011**, *32* (11), 2812-2820.
165. Jiang, J.; Hao, W.; Li, Y.; Yao, J.; Shao, Z.; Li, H.; Yang, J.; Chen, S., Hydroxyapatite/regenerated silk fibroin scaffold-enhanced osteoinductivity and osteoconductivity of bone marrow-derived mesenchymal stromal cells. *Biotechnology Letters* **2013**, *35* (4), 657-661.
166. Bessa, P. C.; Casal, M.; Reis, R. L., Bone morphogenetic proteins in tissue engineering: the road from laboratory to clinic, part II (BMP delivery). *Journal of tissue engineering and regenerative medicine* **2008**, *2* (2-3), 81-96.
167. Zhang, Y.; Fan, W.; Nothdurft, L.; Wu, C.; Zhou, Y.; Crawford, R.; Xiao, Y., In Vitro and In Vivo Evaluation of Adenovirus Combined Silk Fibroin Scaffolds for Bone Morphogenetic Protein-7 Gene Delivery. *Tissue Engineering Part C: Methods* **2011**, *17* (8), 789-797.
168. Kirker-Head, C.; Karageorgiou, V.; Hofmann, S.; Fajardo, R.; Betz, O.; Merkle, H. P.; Hilbe, M.; von Rechenberg, B.; McCool, J.; Abrahamsen, L.; Nazarian, A.; Cory, E.; Curtis, M.; Kaplan, D.; Meinel, L., BMP-silk composite matrices heal critically sized femoral defects. *Bone* **2007**, *41* (2), 247-255.
169. Li, C.; Vepari, C.; Jin, H.-J.; Kim, H. J.; Kaplan, D. L., Electrospun silk-BMP-2 scaffolds for bone tissue engineering. *Biomaterials* **2006**, *27* (16), 3115-3124.
170. Ding, X.; Wei, X.; Huang, Y.; Guan, C.; Zou, T.; Wang, S.; Liu, H.; Fan, Y., Delivery of demineralized bone matrix powder using a salt-leached silk fibroin carrier for bone regeneration. *Journal of Materials Chemistry B* **2015**, *3* (16), 3177-3188.
171. Ghanaati, S.; Unger, R. E.; Webber, M. J.; Barbeck, M.; Orth, C.; Kirkpatrick, J. A.; Booms, P.; Motta, A.; Migliaresi, C.; Sader, R. A.; Kirkpatrick, C. J., Scaffold vascularization in vivo driven by primary human osteoblasts in concert with host inflammatory cells. *Biomaterials* **2011**, *32* (32), 8150-8160.
172. Unger, R. E.; Sartoris, A.; Peters, K.; Motta, A.; Migliaresi, C.; Kunkel, M.; Bulnheim, U.; Rychly, J.; James Kirkpatrick, C., Tissue-like self-assembly in cocultures of endothelial cells and osteoblasts and the formation of microcapillary-like structures on three-dimensional porous biomaterials. *Biomaterials* **2007**, *28* (27), 3965-3976.
173. Fuchs, S.; Jiang, X.; Schmidt, H.; Dohle, E.; Ghanaati, S.; Orth, C.; Hofmann, A.; Motta, A.; Migliaresi, C.; Kirkpatrick, C. J., Dynamic processes involved in the pre-vascularization of silk fibroin constructs for bone regeneration using outgrowth endothelial cells. *Biomaterials* **2009**, *30* (7), 1329-1338.
174. Unger, R. E.; Ghanaati, S.; Orth, C.; Sartoris, A.; Barbeck, M.; Halstenberg, S.; Motta, A.; Migliaresi, C.; Kirkpatrick, C. J., The rapid anastomosis between prevascularized networks

- on silk fibroin scaffolds generated in vitro with cocultures of human microvascular endothelial and osteoblast cells and the host vasculature. *Biomaterials* **2010**, *31* (27), 6959-6967.
175. Kanczler, J. M.; Ginty, P. J.; White, L.; Clarke, N. M. P.; Howdle, S. M.; Shakesheff, K. M.; Oreffo, R. O. C., The effect of the delivery of vascular endothelial growth factor and bone morphogenic protein-2 to osteoprogenitor cell populations on bone formation. *Biomaterials* **2010**, *31* (6), 1242-1250.
176. Farokhi, M.; Mottaghitalab, F.; Shokrgozar, M. A.; Ai, J.; Hadjati, J.; Azami, M., Bio-hybrid silk fibroin/calcium phosphate/PLGA nanocomposite scaffold to control the delivery of vascular endothelial growth factor. *Materials Science and Engineering: C* **2014**, *35*, 401-410.
177. Chung, C.; Burdick, J. A., Engineering cartilage tissue. *Advanced Drug Delivery Reviews* **2008**, *60* (2), 243-262.
178. Huey, D. J.; Hu, J. C.; Athanasiou, K. A., Unlike Bone, Cartilage Regeneration Remains Elusive. *Science* **2012**, *338* (6109), 917-921.
179. Bhardwaj, N.; Singh, Y. P.; Devi, D.; Kandimalla, R.; Kotoky, J.; Mandal, B. B., Potential of silk fibroin/chondrocyte constructs of muga silkworm *Antheraea assamensis* for cartilage tissue engineering. *Journal of Materials Chemistry B* **2016**, *4* (21), 3670-3684.
180. Wang, Y.; Blasioli, D. J.; Kim, H.-J.; Kim, H. S.; Kaplan, D. L., Cartilage tissue engineering with silk scaffolds and human articular chondrocytes. *Biomaterials* **2006**, *27* (25), 4434-4442.
181. Wang, Y.; Kim, U.-J.; Blasioli, D. J.; Kim, H.-J.; Kaplan, D. L., In vitro cartilage tissue engineering with 3D porous aqueous-derived silk scaffolds and mesenchymal stem cells. *Biomaterials* **2005**, *26* (34), 7082-7094.
182. Uebersax, L.; Merkle, H. P.; Meinel, L., Insulin-like growth factor I releasing silk fibroin scaffolds induce chondrogenic differentiation of human mesenchymal stem cells. *Journal of Controlled Release* **2008**, *127* (1), 12-21.
183. Ding, F.; Deng, H.; Du, Y.; Shi, X.; Wang, Q., Emerging chitin and chitosan nanofibrous materials for biomedical applications. *Nanoscale* **2014**, *6* (16), 9477-9493.
184. Bhardwaj, N.; Nguyen, Q. T.; Chen, A. C.; Kaplan, D. L.; Sah, R. L.; Kundu, S. C., Potential of 3-D tissue constructs engineered from bovine chondrocytes/silk fibroin-chitosan for in vitro cartilage tissue engineering. *Biomaterials* **2011**, *32* (25), 5773-5781.
185. Silva, S. S.; Motta, A.; Rodrigues, M. T.; Pinheiro, A. F. M.; Gomes, M. E.; Mano, J. F.; Reis, R. L.; Migliaresi, C., Novel Genipin-Cross-Linked Chitosan/Silk Fibroin Sponges for Cartilage Engineering Strategies. *Biomacromolecules* **2008**, *9* (10), 2764-2774.
186. Lien, S.-M.; Ko, L.-Y.; Huang, T.-J., Effect of pore size on ECM secretion and cell growth in gelatin scaffold for articular cartilage tissue engineering. *Acta Biomaterialia* **2009**, *5* (2), 670-679.
187. Ghezzi, C. E.; Marelli, B.; Donelli, I.; Alessandrino, A.; Freddi, G.; Nazhat, S. N., The role of physiological mechanical cues on mesenchymal stem cell differentiation in an airway tract-like dense collagen-silk fibroin construct. *Biomaterials* **2014**, *35* (24), 6236-6247.
188. Shi, W.; Sun, M.; Hu, X.; Ren, B.; Cheng, J.; Li, C.; Duan, X.; Fu, X.; Zhang, J.; Chen, H.; Ao, Y., Structurally and Functionally Optimized Silk-Fibroin-Gelatin Scaffold Using 3D Printing to Repair Cartilage Injury In Vitro and In Vivo. *Adv Mater* **2017**, *29* (29), 1701089. <https://doi.org/10.1002/adma.201701089>.
189. Singh, N.; Rahatekar, S. S.; Koziol, K. K. K.; Ng, T. H. S.; Patil, A. J.; Mann, S.; Hollander, A. P.; Kafienah, W., Directing Chondrogenesis of Stem Cells with Specific Blends of Cellulose and Silk. *Biomacromolecules* **2013**, *14* (5), 1287-1298.
190. Foss, C.; Merzari, E.; Migliaresi, C.; Motta, A., Silk Fibroin/Hyaluronic Acid 3D Matrices for Cartilage Tissue Engineering. *Biomacromolecules* **2013**, *14* (1), 38-47.
191. Singh, Y. P.; Bhardwaj, N.; Mandal, B. B., Potential of Agarose/Silk Fibroin Blended Hydrogel for in Vitro Cartilage Tissue Engineering. *ACS Applied Materials & Interfaces* **2016**, *8* (33), 21236-21249.

192. Cai, K.; Yao, K.; Lin, S.; Yang, Z.; Li, X.; Xie, H.; Qing, T.; Gao, L., Poly(d,l-lactic acid) surfaces modified by silk fibroin: effects on the culture of osteoblast in vitro. *Biomaterials* **2002**, *23* (4), 1153-1160.
193. Baek, H. S.; Park, Y. H.; Ki, C. S.; Park, J.-C.; Rah, D. K., Enhanced chondrogenic responses of articular chondrocytes onto porous silk fibroin scaffolds treated with microwave-induced argon plasma. *Surface and Coatings Technology* **2008**, *202* (22), 5794-5797.
194. Jin, S. C.; Baek, H. S.; Woo, Y. I.; Lee, M. H.; Kim, J.-S.; Park, J.-C.; Park, Y. H.; Rah, D. K.; Chung, K.-H.; Lee, S. J.; Han, I. H., Beneficial effects of microwave-induced argon plasma treatment on cellular behaviors of articular chondrocytes onto nanofibrous silk fibroin mesh. *Macromolecular Research* **2009**, *17* (9), 703-708.
195. Cheon, Y. W.; Lee, W. J.; Baek, H. S.; Lee, Y. D.; Park, J.-C.; Park, Y. H.; Ki, C. S.; Chung, K.-H.; Rah, D. K., Enhanced Chondrogenic Responses of Human Articular Chondrocytes Onto Silk Fibroin/Wool Keratose Scaffolds Treated With Microwave-Induced Argon Plasma. *Artificial Organs* **2010**, *34* (5), 384-392.
196. Tıǧlı, R. S.; Cannizaro, C.; Gümüşderelioǧlu, M.; Kaplan, D. L., Chondrogenesis in perfusion bioreactors using porous silk scaffolds and hESC-derived MSCs. *Journal of Biomedical Materials Research Part A* **2011**, *96A* (1), 21-28.
197. Shangkai, C.; Naohide, T.; Koji, Y.; Yasuji, H.; Masaaki, N.; Tomohiro, T.; Yasushi, T., Transplantation of Allogeneic Chondrocytes Cultured in Fibroin Sponge and Stirring Chamber to Promote Cartilage Regeneration. *Tissue engineering* **2007**, *13* (3), 483-492.
198. Seda Tıǧlı, R.; Ghosh, S.; Laha, M. M.; Shevde, N. K.; Daheron, L.; Gimble, J.; Gümüşderelioǧlu, M.; Kaplan, D. L., Comparative chondrogenesis of human cell sources in 3D scaffolds. *Journal of tissue engineering and regenerative medicine* **2009**, *3* (5), 348-360.
199. Kuo, C. K.; Marturano, J. E.; Tuan, R. S., Novel strategies in tendon and ligament tissue engineering: Advanced biomaterials and regeneration motifs. *BMC Sports Science, Medicine and Rehabilitation* **2010**, *2* (1), 20.
200. Tatara, A. M.; Mikos, A. G., Tissue Engineering in Orthopaedics. *J Bone Joint Surg Am* **2016**, *98* (13), 1132-1139.
201. Liu, H.; Fan, H.; Wang, Y.; Toh, S. L.; Goh, J. C. H., The interaction between a combined knitted silk scaffold and microporous silk sponge with human mesenchymal stem cells for ligament tissue engineering. *Biomaterials* **2008**, *29* (6), 662-674.
202. Fan, H.; Liu, H.; Wong, E. J. W.; Toh, S. L.; Goh, J. C. H., In vivo study of anterior cruciate ligament regeneration using mesenchymal stem cells and silk scaffold. *Biomaterials* **2008**, *29* (23), 3324-3337.
203. Fan, H.; Liu, H.; Toh, S. L.; Goh, J. C. H., Anterior cruciate ligament regeneration using mesenchymal stem cells and silk scaffold in large animal model. *Biomaterials* **2009**, *30* (28), 4967-4977.
204. Chen, X.; Qi, Y.-Y.; Wang, L.-L.; Yin, Z.; Yin, G.-L.; Zou, X.-H.; Ouyang, H.-W., Ligament regeneration using a knitted silk scaffold combined with collagen matrix. *Biomaterials* **2008**, *29* (27), 3683-3692.
205. Chen, J.; Altman, G. H.; Karageorgiou, V.; Horan, R.; Collette, A.; Volloch, V.; Colabro, T.; Kaplan, D. L., Human bone marrow stromal cell and ligament fibroblast responses on RGD-modified silk fibers. *Journal of Biomedical Materials Research Part A* **2003**, *67A* (2), 559-570.
206. Moreau, J. E.; Chen, J.; Horan, R. L.; Kaplan, D. L.; Altman, G. H., Sequential Growth Factor Application in Bone Marrow Stromal Cell Ligament Engineering. *Tissue engineering* **2005**, *11* (11-12), 1887-1897.
207. Moreau, J.; Chen, J.; Kaplan, D.; Altman, G., Sequential Growth Factor Stimulation of Bone Marrow Stromal Cells in Extended Culture. *Tissue engineering* **2006**, *12* (10), 2905-2912.
208. Moreau, J. E.; Bramono, D. S.; Horan, R. L.; Kaplan, D. L.; Altman, G. H., Sequential Biochemical and Mechanical Stimulation in the Development of Tissue-Engineered Ligaments. *Tissue Engineering Part A* **2008**, *14* (7), 1161-1172.

209. Takezawa, T.; Ozaki, K.; Takabayashi, C., Reconstruction of a Hard Connective Tissue Utilizing a Pressed Silk Sheet and Type-I Collagen as the Scaffold for Fibroblasts. *Tissue engineering* **2007**, *13* (6), 1357-1366.
210. Seo, Y.-K.; Yoon, H.-H.; Song, K.-Y.; Kwon, S.-Y.; Lee, H.-S.; Park, Y.-S.; Park, J.-K., Increase in cell migration and angiogenesis in a composite silk scaffold for tissue-engineered ligaments. *Journal of Orthopaedic Research* **2009**, *27* (4), 495-503.
211. Fan, H.; Liu, H.; Toh, S. L.; Goh, J. C. H., Enhanced differentiation of mesenchymal stem cells co-cultured with ligament fibroblasts on gelatin/silk fibroin hybrid scaffold. *Biomaterials* **2008**, *29* (8), 1017-1027.
212. Bosetti, M.; Boccafocchi, F.; Calarco, A.; Leigheb, M.; Gatti, S.; Piffanelli, V.; Peluso, G.; Cannas, M., Behaviour of human mesenchymal stem cells on a polyelectrolyte-modified HEMA hydrogel for silk-based ligament tissue engineering. *Journal of Biomaterials Science, Polymer Edition* **2008**, *19* (9), 1111-1123.
213. Sahoo, S.; Toh, S. L.; Goh, J. C. H., A bFGF-releasing silk/PLGA-based biohybrid scaffold for ligament/tendon tissue engineering using mesenchymal progenitor cells. *Biomaterials* **2010**, *31* (11), 2990-2998.
214. Chua, A. W. C.; Khoo, Y. C.; Tan, B. K.; Tan, K. C.; Foo, C. L.; Chong, S. J., Skin tissue engineering advances in severe burns: review and therapeutic applications. *Burns & Trauma* **2016**, *4* (1), 3.
- *215. Farokhi, M.; Mottaghtalab, F.; Fatahi, Y.; Khademhosseini, A.; Kaplan, D. L., Overview of Silk Fibroin Use in Wound Dressings. *Trends in Biotechnology* **2018**, *36* (9), 907-922.
216. Jeong, L.; Yeo, I.-S.; Kim, H. N.; Yoon, Y. I.; Jang, D. H.; Jung, S. Y.; Min, B.-M.; Park, W. H., Plasma-treated silk fibroin nanofibers for skin regeneration. *International journal of biological macromolecules* **2009**, *44* (3), 222-228.
217. Kong, M.; Chen, X. G.; Xing, K.; Park, H. J., Antimicrobial properties of chitosan and mode of action: A state of the art review. *International Journal of Food Microbiology* **2010**, *144* (1), 51-63.
218. Xu, Y.; Li, L.; Yu, X.; Gu, Z.; Zhang, X., Feasibility study of a novel crosslinking reagent (alginate dialdehyde) for biological tissue fixation. *Carbohydrate Polymers* **2012**, *87* (2), 1589-1595.
219. Gu, Z.; Xie, H.; Huang, C.; Li, L.; Yu, X., Preparation of chitosan/silk fibroin blending membrane fixed with alginate dialdehyde for wound dressing. *International journal of biological macromolecules* **2013**, *58*, 121-126.
220. Guang, S.; An, Y.; Ke, F.; Zhao, D.; Shen, Y.; Xu, H., Chitosan/silk fibroin composite scaffolds for wound dressing. *Journal of Applied Polymer Science* **2015**, *132* (35), 42503,10.1002/app.42503.
221. Gupta K, A.; Mita, K.; Arunkumar, K. P.; Nagaraju, J., Molecular architecture of silk fibroin of Indian golden silkworm, *Antheraea assama*. *Scientific Reports* **2015**, *5*, 12706.
222. Chouhan, D.; Lohe, T.-u.; Samudrala, P. K.; Mandal, B. B., In Situ Forming Injectable Silk Fibroin Hydrogel Promotes Skin Regeneration in Full Thickness Burn Wounds. *Advanced Healthcare Materials* **2018**, *7* (24), 1801092.
223. Srivastava, C. M.; Purwar, R.; Kannaujia, R.; Sharma, D., Flexible silk fibroin films for wound dressing. *Fibers and Polymers* **2015**, *16* (5), 1020-1030.
224. Navone, S. E.; Pascucci, L.; Dossena, M.; Ferri, A.; Invernici, G.; Acerbi, F.; Cristini, S.; Bedini, G.; Tosetti, V.; Ceserani, V.; Bonomi, A.; Pessina, A.; Freddi, G.; Alessandrino, A.; Ceccarelli, P.; Campanella, R.; Marfia, G.; Alessandri, G.; Parati, E. A., Decellularized silk fibroin scaffold primed with adipose mesenchymal stromal cells improves wound healing in diabetic mice. *Stem Cell Research & Therapy* **2014**, *5* (1), 7.
225. Yang, X.; Fan, L.; Ma, L.; Wang, Y.; Lin, S.; Yu, F.; Pan, X.; Luo, G.; Zhang, D.; Wang, H., Green electrospun Manuka honey/silk fibroin fibrous matrices as potential wound dressing. *Materials & Design* **2017**, *119*, 76-84.

226. Jeong, L.; Kim, M. H.; Jung, J.-Y.; Min, B. M.; Park, W. H., Effect of silk fibroin nanofibers containing silver sulfadiazine on wound healing. *Int J Nanomedicine* **2014**, *9*, 5277-5287.
227. Yeo, I.-S.; Oh, J.-E.; Jeong, L.; Lee, T. S.; Lee, S. J.; Park, W. H.; Min, B.-M., Collagen-Based Biomimetic Nanofibrous Scaffolds: Preparation and Characterization of Collagen/Silk Fibroin Bicomponent Nanofibrous Structures. *Biomacromolecules* **2008**, *9* (4), 1106-1116.
228. Yoo, C. R.; Yeo, I.-S.; Park, K. E.; Park, J. H.; Lee, S. J.; Park, W. H.; Min, B.-M., Effect of chitin/silk fibroin nanofibrous bicomponent structures on interaction with human epidermal keratinocytes. *International journal of biological macromolecules* **2008**, *42* (4), 324-334.
229. Teh, B. M.; Marano, R. J.; Shen, Y.; Friedland, P. L.; Dilley, R. J.; Atlas, M. D., Tissue engineering of the tympanic membrane. *Tissue Eng Part B Rev* **2013**, *19* (2), 116-32.
230. Villar-Fernandez, M. A.; Lopez-Escamez, J. A., Outlook for Tissue Engineering of the Tympanic Membrane. *Audiol Res* **2015**, *5* (1), 117.
231. Wang, A. Y.; Shen, Y.; Liew, L. J.; Wang, J. T.; von Unge, M.; Atlas, M. D.; Dilley, R. J., Rat model of chronic tympanic membrane perforation: Ventilation tube with mitomycin C and dexamethasone. *International Journal of Pediatric Otorhinolaryngology* **2016**, *80*, 61-68.
232. Unger, R. E.; Wolf, M.; Peters, K.; Motta, A.; Migliaresi, C.; James Kirkpatrick, C., Growth of human cells on a non-woven silk fibroin net: a potential for use in tissue engineering. *Biomaterials* **2004**, *25* (6), 1069-1075.
233. Levin, B.; Redmond, S. L.; Rajkhowa, R.; Eikelboom, R. H.; Marano, R. J.; Atlas, M. D., Preliminary results of the application of a silk fibroin scaffold to otology. *Otolaryngology - Head and Neck Surgery* **2010**, *142* (3, Supplement 1), S33-S35.
234. Ghassemifar, R.; Redmond, S.; Zainuddin; Chirila, T. V., Advancing towards a tissue-engineered tympanic membrane: silk fibroin as a substratum for growing human eardrum keratinocytes. *Journal of biomaterials applications* **2010**, *24* (7), 591-606.
235. Shen, Y.; Redmond, S. L.; Teh, B. M.; Yan, S.; Wang, Y.; Zhou, L.; Budgeon, C. A.; Eikelboom, R. H.; Atlas, M. D.; Dilley, R. J.; Zheng, M.; Marano, R. J., Scaffolds for tympanic membrane regeneration in rats. *Tissue Eng Part A* **2013**, *19* (5-6), 657-68.
236. Shen, Y.; Redmond, S. L.; Teh, B. M.; Yan, S.; Wang, Y.; Atlas, M. D.; Dilley, R. J.; Zheng, M.; Marano, R. J., Tympanic membrane repair using silk fibroin and acellular collagen scaffolds. *The Laryngoscope* **2013**, *123* (8), 1976-1982.
237. Shen, Y.; Redmond, S. L.; Papadimitriou, J. M.; Teh, B. M.; Yan, S.; Wang, Y.; Atlas, M. D.; Marano, R. J.; Zheng, M.; Dilley, R. J., The biocompatibility of silk fibroin and acellular collagen scaffolds for tissue engineering in the ear. *Biomed Mater* **2014**, *9* (1), 015015.
238. Allardyce, B. J.; Rajkhowa, R.; Dilley, R. J.; Xie, Z.; Campbell, L.; Keating, A.; Atlas, M. D.; von Unge, M.; Wang, X., Comparative acoustic performance and mechanical properties of silk membranes for the repair of chronic tympanic membrane perforations. *Journal of the Mechanical Behavior of Biomedical Materials* **2016**, *64*, 65-74.
239. Caliarì, S. R.; Burdick, J. A., A practical guide to hydrogels for cell culture. *Nature Methods* **2016**, *13* (5), 405-414.
240. Tan, A.; Rajadas, J.; Seifalian, A. M., Biochemical engineering nerve conduits using peptide amphiphiles. *Journal of Controlled Release* **2012**, *163* (3), 342-352.
- *241. Yang, Z.; Xu, H.; Zhao, X., Designer Self-Assembling Peptide Hydrogels to Engineer 3D Cell Microenvironments for Cell Constructs Formation and Precise Oncology Remodeling in Ovarian Cancer. *Advanced Science* **2020**, *7* (9), 1903718.
242. Asghar, W.; El Assal, R.; Shafiee, H.; Pitteri, S.; Paulmurugan, R.; Demirci, U., Engineering cancer microenvironments for in vitro 3-D tumor models. *Materials Today* **2015**, *18* (10), 539-553.
243. Peela, N.; Truong, D.; Saini, H.; Chu, H.; Mashaghi, S.; Ham, S. L.; Singh, S.; Tavana, H.; Mosadegh, B.; Nikkhah, M., Advanced biomaterials and microengineering technologies to recapitulate the stepwise process of cancer metastasis. *Biomaterials* **2017**, *133*, 176-207.

244. Chen, J.; Zou, X., Self-assemble peptide biomaterials and their biomedical applications. *Bioactive Materials* **2019**, *4*, 120-131.
245. Zhang, S.; Holmes, T.; Lockshin, C.; Rich, A., Spontaneous assembly of a self-complementary oligopeptide to form a stable macroscopic membrane. *Proceedings of the National Academy of Sciences* **1993**, *90* (8), 3334-3338.
- **246. Li, J.; Wang, J.; Zhao, Y.; Zhou, P.; Carter, J.; Li, Z.; Waigh, T. A.; Lu, J. R.; Xu, H., Surfactant-like peptides: From molecular design to controllable self-assembly with applications. *Coordination Chemistry Reviews* **2020**, *421*, 213418.
247. Acar, H.; Srivastava, S.; Chung, E. J.; Schnorenberg, M. R.; Barrett, J. C.; LaBelle, J. L.; Tirrell, M., Self-assembling peptide-based building blocks in medical applications. *Advanced Drug Delivery Reviews* **2017**, *110-111*, 65-79.
248. Lakshmanan, A.; Zhang, S.; Hauser, C. A. E., Short self-assembling peptides as building blocks for modern nanodevices. *Trends in Biotechnology* **2012**, *30* (3), 155-165.
249. Ulijn, R. V.; Smith, A. M., Designing peptide based nanomaterials. *Chemical Society Reviews* **2008**, *37* (4), 664-675.
- **250. Zhao, X.; Pan, F.; Xu, H.; Yaseen, M.; Shan, H.; Hauser, C. A. E.; Zhang, S.; Lu, J. R., Molecular self-assembly and applications of designer peptide amphiphiles. *Chemical Society Reviews* **2010**, *39* (9), 3480-3498.
251. Zhang, J.; Zhao, Y.; Han, S.; Chen, C.; Xu, H., Self-assembly of surfactant-like peptides and their applications. *Science China Chemistry* **2014**, *57* (12), 1634-1645.
252. Dasgupta, A.; Das, D., Designer Peptide Amphiphiles: Self-Assembly to Applications. *Langmuir* **2019**, *35* (33), 10704-10724.
253. Fleming, S.; Ulijn, R. V., Design of nanostructures based on aromatic peptide amphiphiles. *Chemical Society Reviews* **2014**, *43* (23), 8150-8177.
254. Dehsorkhi, A.; Castelletto, V.; Hamley, I. W., Self-assembling amphiphilic peptides. *Journal of Peptide Science* **2014**, *20* (7), 453-467.
255. Hamley, I. W., Self-assembly of amphiphilic peptides. *Soft Matter* **2011**, *7* (9), 4122-4138.
- *256. Hartgerink, J. D.; Beniash, E.; Stupp, S. I., Self-Assembly and Mineralization of Peptide-Amphiphile Nanofibers. *Science* **2001**, *294* (5547), 1684-1688.
257. Miotto, M.; Gouveia, R. M.; Connon, C. J., Peptide Amphiphiles in Corneal Tissue Engineering. *J Funct Biomater* **2015**, *6* (3), 687-707.
258. Hosseinkhani, H.; Hong, P.-D.; Yu, D.-S., Self-Assembled Proteins and Peptides for Regenerative Medicine. *Chemical Reviews* **2013**, *113* (7), 4837-4861.
- *259. Dobbs, R.; Choe, S.; Kalmanek, E.; Harrington, D. A.; Stupp, S. I.; McVary, K. T.; Podlasek, C. A., Peptide amphiphile delivery of sonic hedgehog protein promotes neurite formation in penile projecting neurons. *Nanomedicine: Nanotechnology, Biology and Medicine* **2018**, *14* (7), 2087-2094.
260. Qiu, F.; Chen, Y.; Tang, C.; Zhao, X., Amphiphilic peptides as novel nanomaterials: design, self-assembly and application. *Int J Nanomedicine* **2018**, *13*, 5003-5022.
261. Cui, H.; Webber, M. J.; Stupp, S. I., Self-assembly of peptide amphiphiles: From molecules to nanostructures to biomaterials. *Peptide Science* **2010**, *94* (1), 1-18.
262. Adler-Abramovich, L.; Gazit, E., The physical properties of supramolecular peptide assemblies: from building block association to technological applications. *Chemical Society Reviews* **2014**, *43* (20), 6881-6893.
263. Zhou, M.; Smith, A. M.; Das, A. K.; Hodson, N. W.; Collins, R. F.; Ulijn, R. V.; Gough, J. E., Self-assembled peptide-based hydrogels as scaffolds for anchorage-dependent cells. *Biomaterials* **2009**, *30* (13), 2523-2530.
264. Guo, H.; Zhang, J.; Xu, T.; Zhang, Z.; Yao, J.; Shao, Z., The Robust Hydrogel Hierarchically Assembled from a pH Sensitive Peptide Amphiphile Based on Silk Fibroin. *Biomacromolecules* **2013**, *14* (8), 2733-2738.

265. Ozbas, B.; Kretsinger, J.; Rajagopal, K.; Schneider, J. P.; Pochan, D. J., Salt-Triggered Peptide Folding and Consequent Self-Assembly into Hydrogels with Tunable Modulus. *Macromolecules* **2004**, *37* (19), 7331-7337.
266. Bowerman, C. J.; Nilsson, B. L., A Reductive Trigger for Peptide Self-Assembly and Hydrogelation. *Journal of the American Chemical Society* **2010**, *132* (28), 9526-9527.
267. Schneider, J. P.; Pochan, D. J.; Ozbas, B.; Rajagopal, K.; Pakstis, L.; Kretsinger, J., Responsive Hydrogels from the Intramolecular Folding and Self-Assembly of a Designed Peptide. *Journal of the American Chemical Society* **2002**, *124* (50), 15030-15037.
268. Mart, R. J.; Osborne, R. D.; Stevens, M. M.; Ulijn, R. V., Peptide-based stimuli-responsive biomaterials. *Soft Matter* **2006**, *2* (10), 822-835.
269. Hauser, C. A. E.; Zhang, S., Designer self-assembling peptide nanofiber biological materials. *Chemical Society Reviews* **2010**, *39* (8), 2780-2790.
270. Zhou, P.; Deng, L.; Wang, Y.; Lu, J. R.; Xu, H., Different nanostructures caused by competition of intra- and inter- β -sheet interactions in hierarchical self-assembly of short peptides. *Journal of Colloid and Interface Science* **2016**, *464*, 219-228.
271. Wang, M.; Wang, J.; Zhou, P.; Deng, J.; Zhao, Y.; Sun, Y.; Yang, W.; Wang, D.; Li, Z.; Hu, X.; King, S. M.; Rogers, S. E.; Cox, H.; Waigh, T. A.; Yang, J.; Lu, J. R.; Xu, H., Nanoribbons self-assembled from short peptides demonstrate the formation of polar zippers between β -sheets. *Nature Communications* **2018**, *9* (1), 5118.
272. Chakrabarty, A.; Kortemme, T.; Baldwin, R. L., Helix propensities of the amino acids measured in alanine-based peptides without helix-stabilizing side-chain interactions. *Protein Sci* **1994**, *3* (5), 843-852.
273. Perutz, M. F.; Staden, R.; Moens, L.; De Baere, I., Polar zippers. *Current Biology* **1993**, *3* (5), 249-253.
274. Smith, A. M.; Williams, R. J.; Tang, C.; Coppo, P.; Collins, R. F.; Turner, M. L.; Saiani, A.; Ulijn, R. V., Fmoc-Diphenylalanine Self Assembles to a Hydrogel via a Novel Architecture Based on π - π Interlocked β -Sheets. *Advanced Materials* **2008**, *20* (1), 37-41.
275. Yan, X.; Zhu, P.; Li, J., Self-assembly and application of diphenylalanine-based nanostructures. *Chemical Society Reviews* **2010**, *39* (6), 1877-1890.
276. Pochan, D. J.; Schneider, J. P.; Kretsinger, J.; Ozbas, B.; Rajagopal, K.; Haines, L., Thermally Reversible Hydrogels via Intramolecular Folding and Consequent Self-Assembly of a de Novo Designed Peptide. *Journal of the American Chemical Society* **2003**, *125* (39), 11802-11803.
277. Zhao, Y.; Deng, L.; Wang, J.; Xu, H.; Lu, J. R., Solvent Controlled Structural Transition of KI4K Self-Assemblies: from Nanotubes to Nanofibrils. *Langmuir* **2015**, *31* (47), 12975-12983.
278. von maltzahn, G.; Vauthey, S.; Santoso, S.; Zhang, S., *Positively Charged Surfactant-like Peptides Self-assemble into Nanostructures*. 2003; Vol. 19.
279. Cui, H.; Muraoka, T.; Cheetham, A.; Stupp, S. I., Self-Assembly of Giant Peptide Nanobelts. *Nano letters* **2009**, *9* (3), 945-951.
280. Wang, W.; Chau, Y., Self-assembled peptide nanorods as building blocks of fractal patterns. *Soft Matter* **2009**, *5* (24), 4893-4898.
281. Santoso, S.; Hwang, W.; Hartman, H.; Zhang, S., Self-assembly of Surfactant-like Peptides with Variable Glycine Tails to Form Nanotubes and Nanovesicles. *Nano Letters* **2002**, *2* (7), 687-691.
282. Novo, M.; Freire, S.; Al-Soufi, W., Critical aggregation concentration for the formation of early Amyloid- β (1-42) oligomers. *Scientific Reports* **2018**, *8* (1), 1783.
283. Löwik, D. W. P. M.; van Hest, J. C. M., Peptide based amphiphiles. *Chemical Society Reviews* **2004**, *33* (4), 234-245.
284. Zhang, S., Fabrication of novel biomaterials through molecular self-assembly. *Nature Biotechnology* **2003**, *21* (10), 1171-1178.
285. Zhao, X.; Pan, F.; Lu, J. R., Recent development of peptide self-assembly. *Progress in Natural Science* **2008**, *18* (6), 653-660.

286. Zhang, S.; Altman, M., Peptide self-assembly in functional polymer science and engineering. *Reactive and Functional Polymers* **1999**, *41* (1), 91-102.
287. Zhang, S., Emerging biological materials through molecular self-assembly. *Biotechnology Advances* **2002**, *20* (5), 321-339.
288. Hauser, C. A. E.; Zhang, S., Designer Self-Assembling Peptide Materials for Diverse Applications. *Macromolecular Symposia* **2010**, *295* (1), 30-48.
289. Moore, A. N.; Hartgerink, J. D., Self-Assembling Multidomain Peptide Nanofibers for Delivery of Bioactive Molecules and Tissue Regeneration. *Accounts of Chemical Research* **2017**, *50* (4), 714-722.
290. Caplan, M. R.; Schwartzfarb, E. M.; Zhang, S.; Kamm, R. D.; Lauffenburger, D. A., Control of self-assembling oligopeptide matrix formation through systematic variation of amino acid sequence. *Biomaterials* **2002**, *23* (1), 219-227.
291. Zhang, S.; Holmes, T. C.; DiPersio, C. M.; Hynes, R. O.; Su, X.; Rich, A., Self-complementary oligopeptide matrices support mammalian cell attachment. *Biomaterials* **1995**, *16* (18), 1385-1393.
292. Seow, W. Y.; Hauser, C. A. E., Short to ultrashort peptide hydrogels for biomedical uses. *Materials Today* **2014**, *17* (8), 381-388.
293. Gelain, F.; Luo, Z.; Zhang, S., Self-Assembling Peptide EAK16 and RADA16 Nanofiber Scaffold Hydrogel. *Chemical Reviews* **2020**, *120* (24), 13434-13460.
294. Yokoi, H.; Kinoshita, T.; Zhang, S., Dynamic reassembly of peptide RADA16 nanofiber scaffold. *Proceedings of the National Academy of Sciences of the United States of America* **2005**, *102* (24), 8414-8419.
295. von Maltzahn, G.; Vauthey, S.; Santoso, S.; Zhang, S., Positively Charged Surfactant-like Peptides Self-assemble into Nanostructures. *Langmuir* **2003**, *19* (10), 4332-4337.
296. Vauthey, S.; Santoso, S.; Gong, H.; Watson, N.; Zhang, S., Molecular self-assembly of surfactant-like peptides to form nanotubes and nanovesicles. *Proceedings of the National Academy of Sciences* **2002**, *99* (8), 5355-5360.
297. Castelletto, V.; Nutt, D. R.; Hamley, I. W.; Bucak, S.; Cenker, Ç.; Olsson, U., Structure of single-wall peptide nanotubes: in situ flow aligning X-ray diffraction. *Chemical Communications* **2010**, *46* (34), 6270-6272.
298. Cox, H.; Georgiades, P.; Xu, H.; Waigh, T. A.; Lu, J. R., Self-Assembly of Mesoscopic Peptide Surfactant Fibrils Investigated by STORM Super-Resolution Fluorescence Microscopy. *Biomacromolecules* **2017**, *18* (11), 3481-3491.
299. Xu, H.; Wang, Y.; Ge, X.; Han, S.; Wang, S.; Zhou, P.; Shan, H.; Zhao, X.; Lu, J. R., Twisted Nanotubes Formed from Ultrashort Amphiphilic Peptide I3K and Their Templating for the Fabrication of Silica Nanotubes. *Chemistry of Materials* **2010**, *22* (18), 5165-5173.
300. Wang, Q.; Zhang, X.; Zheng, J.; Liu, D., Self-assembled peptide nanotubes as potential nanocarriers for drug delivery. *RSC Advances* **2014**, *4* (48), 25461-25469.
301. Han, S.; Cao, S.; Wang, Y.; Wang, J.; Xia, D.; Xu, H.; Zhao, X.; Lu, J. R., Self-Assembly of Short Peptide Amphiphiles: The Cooperative Effect of Hydrophobic Interaction and Hydrogen Bonding. *Chemistry – A European Journal* **2011**, *17* (46), 13095-13102.
302. Cao, C.; Cao, M.; Fan, H.; Xia, D.; Xu, H.; Lu, J. R., Redox modulated hydrogelation of a self-assembling short peptide amphiphile. *Chinese Science Bulletin* **2012**, *57* (33), 4296-4303.
303. Xu, H.; Wang, J.; Han, S.; Wang, J.; Yu, D.; Zhang, H.; Xia, D.; Zhao, X.; Waigh, T. A.; Lu, J. R., Hydrophobic-Region-Induced Transitions in Self-Assembled Peptide Nanostructures. *Langmuir* **2009**, *25* (7), 4115-4123.
304. Zhao, Y.; Wang, J.; Deng, L.; Zhou, P.; Wang, S.; Wang, Y.; Xu, H.; Lu, J. R., Tuning the Self-Assembly of Short Peptides via Sequence Variations. *Langmuir* **2013**, *29* (44), 13457-13464.
305. Wang, M.; Zhou, P.; Wang, J.; Zhao, Y.; Ma, H.; Lu, J. R.; Xu, H., Left or Right: How Does Amino Acid Chirality Affect the Handedness of Nanostructures Self-Assembled from Short Amphiphilic Peptides? *Journal of the American Chemical Society* **2017**, *139* (11), 4185-4194.

306. Garcia, A. M.; Iglesias, D.; Parisi, E.; Styan, K. E.; Waddington, L. J.; Deganutti, C.; De Zorzi, R.; Grassi, M.; Melchionna, M.; Vargiu, A. V.; Marchesan, S., Chirality Effects on Peptide Self-Assembly Unraveled from Molecules to Materials. *Chem* **2018**, *4* (8), 1862-1876.
307. Hamley, I. W., Lipopeptides: from self-assembly to bioactivity. *Chemical Communications* **2015**, *51* (41), 8574-8583.
308. Mnif, I.; Ghribi, D., Review lipopeptides biosurfactants: Mean classes and new insights for industrial, biomedical, and environmental applications. *Peptide Science* **2015**, *104* (3), 129-147.
309. Heerklotz, H.; Seelig, J., Detergent-Like Action of the Antibiotic Peptide Surfactin on Lipid Membranes. *Biophysical Journal* **2001**, *81* (3), 1547-1554.
310. Singh, P.; Cameotra, S. S., Potential applications of microbial surfactants in biomedical sciences. *Trends Biotechnol* **2004**, *22* (3), 142-146.
311. Steller, S.; Vollenbroich, D.; Leenders, F.; Stein, T.; Conrad, B.; Hofemeister, J.; Jacques, P.; Thonart, P.; Vater, J., Structural and functional organization of the fengycin synthetase multienzyme system from *Bacillus subtilis* b213 and A1/3. *Chemistry & Biology* **1999**, *6* (1), 31-41.
312. Raaijmakers, J. M.; De Bruijn, I.; Nybroe, O.; Ongena, M., Natural functions of lipopeptides from *Bacillus* and *Pseudomonas*: more than surfactants and antibiotics. *FEMS Microbiology Reviews* **2010**, *34* (6), 1037-1062.
313. Carolin C, F.; Kumar, P. S.; Ngueagni, P. T., A review on new aspects of lipopeptide biosurfactant: Types, production, properties and its application in the bioremediation process. *Journal of Hazardous Materials* **2021**, *407*, 124827.
314. Peypoux, F.; Bonmatin, J. M.; Wallach, J., Recent trends in the biochemistry of surfactin. *Applied Microbiology and Biotechnology* **1999**, *51* (5), 553-563.
315. Ongena, M.; Jacques, P., *Bacillus* lipopeptides: versatile weapons for plant disease biocontrol. *Trends Microbiol* **2007**, *16* (3), 115-125.
316. Yan, L.; Liu, G.; Zhao, B.; Pang, B.; Wu, W.; Ai, C.; Zhao, X.; Wang, X.; Jiang, C.; Shao, D.; Liu, Q.; Li, M.; Wang, L.; Shi, J., Novel Biomedical Functions of Surfactin A from *Bacillus subtilis* in Wound Healing Promotion and Scar Inhibition. *Journal of Agricultural and Food Chemistry* **2020**, *68* (26), 6987-6997.
317. Zhao, H.; Zhao, X.; Lei, S.; Zhang, Y.; Shao, D.; Jiang, C.; Sun, H.; Shi, J., Effect of cell culture models on the evaluation of anticancer activity and mechanism analysis of the potential bioactive compound, iturin A, produced by *Bacillus subtilis*. *Food & Function* **2019**, *10* (3), 1478-1489.
318. Matthew, J. W.; Jörn, T.; Christina, J. N.; Katja-Theres, M.; Johann, B.; Douglas, W. L.; Samuel, I. S., Supramolecular nanostructures that mimic VEGF as a strategy for ischemic tissue repair. *Proc Natl Acad Sci U S A* **2011**, *108* (33), 13438-13443.
319. Ramille, N. S.; Nirav, A. S.; Marc, M. D. R. L.; Caleb, H.; Gordon, N.; Samuel, I. S.; Robert, L., Supramolecular Design of Self-Assembling Nanofibers for Cartilage Regeneration. *Proc Natl Acad Sci U S A* **2010**, *107* (8), 3293-3298.
320. Paramonov, S. E.; Jun, H.-W.; Hartgerink, J. D., Self-Assembly of Peptide–Amphiphile Nanofibers: The Roles of Hydrogen Bonding and Amphiphilic Packing. *J. Am. Chem. Soc* **2006**, *128* (22), 7291-7298.
321. Hutchinson, J. A.; Burholt, S.; Hamley, I. W., Peptide hormones and lipopeptides: from self-assembly to therapeutic applications. *Journal of Peptide Science* **2017**, *23* (2), 82-94.
322. Niece, K. L.; Czeisler, C.; Sahni, V.; Tysseling-Mattiace, V.; Pashuck, E. T.; Kessler, J. A.; Stupp, S. I., Modification of gelation kinetics in bioactive peptide amphiphiles. *Biomaterials* **2008**, *29* (34), 4501-4509.
323. Yoshida, T.; Lai, T. C.; Kwon, G. S.; Sako, K., pH- and ion-sensitive polymers for drug delivery. *Expert Opin Drug Deliv* **2013**, *10* (11), 1497-1513.

324. Gabriel, A. S.; Catherine, C.; Krista, L. N.; Elia, B.; Daniel, A. H.; John, A. K.; Samuel, I. S., Selective Differentiation of Neural Progenitor Cells by High-Epitope Density Nanofibers. *Science* **2004**, *303* (5662), 1352-1355.
325. Niece, K. L.; Hartgerink, J. D.; Donners, J. J. J. M.; Stupp, S. I., Self-Assembly Combining Two Bioactive Peptide-Amphiphile Molecules into Nanofibers by Electrostatic Attraction. *J. Am. Chem. Soc* **2003**, *125* (24), 7146-7147.
326. Dasgupta, A., Exploring architectures at the nanoscale: The interplay between hydrophobic twin lipid chains and head groups of designer peptide amphiphiles in the self-assembly process and application. *Soft Matter* **2016**, *12* (19), 4352-4360.
327. Gore, T.; Dori, Y.; Talmon, Y.; Tirrell, M.; Bianco-Peled, H., Self-Assembly of Model Collagen Peptide Amphiphiles. *Langmuir* **2001**, *17* (17), 5352-5360.
328. Dasgupta, A.; Mondal, J. H.; Das, D., Peptide hydrogels. *RSC advances* **2013**, *3* (24), 9117-9149.
329. Kumar, M.; Ing, N. L.; Narang, V.; Wijerathne, N. K.; Hochbaum, A. I.; Ulijn, R. V., Amino-acid-encoded biocatalytic self-assembly enables the formation of transient conducting nanostructures. *Nat Chem* **2018**, *10* (7), 696-703.
330. Wang, H.; Feng, Z.; Xu, B., Bioinspired assembly of small molecules in cell milieu. *Chem Soc Rev* **2017**, *46* (9), 2421-2436.
331. Al Kobaisi, M.; Bhosale, S. V.; Latham, K.; Raynor, A. M.; Bhosale, S. V., Functional Naphthalene Diimides: Synthesis, Properties, and Applications. *Chem. Rev* **2016**, *116* (19), 11685-11796.
332. Schon, T. B.; Tilley, A. J.; Kynaston, E. L.; Seferos, D. S., Three-Dimensional Arylene Diimide Frameworks for Highly Stable Lithium Ion Batteries. *ACS Appl. Mater. Interfaces* **2017**, *9* (18), 15631-15637.
333. Singha, N.; Gupta, P.; Pramanik, B.; Ahmed, S.; Dasgupta, A.; Ukil, A.; Das, D., Hydrogelation of a Naphthalene Diimide Appended Peptide Amphiphile and Its Application in Cell Imaging and Intracellular pH Sensing. *Biomacromolecules* **2017**, *18* (11), 3630-3641.
334. Pramanik, B.; Ahmed, S.; Singha, N.; Das, D., Self-Assembly Assisted Tandem Sensing of Pd²⁺ and CN⁻ by a Perylenediimide-Peptide Conjugate. *ChemistrySelect (Weinheim)* **2017**, *2* (31), 10061-10066.
335. Cao, H.; Yuan, Q.; Zhu, X.; Zhao, Y.-P.; Liu, M., Hierarchical Self-Assembly of Achiral Amino Acid Derivatives into Dendritic Chiral Nanotwists. *Langmuir* **2012**, *28* (43), 15410-15417.
336. Ahmed, S.; Mondal, J. H.; Behera, N.; Das, D., Self-Assembly of Peptide-Amphiphile Forming Helical Nanofibers and in Situ Template Synthesis of Uniform Mesoporous Single Wall Silica Nanotubes. *Langmuir* **2013**, *29* (46), 14274-14283.
337. Zhang, X.; Wang, C., Supramolecular amphiphiles. *Chem Soc Rev* **2010**, *4* (1), 94-11.
338. Yu, G.; Jie, K.; Huang, F., Supramolecular Amphiphiles Based on Host-Guest Molecular Recognition Motifs. *Chem Rev* **2015**, *115* (15), 7240-7303.
339. Wang, C.; Wang, Z.; Zhang, X., Amphiphilic Building Blocks for Self-Assembly: From Amphiphiles to Supra-amphiphiles. *Acc. Chem. Res* **2012**, *45* (4), 608-618.
340. Loh, X. J., Supramolecular host-guest polymeric materials for biomedical applications. *Materials horizons* **2014**, *1* (2), 185-195.
341. Bidarra, S. J.; Barrias, C. C.; Granja, P. L., Injectable alginate hydrogels for cell delivery in tissue engineering. *Acta Biomaterialia* **2014**, *10* (4), 1646-1662.
342. Yan, X.; Chen, Y.-R.; Song, Y.-F.; Ye, J.; Yang, M.; Xu, B.-B.; Zhang, J.-y.; Wang, X.; Yu, J.-K., Advances in the Application of Supramolecular Hydrogels for Stem Cell Delivery and Cartilage Tissue Engineering. *Front Bioeng Biotechnol* **2020**, *8* (847).
343. Versluis, F.; Tomatsu, I.; Kehr, S.; Fregonese, C.; Tepper, A. W. J. W.; Stuart, M. C. A.; Ravoo, B. J.; Koning, R. I.; Kros, A., Shape and Release Control of a Peptide Decorated Vesicle through pH Sensitive Orthogonal Supramolecular Interactions. *J. Am. Chem. Soc* **2009**, *131* (37), 13186-13187.

344. Hong, K. H.; Song, S.-C., 3D hydrogel stem cell niche controlled by host-guest interaction affects stem cell fate and survival rate. *Biomaterials* **2019**, *218*, 119338-119338.
345. Cheng, X.-J.; Liang, L.-L.; Chen, K.; Ji, N.-N.; Xiao, X.; Zhang, J.-X.; Zhang, Y.-Q.; Xue, S.-F.; Zhu, Q.-J.; Ni, X.-L.; Tao, Z., Twisted Cucurbit[14]uril. *Angewandte Chemie International Edition* **2013**, *52* (28), 7252-7255.
346. Das, D.; Scherman, O. A., Cucurbituril: At the Interface of Small Molecule Host–Guest Chemistry and Dynamic Aggregates. *Israel journal of chemistry* **2011**, *51* (5–6), 537-550.
347. Mondal, J. H.; Ahmed, S.; Das, D., Physicochemical Analysis of Mixed Micelles of a Viologen Surfactant: Extended to Water-in-Oil (w/o) Microemulsion and Cucurbit[8]uril-Assisted Vesicle Formation. *Langmuir* **2014**, *30* (28), 8290-8299.
348. Mondal, J. H.; Ghosh, T.; Ahmed, S.; Das, D., Dual Self-Sorting by Cucurbit[8]uril To Transform a Mixed Micelle to Vesicle. *Langmuir* **2014**, *30* (39), 11528-11534.
349. Jiao, D.; Geng, J.; Loh, X. J.; Das, D.; Lee, T. C.; Scherman, O. A., Supramolecular Peptide Amphiphile Vesicles through Host–Guest Complexation. *Angew Chem Int Ed Engl* **2012**, *51* (38), 9633-9637.
350. Mondal, J. H.; Ahmed, S.; Ghosh, T.; Das, D., Reversible deformation-formation of a multistimuli responsive vesicle by a supramolecular peptide amphiphile. *Soft Matter* **2015**, *11* (24), 4912-4920.
351. Loh, X. J.; Del Barrio, J.; Lee, T.-C.; Scherman, O. A., Supramolecular polymeric peptide amphiphile vesicles for the encapsulation of basic fibroblast growth factor. *Chem Commun (Camb)* **2014**, *50* (23), 3033-3035.
352. Wei, G.; Su, Z.; Reynolds, N. P.; Arosio, P.; Hamley, I. W.; Gazit, E.; Mezzenga, R., Self-assembling peptide and protein amyloids: from structure to tailored function in nanotechnology. *Chemical Society Reviews* **2017**, *46* (15), 4661-4708.
353. Mahadevi, A. S.; Sastry, G. N., Cooperativity in Noncovalent Interactions. *Chemical Reviews* **2016**, *116* (5), 2775-2825.
354. Huang, R.; Wang, Y.; Qi, W.; Su, R.; He, Z., Temperature-induced reversible self-assembly of diphenylalanine peptide and the structural transition from organogel to crystalline nanowires. *Nanoscale Research Letters* **2014**, *9* (1), 653.
355. Zhu, P.; Yan, X.; Su, Y.; Yang, Y.; Li, J., Solvent-Induced Structural Transition of Self-Assembled Dipeptide: From Organogels to Microcrystals. *Chemistry – A European Journal* **2010**, *16* (10), 3176-3183.
356. Lu, S.; Chen, P., Constructing biomaterials using self-assembling peptide building blocks. *Frontiers of Materials Science in China* **2010**, *4* (2), 145-151.
357. Muraoka, T.; Cui, H.; Stupp, S. I., Quadruple Helix Formation of a Photoresponsive Peptide Amphiphile and Its Light-Triggered Dissociation into Single Fibers. *Journal of the American Chemical Society* **2008**, *130* (10), 2946-2947.
358. Haines, L. A.; Rajagopal, K.; Ozbas, B.; Salick, D. A.; Pochan, D. J.; Schneider, J. P., Light-Activated Hydrogel Formation via the Triggered Folding and Self-Assembly of a Designed Peptide. *Journal of the American Chemical Society* **2005**, *127* (48), 17025-17029.
359. Zhou, J.; Xu, B., Enzyme-Instructed Self-Assembly: A Multistep Process for Potential Cancer Therapy. *Bioconjugate Chemistry* **2015**, *26* (6), 987-999.
360. Kim, B. J.; Xu, B., Enzyme-Instructed Self-Assembly for Cancer Therapy and Imaging. *Bioconjugate Chemistry* **2020**, *31* (3), 492-500.
361. Feng, Z.; Zhang, T.; Wang, H.; Xu, B., Supramolecular catalysis and dynamic assemblies for medicine. *Chemical Society Reviews* **2017**, *46* (21), 6470-6479.
362. Gao, J.; Zhan, J.; Yang, Z., Enzyme-Instructed Self-Assembly (EISA) and Hydrogelation of Peptides. *Advanced Materials* **2020**, *32* (3), 1805798.
363. Williams, R. J.; Smith, A. M.; Collins, R.; Hodson, N.; Das, A. K.; Ulijn, R. V., Enzyme-assisted self-assembly under thermodynamic control. *Nature Nanotechnology* **2009**, *4* (1), 19-24.

364. Vigier-Carrière, C.; Wagner, D.; Chaumont, A.; Durr, B.; Lupattelli, P.; Lambour, C.; Schmutz, M.; Hemmerlé, J.; Senger, B.; Schaaf, P.; Boulmedais, F.; Jierry, L., Control of Surface-Localized, Enzyme-Assisted Self-Assembly of Peptides through Catalyzed Oligomerization. *Langmuir* **2017**, *33* (33), 8267-8276.
365. Vigier-Carrière, C.; Garnier, T.; Wagner, D.; Lavallo, P.; Rabineau, M.; Hemmerlé, J.; Senger, B.; Schaaf, P.; Boulmedais, F.; Jierry, L., Bioactive Seed Layer for Surface-Confined Self-Assembly of Peptides. *Angewandte Chemie International Edition* **2015**, *54* (35), 10198-10201.
- *366. Ding, X.; Zhao, H.; Li, Y.; Lee, A. L.; Li, Z.; Fu, M.; Li, C.; Yang, Y. Y.; Yuan, P., Synthetic peptide hydrogels as 3D scaffolds for tissue engineering. *Adv Drug Deliv Rev* **2020**, *160*, 78-104.
- **367. Gelain, F.; Luo, Z.; Rioult, M.; Zhang, S., Self-assembling peptide scaffolds in the clinic. *NPJ Regen Med* **2021**, *6* (1), 9-9.
368. Pugliese, R.; Fontana, F.; Marchini, A.; Gelain, F., Branched peptides integrate into self-assembled nanostructures and enhance biomechanics of peptidic hydrogels. *Acta Biomater* **2018**, *66*, 258-271.
369. Pugliese, R.; Marchini, A.; Saracino, G. A. A.; Zuckermann, R. N.; Gelain, F., Cross-linked self-assembling peptide scaffolds. *Nano Research* **2018**, *11* (1), 586-602.
370. Pugliese, R.; Maleki, M.; Zuckermann, R. N.; Gelain, F., Self-assembling peptides cross-linked with genipin: Resilient hydrogels and self-standing electrospun scaffolds for tissue engineering applications. *Biomater Sci* **2019**, *7* (1), 76-91.
371. Silva, D.; Natalello, A.; Sanii, B.; Vasita, R.; Saracino, G.; Zuckermann, R. N.; Doglia, S. M.; Gelain, F., Synthesis and characterization of designed BMHP1-derived self-assembling peptides for tissue engineering applications Electronic supplementary information (ESI) available. See DOI: 10.1039/c2nr32656f. **2012**, *5* (2), 74-718.
372. Chen, C.; Gu, Y.; Deng, L.; Han, S.; Sun, X.; Chen, Y.; Lu, J. R.; Xu, H., Tuning Gelation Kinetics and Mechanical Rigidity of β -Hairpin Peptide Hydrogels via Hydrophobic Amino Acid Substitutions. *ACS Appl. Mater. Interfaces* **2014**, *6* (16), 14360-14368.
373. Garg, T.; Singh, O.; Arora, S.; Murthy, R. S. R., Dendrimer- a novel scaffold for drug delivery. *International journal of pharmaceutical sciences review and research* **2011**, *7* (2), 211-220.
374. Gervaso, F.; Sannino, A.; Peretti, G. M., The biomaterialist's task: scaffold biomaterials and fabrication technologies. *Joints* **2013**, *1* (3), 130-137.
375. Lu, T.; Li, Y.; Chen, T., Techniques for fabrication and construction of three-dimensional scaffolds for tissue engineering. *Int J Nanomedicine* **2013**, *8* (1), 337-350.
376. Rahmati, M.; Mills, D. K.; Urbanska, A. M.; Saeb, M. R.; Venugopal, J. R.; Ramakrishna, S.; Mozafari, M., Electrospinning for tissue engineering applications. *Progress in materials science* **2021**, *117*, 100721.
377. Li, J.; Pan, K.; Tian, H.; Yin, L., The Potential of Electrospinning/Electrospraying Technology in the Rational Design of Hydrogel Structures. *Macromolecular materials and engineering* **2020**, *305* (8), 2000285-n/a.
378. Maleki, M.; Natalello, A.; Pugliese, R.; Gelain, F., Fabrication of nanofibrous electrospun scaffolds from a heterogeneous library of co- and self-assembling peptides. *Acta Biomater* **2017**, *51*, 268-278.
379. Singh, G.; Bittner, A. M.; Loscher, S.; Malinowski, N.; Kern, K., Electrospinning of Diphenylalanine Nanotubes. *Advanced materials (Weinheim)* **2008**, *20* (12), 2332-2336.
380. Tayi, A. S.; Pashuck, E. T.; Newcomb, C. J.; McClendon, M. T.; Stupp, S. I., Electrospinning Bioactive Supramolecular Polymers from Water. *Biomacromolecules* **2014**, *15* (4), 1323-1327.
381. Bruggeman, K. F.; Wang, Y.; Maclean, F. L.; Parish, C. L.; Williams, R. J.; Nisbet, D. R., Temporally controlled growth factor delivery from a self-assembling peptide hydrogel and electrospun nanofibre composite scaffold. *Nanoscale* **2017**, *9* (36), 13661-13669.

382. Hamedani, Y.; Macha, P.; Evangelista, E. L.; Sammeta, V. R.; Chalivendra, V.; Rasapalli, S.; Vasudev, M. C., Electrospinning of tyrosine-based oligopeptides: Self-assembly or forced assembly? *J Biomed Mater Res A* **2020**, *108* (4), 829-838.
383. Pati, F.; Gantelius, J.; Svahn, H. A., 3D Bioprinting of Tissue/Organ Models. *Angew Chem Int Ed Engl* **2016**, *55* (15), 4650-4665.
384. Malda, J.; Visser, J.; Melchels, F. P.; Jüngst, T.; Hennink, W. E.; Dhert, W. J. A.; Groll, J.; Hutmacher, D. W., 25th Anniversary Article: Engineering Hydrogels for Biofabrication. *Adv Mater* **2013**, *25* (36), 5011-5028.
385. Hedegaard, C. L.; Collin, E. C.; Redondo-Gómez, C.; Nguyen, L. T. H.; Ng, K. W.; Castrejón-Pita, A. A.; Castrejón-Pita, J. R.; Mata, A., Hydrodynamically Guided Hierarchical Self-Assembly of Peptide-Protein Bioinks. *Advanced functional materials* **2018**, *28* (16), 1703716-n/a.
386. Loo, Y.; Lakshmanan, A.; Ni, M.; Toh, L. L.; Wang, S.; Hauser, C. A. E., Peptide Bioink: Self-Assembling Nanofibrous Scaffolds for Three-Dimensional Organotypic Cultures. *Nano Lett* **2015**, *15* (10), 6919-6925.
387. Dubbin, K.; Hori, Y.; Lewis, K. K.; Heilshorn, S. C., Dual-Stage Crosslinking of a Gel-Phase Bioink Improves Cell Viability and Homogeneity for 3D Bioprinting. *Adv Healthc Mater* **2016**, *5* (19), 2488-2492.
388. Yan, M.; Lewis, P. L.; Shah, R. N., Tailoring nanostructure and bioactivity of 3D-printable hydrogels with self-assemble peptides amphiphile (PA) for promoting bile duct formation. *Biofabrication* **2018**, *10* (3), 035010-035010.
389. Raphael, B.; Khalil, T.; Workman, V. L.; Smith, A.; Brown, C. P.; Streuli, C.; Saiani, A.; Domingos, M., 3D cell bioprinting of self-assembling peptide-based hydrogels. *Materials letters* **2017**, *190*, 103-106.
390. Ouyang, L.; Armstrong, J. P. K.; Salmeron-Sanchez, M.; Stevens, M. M., Assembling Living Building Blocks to Engineer Complex Tissues. *Advanced functional materials* **2020**, *30* (26), 1909009-n/a.
391. Koons, G. L.; Diba, M.; Mikos, A. G., Materials design for bone-tissue engineering. *Nature reviews. Materials* **2020**, *5* (8), 584-603.
392. Bose, S.; Vahabzadeh, S.; Bandyopadhyay, A., Bone tissue engineering using 3D printing. *Materials today (Kidlington, England)* **2013**, *16* (12), 496-504.
393. Li, A.; Xie, J.; Li, J., Recent advances in functional nanostructured materials for bone-related diseases. *J Mater Chem B* **2019**, *7* (4), 59-527.
394. Yao, Q.; Cosme, J. G. L.; Xu, T.; Miszuk, J. M.; Picciani, P. H. S.; Fong, H.; Sun, H., Three dimensional electrospun PCL/PLA blend nanofibrous scaffolds with significantly improved stem cells osteogenic differentiation and cranial bone formation. *Biomaterials* **2016**, *115*, 115-127.
395. Misawa, H.; Kobayashi, N.; Soto-Gutierrez, A.; Chen, Y.; Yoshida, A.; Rivas-Carrillo, J. D.; Navarro-Alvarez, N.; Tanaka, K.; Miki, A.; Takei, J.; Ueda, T.; Tanaka, M.; Endo, H.; Tanaka, N.; Ozaki, T., PuraMatrix™ Facilitates Bone Regeneration in Bone Defects of Calvaria in Mice. *Cell Transplant* **2006**, *15* (10), 903-910.
396. He, B.; Ou, Y.; Chen, S.; Zhao, W.; Zhou, A.; Zhao, J.; Li, H.; Jiang, D.; Zhu, Y., Designer bFGF-incorporated d-form self-assembly peptide nanofiber scaffolds to promote bone repair. *Materials Science and Engineering: C* **2017**, *74*, 451-458.
397. Liu, Y.; Zhang, L.; Wei, W., Effect of noncovalent interaction on the self-assembly of a designed peptide and its potential use as a carrier for controlled bFGF release. *Int J Nanomedicine* **2017**, *12*, 659-670.
398. Luong, L. N.; Ramaswamy, J.; Kohn, D. H., Effects of osteogenic growth factors on bone marrow stromal cell differentiation in a mineral-based delivery system. *Biomaterials* **2011**, *33* (1), 283-294.

399. He, B.; Ou, Y.; Zhou, A.; Chen, S.; Zhao, W.; Zhao, J.; Li, H.; Zhu, Y.; Zhao, Z.; Jiang, D., Functionalized D-form self-assembling peptide hydrogels for bone regeneration. *Drug Des Devel Ther* **2016**, *10*, 1379-1388.
400. Ikeno, M.; Hibi, H.; Kinoshita, K.; Hattori, H.; Ueda, M., Effects of self-assembling peptide hydrogel scaffold on bone regeneration with recombinant human bone morphogenetic protein-2. *Int J Oral Maxillofac Implants* **2013**, *28* (5), e283-9.
401. Panek, M.; Antunović, M.; Pribolšan, L.; Ivković, A.; Gotić, M.; Vukasović, A.; Mihalić, K. C.; Pušić, M.; Jurkin, T.; Marijanović, I., Bone tissue engineering in a perfusion bioreactor using dexamethasone-loaded peptide hydrogel. *Materials (Basel)* **2019**, *16* (6), 919.
402. Rey-Rico, A.; Venkatesan, J. K.; Frisch, J.; Schmitt, G.; Monge-Marcet, A.; Lopez-Chicon, P.; Mata, A.; Semino, C.; Madry, H.; Cucchiaroni, M., Effective and durable genetic modification of human mesenchymal stem cells via controlled release of rAAV vectors from self-assembling peptide hydrogels with a maintained differentiation potency. *Acta Biomater* **2015**, *18*, 118-127.
403. Tsukamoto, J.; Naruse, K.; Nagai, Y.; Kan, S.; Nakamura, N.; Hata, M.; Omi, M.; Hayashi, T.; Kawai, T.; Matsubara, T., Efficacy of a self-Assembling peptide hydrogel, spg-178-gel, for bone regeneration and three-dimensional osteogenic induction of dental pulp stem cells. *Tissue Eng Part A* **2017**, *23* (23-24), 1394-1402.
404. Castillo Diaz, L. A.; Elsayy, M.; Saiani, A.; Gough, J. E.; Miller, A. F., Osteogenic differentiation of human mesenchymal stem cells promotes mineralization within a biodegradable peptide hydrogel. *J Tissue Eng* **2016**, *7*, 2041731416649789-2041731416649789.
405. Ghosh, M.; Halperin-Sternfeld, M.; Grinberg, I.; Adler-Abramovich, L., Injectable Alginate-Peptide Composite Hydrogel as a Scaffold for Bone Tissue Regeneration. *Nanomaterials (Basel)* **2019**, *9* (4), 497.
406. Palmer, L. C.; Newcomb, C. J.; Kaltz, S. R.; Spoerke, E. D.; Stupp, S. I., Biomimetic Systems for Hydroxyapatite Mineralization Inspired By Bone and Enamel. *Chem. Rev* **2008**, *108* (11), 4754-4783.
407. Mata, A.; Geng, Y.; Henrikson, K. J.; Aparicio, C.; Stock, S. R.; Satcher, R. L.; Stupp, S. I., Bone regeneration mediated by biomimetic mineralization of a nanofiber matrix. *Biomaterials* **2010**, *31* (23), 6004-6012.
408. Anderson, J. M.; Vines, J. B.; Patterson, J. L.; Chen, H.; Javed, A.; Jun, H.-W., Osteogenic differentiation of human mesenchymal stem cells synergistically enhanced by biomimetic peptide amphiphiles combined with conditioned medium. *Acta Biomater* **2011**, *7* (2), 675-682.
409. Anderson, J. M.; Patterson, J. L.; Vines, J. B.; Javed, A.; Gilbert, S. R.; Jun, H.-W., Biphasic Peptide Amphiphile Nanomatrix Embedded with Hydroxyapatite Nanoparticles for Stimulated Osteoinductive Response. *ACS Nano* **2011**, *5* (12), 9463-9479.
410. Tansik, G.; Kilic, E.; Beter, M.; Demiralp, B.; Kiziltas Sendur, G.; Can, N.; Ozkan, H.; Ergul, E.; Guler, M. O.; Tekinay, A. B., A glycosaminoglycan mimetic peptide nanofiber gel as an osteoinductive scaffold. *Biomater Sci* **2016**, *4* (9), 1328-1339.
411. Gulseren, G.; Yasa, I. C.; Ustahuseyin, O.; Tekin, E. D.; Tekinay, A. B.; Guler, M. O., Alkaline Phosphatase-Mimicking Peptide Nanofibers for Osteogenic Differentiation. *Biomacromolecules* **2015**, *16* (7), 2198-2208.
412. Lee, S. S.; Fyrner, T.; Chen, F.; Álvarez, Z.; Sleep, E.; Chun, D. S.; Weiner, J. A.; Cook, R. W.; Freshman, R. D.; Schallmo, M. S.; Katchko, K. M.; Schneider, A. D.; Smith, J. T.; Yun, C.; Singh, G.; Hashmi, S. Z.; McClendon, M. T.; Yu, Z.; Stock, S. R.; Hsu, W. K.; Hsu, E. L.; Stupp, S. I., Sulfated glycopeptide nanostructures for multipotent protein activation. *Nat Nanotechnol* **2017**, *12* (8), 821-829.
413. Sargeant, T. D.; Rao, M. S.; Koh, C.-Y.; Stupp, S. I., Covalent functionalization of NiTi surfaces with bioactive peptide amphiphile nanofibers. *Biomaterials* **2007**, *29* (8), 1085-1098.

414. Sargeant, T. D.; Guler, M. O.; Oppenheimer, S. M.; Mata, A.; Satcher, R. L.; Dunand, D. C.; Stupp, S. I., Hybrid bone implants: Self-assembly of peptide amphiphile nanofibers within porous titanium. *Biomaterials* **2007**, *29* (2), 161-171.
415. Vinatier, C.; Guicheux, J., Cartilage tissue engineering: From biomaterials and stem cells to osteoarthritis treatments. *Annals of Physical and Rehabilitation Medicine* **2016**, *59* (3), 139-144.
416. Huang, B. J.; Hu, J. C.; Athanasiou, K. A., Cell-based tissue engineering strategies used in the clinical repair of articular cartilage. *Biomaterials* **2016**, *98*, 1-22.
417. Kisiday, J.; Jin, M.; Kurz, B.; Hung, H.; Semino, C.; Zhang, S.; Grodzinsky, A. J., Self-Assembling Peptide Hydrogel Fosters Chondrocyte Extracellular Matrix Production and Cell Division: Implications for Cartilage Tissue Repair. *Proc Natl Acad Sci U S A* **2002**, *99* (15), 9996-10001.
418. Lee, H. Y.; Kopesky, P. W.; Plaas, A.; Sandy, J.; Kisiday, J.; Frisbie, D.; Grodzinsky, A. J.; Ortiz, C., Adult bone marrow stromal cell-based tissue-engineered aggrecan exhibits ultrastructure and nanomechanical properties superior to native cartilage. *Osteoarthritis Cartilage* **2010**, *18* (11), 1477-1486.
419. Miller, R. E.; Grodzinsky, A. J.; Vanderploeg, E. J.; Lee, C.; Ferris, D. J.; Barrett, M. F.; Kisiday, J. D.; Frisbie, D. D., Effect of self-assembling peptide, chondrogenic factors, and bone marrow-derived stromal cells on osteochondral repair. *Osteoarthritis and Cartilage* **2010**, *18* (12), 1608-1619.
420. Liebesny, P. H.; Mrosczyk, K.; Zlotnick, H.; Hung, H.-H.; Frank, E.; Kurz, B.; Zanotto, G.; Frisbie, D.; Grodzinsky, A. J., Enzyme Pretreatment plus Locally Delivered HB-IGF-1 Stimulate Integrative Cartilage Repair In Vitro. *Tissue Eng Part A* **2019**, *25* (17-18), 1191-1201.
421. Zanotto, G.; Liebesny, P.; Barrett, M.; Zlotnick, H.; Grodzinsky, A.; Frisbie, D., Trypsin Pre-Treatment Combined With Growth Factor Functionalized Self-Assembling Peptide Hydrogel Improves Cartilage Repair in Rabbit Model. *J Orthop Res* **2019**, *37* (11), 2307-2315.
422. Li, R.; Xu, J.; Wong, D. S. H.; Li, J.; Zhao, P.; Bian, L., Self-assembled N-cadherin mimetic peptide hydrogels promote the chondrogenesis of mesenchymal stem cells through inhibition of canonical Wnt/ β -catenin signaling. *Biomaterials* **2017**, *145*, 33-43.
423. Florine, E. M.; Miller, R. E.; Liebesny, P. H.; Mrosczyk, K. A.; Lee, R. T.; Patwari, P.; Grodzinsky, A. J., Delivering Heparin-Binding Insulin-Like Growth Factor 1 with Self-Assembling Peptide Hydrogels. *Tissue Eng Part A* **2015**, *21* (3-4), 637-646.
424. Lu, J.; Shen, X.; Sun, X.; Yin, H.; Yang, S.; Lu, C.; Wang, Y.; Liu, Y.; Huang, Y.; Yang, Z.; Dong, X.; Wang, C.; Guo, Q.; Zhao, L.; Sun, X.; Lu, S.; Mikos, A. G.; Peng, J.; Wang, X., Increased recruitment of endogenous stem cells and chondrogenic differentiation by a composite scaffold containing bone marrow homing peptide for cartilage regeneration. *Theranostics* **2018**, *8* (18), 5039-5058.
425. Ustun, S.; Tombuloglu, A.; Kilinc, M.; Guler, M. O.; Tekinay, A. B., Growth and Differentiation of Prechondrogenic Cells on Bioactive Self-Assembled Peptide Nanofibers. *Biomacromolecules* **2013**, *14* (1), 17-26.
426. Ustun Yaylaci, S.; Sardan Ekiz, M.; Arslan, E.; Can, N.; Kilic, E.; Ozkan, H.; Orujalipoor, I.; Ide, S.; Tekinay, A. B.; Guler, M. O., Supramolecular GAG-like Self-Assembled Glycopeptide Nanofibers Induce Chondrogenesis and Cartilage Regeneration. *Biomacromolecules* **2016**, *17* (2), 679-689.
427. Hong, K. H.; Kim, Y. M.; Song, S. C., Fine-Tunable and Injectable 3D Hydrogel for On-Demand Stem Cell Niche. *Adv Sci (Weinh)* **2019**, *6* (17), 1900597-n/a.
- *428. Papadimitriou, L.; Manganas, P.; Ranella, A.; Stratakis, E., Biofabrication for neural tissue engineering applications. *Materials Today Bio* **2020**, *6*, 100043.
429. Subramanian, A.; Krishnan, U. M.; Sethuraman, S., Development of biomaterial scaffold for nerve tissue engineering: Biomaterial mediated neural regeneration. *J Biomed Sci* **2009**, *16* (1), 108-108.

430. Todd, C. H.; Sonsoles de, L.; Xing, S.; Guosong, L.; Alexander, R.; Shuguang, Z., Extensive Neurite Outgrowth and Active Synapse Formation on Self-Assembling Peptide Scaffolds. *Proc Natl Acad Sci U S A* **2000**, *97* (12), 6728-6733.
431. Gelain, F.; Bottai, D.; Vescovi, A.; Zhang, S., Designer Self-Assembling Peptide Nanofiber Scaffolds for Adult Mouse Neural Stem Cell 3-Dimensional Cultures. *PLOS ONE* **2006**, *1* (1), e119.
432. Cunha, C.; Panseri, S.; Villa, O.; Silva, D.; Gelain, F., 3D culture of adult mouse neural stem cells within functionalized self-assembling peptide scaffolds. *Int J Nanomedicine* **2011**, *6*, 943-955.
433. Sun, Y.; Li, W.; Wu, X.; Zhang, N.; Zhang, Y.; Ouyang, S.; Song, X.; Fang, X.; Seeram, R.; Xue, W.; He, L.; Wu, W., Functional Self-Assembling Peptide Nanofiber Hydrogels Designed for Nerve Degeneration. *ACS Appl. Mater. Interfaces* **2016**, *8* (3), 2348-2359.
434. Wu, X.; He, L.; Li, W.; Li, H.; Wong, W.-M.; Ramakrishna, S.; Wu, W., Functional self-assembling peptide nanofiber hydrogel for peripheral nerve regeneration. *Regenerative biomaterials* **2017**, *4* (1), 21-30.
435. Lu, C.; Wang, Y.; Yang, S.; Wang, C.; Sun, X.; Lu, J.; Yin, H.; Jiang, W.; Meng, H.; Rao, F.; Wang, X.; Peng, J., Bioactive Self-Assembling Peptide Hydrogels Functionalized with Brain-Derived Neurotrophic Factor and Nerve Growth Factor Mimicking Peptides Synergistically Promote Peripheral Nerve Regeneration. *ACS Biomater. Sci. Eng* **2018**, *4* (8), 2994-3005.
436. Guo, J. P.; Leung, K. K. G. M. D.; Su, H. P.; Yuan, Q. P.; Wang, L. P.; Chu, T.-H. P.; Zhang, W. M. D.; Pu, J. K. S. M. D.; Ng, G. K. P. B.; Wong, W. M. M. S.; Dai, X. M. D.; Wu, W. M. D. P., Self-assembling peptide nanofiber scaffold promotes the reconstruction of acutely injured brain. *Nanomedicine* **2009**, *5* (3), 345-351.
437. Sang, L. Y.-H. P.; Liang, Y.-X. P.; Li, Y. P.; Wong, W.-M. M.; Tay, D. K.-C. P.; So, K.-F. P.; Ellis-Behnke, R. G. P.; Wu, W. P.; Cheung, R. T.-F. P., A self-assembling nanomaterial reduces acute brain injury and enhances functional recovery in a rat model of intracerebral hemorrhage. *Nanomedicine* **2015**, *11* (3), 611-620.
438. Francis, N. L.; Bennett, N. K.; Halikere, A.; Pang, Z. P.; Moghe, P. V., Self-Assembling Peptide Nanofiber Scaffolds for 3-D Reprogramming and Transplantation of Human Pluripotent Stem Cell-Derived Neurons. *ACS Biomaterials Science & Engineering* **2016**, *2* (6), 1030-1038.
439. Shi, W.; Huang, C. J.; Xu, X. D.; Jin, G. H.; Huang, R. Q.; Huang, J. F.; Chen, Y. N.; Ju, S. Q.; Wang, Y.; Shi, Y. W.; Qin, J. B.; Zhang, Y. Q.; Liu, Q. Q.; Wang, X. B.; Zhang, X. H.; Chen, J., Transplantation of RADA16-BDNF peptide scaffold with human umbilical cord mesenchymal stem cells forced with CXCR4 and activated astrocytes for repair of traumatic brain injury. *Acta Biomater* **2016**, *45*, 247-261.
440. Jahanbazi Jahan-Abad, A.; Sahab Negah, S.; Hosseini Ravandi, H.; Ghasemi, S.; Borhani-Haghighi, M.; Stummer, W.; Gorji, A.; Khaleghi Ghadiri, M., Human Neural Stem/Progenitor Cells Derived From Epileptic Human Brain in a Self-Assembling Peptide Nanoscaffold Improve Traumatic Brain Injury in Rats. *Mol Neurobiol* **2018**, *55* (12), 9122-9138.
441. Gelain, F.; Cigognini, D.; Caprini, A.; Silva, D.; Colleoni, B.; Donegá, M.; Antonini, S.; Cohen, B. E.; Vescovi, A., New bioactive motifs and their use in functionalized self-assembling peptides for NSC differentiation and neural tissue engineering. *Nanoscale* **2012**, *4* (9), 2946-2957.
442. Pugliese, R.; Gelain, F., Characterization of elastic, thermo-responsive, self-healable supramolecular hydrogel made of self-assembly peptides and guar gum. *Materials & Design* **2020**, *186*, 108370.
443. Liu, Y.; Ye, H.; Satkunendrarajah, K.; Yao, G. S.; Bayon, Y.; Fehlings, M. G., A self-assembling peptide reduces glial scarring, attenuates post-traumatic inflammation and promotes neurological recovery following spinal cord injury. *Acta Biomaterialia* **2013**, *9* (9), 8075-8088.
444. Iwasaki, M.; Wilcox, J. T.; Nishimura, Y.; Zweckberger, K.; Suzuki, H.; Wang, J.; Liu, Y.; Karadimas, S. K.; Fehlings, M. G., Synergistic effects of self-assembling peptide and neural

- stem/progenitor cells to promote tissue repair and forelimb functional recovery in cervical spinal cord injury. *Biomaterials* **2014**, *35* (9), 2617-2629.
445. Zweckberger, K.; Ahuja, C. S.; Liu, Y.; Wang, J.; Fehlings, M. G., Self-assembling peptides optimize the post-traumatic milieu and synergistically enhance the effects of neural stem cell therapy after cervical spinal cord injury. *Acta Biomaterialia* **2016**, *42*, 77-89.
446. Nam, J.; Lim, H.-K.; Kim, N. H.; Park, J. K.; Kang, E. S.; Kim, Y.-T.; Heo, C.; Lee, O.-S.; Kim, S.-G.; Yun, W. S.; Suh, M.; Kim, Y. H., Supramolecular Peptide Hydrogel-Based Soft Neural Interface Augments Brain Signals through a Three-Dimensional Electrical Network. *ACS Nano* **2020**, *14* (1), 664-675.
447. Tysseling-Mattiace, V. M.; Sahni, V.; Niece, K. L.; Birch, D.; Czeisler, C.; Fehlings, M. G.; Stupp, S. I.; Kessler, J. A., Self-Assembling Nanofibers Inhibit Glial Scar Formation and Promote Axon Elongation after Spinal Cord Injury. *J Neurosci* **2008**, *28* (14), 3814-3823.
448. Tysseling, V. M.; Sahni, V.; Pashuck, E. T.; Birch, D.; Hebert, A.; Czeisler, C.; Stupp, S. I.; Kessler, J. A., Self-assembling peptide amphiphile promotes plasticity of serotonergic fibers following spinal cord injury. *J. Neurosci. Res* **2010**, *88* (14), 3161-3170.
449. Zou, Z.; Zheng, Q.; Wu, Y.; Song, Y.; Wu, B., Growth of rat dorsal root ganglion neurons on a novel self-assembling scaffold containing IKVAV sequence. *Materials Science and Engineering: C* **2009**, *29* (7), 2099-2103.
450. Berns, E. J.; Sur, S.; Pan, L.; Goldberger, J. E.; Suresh, S.; Zhang, S.; Kessler, J. A.; Stupp, S. I., Aligned neurite outgrowth and directed cell migration in self-assembled monodomain gels. *Biomaterials* **2014**, *35* (1), 185-195.
451. Li, A.; Hokugo, A.; Yalom, A.; Berns, E. J.; Stephanopoulos, N.; McClendon, M. T.; Segovia, L. A.; Spigelman, I.; Stupp, S. I.; Jarrahy, R., A bioengineered peripheral nerve construct using aligned peptide amphiphile nanofibers. *Biomaterials* **2014**, *35* (31), 8780-8790.
452. Motalleb, R.; Berns, E. J.; Patel, P.; Gold, J.; Stupp, S. I.; Kuhn, H. G., In vivo migration of endogenous brain progenitor cells guided by an injectable peptide amphiphile biomaterial. *Journal of tissue engineering and regenerative medicine* **2018**, *12* (4), e2123-e2133.
453. Zhao, X.; Pan, F.; Perumal, S.; Xu, H.; Lu, J. R.; Webster, J. R. P., Interfacial assembly of cationic peptide surfactants. *Soft Matter* **2009**, *5* (8), 1630.
454. Shinato, K. W.; Huang, F.; Jin, Y., Principle and application of atomic force microscopy (AFM) for nanoscale investigation of metal corrosion. *Corrosion Reviews* **2020**, *38* (5), 423-432.
455. Shi, X.; Qing, W.; Marhaba, T.; Zhang, W., Atomic force microscopy - Scanning electrochemical microscopy (AFM-SECM) for nanoscale topographical and electrochemical characterization: Principles, applications and perspectives. *Electrochimica Acta* **2020**, *332*, 135472.
456. Carvalho, F. A.; Santos, N. C., Atomic force microscopy-based force spectroscopy — biological and biomedical applications. *IUBMB Life* **2012**, *64* (6), 465-472.
457. Poggi, M. A.; McFarland, A. W.; Colton, J. S.; Bottomley, L. A., A Method for Calculating the Spring Constant of Atomic Force Microscopy Cantilevers with a Nonrectangular Cross Section. *Anal. Chem* **2005**, *77* (4), 1192-1195.
458. Johnson, D.; Hilal, N., Characterisation and quantification of membrane surface properties using atomic force microscopy: A comprehensive review. *Desalination* **2015**, *356*, 149-164.
459. García, R.; Pérez, R., Dynamic atomic force microscopy methods. *Surface Science Reports* **2002**, *47* (6), 197-301.
460. Efimov, T. A.; Rassolov, E. A.; Andryukov, B. G.; Zaporozhets, T. S.; Romashko, R. V., Calculation of Resonant Frequencies of Silicon AFM Cantilevers. *J. Phys.: Conf. Ser* **2020**, *1439* (1), 12006.
461. Zhong, Q.; Inniss, D.; Kjoller, K.; Elings, V. B., Fractured polymer/silica fiber surface studied by tapping mode atomic force microscopy. *Surface science* **1993**, *290* (1), L688-L692.

462. Cheong, L.-Z.; Zhao, W.; Song, S.; Shen, C., Lab on a tip: Applications of functional atomic force microscopy for the study of electrical properties in biology. *Acta Biomaterialia* **2019**, *99*, 33-52.
463. Trtik, P.; Kaufmann, J.; Volz, U., On the use of peak-force tapping atomic force microscopy for quantification of the local elastic modulus in hardened cement paste. *Cement and Concrete Research* **2012**, *42* (1), 215-221.
464. Heu, C.; Berquand, A.; Elie-Caille, C.; Nicod, L., Glyphosate-induced stiffening of HaCaT keratinocytes, a Peak Force Tapping study on living cells. *Journal of Structural Biology* **2012**, *178* (1), 1-7.
465. Di Gianfrancesco, A., 8 - Technologies for chemical analyses, microstructural and inspection investigations. In *Materials for Ultra-Supercritical and Advanced Ultra-Supercritical Power Plants*, Di Gianfrancesco, A., Ed. Woodhead Publishing: 2017; pp 197-245.
466. Goodwin, P. C., A primer on the fundamental principles of light microscopy: Optimizing magnification, resolution, and contrast. *Molecular Reproduction and Development* **2015**, *82* (7-8), 502-507.
467. Thorn, K., A quick guide to light microscopy in cell biology. *Mol Biol Cell* **2016**, *27* (2), 219-222.
468. Sanderson, M. J.; Smith, I.; Parker, I.; Bootman, M. D., Fluorescence microscopy. *Cold Spring Harb Protoc* **2014**, *2014* (10), pdb.top071795-pdb.top071795.
469. Combs, C. A.; Shroff, H., Fluorescence Microscopy: A Concise Guide to Current Imaging Methods. *Current Protocols in Neuroscience* **2017**, *79* (1), 2.1.1-2.1.25.
470. Jonkman, J.; Brown, C. M.; Wright, G. D.; Anderson, K. I.; North, A. J., Tutorial: guidance for quantitative confocal microscopy. *Nature Protocols* **2020**, *15* (5), 1585-1611.
471. Prasad, V.; Semwogerere, D.; Weeks, E. R., Confocal microscopy of colloids. *Journal of Physics: Condensed Matter* **2007**, *19* (11), 113102.
472. Croix, C. M. S.; Shand, S. H.; Watkins, S. C., Confocal microscopy: comparisons, applications, and problems. *BioTechniques* **2005**, *39* (6S), S2-S5.
473. Mishra, A.; Bhatt, N.; Bajpai, A. K., Chapter 12 - Nanostructured superhydrophobic coatings for solar panel applications. In *Nanomaterials-Based Coatings*, Nguyen Tri, P.; Rtimi, S.; Ouellet Plamondon, C. M., Eds. Elsevier: 2019; pp 397-424.
474. Kumar, A.; Nanda, D., Chapter 3 - Methods and fabrication techniques of superhydrophobic surfaces. In *Superhydrophobic Polymer Coatings*, Samal, S. K.; Mohanty, S.; Nayak, S. K., Eds. Elsevier: 2019; pp 43-75.
475. Boudrioua, A.; Chakaroun, M.; Fischer, A., 2 - Organic Light-emitting Diodes. In *Organic Lasers*, Boudrioua, A.; Chakaroun, M.; Fischer, A., Eds. Elsevier: 2017; pp 49-93.
476. Li, X.; Liu, B.; Pei, B.; Chen, J.; Zhou, D.; Peng, J.; Zhang, X.; Jia, W.; Xu, T., Inkjet Bioprinting of Biomaterials. *Chemical Reviews* **2020**, *120* (19), 10793-10833.
477. Gu, Z.; Fu, J.; Lin, H.; He, Y., Development of 3D bioprinting: From printing methods to biomedical applications. *Asian Journal of Pharmaceutical Sciences* **2020**, *15* (5), 529-557.
478. Zhang, Y.; Kumar, P.; Lv, S.; Xiong, D.; Zhao, H.; Cai, Z.; Zhao, X., Recent advances in 3D bioprinting of vascularized tissues. *Materials & Design* **2021**, *199*, 109398.
479. Im, K.; Mareninov, S.; Diaz, M. F. P.; Yong, W. H., An Introduction to Performing Immunofluorescence Staining. *Methods Mol Biol* **2019**, *1897*, 299-311.
480. Hoffman, E. A.; Frey, B. L.; Smith, L. M.; Auble, D. T., Formaldehyde Crosslinking: A Tool for the Study of Chromatin Complexes *. *Journal of Biological Chemistry* **2015**, *290* (44), 26404-26411.
481. Stiefel, P.; Schmidt-Emrich, S.; Maniura-Weber, K.; Ren, Q., Critical aspects of using bacterial cell viability assays with the fluorophores SYTO9 and propidium iodide. *BMC Microbiol* **2015**, *15*, 36-36.
482. Robertson, J.; McGoverin, C.; Vanholsbeeck, F.; Swift, S., Optimisation of the Protocol for the LIVE/DEAD® BacLight™ Bacterial Viability Kit for Rapid Determination of Bacterial Load. *Frontiers in Microbiology* **2019**, *10* (801).

483. Kuete, V.; Karaosmanoğlu, O.; Sivas, H., Chapter 10 - Anticancer Activities of African Medicinal Spices and Vegetables. In *Medicinal Spices and Vegetables from Africa*, Kuete, V., Ed. Academic Press: 2017; pp 271-297.
484. Csepregi, R.; Lemli, B.; Kunsági-Máté, S.; Szente, L.; Kószegi, T.; Németi, B.; Poór, M., Complex Formation of Resorufin and Resazurin with B-Cyclodextrins: Can Cyclodextrins Interfere with a Resazurin Cell Viability Assay? *Molecules* **2018**, *23* (2), 382.
485. Riss, T. L.; Moravec, R. A.; Niles, A. L.; Duellman, S.; Benink, H. A.; Worzella, T. J.; Minor, L., Cell Viability Assays. In *Assay Guidance Manual*, Markossian, S.; Grossman, A.; Brimacombe, K.; Arkin, M.; Auld, D.; Austin, C. P.; Baell, J.; Chung, T. D. Y.; Coussens, N. P.; Dahlin, J. L.; Devanarayan, V.; Foley, T. L.; Glicksman, M.; Hall, M. D.; Haas, J. V.; Hoare, S. R. J.; Inglese, J.; Iversen, P. W.; Kales, S. C.; Lal-Nag, M.; Li, Z.; McGee, J.; McManus, O.; Riss, T.; Saradjian, P.; Sittampalam, G. S.; Tarselli, M.; Trask, O. J., Jr.; Wang, Y.; Weidner, J. R.; Wildey, M. J.; Wilson, K.; Xia, M.; Xu, X., Eds. Eli Lilly & Company and the National Center for Advancing Translational Sciences: Bethesda (MD), 2004.
486. Singh, D.; Harding, A. J.; Albadawi, E.; Boissonade, F. M.; Haycock, J. W.; Claeysens, F., Additive manufactured biodegradable poly(glycerol sebacate methacrylate) nerve guidance conduits. *Acta Biomater* **2018**, *78*, 48-63.
487. Koh, H. S.; Yong, T.; Chan, C. K.; Ramakrishna, S., Enhancement of neurite outgrowth using nano-structured scaffolds coupled with laminin. *Biomaterials* **2008**, *29* (26), 3574-82.
488. Sensharma, P.; Madhumathi, G.; Jayant, R. D.; Jaiswal, A. K., Biomaterials and cells for neural tissue engineering: Current choices. *Mater Sci Eng C Mater Biol Appl* **2017**, *77*, 1302-1315.
489. Schnell, E.; Klinkhammer, K.; Balzer, S.; Brook, G.; Klee, D.; Dalton, P.; Mey, J., Guidance of glial cell migration and axonal growth on electrospun nanofibers of poly-epsilon-caprolactone and a collagen/poly-epsilon-caprolactone blend. *Biomaterials* **2007**, *28* (19), 3012-25.
490. He, Q.; Sudibya, H. G.; Yin, Z.; Wu, S.; Li, H.; Boey, F.; Huang, W.; Chen, P.; Zhang, H., Centimeter-Long and Large-Scale Micropatterns of Reduced Graphene Oxide Films: Fabrication and Sensing Applications. *ACS Nano* **2010**, *4* (6), 3201-3208.
491. Kang, B.; Shin, J.; Park, H.-J.; Rhyou, C.; Kang, D.; Lee, S.-J.; Yoon, Y.-s.; Cho, S.-W.; Lee, H., High-resolution acoustophoretic 3D cell patterning to construct functional collateral cylindroids for ischemia therapy. *Nature Communications* **2018**, *9* (1), 5402.
492. Théry, M., Micropatterning as a tool to decipher cell morphogenesis and functions. *Journal of Cell Science* **2010**, *123* (24), 4201-4213.
493. Malkoc, V.; Gallego-Perez, D.; Nelson, T.; Lannutti, J. J.; Hansford, D. J., Controlled neuronal cell patterning and guided neurite growth on micropatterned nanofiber platforms. *Journal of Micromechanics and Microengineering* **2015**, *25* (12), 125001.
- **494. Chen, L.; Yan, C.; Zheng, Z., Functional polymer surfaces for controlling cell behaviors. *Materials Today* **2018**, *21* (1), 38-59.
495. Ren, D.; Xia, Y.; Wang, J.; You, Z., Micropatterning of single cell arrays using the PEG-Silane and Biotin-(Strept)Avidin System with photolithography and chemical vapor deposition. *Sensors and Actuators B: Chemical* **2013**, *188*, 340-346.
496. Wang, Y.; Xu, Z.; Kam, L. C.; Shi, P., Site-Specific Differentiation of Neural Stem Cell Regulated by Micropatterned Multicomponent Interfaces. *Advanced Healthcare Materials* **2014**, *3* (2), 214-220.
497. Xia, Y.; Whitesides, G. M., Soft Lithography. *Annual Review of Materials Science* **1998**, *28* (1), 153-184.
498. Martinez-Rivas, A.; Gonzalez-Quijano, G. K.; Proa-Coronado, S.; Severac, C.; Dague, E., Methods of Micropatterning and Manipulation of Cells for Biomedical Applications. *Micromachines (Basel)* **2017**, *8* (12).
499. Mecozzi, L.; Gennari, O.; Rega, R.; Battista, L.; Ferraro, P.; Grilli, S., Simple and Rapid Bioink Jet Printing for Multiscale Cell Adhesion Islands. *Macromol Biosci* **2017**, *17* (3).

500. Nahmias, Y.; Odde, D. J., Micropatterning of living cells by laser-guided direct writing: application to fabrication of hepatic–endothelial sinusoid-like structures. *Nature Protocols* **2006**, *1* (5), 2288-2296.
501. Naseer, S. M.; Manbachi, A.; Samandari, M.; Walch, P.; Gao, Y.; Zhang, Y. S.; Davoudi, F.; Wang, W.; Abrinia, K.; Cooper, J. M.; Khademhosseini, A.; Shin, S. R., Surface acoustic waves induced micropatterning of cells in gelatin methacryloyl (GelMA) hydrogels. *Biofabrication* **2017**, *9* (1), 015020.
502. Tse, C. C. W.; Ng, S. S.; Stringer, J.; MacNeil, S.; Haycock, J. W.; Smith, P. J., Utilising Inkjet Printed Paraffin Wax for Cell Patterning Applications. *International Journal of Bioprinting* **2016**, *2* (0).
503. Xu, F.-J., Deciphering the impact of PEG antifouling layer on surface attached functional peptides in regulating cell behaviors. *Chinese Chemical Letters* **2019**, *30* (12), 2051-2052.
504. Cui, X.; Boland, T.; D'Lima, D. D.; Lotz, M. K., Thermal inkjet printing in tissue engineering and regenerative medicine. *Recent Pat Drug Deliv Formul* **2012**, *6* (2), 149-55.
505. Zhang, C.; Zhang, Y.; Shao, H.; Hu, X., Hybrid Silk Fibers Dry-Spun from Regenerated Silk Fibroin/Graphene Oxide Aqueous Solutions. *ACS Appl Mater Interfaces* **2016**, *8* (5), 3349-58.
506. Correia, C.; Bhumiratana, S.; Yan, L. P.; Oliveira, A. L.; Gimble, J. M.; Rockwood, D.; Kaplan, D. L.; Sousa, R. A.; Reis, R. L.; Vunjak-Novakovic, G., Development of silk-based scaffolds for tissue engineering of bone from human adipose-derived stem cells. *Acta Biomater* **2012**, *8* (7), 2483-92.
507. Zhu, M.; Wang, K.; Mei, J.; Li, C.; Zhang, J.; Zheng, W.; An, D.; Xiao, N.; Zhao, Q.; Kong, D.; Wang, L., Fabrication of highly interconnected porous silk fibroin scaffolds for potential use as vascular grafts. *Acta Biomater* **2014**, *10* (5), 2014-23.
508. Qi, Y.; Wang, H.; Wei, K.; Yang, Y.; Zheng, R.-Y.; Kim, I.; Zhang, K.-Q., A Review of Structure Construction of Silk Fibroin Biomaterials from Single Structures to Multi-Level Structures. *International Journal of Molecular Sciences* **2017**, *18* (3), 237.
509. Jackman, S. L.; Chen, C. H.; Chettih, S. N.; Neufeld, S. Q.; Drew, I. R.; Agba, C. K.; Flaquer, I.; Stefano, A. N.; Kennedy, T. J.; Belinsky, J. E.; Roberston, K.; Beron, C. C.; Sabatini, B. L.; Harvey, C. D.; Regehr, W. G., Silk Fibroin Films Facilitate Single-Step Targeted Expression of Optogenetic Proteins. *Cell Rep* **2018**, *22* (12), 3351-3361.
510. Tamada, Y., New Process to Form a Silk Fibroin Porous 3-D Structure. *Biomacromolecules* **2005**, *6* (6), 3100-3106.
511. Borkner, C. B.; Elsner, M. B.; Scheibel, T., Coatings and films made of silk proteins. *ACS Appl Mater Interfaces* **2014**, *6* (18), 15611-25.
512. Kinahan, M. E.; Filippidi, E.; Köster, S.; Hu, X.; Evans, H. M.; Pfohl, T.; Kaplan, D. L.; Wong, J., Tunable Silk: Using Microfluidics to Fabricate Silk Fibers with Controllable Properties. *Biomacromolecules* **2011**, *12* (5), 1504-1511.
513. Jacobsen, M. M.; Li, D.; Gyune Rim, N.; Backman, D.; Smith, M. L.; Wong, J. Y., Silk-fibronectin protein alloy fibres support cell adhesion and viability as a high strength, matrix fibre analogue. *Sci Rep* **2017**, *7*, 45653.
514. Kim, Y. H.; Baek, N. S.; Han, Y. H.; Chung, M.-A.; Jung, S.-D., Enhancement of neuronal cell adhesion by covalent binding of poly-d-lysine. *Journal of Neuroscience Methods* **2011**, *202* (1), 38-44.
515. Lam, D.; Enright, H. A.; Cadena, J.; Peters, S. K. G.; Sales, A. P.; Osburn, J. J.; Socia, D. A.; Kulp, K. S.; Wheeler, E. K.; Fischer, N. O., Tissue-specific extracellular matrix accelerates the formation of neural networks and communities in a neuron-glia co-culture on a multi-electrode array. *Scientific Reports* **2019**, *9* (1), 4159.
516. Koss, K. M.; Churchward, M. A.; Nguyen, A. T.; Yager, J. Y.; Todd, K. G.; Unsworth, L. D., Brain biocompatibility and microglia response towards engineered self-assembling (RADA)4 nanoscaffolds. *Acta Biomater* **2016**, *35*, 127-37.

517. Badylak, S. F., The extracellular matrix as a scaffold for tissue reconstruction. *Seminars in Cell & Developmental Biology* **2002**, *13* (5), 377-383.
518. Lee, J. W.; Lee, K. Y., Dual peptide-presenting hydrogels for controlling the phenotype of PC12 cells. *Colloids Surf B Biointerfaces* **2017**, *152*, 36-41.
519. Yang, Y. H.; Khan, Z.; Ma, C.; Lim, H. J.; Smith Callahan, L. A., Optimization of adhesive conditions for neural differentiation of murine embryonic stem cells using hydrogels functionalized with continuous Ile-Lys-Val-Ala-Val concentration gradients. *Acta Biomater* **2015**, *21*, 55-62.
520. Kim, W. H.; Schnaper, H. W.; Nomizu, M.; Yamada, Y.; Kleinman, H. K., Apoptosis in Human Fibrosarcoma Cells Is Induced by a Multimeric Synthetic Tyr-Ile-Gly-Ser-Arg (YIGSR)-containing Polypeptide from Laminin. *Cancer Research* **1994**, *54* (18), 5005-5010.
521. Motta, C. M. M.; Endres, K. J.; Wesdemiotis, C.; Willits, R. K.; Becker, M. L., Enhancing Schwann cell migration using concentration gradients of laminin-derived peptides. *Biomaterials* **2019**, *218*, 119335.
522. Ma, Z.; Kotaki, M.; Inai, R.; Ramakrishna, S., Potential of Nanofiber Matrix as Tissue-Engineering Scaffolds. *Tissue engineering* **2005**, *11* (1-2), 101-109.
- *523. Zhang, S., Fabrication of novel biomaterials through molecular self-assembly. *Nature Biotechnology* **2003**, *21*, 1171.
- **524. Zhao, X.; Pan, F.; Xu, H.; Yaseen, M.; Shan, H.; Hauser, C. A.; Zhang, S.; Lu, J. R., Molecular self-assembly and applications of designer peptide amphiphiles. *Chem Soc Rev* **2010**, *39* (9), 3480-98.
525. Genové, E.; Shen, C.; Zhang, S.; Semino, C. E., The effect of functionalized self-assembling peptide scaffolds on human aortic endothelial cell function. *Biomaterials* **2005**, *26* (16), 3341-3351.
526. Ellis-Behnke, R. G.; Liang, Y.-X.; You, S.-W.; Tay, D. K. C.; Zhang, S.; So, K.-F.; Schneider, G. E., Nano neuro knitting: Peptide nanofiber scaffold for brain repair and axon regeneration with functional return of vision. *Proceedings of the National Academy of Sciences of the United States of America* **2006**, *103* (13), 5054-5059.
527. Davis, M. E.; Motion, J. P. M.; Narmoneva, D. A.; Takahashi, T.; Hakuno, D.; Kamm, R. D.; Zhang, S.; Lee, R. T., Injectable self-assembling peptide nanofibers create intramyocardial microenvironments for endothelial cells. *Circulation* **2005**, *111* (4), 442-450.
528. Yanlian, Y.; Ulung, K.; Xiumei, W.; Horii, A.; Yokoi, H.; Shuguang, Z., Designer self-assembling peptide nanomaterials. *Nano Today* **2009**, *4* (2), 193-210.
529. Wu, E. C.; Zhang, S.; Hauser, C. A. E., Self-Assembling Peptides as Cell-Interactive Scaffolds. *Advanced Functional Materials* **2012**, *22* (3), 456-468.
- **530. Chen, C.; Zhang, Y.; Fei, R.; Cao, C.; Wang, M.; Wang, J.; Bai, J.; Cox, H.; Waigh, T.; Lu, J. R.; Xu, H., Hydrogelation of the Short Self-Assembling Peptide I3QGK Regulated by Transglutaminase and Use for Rapid Hemostasis. *ACS Appl Mater Interfaces* **2016**, *8* (28), 17833-41.
531. Wang, T.; Qu, G.; Deng, Y.; Shang, J.; Feng, Z.; Yang, F.; He, N.; Zheng, J., Post-self-repair process of neuron cells under the influence of neutral and cationic nanoparticles. *Chinese Chemical Letters* **2019**, *30* (12), 2368-2374.
532. Wang, H. Y.; Zhang, Y. Q., Processing and characterisation of a novel electropolymerized silk fibroin hydrogel membrane. *Sci Rep* **2014**, *4*, 6182.
533. Westerink, R. H.; Ewing, A. G., The PC12 cell as model for neurosecretion. *Acta Physiol (Oxf)* **2008**, *192* (2), 273-85.
534. Levi, A.; Eldridge, J.; Paterson, B., Molecular cloning of a gene sequence regulated by nerve growth factor. *Science* **1985**, *229* (4711), 393-395.
535. Aznar-Cervantes, S.; Pagan, A.; Martinez, J. G.; Bernabeu-Esclapez, A.; Otero, T. F.; Meseguer-Olmo, L.; Paredes, J. I.; Cenis, J. L., Electrospun silk fibroin scaffolds coated with reduced graphene promote neurite outgrowth of PC-12 cells under electrical stimulation. *Mater Sci Eng C Mater Biol Appl* **2017**, *79*, 315-325.

536. Cao, H.; Liu, T.; Chew, S. Y., The application of nanofibrous scaffolds in neural tissue engineering. *Adv Drug Deliv Rev* **2009**, *61* (12), 1055-64.
537. Silva, G. A.; Czeisler, C.; Niece, K. L.; Beniash, E.; Harrington, D. A.; Kessler, J. A.; Stupp, S. I., Selective Differentiation of Neural Progenitor Cells by High-Epitope Density Nanofibers. *Science* **2004**, *303* (5662), 1352-1355.
- **538. Khalili, A. A.; Ahmad, M. R., A Review of Cell Adhesion Studies for Biomedical and Biological Applications. *Int J Mol Sci* **2015**, *16* (8), 18149-84.
539. Okano, T.; Yamada, N.; Okuhara, M.; Sakai, H.; Sakurai, Y., Mechanism of cell detachment from temperature-modulated, hydrophilic-hydrophobic polymer surfaces. *Biomaterials* **1995**, *16* (4), 297-303.
540. Ghahari, A.; Enderle, J. D., A physiological neural controller of a muscle fiber oculomotor plant in horizontal monkey saccades. *ISRN Ophthalmol* **2014**, *2014*, 406210-406210.
541. Lee, E.-j.; Chan, E. W. L.; Luo, W.; Yousaf, M. N., Ligand slope, density and affinity direct cell polarity and migration on molecular gradient surfaces. *RSC Advances* **2014**, *4* (60), 31581-31588.
542. Guenard, V.; Kleitman, N.; Morrissey, T.; Bunge, R.; Aebischer, P., Syngenic Schwann cells derived from adult nerves seeded in semipermeable guidance channels enhance peripheral nerve regeneration. *The Journal of Neuroscience* **1992**, *12* (9), 3310-3320.
543. Li, Y.; Huang, G.; Zhang, X.; Wang, L.; Du, Y.; Lu, T. J.; Xu, F., Engineering cell alignment in vitro. *Biotechnol Adv* **2014**, *32* (2), 347-65.
544. Guo, J.; Ling, S.; Li, W.; Chen, Y.; Li, C.; Omenetto, F. G.; Kaplan, D. L., Coding Cell Micropatterns Through Peptide Inkjet Printing for Arbitrary Biomineralized Architectures. *Advanced Functional Materials* **2018**, *28* (19), 1800228.
545. Phillippi, J. A.; Miller, E.; Weiss, L.; Huard, J.; Waggoner, A.; Campbell, P., Microenvironments engineered by inkjet bioprinting spatially direct adult stem cells toward muscle- and bone-like subpopulations. *Stem Cells* **2008**, *26* (1), 127-34.
- *546. He, P.; Derby, B., Controlling Coffee Ring Formation during Drying of Inkjet Printed 2D Inks. *Advanced Materials Interfaces* **2017**, *4* (22), 1700944.
547. Kawaguchi, K.; Kageyama, R.; Sano, M., Topological defects control collective dynamics in neural progenitor cell cultures. *Nature* **2017**, *545* (7654), 327-331.
548. Ye, W.; Li, H.; Yu, K.; Xie, C.; Wang, P.; Zheng, Y.; Zhang, P.; Xiu, J.; Yang, Y.; Zhang, F.; He, Y.; Gao, Q., 3D printing of gelatin methacrylate-based nerve guidance conduits with multiple channels. *Materials & Design* **2020**, *192*, 108757.
549. Tojima, T.; Yamane, Y.; Takahashi, M.; Ito, E., Acquisition of neuronal proteins during differentiation of NG108-15 cells. *Neuroscience research* **2000**, *37* (2), 153-61.
550. Lee, C. J.; Huie, P.; Leng, T.; Peterman, M. C.; Marmor, M. F.; Blumenkranz, M. S.; Bent, S. F.; Fishman, H. A., Microcontact Printing on Human Tissue for Retinal Cell Transplantation. *Archives of Ophthalmology* **2002**, *120* (12), 1714-1718.
551. Singhvi, R.; Kumar, A.; Lopez, G.; Stephanopoulos, G.; Wang, D.; Whitesides, G.; Ingber, D., Engineering cell shape and function. *Science* **1994**, *264* (5159), 696-698.
552. Zhu, Y.; Crowley, S. C.; Latimer, A. J.; Lewis, G. M.; Nash, R.; Kucenas, S., Migratory Neural Crest Cells Phagocytose Dead Cells in the Developing Nervous System. *Cell* **2019**, *179* (1), 74-89 e10.
553. Bertram, L.; Tanzi, R. E., The genetic epidemiology of neurodegenerative disease. *The Journal of Clinical Investigation* **2005**, *115* (6), 1449-1457.
554. Boni, R.; Ali, A.; Shavandi, A.; Clarkson, A. N., Current and novel polymeric biomaterials for neural tissue engineering. *Journal of Biomedical Science* **2018**, *25* (1), 90.
555. Schmidt, C. E.; Leach, J. B., Neural Tissue Engineering: Strategies for Repair and Regeneration. *Annual Review of Biomedical Engineering* **2003**, *5* (1), 293-347.
556. Bell, J. H. A.; Haycock, J. W., Next Generation Nerve Guides: Materials, Fabrication, Growth Factors, and Cell Delivery. *Tissue Engineering Part B: Reviews* **2012**, *18* (2), 116-128.

557. Gu, X.; Ding, F.; Williams, D. F., Neural tissue engineering options for peripheral nerve regeneration. *Biomaterials* **2014**, *35* (24), 6143-6156.
558. Huebner, E. A.; Strittmatter, S. M., Axon regeneration in the peripheral and central nervous systems. *Results Probl Cell Differ* **2009**, *48*, 339-351.
559. Bédier, A.; Vieu, C.; Arnauduc, F.; Sol, J.-C.; Loubinoux, I.; Vaysse, L., Engineering of adult human neural stem cells differentiation through surface micropatterning. *Biomaterials* **2012**, *33* (2), 504-514.
560. Solanki, A.; Shah, S.; Memoli, K. A.; Park, S. Y.; Hong, S.; Lee, K.-B., Controlling Differentiation of Neural Stem Cells Using Extracellular Matrix Protein Patterns. *Small* **2010**, *6* (22), 2509-2513.
561. Poudel, I.; Lee, J. S.; Tan, L.; Lim, J. Y., Micropatterning-retinoic acid co-control of neuronal cell morphology and neurite outgrowth. *Acta Biomaterialia* **2013**, *9* (1), 4592-4598.
562. Wu, Y.; Wang, L.; Hu, T.; Ma, P. X.; Guo, B., Conductive micropatterned polyurethane films as tissue engineering scaffolds for Schwann cells and PC12 cells. *Journal of Colloid and Interface Science* **2018**, *518*, 252-262.
563. Sun, W.; Gregory, D. A.; Tomeh, M. A.; Zhao, X., Silk Fibroin as a Functional Biomaterial for Tissue Engineering. *International Journal of Molecular Sciences* **2021**, *22* (3), 1499.
564. Zhu, M.; Wang, K.; Mei, J.; Li, C.; Zhang, J.; Zheng, W.; An, D.; Xiao, N.; Zhao, Q.; Kong, D.; Wang, L., Fabrication of highly interconnected porous silk fibroin scaffolds for potential use as vascular grafts. *Acta Biomaterialia* **2014**, *10* (5), 2014-2023.
565. Ananthanarayanan, B.; Little, L.; Schaffer, D. V.; Healy, K. E.; Tirrell, M., Neural stem cell adhesion and proliferation on phospholipid bilayers functionalized with RGD peptides. *Biomaterials* **2010**, *31* (33), 8706-8715.
566. Leal-Egaña, A.; Scheibel, T., Interactions of cells with silk surfaces. *Journal of Materials Chemistry* **2012**, *22* (29), 14330-14336.
567. Sofia, S.; McCarthy, M. B.; Gronowicz, G.; Kaplan, D. L., Functionalized silk-based biomaterials for bone formation. *Journal of Biomedical Materials Research* **2001**, *54* (1), 139-148.
568. Aznar-Cervantes, S.; Pagán, A.; Martínez, J. G.; Bernabeu-Esclapez, A.; Otero, T. F.; Meseguer-Olmo, L.; Paredes, J. I.; Cenis, J. L., Electrospun silk fibroin scaffolds coated with reduced graphene promote neurite outgrowth of PC-12 cells under electrical stimulation. *Materials Science and Engineering: C* **2017**, *79*, 315-325.
569. Wang, J.; Tian, L.; Chen, N.; Ramakrishna, S.; Mo, X., The cellular response of nerve cells on poly-L-lysine coated PLGA-MWCNTs aligned nanofibers under electrical stimulation. *Materials Science and Engineering: C* **2018**, *91*, 715-726.
570. Wang, H.-Y.; Zhang, Y.-Q., Processing and characterisation of a novel electropolymerized silk fibroin hydrogel membrane. *Scientific Reports* **2014**, *4*, 6182.
571. Dufrêne, Y. F.; Ando, T.; Garcia, R.; Alsteens, D.; Martinez-Martin, D.; Engel, A.; Gerber, C.; Müller, D. J., Imaging modes of atomic force microscopy for application in molecular and cell biology. *Nature Nanotechnology* **2017**, *12*, 295.
572. Shi, W.; Sun, M.; Hu, X.; Ren, B.; Cheng, J.; Li, C.; Duan, X.; Fu, X.; Zhang, J.; Chen, H.; Ao, Y., Structurally and Functionally Optimized Silk-Fibroin-Gelatin Scaffold Using 3D Printing to Repair Cartilage Injury In Vitro and In Vivo. *Adv Mater* **2017**, *29* (29).
573. Lakkaraju, S. K.; Hwang, W., Critical buckling length vs. persistence length: What governs a biofilament conformation? *Physical review letters* **2009**, *102* (11), 118102-118102.
574. Ito, E.; Suzuki, K.; Yamato, M.; Yokoyama, M.; Sakurai, Y.; Okano, T., Active platelet movements on hydrophobic/hydrophilic microdomain-structured surfaces. *Journal of Biomedical Materials Research* **1998**, *42* (1), 148-155.
575. Kikuchi, A.; Okano, T., Nanostructured designs of biomedical materials: applications of cell sheet engineering to functional regenerative tissues and organs. *Journal of Controlled Release* **2005**, *101* (1), 69-84.

576. Gupta, P.; Agrawal, A.; Murali, K.; Varshney, R.; Beniwal, S.; Manhas, S.; Roy, P.; Lahiri, D., Differential neural cell adhesion and neurite outgrowth on carbon nanotube and graphene reinforced polymeric scaffolds. *Materials Science and Engineering: C* **2019**, *97*, 539-551.
577. Sbricoli, L.; Guazzo, R.; Annunziata, M.; Gobbato, L.; Bressan, E.; Nastro, L., Selection of Collagen Membranes for Bone Regeneration: A Literature Review. *Materials (Basel)* **2020**, *13* (3).
578. Lü, X.; Zhang, H.; Huang, Y.; Zhang, Y., A proteomics study to explore the role of adsorbed serum proteins for PC12 cell adhesion and growth on chitosan and collagen/chitosan surfaces. *Regenerative Biomaterials* **2018**, *5* (5), 261-273.
579. Wiatrak, B.; Kubis-Kubiak, A.; Piwowar, A.; Barg, E., PC12 Cell Line: Cell Types, Coating of Culture Vessels, Differentiation and Other Culture Conditions. *Cells* **2020**, *9* (4).
580. Dong, C.; Lv, Y., Application of Collagen Scaffold in Tissue Engineering: Recent Advances and New Perspectives. *Polymers (Basel)* **2016**, *8* (2).
581. Pateman, C. J.; Harding, A. J.; Glen, A.; Taylor, C. S.; Christmas, C. R.; Robinson, P. P.; Rimmer, S.; Boissonade, F. M.; Claeysens, F.; Haycock, J. W., Nerve guides manufactured from photocurable polymers to aid peripheral nerve repair. *Biomaterials* **2015**, *49*, 77-89.
582. Soltman, D.; Subramanian, V., Inkjet-Printed Line Morphologies and Temperature Control of the Coffee Ring Effect. *Langmuir* **2008**, *24* (5), 2224-2231.
583. Li, Y.; Huang, G.; Zhang, X.; Wang, L.; Du, Y.; Lu, T. J.; Xu, F., Engineering cell alignment in vitro. *Biotechnology Advances* **2014**, *32* (2), 347-365.
584. Kawaguchi, K.; Kageyama, R.; Sano, M., Topological defects control collective dynamics in neural progenitor cell cultures. *Nature* **2017**, *545*, 327.
585. Han, S.; Cao, S.; Wang, Y.; Wang, J.; Xia, D.; Xu, H.; Zhao, X.; Lu, J. R., Self-assembly of short peptide amphiphiles: the cooperative effect of hydrophobic interaction and hydrogen bonding. *Chemistry* **2011**, *17* (46), 13095-102.
586. Zheng, S.; Guan, Y.; Yu, H.; Huang, G.; Zheng, C., Poly-L-lysine-coated PLGA/poly(amino acid)-modified hydroxyapatite porous scaffolds as efficient tissue engineering scaffolds for cell adhesion, proliferation, and differentiation. *New Journal of Chemistry* **2019**, *43* (25), 9989-10002.
587. Kouhi, M.; Fathi, M.; Prabhakaran, M. P.; Shamanian, M.; Ramakrishna, S., Poly L lysine-modified PHBV based nanofibrous scaffolds for bone cell mineralization and osteogenic differentiation. *Applied Surface Science* **2018**, *457*, 616-625.
588. Hall, A.; Wu, L.-P.; Parhamifar, L.; Moghimi, S. M., Differential modulation of cellular bioenergetics by poly(L-lysine)s of different molecular weights. *Biomacromolecules* **2015**, *16* (7), 2119-2126.
589. Zheng, M.; Pan, M.; Zhang, W.; Lin, H.; Wu, S.; Lu, C.; Tang, S.; Liu, D.; Cai, J., Poly(α -L-lysine)-based nanomaterials for versatile biomedical applications: Current advances and perspectives. *Bioactive Materials* **2021**, *6* (7), 1878-1909.
590. Rider, P.; Zhang, Y.; Tse, C.; Zhang, Y.; Jayawardane, D.; Stringer, J.; Callaghan, J.; Brook, I. M.; Miller, C. A.; Zhao, X.; Smith, P. J., Biocompatible silk fibroin scaffold prepared by reactive inkjet printing. *J Mater Sci* **2016**, *51* (18), 8625-8630.
591. Lee, C. J.; Huie, P.; Leng, T.; Peterman, M. C.; Marmor, M. F.; Blumenkranz, M. S.; Bent, S. F.; Fishman, H. A., Microcontact Printing on Human Tissue for Retinal Cell Transplantation. *JAMA Ophthalmology* **2002**, *120* (12), 1714-1718.
592. Lizarraga-Valderrama, L. R.; Nigmatullin, R.; Ladino, B.; Taylor, C. S.; Boccaccini, A. R.; Knowles, J. C.; Claeysens, F.; Haycock, J. W.; Roy, I., Modulation of neuronal cell affinity of composite scaffolds based on polyhydroxyalkanoates and bioactive glasses. *Biomedical Materials* **2020**, *15* (4), 045024.
593. Curcio, M.; Bradke, F., Axon Regeneration in the Central Nervous System: Facing the Challenges from the Inside. *Annual Review of Cell and Developmental Biology* **2018**, *34* (1), 495-521.

594. Mendibil, X.; González-Pérez, F.; Bazan, X.; Díez-Ahedo, R.; Quintana, I.; Rodríguez, F. J.; Basnett, P.; Nigmatullin, R.; Lukasiewicz, B.; Roy, I.; Taylor, C. S.; Glen, A.; Claeysens, F.; Haycock, J. W.; Schaafsma, W.; González, E.; Castro, B.; Duffy, P.; Merino, S., Bioresorbable and Mechanically Optimized Nerve Guidance Conduit Based on a Naturally Derived Medium Chain Length Polyhydroxyalkanoate and Poly(ϵ -Caprolactone) Blend. *ACS Biomaterials Science & Engineering* **2021**, *7* (2), 672-689.
595. Chaudhuri, O.; Koshy, S. T.; Branco da Cunha, C.; Shin, J.-W.; Verbeke, C. S.; Allison, K. H.; Mooney, D. J., Extracellular matrix stiffness and composition jointly regulate the induction of malignant phenotypes in mammary epithelium. *Nature Materials* **2014**, *13* (10), 970-978.
596. Watt, F. M.; Huck, W. T. S., Role of the extracellular matrix in regulating stem cell fate. *Nature Reviews Molecular Cell Biology* **2013**, *14* (8), 467-473.
597. Gonzalez-Perez, F.; Udina, E.; Navarro, X., Chapter Ten - Extracellular Matrix Components in Peripheral Nerve Regeneration. In *International Review of Neurobiology*, Geuna, S.; Perroteau, I.; Tos, P.; Battiston, B., Eds. Academic Press: 2013; Vol. 108, pp 257-275.
598. Zhu, M.; Li, W.; Dong, X.; Yuan, X.; Midgley, A. C.; Chang, H.; Wang, Y.; Wang, H.; Wang, K.; Ma, P. X.; Wang, H.; Kong, D., In vivo engineered extracellular matrix scaffolds with instructive niches for oriented tissue regeneration. *Nature Communications* **2019**, *10* (1), 4620.
599. Jiang, H.; Qian, Y.; Fan, C.; Ouyang, Y., Polymeric Guide Conduits for Peripheral Nerve Tissue Engineering. *Front Bioeng Biotechnol* **2020**, *8* (1140).
600. Georgiou, M.; Bunting, S. C. J.; Davies, H. A.; Loughlin, A. J.; Golding, J. P.; Phillips, J. B., Engineered neural tissue for peripheral nerve repair. *Biomaterials* **2013**, *34* (30), 7335-7343.
601. Pawelec, K. M.; Best, S. M.; Cameron, R. E., Collagen: a network for regenerative medicine. *J Mater Chem B* **2016**, *4* (40), 6484-6496.
602. Parenteau-Bareil, R.; Gauvin, R.; Berthod, F., Collagen-Based Biomaterials for Tissue Engineering Applications. *Materials* **2010**, *3* (3), 1863-1887.
603. Wu, Y.; Zheng, Q.; Du, J.; Song, Y.; Wu, B.; Guo, X., Self-assembled IKVAV peptide nanofibers promote adherence of PC12 cells. *Journal of Huazhong University of Science and Technology* **2006**, *26* (5), 594-596.
604. Lee, J. W.; Lee, K. Y., Dual peptide-presenting hydrogels for controlling the phenotype of PC12 cells. *Colloids and Surfaces B: Biointerfaces* **2017**, *152*, 36-41.
605. Llacua, A.; de Haan, B. J.; Smink, S. A.; de Vos, P., Extracellular matrix components supporting human islet function in alginate-based immunoprotective microcapsules for treatment of diabetes. *Journal of Biomedical Materials Research Part A* **2016**, *104* (7), 1788-1796.
606. Gelain, F.; Luo, Z.; Rioult, M.; Zhang, S., Self-assembling peptide scaffolds in the clinic. *npj Regenerative Medicine* **2021**, *6* (1), 9.
607. Koss, K. M.; Churchward, M. A.; Nguyen, A. T.; Yager, J. Y.; Todd, K. G.; Unsworth, L. D., Brain biocompatibility and microglia response towards engineered self-assembling (RADA)4 nanoscaffolds. *Acta Biomaterialia* **2016**, *35*, 127-137.
608. Sun, W.; Taylor, C. S.; Zhang, Y.; Gregory, D. A.; Tomeh, M. A.; Haycock, J. W.; Smith, P. J.; Wang, F.; Xia, Q.; Zhao, X., Cell guidance on peptide micropatterned silk fibroin scaffolds. *Journal of Colloid and Interface Science* **2021**, *603*, 380-390.
609. Leal-Egaña, A.; Scheibel, T., Interactions of cells with silk surfaces. *Journal of materials chemistry* **2012**, *22* (29), 1433-14336.
610. Al-Ghobashy, M. A., Electrophoretic behavior of charge regulated zwitter ionic buffers in covalently and dynamically coated fused silica capillaries. *Bulletin of Faculty of Pharmacy, Cairo University* **2014**, *52* (1), 71-78.
611. Morgan, A. A.; Rubenstein, E., Proline: The Distribution, Frequency, Positioning, and Common Functional Roles of Proline and Polyproline Sequences in the Human Proteome. *PLOS ONE* **2013**, *8* (1), e53785.

612. Wang, J.; Han, S.; Meng, G.; Xu, H.; Xia, D.; Zhao, X.; Schweins, R.; Lu, J. R., Dynamic self-assembly of surfactant-like peptides A6K and A9K. *Soft Matter* **2009**, *5* (20), 3870-3878.
613. Restuccia, A.; Seroski, D. T.; Kelley, K. L.; O'Bryan, C. S.; Kurian, J. J.; Knox, K. R.; Farhadi, S. A.; Angelini, T. E.; Hudalla, G. A., Hierarchical self-assembly and emergent function of densely glycosylated peptide nanofibers. *Communications Chemistry* **2019**, *2* (1), 53.
614. Zheng, H.; Tian, Y.; Gao, Q.; Yu, Y.; Xia, X.; Feng, Z.; Dong, F.; Wu, X.; Sui, L., Hierarchical Micro-Nano Topography Promotes Cell Adhesion and Osteogenic Differentiation via Integrin α 2-PI3K-AKT Signaling Axis. *Front Bioeng Biotechnol* **2020**, *8* (463).
615. Johnston, E. R.; Miyagi, Y.; Chuah, J.-A.; Numata, K.; Serban, M. A., The interplay between silk fibroin's structure and its adhesive properties. *ACS biomaterials science & engineering* **2018**, *4* (8), 2815-2824.
616. Wiatrak, B.; Kubis-Kubiak, A.; Piwowar, A.; Barg, E., PC12 Cell Line: Cell Types, Coating of Culture Vessels, Differentiation and Other Culture Conditions. *Cells* **2020**, *9* (4), 958.
617. Lam, J.; Carmichael, S. T.; Lowry, W. E.; Segura, T., Hydrogel design of experiments methodology to optimize hydrogel for iPSC-NPC culture. *Advanced healthcare materials* **2015**, *4* (4), 534-539.
618. Jain, R.; Roy, S., Controlling Neuronal Cell Growth through Composite Laminin Supramolecular Hydrogels. *ACS Biomaterials Science & Engineering* **2020**, *6* (5), 2832-2846.
619. Zhao, Y.; Zhu, Z. S.; Guan, J.; Wu, S. J., Processing, mechanical properties and bio-applications of silk fibroin-based high-strength hydrogels. *Acta Biomaterialia* **2021**, *125*, 57-71.
620. Mao, Z.; Bi, X.; Ye, F.; Shu, X.; Sun, L.; Guan, J.; Ritchie, R. O.; Wu, S., Controlled Cryogelation and Catalytic Cross-Linking Yields Highly Elastic and Robust Silk Fibroin Scaffolds. *ACS Biomaterials Science & Engineering* **2020**, *6* (8), 4512-4522.
621. Mohammadzadehmoghadam, S.; Dong, Y., Fabrication and Characterization of Electrospun Silk Fibroin/Gelatin Scaffolds Crosslinked With Glutaraldehyde Vapor. *Frontiers in Materials* **2019**, *6* (91).
622. Askari, M.; Afzali Naniz, M.; Kouhi, M.; Saberi, A.; Zolfagharian, A.; Bodaghi, M., Recent progress in extrusion 3D bioprinting of hydrogel biomaterials for tissue regeneration: a comprehensive review with focus on advanced fabrication techniques. *Biomaterials Science* **2021**, *9* (3), 535-573.
623. Thakur, A.; Jaiswal, M. K.; Peak, C. W.; Carrow, J. K.; Gentry, J.; Dolatshahi-Pirouz, A.; Gaharwar, A. K., Injectable shear-thinning nanoengineered hydrogels for stem cell delivery. *Nanoscale* **2016**, *8* (24), 12362-12372.
624. Cross, L. M.; Shah, K.; Palani, S.; Peak, C. W.; Gaharwar, A. K., Gradient nanocomposite hydrogels for interface tissue engineering. *Nanomedicine: Nanotechnology, Biology and Medicine* **2018**, *14* (7), 2465-2474.
625. Kirillova, A.; Maxson, R.; Stoychev, G.; Gomillion, C. T.; Ionov, L., 4D Biofabrication Using Shape-Morphing Hydrogels. *Advanced Materials* **2017**, *29* (46), 1703443.
626. Morouço, P.; Lattanzi, W.; Alves, N., Four-Dimensional Bioprinting As a New Era for Tissue Engineering and Regenerative Medicine. *Front Bioeng Biotechnol* **2017**, *5*, 61-61.
627. Gao, B.; Yang, Q.; Zhao, X.; Jin, G.; Ma, Y.; Xu, F., 4D Bioprinting for Biomedical Applications. *Trends in Biotechnology* **2016**, *34* (9), 746-756.
628. Kim, S. H.; Seo, Y. B.; Yeon, Y. K.; Lee, Y. J.; Park, H. S.; Sultan, M. T.; Lee, J. M.; Lee, J. S.; Lee, O. J.; Hong, H.; Lee, H.; Ajiteru, O.; Suh, Y. J.; Song, S.-H.; Lee, K.-H.; Park, C. H., 4D-bioprinted silk hydrogels for tissue engineering. *Biomaterials* **2020**, *260*, 120281.
629. Singha, N.; Srivastava, A.; Pramanik, B.; Ahmed, S.; Dowari, P.; Chowdhuri, S.; Das, B. K.; Debnath, A.; Das, D., Unusual confinement properties of a water insoluble small peptide hydrogel. *Chemical Science* **2019**, *10* (23), 5920-5928.
630. Huebsch, N.; Gilbert, M.; Healy, K. E., Analysis of sterilization protocols for peptide-modified hydrogels. *Journal of Biomedical Materials Research Part B: Applied Biomaterials* **2005**, *74B* (1), 440-447.